Investigation of static and dynamic shear behavior of bonded concrete-rock interfaces under low normal loading : experimental and numerical analysis

Menes Badika Kiyedi

THÈSE

Pour obtenir le grade de

DOCTEUR DE L'UNIVERSITÉ GRENOBLE ALPES

École doctorale : I-MEP2 - Ingénierie - Matériaux, Mécanique, Environnement, Energétique, Procédés, Production
Spécialité : 2MGE - Matériaux, Mécanique, Génie civil, Electrochimie
Unité de recherche : Laboratoire Sols, Solides, Structures et Risques

Étude du comportement statique et dynamique d'interfaces béton-roche en cisaillement sous charge normale faible: analyses expérimentales et numériques

Investigation of static and dynamic shear behavior of bonded concrete-rock interfaces under low normal loading: experimental and numerical analysis

Présentée par :

Menes BADIKA KIYEDI

Direction de thèse :

Dominique SALETTI MAITRE DE CONFERENCES, Université Grenoble Alpes	Directeur de thèse
Matthieu BRIFFAUT Centrale Lille Institut	Co-directeur de thèse
Sophie CAPDEVIELLE ENSEIGNANTE CHERCHEUSE, Université Grenoble Alpes	Co-encadrante de thèse

Rapporteurs :

Fabrice GATUINGT
PROFESSEUR DES UNIVERSITES, ENS Paris-Saclay
David BERTRAND
MAITRE DE CONFERENCES HDR, INSA Lyon

Thèse soutenue publiquement le **8 novembre 2023**, devant le jury composé de :

Dominique SALETTI DOCTEUR EN SCIENCES, Université Grenoble Alpes	Directeur de thèse
Marion BOST DIRECTRICE DE RECHERCHE, Université Gustave Eiffel	Examinatrice
Jean-Baptiste COLLIAT PROFESSEUR DES UNIVERSITES, Université de Lille	Examinateur
Yann MALECOT PROFESSEUR DES UNIVERSITES, Université Grenoble Alpes	Président
Matthieu BRIFFAUT PROFESSEUR DES UNIVERSITES, Université de Lille	Co-directeur de thèse
Fabrice GATUINGT PROFESSEUR DES UNIVERSITES, ENS Paris-Saclay	Rapporteur
David BERTRAND MAITRE DE CONFERENCES HDR, INSA Lyon	Rapporteur

Invitée:
Sophie CAPDEVIELLE
Université Grenoble Alpes

Acknowledgments

I express my gratitude for the opportunity to my thesis supervisors, Dominique Saletti, Matthieu Briffaut, and Sophie Capdevielle. Thank you very much for your encouragement, support, and guidance during the three years of this thesis.

I am grateful to Frédéric-Victor Donzé and Christophe Dano for evaluating the progress of this thesis. I appreciate your interest in my work.

I acknowledge the jury members for agreeing to assess my work, especially Fabrice Gatuingt and David Bertrand, for reporting on my thesis.

I am thankful to the many incredible people I have come to know at the 3SR laboratory. I especially thank Cino Viggiani, head of the master's program GCER, which first brought me to Grenoble and played a crucial role in my decision to pursue a Ph.D.

I thank Stephen Fityus and Klaus Thoeni, who supervised my master’s thesis project at the University of Newcastle in Australia. I also thank Anna Giacomini, who made this project possible. The scientific and personal growth I gained from this experience proved useful during my thesis.

I thank wholeheartedly the amazing group of the rock mechanics laboratory of the Federal University of Minas Gerais, Brazil, for so many things on personal and academic levels. I especially thank Cláudio Lúcio, an inspiring teacher and experimentalist.

Thanks to my friends in DR Congo, Brazil, and France for their support and understanding during this process.

I will never have enough words to thank my family for always being there for me.

Abstract

The shear behavior of rock-rock and concrete-rock interfaces is investigated for the design and structural stability assessment of geotechnical structures (tunnels, concrete-gravity dams). Most of the studies focused on the static shear behavior of rock-rock interfaces. These studies show that the shear resistance of rock-rock interfaces depends mainly on normal stress and roughness. However, the investigation of the static shear behavior of concrete-rock interfaces under low normal loadings shows that the concrete-rock bonds significantly influence the shear resistance beyond the normal stress and roughness. Despite this progress, more experimental and numerical work is required to further understand the shear behavior of concrete-rock interfaces. In particular, it is relevant to investigate the dynamic shear behavior of concrete-rock interfaces.

This thesis investigates the influence of roughness and concrete-rock bonds on the shear behavior of concrete-rock interfaces subjected to low normal loading. A two-fold approach combining experimental and numerical modeling is adopted. The experimental work includes a pioneering experimental campaign to investigate the dynamic shear behavior of concrete-rock interfaces focusing on impact shear loading.

The interpretation of recent experimental works, particularly concrete-granite interfaces, has distinguished the influence of the roughness scales on the shear behavior of concrete-rock interfaces. The unevenness (micro-roughness) is responsible for forming concrete-rock bonds. The waviness (macro-roughness) contributes to the shear resistance of concrete-rock interfaces through surface interlocking. The numerical modeling of these interfaces is based on this separation. The cohesive-frictional model simulates the influence of the unevenness and, therefore, the concrete-rock bonds. In contrast, the influence of the waviness is taken into account by the explicit representation of the 3D morphology of the interface through surface interlocking. This model is validated by performing a comparative evaluation of the results of experimental tests and the results of simulations of direct shear tests.

A new approach has been proposed to investigate the influence of roughness on the shear resistance of concrete-rock interfaces based on the validated numerical modeling. The approach consists of generating synthetic rough rock surfaces through random field simulations and performing simulations of direct shear tests of concrete-rock interfaces comprising the generated surfaces. The analysis of the results of these tests leads to the proposition of two failure criteria. The first is an analytical relationship, while the second is a neural network model.

The dynamic shear behavior of concrete-rock interfaces has been investigated as well. The dynamic shear loading is applied using a modified split Hopkinson pressure bar system with one input bar and two output bars. A modified confinement ring is used to generate low normal stresses. The outcomes of this study show that, like the static shear behavior, the dynamic shear behavior of concrete-rock interfaces depends on the concrete-rock bonds and friction. However, there is a double mobilization of concrete-rock bonds and friction in the pre-peak and the post-peak stages. The dynamic shear resistance is not strongly dependent on the normal stress. Furthermore, the dynamic shear resistance is three to four times the static shear resistance of interfaces.

The interpretation of the recent static experimental studies, the numerical simulations of rough concrete-rock interfaces, the analytical models proposed to estimate the shear resistance of concrete-rock interfaces, and the pioneering dynamic testing of concrete-rock interfaces have all provided new insights into the understanding of the shear behavior of concrete-rock interfaces.

Keywords: Concrete–rock interfaces, Dynamic shear behavior, Static shear behavior, Roughness, Concrete–rock bonds, Cohesive-frictional model

Résumé

L'étude du comportement en cisaillement des interfaces roche-roche et béton-roche est cruciale pour la conception et l'analyse de la stabilité structurelle de certains ouvrages géotechniques (tunnels, barrage-poids, …). Une grande majorité des études menées ne s'intéresse qu'aux interfaces roche-roche. Ces études montrent que la résistance au cisaillement est principalement influencée par la contrainte normale et la rugosité de l'interface. A contrario, l'examen du comportement en cisaillement des interfaces béton-roche semble montrer que la résistance au pic de ces interfaces dépend également fortement de l'adhésion béton-roche justifiant ainsi la nécessité de nouvelles investigations aussi bien du point de vue expérimental que numérique.

Ces travaux étudient donc la problématique de l'influence de la rugosité et de l'adhésion sur le comportement de cisaillement des interfaces béton-roche dans le cas de contrainte normale modérée par une approche combinant expérimentations et modélisation. En parallèle, une étude pionnière du comportement de cisaillement de ces interfaces sous chargement dynamique de type impact est aussi menée.

Partant de travaux récents sur le comportement en cisaillement d'interfaces béton-granit, une nouvelle interprétation de la contribution de la rugosité à la résistance au cisaillement est proposée. Les irrégularités de surface ou micro-rugosité sont supposées responsables de la formation des liens béton-roche constituant l'adhésion alors que les ondulations de surface ou macro-rugosité contribuent à la résistance au cisaillement par effet d'imbrication. Ainsi la modélisation s'appuie sur une séparation des échelles: l'influence de l'adhésion est simulée par une loi de comportement cohésif et frictionnel et l'influence des ondulations est reproduite en utilisant la géométrie réelle de l'interface. Une validation de l'approche est ensuite proposée par comparaison des résultats des simulations et des résultats expérimentaux.

A partir de cette modélisation numérique, une nouvelle approche pour étudier l'influence de la rugosité dans la résistance au cisaillement des interfaces béton-roche est développée. L'approche consiste à générer des surfaces rocheuses en utilisant la génération par champs aléatoires. Une série d'essais virtuels de cisaillement d'interfaces permet d'établir alors deux modèles pour estimer la résistance au cisaillement. Le premier est constitué d'une modélisation analytique alors que le second repose sur l'utilisation d'une intelligence artificielle de type réseau de neurones.

Finalement, l'étude du comportement en cisaillement des interfaces béton-roche sous chargement dynamique a également été menée. Pour cette étude, un dispositif expérimental permettant de solliciter une éprouvette sous cisaillement confiné a été adapté aux interfaces béton-roche. Les résultats de ces tests montrent que, similaire au test sous sollicitation quasi-statique, la résistance au cisaillement des interfaces béton-roche dépend de liens chimiques béton-roche constituant l'adhésion et de la friction. En outre, la résistance au cisaillement sous chargement dynamique est trois à quatre fois plus importante que la résistance sous chargement statique.

L'interprétation de l'influence de la rugosité sur le comportement de cisaillement, la simulation numérique des essais de cisaillement, la proposition des modèles pour estimer la résistance au cisaillement et les résultats des essais de cisaillement sous chargement dynamique constituent les apports de cette étude sur la compréhension du comportement de cisaillement des interfaces béton-roche.

Mots clés: Interfaces béton-roche, Rugosité, Cisaillement, Comportement statique, Comportement dynamique, Adhésion béton-roche, Modèle cohésif-frictionnel.

Contents

Acknowledgments i
Abstract iii
Résumé v
Contents vii
Introduction 1
1. State of the art 3
1.1 Estimation of the shear resistance of interfaces 4
1.1.1 Mohr-Coulomb failure criterion 4
1.1.2 Patton failure criterion 5
1.1.3 Failure criteria for partially bonded interfaces 6
1.1.4 Barton and Choubey failure criterion 6
1.1.5 Grasselli and Egger failure criterion 8
1.1.6 Summary 8
1.2 Characterization of roughness 9
1.2.1 Measurement systems 9
1.2.2 3SR Laser-based scanner 11
1.2.3 Roughness parameters 12
1.2.3.1 Joint roughness coefficient - JRC 13
1.2.3.2 3D roughness parameter for rock surfaces 15
1.2.4 Measurement resolution 17
1.3 Shear response of concrete-rock interfaces 19
1.3.1 Testing methods 19
1.3.2 Shear evolution of concrete-rock interfaces. 21
1.3.2.1 Experimental studies of the shear behavior of concrete-rock interfaces 21
1.3.2.2 Influence of roughness on the shear resistance of concrete-granite interfaces 25
1.3.3 Summary 28
1.4 Consideration for dynamic shear testing of interfaces 28
1.4.1 Principle of the SHPB 28
1.4.2 Dynamic testing of geomaterials 29
1.4.2.2 Dynamic tensile test 30
1.4.2.3 Dynamic shear test 30
1.4.3 Dynamic responses of interfaces 31
1.5 Numerical modeling of the shear behavior of interfaces 32
1.5.1 Numerical modeling of the shear behavior of unbonded interfaces 32
1.5.1.1 Case of rock-rock interfaces 32

1.5.1.2 Case of concrete-rock interfaces 34
1.5.2 Numerical modeling of the shear behavior of bonded interfaces 35
1.5.2.1 Case of cemented bolt interfaces 35
1.5.2.2 Case of concrete-rock interfaces 35
1.6 Generation of random fields 37
1.6.1 Concepts of random field theory 37
1.6.1.1 Stationarity 38
1.6.1.2 Data transformation 38
1.6.1.3 Characterization of the field for random field simulations 40
1.6.2 Random field generators 41
1.6.3 Application of random field simulations 42
1.7 Concluding remarks 42
2. Numerical simulation of concrete-rock interfaces 45
2.1 Experimental contextualization 45
2.2 Numerical Modeling 46
2.2.1 Behavior law of the concrete-rock interface 46
2.2.2 Simulation of the direct shear test 48
2.2.2.1 Material properties 48
2.2.2.2 Boundary conditions 49
2.2.2.3 Mesh generation 49
2.2.2.4 Parameter of the behavior law of the concrete-rock interface 51
2.2.2.5 Calibration and simulation: bush-hammered interfaces 52
2.2.3 Prediction of the shear response of rough concrete-granite interfaces 54
2.2.3.1 Generation of solids 54
2.2.3.2 Analysis of the simulation of rough concrete-granite interfaces 57
2.2.3.3 Results and discussion of numerical simulations of rough concrete-granite interfaces 63
2.3 Concluding remarks 66
3. Influence of roughness on the shear resistance of interfaces: a new approach 69
3.1 Generation of synthetic rough rock surfaces 69
3.1.1 The roughness of rough rock surfaces as a random function 69
3.1.2 Statistical and geostatistical data processing 69
3.1.3 Simulation of random fields using the turning band method 72
3.1.4 Synthetic rough rock surface generator 74
3.2 Results of the finite element simulations 76
3.3 New peak shear strength criterion for concrete-rock interface 78
3.3.1 Development of failure criterion for concrete-rock interfaces 78

3.3.2 Validation of the new failure criterion 79
3.4 Estimation of peak shear strength of concrete-rock interfaces using neural network modeling 81
3.4.1 Applications of neural network modeling in mechanics of geomaterials 81
3.4.2 Neural network modeling 81
3.4.3 Results of the neural network modeling 85
3.4.3.1 Hyperparameters analysis 85
3.4.3.2 Performance of the neural network model 87
3.5 Assessment of the analytical and the neural network model using experimental data 89
3.6 Discussion: analytical and neural network model 90
3.7 Neural network-based estimation of the shear response of concrete-rock interfaces 92
3.7.1 Neural network modeling for the prediction of the shear response of concrete-rock interfaces 92
3.7.2 Results of the neural network modeling to estimate the shear response of concrete-rock interfaces 94
3.7.2.1 Prediction of the peak shear strength using neural network model 94
3.7.2.2 Prediction of the peak shear strength obtained experimentally using neural network model 95
3.7.2.3 Prediction of the shear response using the validation dataset 95
3.7.2.4 Prediction of the shear response using the experimental data 96
3.7.3 Comparative analysis of the neural networks models 100
3.8 Concluding remarks 101
4. Static and dynamic shear resistance of concrete-rock interfaces 103
4.1 Materials and methods 104
4.1.1 Materials 104
4.1.1.1 Rock 104
4.1.1.2 Concrete 105
4.1.1.3 Concrete-rock sample 106
4.1.1.4 Testing program 107
4.1.2 Methods 107
4.1.2.1 Operation of the confinement ring 107
4.1.2.2 Modification of the confinement ring 108
4.1.2.3 Calibration of the confinement ring 110
4.1.2.4 Static shear test 113
4.1.2.5 Dynamic shear test 114
4.2 Test results 117
4.2.1 Quasi-static tests 117
4.2.1.1 Smooth concrete-sandstone interfaces 117

4.2.1.2 Bush-hammered concrete-granite interfaces 118
4.2.1.3 Rough concrete-granite interface 119
4.2.2 Dynamic tests 120
4.2.2.1 Smooth concrete-sandstone interfaces 121
4.2.2.2 Bush-hammered concrete-granite interfaces 122
4.2.2.3 Rough concrete-granite interface 123
4.3 Discussion 125
4.3.1 Description of the shear evolution 125
4.3.1.1 Static shear response of concrete-rock interfaces 125
4.3.1.2 Dynamic shear response of concrete-rock interfaces 127
4.3.2 Shear resistance of concrete-rock interfaces 129
4.3.3 Comparative evaluation of the static and dynamic peak shear strength of concrete-rock interfaces 131
4.4 Concluding remarks 132
5. Conclusions and perspectives 133
5.1 Conclusions 133
5.2 Perspectives 135
6. Bibliography 139
List of Figures 151
List of Tables 157

Introduction

Investigating the shear behavior of rock-rock and concrete-rock interfaces is relevant in the stability analysis and design of many geotechnical structures. Such structures include concrete-gravity dams (Fishman, 2008, 2009) and rock support systems (Saiang, Malmgren and Nordlund, 2005). In particular, a better understanding of the shear behavior of concrete-rock interfaces is required to reduce conservative considerations assumed in the design and structural stability assessment of concrete-gravity dams. Examples of such considerations include likening the shear behavior of bonded concrete-rock interfaces to the shear behavior of unbonded interfaces. This consideration ignores totally or partially the influence of the cohesion or the strength of the concrete-rock bonds on the shear resistance of concrete-rock interfaces (Krounis, 2016). However, recent studies on the shear behavior of concrete-rock interfaces show that under the conditions of lower normal loadings, which includes most cases of concrete-gravity dams, the shear resistance of concrete-rock interfaces depends mainly on the strength of concrete-rock bonds (Saiang, Malmgren and Nordlund, 2005; Z. A. Moradian *et al.*, 2010; Krounis, Johansson and Larsson, 2016; Badika *et al.*, 2022).

Furthermore, some guidelines for the design and structural stability analysis of concrete-gravity dams recommend using the Mohr-Coulomb failure criterion to estimate the shear resistance of concrete-rock interfaces (EPRI, 1992). This recommendation is problematic because it ignores the influence of roughness on the shear resistance of concrete-rock interfaces, despite the consensus of published works (Barton and Choubey, 1977; Grasselli and Egger, 2003) regarding the influence of roughness on the shear resistance of interfaces under lower normal loadings.

Until recently, most studies investigating the shear behavior of interfaces focused on the shear behavior of rock-rock interfaces. From these studies, the normal stress and the roughness of the interfaces are identified as the most important parameters. Nonetheless, much research has recently been conducted to investigate the shear behavior of concrete-rock interfaces. These studies show that in conditions of low normal loading, the concrete-rock bonds strongly influence the shear behavior of concrete-rock interfaces.

However, gaps in understanding the shear behavior of rock-rock and concrete-rock interfaces remain. A deeper assessment of the influence of roughness on the shear resistance of interfaces is required. The parameters influencing the formation of concrete-rock bonds deserve to be investigated. Since most of the studies in the literature focus on the static shear behavior of rock-rock and concrete-rock interfaces, it is necessary to consider the possibility of dynamic shear loading.

The main objective of this thesis is to investigate the shear behavior of concrete-rock interfaces, focusing on four main aspects. First, it is crucial to understand the influence of roughness on the formation of concrete-rock bonds and the overall shear behavior of concrete-rock interfaces. Second, it is necessary to propose numerical modeling to simulate the shear behavior of concrete-rock interfaces, considering the three-dimensional representation of the roughness of the concrete-rock interfaces. Third, it is essential to propose a different investigative approach to study the influence of roughness on the shear behavior of concrete-rock interfaces beyond the limitations of experimental studies. Fourth, it is fundamental to propose a methodology to investigate the dynamic shear behavior of concrete-rock interfaces focusing on dynamic shear loading generated by high strain rate loading.

This thesis is separated into five parts. The first chapter presents a literature review of the shear behavior of rock-rock and concrete-rock interfaces. This chapter highlights a thorough compilation and analysis of the experimental studies published in the last two decades, which ascertained that the understanding acquired so far is sufficient to move toward numerical modeling of concrete-rock interfaces.

The second chapter proposes the numerical modeling of concrete-rock interfaces submitted to lower normal loadings based on the interpretation of all the major experimental studies reviewed. With the proposed model, a methodology is presented to simulate the direct shear tests of concrete-rock interfaces with an explicit three-dimensional representation of the roughness of the concrete-rock interfaces. The numerical model is calibrated and assessed using the experimental studies encountered in the literature.

The third chapter presents a new investigative approach to studying the influence of roughness on the shear behavior of interfaces using concrete-rock interfaces as a case study. The first part of this approach consists of generating a large and well-distributed database of synthetic rough rock surfaces using random field simulation. The second part is the simulation of the shear behavior of concrete-rock interfaces created using the database of synthetic rough rock surfaces. The last step is the analysis of the results of the simulation. Such analysis leads to more robust models for estimating the shear resistance of interfaces.

The fourth chapter introduces a methodology to investigate the shear behavior of interfaces with the shear loading generated by impact. The methodology maintains the basic concepts of the conventional direct shear test. The first step consists of applying confinement stress to the interfaces, which is done using a modified confinement ring. The second step is the application of the impact shear loading using a split Hopkinson pressure bar system. With this testing method, an experimental campaign was designed to investigate the dynamic shear behavior of smooth concrete-sandstone, bush-hammered concrete-granite, and rough concrete-granite interfaces. The outcomes of this campaign validate the testing method and provide new insights into the shear behavior of concrete-rock interfaces.

The fifth chapter presents the major outcomes of the thesis and proposes perspectives for further works.

1. State of the art

The shear behavior of interfaces, principally rock-rock interfaces, has been and is still one of the most investigated topics in rock mechanics. The results of these studies have helped delineate the most influencing parameters of the shear resistance of rock-rock interfaces. These parameters include the normal stress (Patton, 1966), the presence of the filling material at the interface (Indraratna, Haque and Aziz, 1999), the matching of the two slabs composing the interface (Zhao, 1997b, 1997a), the roughness of the rock surfaces (Patton, 1966; Barton and Choubey, 1977; Grasselli and Egger, 2003; Barton, Wang and Yong, 2023), the scale effect (Bandis, Lumsden and Barton, 1981), the rock lithology, and the hydromechanical properties of the interfaces (Brown and Scholz, 1985). Since this thesis focuses on perfectly matched interfaces experiencing shear under a relatively low normal loading at the laboratory scale, only the normal stress, the rock lithology, and the roughness of rock surfaces are directly addressed. The normal stress significantly affects the shear resistance of the interfaces and drives the failure mode activated during the shear process. The mechanical properties of the rock and the rock surfaces, such as mineral composition and state of weathering, can significantly influence the shear resistance of interfaces. The roughness of the rock surface contributes considerably to the shear resistance of interfaces when the normal stress is low.

The normal stress and rock lithology can be determined and characterized easily. The normal stress is usually the weight of the hanging block. At the same time, the properties of the rock can be determined through well-established testing methods (tilt test, Schmidt hammer test, uniaxial compression test, triaxial test, tensile test, etc.). However, the contribution of the roughness in the shear resistance of interfaces is complex and has been the focus of the evolution of shear failure criteria of rock-rock interfaces (Patton, 1966; Barton and Choubey, 1977; Grasselli and Egger, 2003; Barton, Wang and Yong, 2023).

The complexity of the computation of the influence of roughness on the shear resistance of interfaces is caused by the difficulty associated with the measurement of roughness data (Grasselli, 2006) and the characterization of roughness overall. Many roughness parameters can be used to characterize the roughness of rock surfaces (Barton and Choubey, 1977; El-Soudani, 1978; Maerz, Franklin and Bennett, 1990; Grasselli and Egger, 2003; Tatone, Grasselli and Cottrell, 2010) but very few of them can be easily associated to existing failure criteria and failure mechanisms during shear.

Compared to the rock-rock interfaces, the investigation of the shear behavior of concrete-rock interfaces is recent but significantly growing. This interest is because considering concrete-rock interfaces as similar or equal to rock-rock interfaces has consequences in the design and structural stability of certain geotechnical structures. For example, such consideration in concrete-gravity dams leads to conservative designs and significantly affects structural stability analysis (Krounis, 2016). This thesis concentrates on the shear behavior of concrete-rock interfaces under low normal loading.

Furthermore, since it is not always possible to investigate all the aspects of the shear evolution through experimental studies, efforts have also been made to simulate the shear behavior of concrete-rock interfaces (Tian *et al.*, 2015; Gutiérrez-Ch *et al.*, 2018; Renaud, Bouaanani and Miquel, 2020).

This chapter discusses the evolution of the shear failure criteria, the roughness measurement and characterization, the experimental studies on the shear behavior of concrete-rock interfaces, the methodology for generating synthetic rough rock surfaces, and the associated numerical analysis.

1.1 Estimation of the shear resistance of interfaces

Failure criteria are models that estimate the shear resistance of interfaces based on the parameters influencing the shear process. The shear resistance of interfaces is an important parameter in the design and stability verification of geotechnical structures such as concrete gravity dams (Sujatha and Kishen, 2003; Fishman, 2008, 2009), rock support systems, and rock socketed piles. Even though this thesis focuses on concrete-rock interfaces, it is important to review the failure criteria of rock-rock interfaces since investigating them has laid the basis for understanding the shear behavior of concrete-rock interfaces. The most used failure criteria are presented.

1.1.1 Mohr-Coulomb failure criterion

The Mohr-Coulomb failure criterion is a generalization of the Coulomb failure criterion. It is expressed as;

$$\tau = c + \sigma_n \tan\phi \tag{1.1}$$

where τ is the shear resistance or shear strength, c is the cohesion, σ_n is the confinement or normal stress, and ϕ is the friction angle.

The cohesion c in Eq. (1.1) is usually assumed to be negligible for unbonded interfaces like the rock-rock interfaces (Krounis, Johansson and Larsson, 2016). Still, it significantly influences the shear resistance of totally bonded interfaces like the concrete-rock interfaces. This influence is particularly strong for shearing interfaces submitted to low normal stresses (Moradian, Ballivy and Rivard, 2012).

Figure 1.1 shows the Mohr-coulomb failure criterion. This failure criterion can be constructed with the results of direct shear tests for the shear resistance of rock-rock and concrete-rock interfaces. The cohesion c is the intercept between the failure envelope and the shear stress axis.

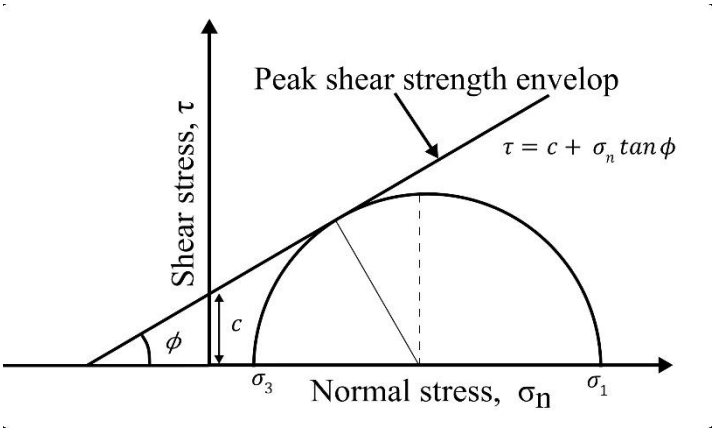

Figure 1.1 Mohr-Coulomb failure criterion for interfaces

The Mohr-Coulomb failure criterion ignores the influence of roughness on the shear resistance of interfaces. Therefore, it is only suitable for estimating the shear resistance of smooth rock-rock and concrete-rock interfaces. Despite this limitation, this failure criterion is recommended for

estimating the shear resistance of interfaces such as concrete-rock interfaces for structural stability assessment of concrete-gravity dams (EPRI, 1992; Ruggeri, 2004).

1.1.2 **Patton failure criterion**

The bi-linear failure criterion introduced by Patton (Patton, 1966) is a modification of the Mohr-Coulomb failure criterion for evaluating the shear resistance of rock-rock interfaces (Figure 1.2). The change consists of including the influence of roughness on the estimation of the shear strength. This criterion is based on the shear tests of rock-rock interfaces with triangular asperities. From these tests, Patton identified two failure modes. The first failure mode is restricted to low normal stress and is characterized by the dilation of the sample. Patton used Eq (1.2) to represent this behavior.

$$\tau = \sigma_n \, tan(\phi_b + i) \tag{1.2}$$

where *i* is the inclination angle of the triangles composing the asperities, σ_n is the normal stress, and ϕ_b is the basic friction angle.

The second failure mode is restricted to high normal stresses, where Patton reported the failure of the triangles composing the asperities and proposed Eq (1.3) to characterize this behavior.

$$\tau = c_f + \sigma_n \, tan(\phi_r) \tag{1.3}$$

where c_f is the cohesion related to the failure of the triangular asperities due to the increase of the normal stress and ϕ_r is the residual friction angle.

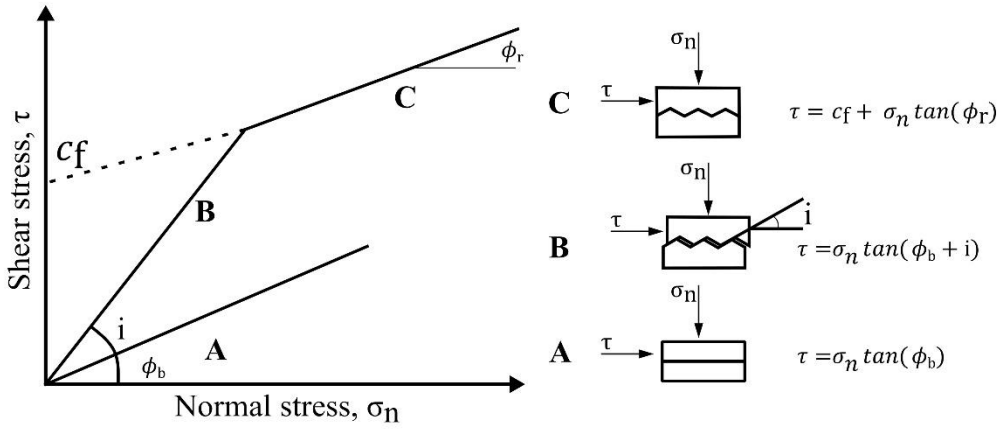

Figure 1.2 Patton failure criterion. Modified from Kounis (Krounis, 2016)

Combining Eq (1.2) and Eq (1.3) forms the Patton failure envelope. This failure envelope is presented in Figure 1.2 for smooth rock-rock interfaces, and rock-rock interfaces with triangular asperities under low and high normal stresses.

The Patton failure criterion is unsuitable for estimating the shear resistance of interfaces with rough rock surfaces because the inclination angle *i* is not designed to characterize the roughness of rough rock surfaces.

1.1.3 Failure criteria for partially bonded interfaces

Lo et al. (Lo KY, Lukajic B, Wang S, Ogawa T, 1990) proposed a Patton-based failure criterion for partially bonded smooth concrete-rock interfaces. This failure criterion assumes the simultaneous mobilization of the bonded and the unbonded part of the interface and is expressed as;

$$\tau = c\left[1-\eta\left(1-\frac{c_s}{c}\right)\right]+\sigma_n\, tan\,\phi_i\left[1-\eta\left(1-\frac{tan\,\Phi_s}{tan\,\Phi_i}\right)\right] \quad (1.4)$$

where η is the ratio of the unbonded part of the interface over the total area of the interface, c is the cohesion, and ϕ_i is the internal friction angle of the bonded part of the interface, c_s and Φ_s are the cohesion and the friction angle of the unbonded part of the interface. c_s is usually negligible.

Dawson et al. (Dawson RV, Curtis DD, 1998) proposed another Patton-based failure criterion for partially bonded concrete-rock interfaces that does not consider the influence of the roughness of the unbonded part of the interface on the shear resistance. This failure criterion is expressed in Eq (1.5).

$$\tau = A_b(c+\sigma_n \tan\phi_i)+(1-A_b)(\sigma_n \tan\phi_b) \quad (1.5)$$

where A_b is the ratio of the bonded part of the interface over the total area of the interface.

Krounis et al. (Krounis, Johansson and Larsson, 2016) performed an assessment of the performance of Lo et al. (Lo KY, Lukajic B, Wang S, Ogawa T, 1990) and Dawson et al. (Dawson RV, Curtis DD, 1998) failure criteria, the results of which indicates that the first criterion outperforms the later in terms of prediction of the shear resistance.

1.1.4 Barton and Choubey failure criterion

Barton and Choubey (Barton and Choubey, 1977) introduced a peak shear strength criterion to estimate the shear strength of rough rock-rock interfaces. This criterion is based on the results of an experimental campaign composed of direct shear tests of rough rock-rock interfaces and is expressed as;

$$\tau = \sigma_n\, tan\left[\phi_r + JRC\, log_{10}\left(\frac{JCS}{\sigma_n}\right)\right] \quad (1.6)$$

where *JRC* is the Joint Roughness Coefficient, a parameter that characterizes the roughness of a rough rock surface, and *JCS* (Joint Compressive Strength) is the compressive strength of the interface. ϕ_r is the residual friction angle. σ_n is the normal stress.

Eq (1.6) can be used to estimate the shear resistance of weathered and unweathered rough rock-rock interfaces.

According to Barton et al. (Barton, Wang and Yong, 2023), the JRC can be determined by back analysis using experimental methods or by visual comparison with the ten standard profiles with defined JRC values (Figure 1.3). The JRC varies between 0 for the smooth surface and 20 for the roughest rock surface. The determination of the JRC by visual comparison is a suggested method for estimating the roughness of rock surfaces (ISRM, 1978) and, therefore, is strongly associated with the failure criterion proposed by Barton and Choubey.

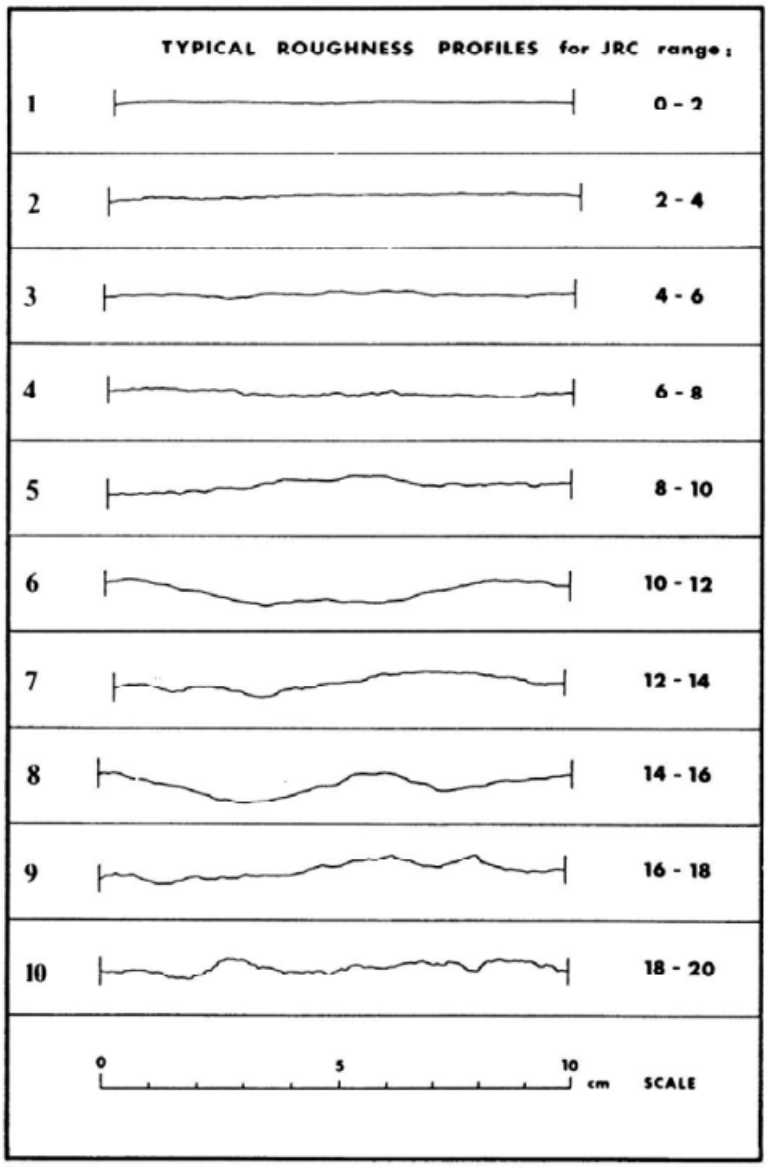

Figure 1.3 Standards roughness profiles with defined JRC (Barton and Choubey, 1977)

The peak shear strength criterion introduced by Barton and Choubey is an evolution of the Patton failure criterion. The main difference between these failure criteria is that the roughness parameter used is the JRC in the model proposed by Barton and Choubey. The JRC can quantify the influence of the roughness of rough rock surfaces differently from the inclination angle used in the model developed by Patton, which is more suited for triangular asperities.

The model presented by Barton and Choubey suffers three significant limitations caused by the method of determination of the JRC. First, the visual comparison used to determine the JRC parameter is not objective and can introduce biases (Beer, Stead and Coggan, 2002; Alameda-Hernández *et al.*, 2014). Furthermore, the back-analysis approach to compute the JRC is less desirable in most geotechnical problems since the interest is usually in preventing failure and not estimating the shear resistance after failure. In the context of laboratory testing, this back-analysis requires more tests to determine the parameters related to the JRC, which is neither convenient nor practical and can be a source of error. The second limitation is the two-dimensional characteristics of the JRC when obtained through visual comparison because it is less realistic to characterize a highly complex three-dimensional entity with a two-dimensional profile. The third limitation is the inability of the JRC determined through visual comparison to faithfully capture the anisotropy of the roughness of rock surfaces.

Despite these limitations, the failure criterion suggested by Barton and Choubey is one of the most used failure criteria for rock-rock interfaces.

1.1.5 **Grasselli and Egger failure criterion**

Grasselli and Egger (Grasselli and Egger, 2003) proposed a peak shear strength criterion to estimate the shear strength of rock-rock and mortar-mortar interfaces, described in Eq (1.7). The proposed shear strength criterion is based on a definition of a brand-new approach to quantify the roughness of rough rock surfaces as a three-dimensional entity and on the analysis of the results of an experimental study composed of direct shear tests of rough rock-rock and rough and unbonded mortar-mortar interfaces.

The proposed roughness approach considers the most probable effective contact areas facing the shear direction. These effective contact areas are expected to play a more significant role in the shear resistance of the interface.

$$\tau = \sigma_n \, tan\left[\phi_b + \left(\frac{\theta^*_{max}}{C}\right)^{1.8}\right]\left[1 + e^{-\left(\frac{\theta^*_{max}}{9A_0C}\right)\left(\frac{\sigma_n}{\sigma_t}\right)}\right] \tag{1.7}$$

where τ is the peak shear strength, σ_n is the normal stress, θ^*_{max} is equivalent to the maximum apparent dip angle in the shear direction considered, C is the fitting parameter related to the roughness of the interfaces, A_0 is the maximum possible contact area during shear in a specific direction, σ_t is the tensile strength of the rock.

A more detailed description of the roughness parameter θ^*_{max}/C introduced by Grasselli and Egger (Grasselli and Egger, 2003) is presented in section 1.2.3.

1.1.6 **Summary**

Since the early fifties, there has been a growing interest in defining failure criteria to estimate the shear strength of rock-rock and concrete-rock interfaces. The earlier effort was mainly focused on the rock-rock interfaces. These studies have significantly improved the failure criteria by incorporating parameters influencing the shear mechanism. Patton (Patton, 1966) modified the Moh-Coulomb failure criteria to include the influence of the inclination angle of the triangles composing the interfaces. Lo et al. (Lo KY, Lukajic B, Wang S, Ogawa T, 1990) and Dawson et al. (Dawson RV, Curtis DD, 1998) presented failure criteria for partially bonded concrete-rock interfaces. Barton and Choubey (Barton and Choubey, 1977) introduced a failure criterion for rock-

rock interfaces that takes into consideration the influence of the roughness of rough rock surfaces in the shear resistance of interfaces. Grasselli and Egger (Grasselli and Egger, 2003) proposed a three-dimensional and directional roughness parameter based on the interpretation of the observed mechanisms during the shear process to improve the characterization of the roughness of rock surfaces. With this roughness parameter, Grasselli and Egger (Grasselli and Egger, 2003) proposed a failure criterion for unbonded rough rock-rock and unbonded mortar-mortar interfaces.

Despite the major progress outlined, the research for a better failure criterion is still ongoing; this is principally motivated by the limitations of the existing failure criteria to estimate the shear resistance of interfaces when used in conditions far different from the experimental studies upon which they were established. These conditions include the range of normal stresses, the failure modes identified, the number and the variation of interfaces in terms of roughness, and the methodology of the roughness measurement. Lastly, there is a clear need for a failure criterion to estimate the shear resistance of bonded concrete-rock interfaces that considers the influence of roughness computed as a three-dimensional entity.

Hereafter, aspects relative to the roughness measurement and computation are addressed.

1.2 **Characterization of roughness**

The study of failure criteria of rock-rock and concrete-rock interfaces (Patton, 1966; Barton and Choubey, 1977; Lo KY, Lukajic B, Wang S, Ogawa T, 1990; Dawson RV, Curtis DD, 1998; Grasselli and Egger, 2003) has demonstrated that roughness is an important parameter in the estimation of the shear resistance of interfaces. Therefore, the characterization of the roughness of rock surfaces is of great significance. This characterization starts with selecting the method to collect the roughness data. After defining such a method, it is important to determine the roughness parameter to characterize the rock surfaces. Many roughness parameters are in the literature, each based on statistical or geomechanical rationale. However, the most important roughness parameters for the study of the shear resistance of interfaces are the ones that can be associated with existing shear failure criteria, or that can be correlated to roughness parameters associated with existing shear failure criteria. The roughness characterization is addressed in investigating the shear resistance of perfectly mated rock-rock and concrete-rock interfaces.

1.2.1 **Measurement systems**

The roughness of rock surfaces is defined in rock mechanics as a combination of unevenness and waviness of a rock surface (Ulusay, 2015). The basic concept of the roughness measurement is to acquire heights of asperities and record them with their respective position in the horizontal plane. The roughness data can be obtained as a two- or three-dimensional measurement, depending on the measurement method.

The two-dimensional data are usually obtained using a profilometer and often involve a motion of the rock surface or the measuring devices. These devices record heights of asperities of a rock surface along a single profile at a time; this means either the x or y axes are fixed during the measurement. Three-dimensional data on the rock surface can be obtained by combining or interpolating a series of two-dimensional profiles.

The two-dimensional methods to collect the roughness data of a rock surface can be separated into two main groups: the contact method and the non-contact method.

The contact method involves contact between the measuring device and the rock surface. Mechanical instruments, principally profilometers, are examples of measuring devices for the

contact method. One of the earliest applications of the contact method for characterizing the roughness of rock surfaces can be found in Barton and Choubey (Barton and Choubey, 1977). These authors used a profile comb to obtain profiles of rock surfaces. The ten standard roughness profiles (Figure 1.3) suggested by the ISRM as references to characterize the roughness of rock surfaces were obtained using the profile comb (Figure 1.4). The profile comb is strongly associated with the characterization of roughness using the JRC parameter (Barton and Choubey, 1977; Serasa *et al.*, 2017; Barton, Wang and Yong, 2023)

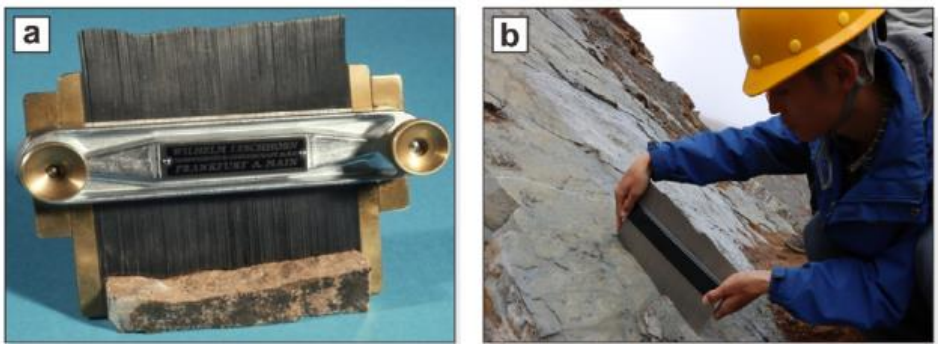

Figure 1.4 Barton's comb (Barton, Wang and Yong, 2023); a) laboratory and b) field

The use of two-dimensional non-contact methods for measuring the roughness of rock surfaces was motivated by the necessity to increase the speed of the measurement, increase the accuracy of the data collected, remove the influence of the operator, and eliminate the risk of damaging rock surfaces due to contact. The development of non-contact methods is driven by the technological progress in sensors and camera design and the availability of more efficient computers. The laser profilometer is the most used device in two-dimensional non-contact methods. The basic concept of the laser profilometer to measure distance consists of emitting a laser beam targeting a rock surface and using the information obtained from this laser beam to compute the distance between the source and the target. As an example of this methodology, Lanaro (Lanaro, 2000) presented a laser-based roughness measurement device composed of a sensor that shoots a laser beam toward a target (rock surface), a series of lenses that transform the beam that hits the target into stripes, and a fixed camera that collects the image of the stripes. Each image of a stripe collected by the cameras is used to generate 600 points located across the stripe. The values of the points obtained constitute a part of a field of heights of asperities composing the rock surface, and the measurement has an accuracy of 0.05 mm. Other devices can also be encountered in the literature (Fardin, Feng and Stephansson, 2004).

The three-dimensional methods to collect roughness measurements consist of a fixed projection and imaging system and a fixed sample holder. These three-dimensional methods generally outperform the two-dimensional methods in terms of speed of measurement, density of the measurement, accuracy of the measurement, and repeatability. As an illustration, Grasselli (Grasselli, 2001) used a scanning device that relies on the advanced topometric sensor (ATS). This device applies the concept of photogrammetry through optical triangulation and interferometry through phase shifting. A white-light fringe is projected onto the rock surface for measurement and recorded using two cameras. The data are then processed through triangulation and image shifting to obtain three-dimensional roughness data with a vertical precision of $\pm$ 50μm. Figure 1.5 shows an example of a scan of a rock surface obtained using this device.

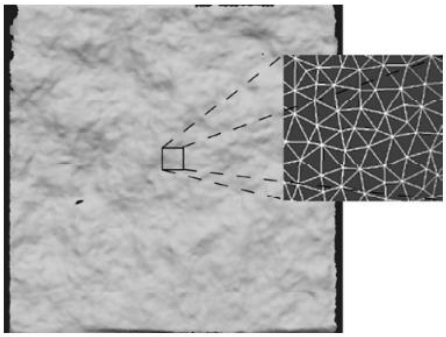

Figure 1.5 Example of an image obtained through the scanner used by Grasselli (Grasselli, 2001)

1.2.2 **3SR Laser-based scanner**

The 3SR laser-based scanner used in the experimental study conducted in this thesis is a non-contact two-dimensional method that can provide high-quality roughness data. This device was developed by Hans and Boulon (Hans and Boulon, 2003). The laser sensor of the device is mounted on a metallic platform powered by two stepper motors so that it can move in the x and y directions (Figure 1.6). The motion of the laser sensor is guided by two LVDT sensors that can measure distance with sub-millimetric accuracy ($\pm$ 10µm). A LabVIEW program controls the stepper motors guided by the LVDT, runs the distance measurement using the laser sensor, and records the height of asperities per profile with precise positions in the x and y directions.

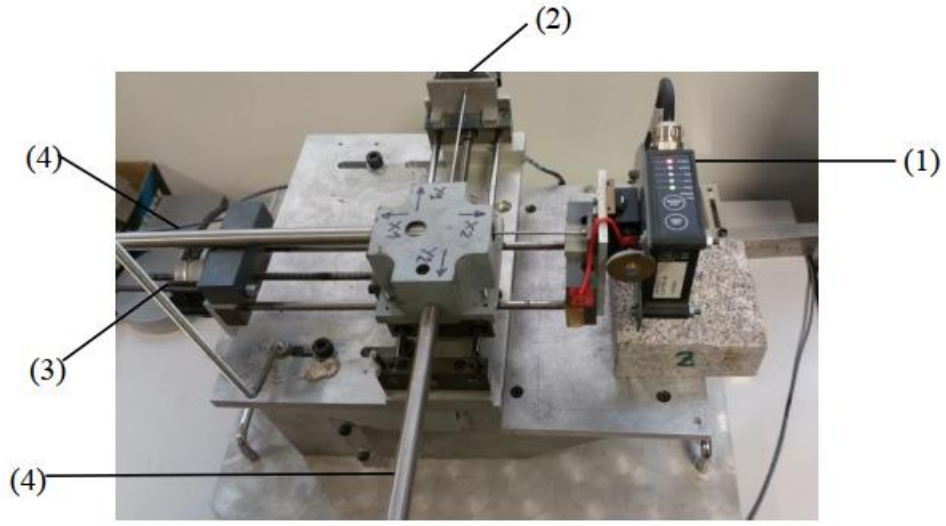

Laser profilometer: (1): Laser sensor, (2): Motor for the Y axis,
(3): Motor for the X axis, (4): Displacement sensors (LVDT)

Figure 1.6 Laser-based scanning device developed by Hans and Boulon (El Merabi, 2018)

The parameters of the LabVIEW program can be set so that many parallel profiles are collected (Figure 1.7). Furthermore, the vertical precision of the distance measured by the laser sensor is $\pm$ 50µm, within the same accuracy range as the scanner used by Grasselli (Grasselli, 2001).

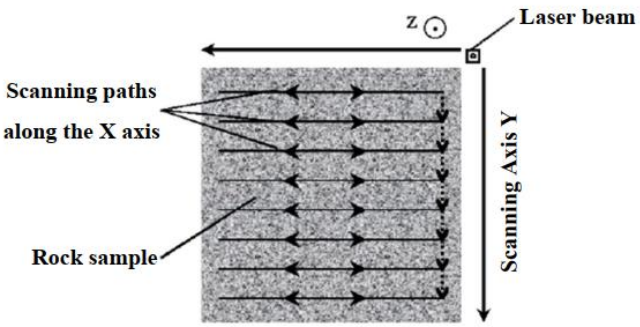

Figure 1.7 Definition of a scanning path (El Merabi, 2018)

The entire procedure of measurement of the roughness data of a rock surface using the device developed by Hans and Boulon is illustrated in Figure 1.8.

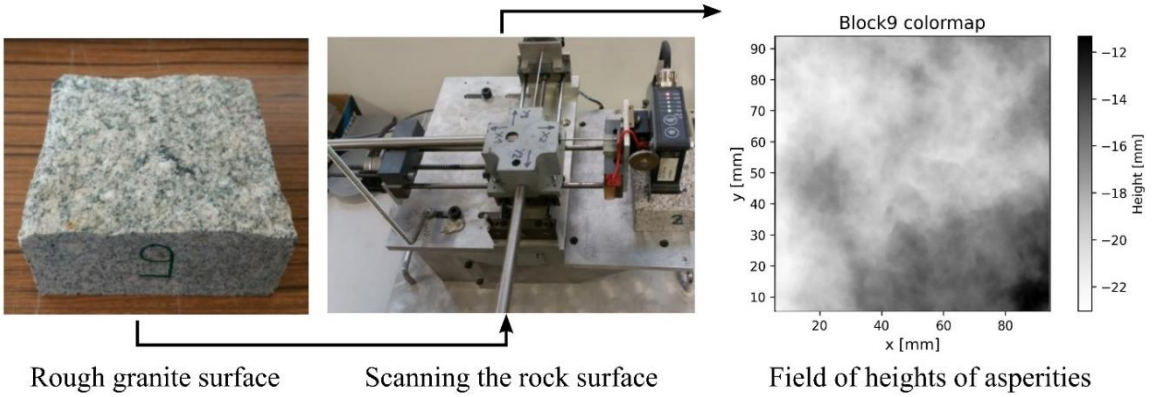

Figure 1.8 Scanning rough rock surfaces using the device developed by Hans and Boulon

The roughness data collected using this device can then be used to characterize the roughness using roughness parameters.

1.2.3 **Roughness parameters**

Characterizing surface unevenness is an important topic in many areas with contact surfaces involving friction, wear, and lubrication. There are many roughness parameters in the literature, but most are unsuitable for estimating the shear strength of rock-rock and concrete-rock interfaces. The roughness parameters for the estimation of the shear resistance of rock-rock and concrete-rock interfaces considered in this study are the ones that fulfill three principal requirements: they can characterize the roughness of natural rough rock surfaces, they take into account the mechanisms driving the shear failure of rock-rock and concrete-rock interfaces, and they can be associated with more used failure criteria. With this orientation, the following presentation focuses on the roughness parameters proposed by Barton and Choubey (Barton and Choubey, 1977), the JRC, and the roughness parameter introduced by Grasselli and Egger (Grasselli and Egger, 2003), the 3D roughness parameter.

1.2.3.1 **Joint roughness coefficient - JRC**

The JRC is the most used roughness parameter in research and engineering applications for estimating the shear resistance of rock-rock interfaces. This popularity can be explained by its simplicity, relative ease of determination, and association with the determination of the shear strength of interfaces (Barton, Wang and Yong, 2023).

Figure 1.9 shows the influence of roughness quantified by the JRC in estimating the shear resistance of rock-rock interfaces using the failure criterion proposed by Barton and Choubey (Barton and Choubey, 1977) and presented in section 1.1.4.

The JRC is a dimensionless value computed as the ratio between the roughness amplitude and the sample length (Barton, Wang and Yong, 2023). It can be obtained by modifying Eq.(1.6), obtaining Eq (1.8):

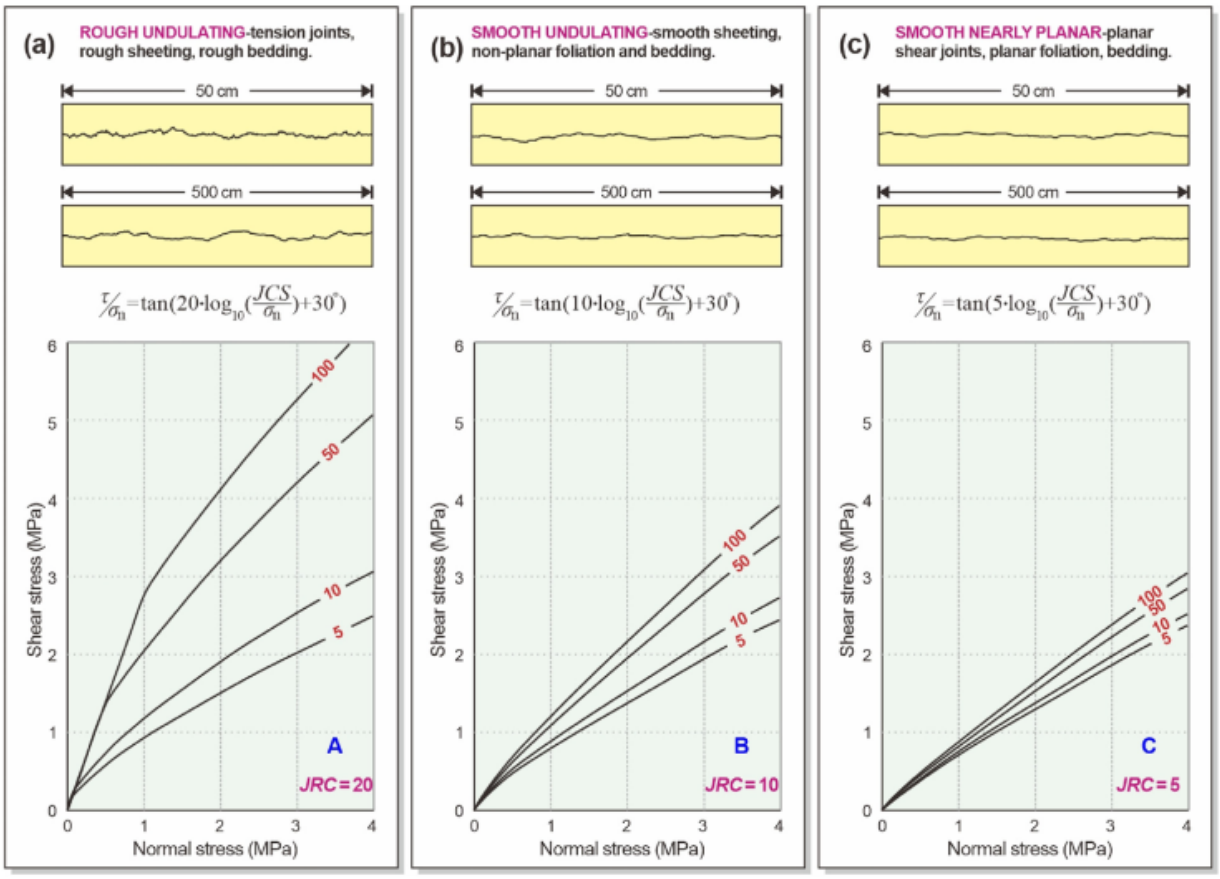

Figure 1.9 Influence of roughness expressed using the JRC on the estimation of the shear strength (a) JRC=20, (b) JRC=10, and (c) JRC=5, for σ_c/σ_n equivalent to 5, 10, 50, and 100 (Barton, Wang and Yong, 2023)

$$JRC = \frac{\tan^{-1}(\tau/\sigma_n) - \phi_r}{log_{10}\left(\frac{JCS}{\sigma_n}\right)} \tag{1.8}$$

where JCS (Joint compressive strength) is equivalent to the unconfined compressive strength for unweathered rock surfaces and is determined using the Schmidt hammer test for weathered rock surfaces. Furthermore, the residual friction angle ϕ_r in Eq. (1.8) can be determined using the Eq. (1.9).

$$\phi_r = \phi_b - 20° + 20r/R \tag{1.9}$$

where ϕ_b is the basic friction angle, an expression of the mineralogical properties of smooth and unweathered rock surfaces. ϕ_b is estimated using the tilt test or the residual phase of a shear test of samples composed of smooth or sand-blasted rock surfaces. r and R can be obtained from the Schmidt hammer test on weathered and unweathered rock surfaces.

Two principal methods to estimate the JRC are visual comparison and experimental. The visual comparison method was proposed by Barton and Choubey (Barton and Choubey, 1977) as a means to account for the influence of roughness on estimating the shear strength of interfaces. To achieve this objective, Barton and Choubey performed over 190 shear tests of rough rock-rock interfaces. With the results of these tests, these authors used Eq. (1.8) to back-calculate the JRC representing the influence of roughness in the shear strength as defined according to Eq. (1.6). The back-calculated JRC is an expression of three-dimensional and directional roughness. Before the shear tests, Barton and Choubey used a profile comb to record three roughness profiles per sample tested, generating a database of 390 roughness profiles. Correlating this database of roughness profiles and the database of back-calculated JRC values, Barton and Choubey proposed ten standard roughness profiles that can be associated with ranges of JRC values (Figure 1.3). These authors then suggested that a visual comparison of a given roughness profile with these ten standard profiles can be used for the estimation of the range of the JRC. The ten standard roughness profiles and the visual comparison method of estimation of the JRC were accepted as suggested methods for characterizing rock surface roughness to estimate rock-rock interface shear resistance (ISRM, 1978).

The JRC defined using the visual comparison method is operator-biased, as pointed out by other publications (Beer, Stead and Coggan, 2002; Alameda-Hernández *et al.*, 2014). Attempting to address this limitation, many researchers have proposed equations correlating statistical-based roughness parameters to the JRC (Tse and Cruden, 1979; Maerz, Franklin and Bennett, 1990; Yu and Vayssade, 1991; Yang, Lo and Di, 2001; Tatone, Grasselli and Cottrell, 2010). Furthermore, correlations of the JRC and fractal-based roughness parameters have also been proposed (Malinverno, 1990; Kulatilake, Um and Pan, 1998; Lanaro, 2000; Fardin, Stephansson and Jing, 2001; Jang, Kang and Jang, 2014). But most of these roughness parameters have serious shortcomings: they usually do not have a proper geomechanical rationale, are not easy to estimate, and cannot include the influence of geological alterations such as weathering (Barton, Wang and Yong, 2023). A more exhaustive list of the correlation relationships between roughness parameters and the JRC can be found in Magsipoc et al. (Magsipoc, Zhao and Grasselli, 2020).

The determination of the JRC using an experimental approach consists of performing laboratory tests and then computing the JRC using a back-analysis relationship similar to the one presented in Eq. (1.8). There are two principal experimental methods for the estimation of the JRC: the direct shear tests, and the tilt tests.

Eq (1.8) and Eq. (1.10) are used in the back-analysis to estimate JRC using the results of the direct shear tests and the tilts tests.

$$JRC = \frac{\alpha - \phi_r}{log_{10}\left(\frac{JCS}{\sigma_n}\right)} \tag{1.10}$$

where α is the tilt angle.

Overall, the JRC is a landmark roughness parameter for the problem of the definition of the shear strength criterion for rock-rock and concrete-rock interfaces. However, the methods for estimating the JRC present some shortcomings; they can be operator-biased, two-dimensional, or require extra experimental tests.

1.2.3.2 **3D roughness parameter for rock surfaces**

The process of defining the 3D roughness parameter introduced by Grasselli (Grasselli, 2001) comes from the necessity to quantify the three-dimensional morphology of rough rock surfaces by taking a closer look at what happens in the contact before, during, and after a shear test. The Grasselli roughness parameter is a geometrical characterization of roughness that considers the interpretation of the shear mechanisms occurring at the contact. For this purpose, Grasselli (Grasselli, 2001) performed a series of direct shear tests of rough rock-rock and unbonded rough mortar-mortar interfaces.

These tests show that at the beginning of the application of the shear loading, the areas of the asperities facing the shear direction start to elastically deform while the asperities dipping in the direction opposite to the shear loading lose contact (Figure 1.10).

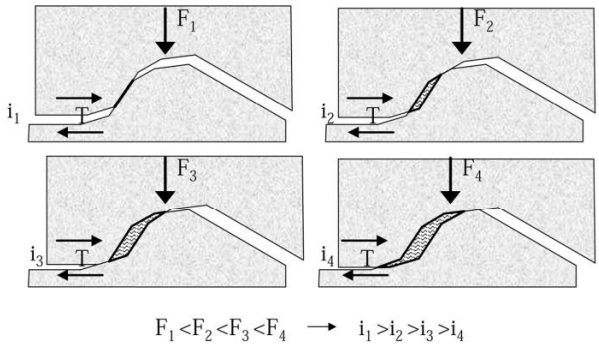

Figure 1.10 Contact area at the beginning of the application of the shear loading. (Grasselli, 2001)

After the test, the post-mortem analysis of the samples showed that damage mainly occurs in the asperities with the steepest inclination angle and facing the shear direction. With this interpretation, Grasselli postulated that the area of the steepest asperities facing the shear direction is the one that plays a more significant role in the shear resistance of interfaces and, therefore, should be considered in the 3D roughness parameter.

The roughness data collected before and after the tests were used to reconstruct the rough rock surfaces. This reconstruction is carried out by triangulation, generating a discretization of the triangulated rock surface. The benefit of using triangles is the simplicity of computing geometrical

properties. The geometrical properties of interest are the direction of the normal vector, the area, and the apparent dip angle of each triangle facing the shear direction (Figure 1.11).

The apparent dip angle of each triangle facing the shear direction is called θ^* and is computed using Eq (1.11):

$$tan\,\theta^* = -\,tan\,\theta\,.cos\,\alpha \qquad (1.11)$$

where θ is the dip angle, the angle between the shear plane and the triangle under consideration. α is the angle between the projection of the vector true dip on the shear plane (n_1 in Figure 1.11) and the vector representing the shear direction (S in Figure 1.11). α is measured clockwise from the shear direction S. Furthermore, n is the vector normal to the triangle under consideration and n_1 is the projection of n in the shear plan.

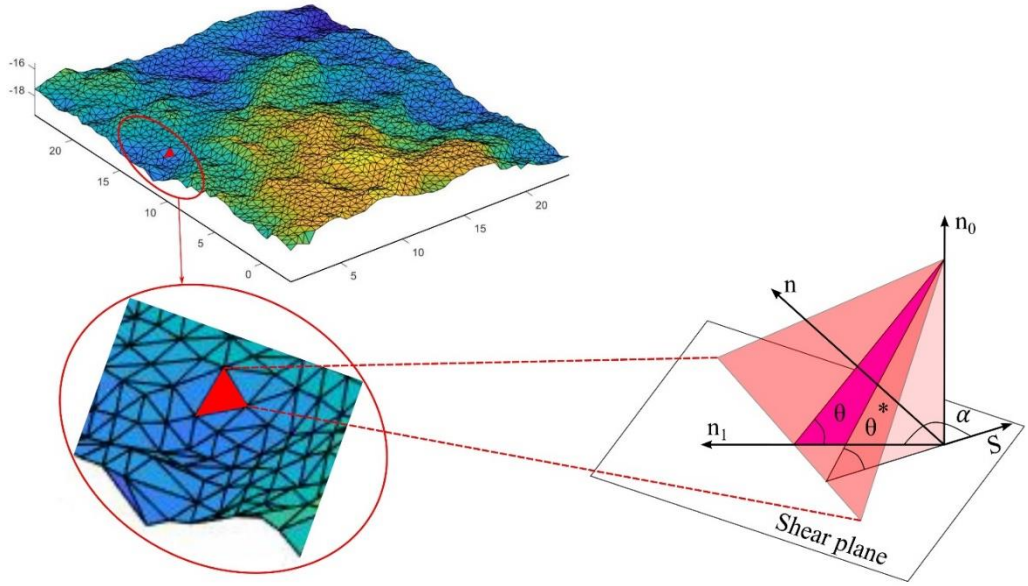

Figure 1.11 Identification of triangles facing the shear direction for roughness analysis. Inspired by Tian et al. (Tian *et al.*, 2018)

With the objective determination of the apparent dip angle θ^*, the last detail of the interpretation to consider is the definition of the limit of the steepest triangle facing the shear direction. To address this problem, Grasselli proposed a limit analysis combined with a regression analysis. This approach proceeds in three steps. First, successive values of θ^* are defined as the lower limit of the inclination of triangles facing the shear direction above which a triangle can be considered more relevant to the shear resistance and accounted for in the computation of roughness. Second, for each value of θ^* considered as the limit, the area A_{θ^*} is computed as the sum of all the areas of the triangles facing the shear direction which have an inclination angle bigger than θ^*. Last, a regression of the plot θ^* versus A_{θ^*} following Eq (1.12) is performed to determine the roughness parameter C.

$$A_{\theta^*} = A_0 \left(\frac{\theta^*_{max} - \theta^*}{\theta^*_{max}} \right)^C \tag{1.12}$$

where A_0 is the sum of areas facing the shear direction when the θ^* limit is equal to 0. θ^*_{max} is the maximum θ^* in the plot θ^* versus A_{θ^*} when A_{θ^*} is first equal to 0. C is a fitting parameter defined by regression and is an expression of the roughness of the interface. Figure 1.12 shows an example of the plot θ^* versus A_{θ^*} (A_C: contact area in Figure 1.12).

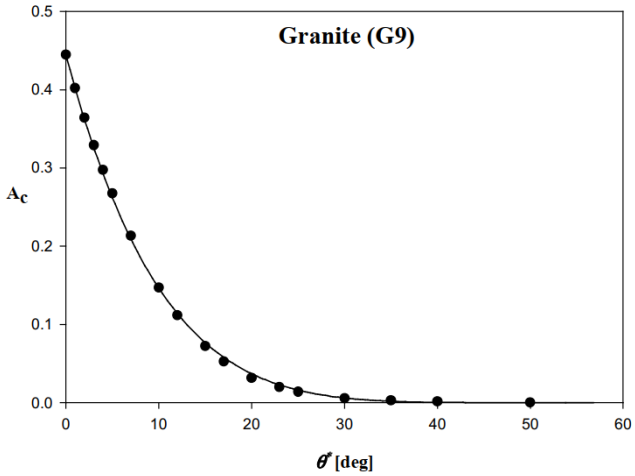

Figure 1.12 3D roughness computation (Grasselli, 2001)

From this analysis, Grasselli and Egger (Grasselli and Egger, 2003) proposed the ratio θ^*_{max}/C as a roughness parameter. This 3D roughness parameter was later updated by Tatone and Grasselli (Bryan S.A. Tatone and Grasselli, 2009) to a more commonly used form given by the Eq (1.13) and which is obtained by integrating A_{θ^*} in Eq (1.12) between 0 and θ^*_{max}

$$\frac{\theta^*_{max}}{(C+1)} \tag{1.13}$$

The 3D roughness parameter, Eq (1.13), developed by Grasselli and his colleagues (Grasselli and Egger, 2003; Bryan S.A. Tatone and Grasselli, 2009) has several advantages when compared to the JRC; it is a 3D roughness parameter that can be determined objectively, it can capture the anisotropy of roughness of rock surface, and it takes into account the morphology of the rock surface with considerations based on a strong geomechanical rationale. For these reasons, this roughness parameter is adopted in this thesis.

However, the computation of the roughness parameter can be influenced by the measurement resolution of roughness data.

1.2.4 **Measurement resolution**

Even with the most advanced roughness measurement devices available today, collecting roughness data without some implicit filtering is almost impossible. This implicit filtering is mainly caused by the resolution of the measurement device (nominal point spacing). In the case of the investigation of the influence of roughness on the shear resistance of interfaces, the

measurement resolution of interest is the one that correctly represents the asperities that contribute to the shearing resistance (Tatone, Grasselli and Cottrell, 2010).

Tatone et al. (Tatone, Grasselli and Cottrell, 2010) investigated the influence of the measurement resolution on the computation of the roughness of rock surfaces. The roughness parameter considered in this study is the 3D roughness parameter introduced by Grasselli and colleagues (Grasselli and Egger, 2003; Bryan S. A. Tatone and Grasselli, 2009). Furthermore, these authors also discussed the influence of the measurement resolution on the shear resistance of interfaces.

As part of the experimental study, Tatone et al. (Tatone, Grasselli and Cottrell, 2010) performed direct shear tests of replicas representing roughness obtained from rock fracture. They collected roughness data before and after the tests using nominal point spacing: 0.044, 0.25, and 0.5 mm.

From the roughness computation, these authors report that $\theta^*_{max}/(C+1)$ tends toward 90° and 0° when the nominal point spacing tends respectively toward 0 mm and a value bigger than the length of the sample (Figure 1.13 (a)).

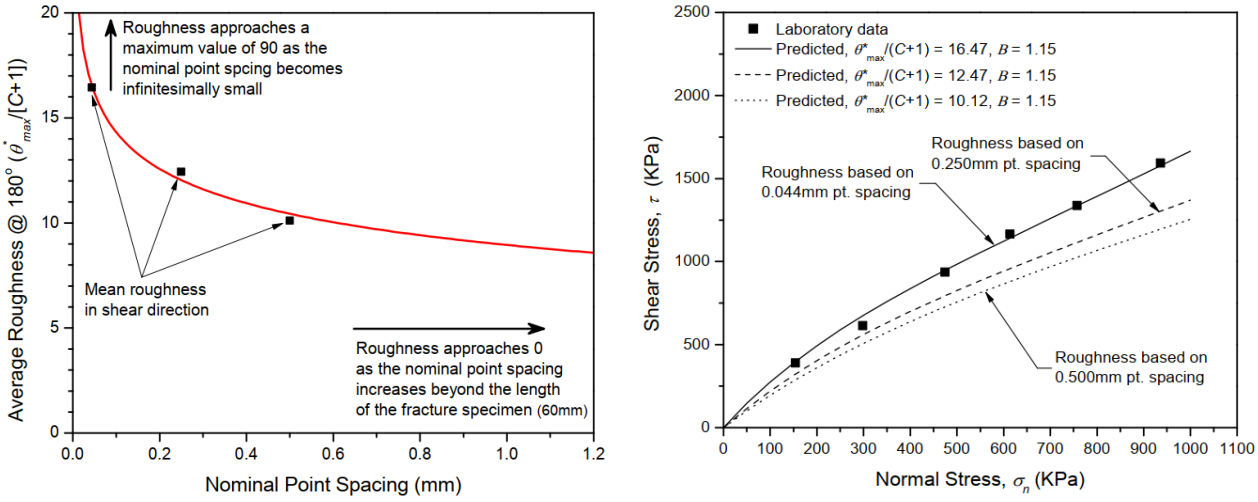

(a) (b)

Figure 1.13 Influence of the measurement resolution on the computation of $\boldsymbol{\theta^*_{max}/(C+1)}$ (Tatone, Grasselli and Cottrell, 2010). 180° represents the shear direction considered in the roughness computation.

To evaluate the influence of the measurement resolution on the shear resistance of the interfaces tested, the authors attempted to estimate the shear strength obtained in the experimental study using the failure criterion introduced by Cottrell (Cottrell, 2009), Eq (1.14); this failure criterion is a modification of the failure criterion proposed by Grasselli and Egger (Grasselli and Egger, 2003);

$$\tau = \left[1 + e^{-\left(\frac{\theta^*_{max}}{(C+1)}\frac{\sigma_n}{9A_0\sigma_t}\right)}\right]\sigma_n \tan\left[\phi_b + \left(\frac{\theta^*_{max}}{C}\right)^B\right] \quad (1.14)$$

where B is a fitting parameter equal to 1.15; the rest of the legend can be found in section 1.1.5.

The result of this analysis is shown in Figure 1.13 (b); from first glance, it seems that the measurement resolution of 0.044 mm is the only adequate nominal point spacing for estimating the shear resistance. However, upon a closer look at Eq (1.14), these authors realized that the fitting parameter B could be easily adjusted to fit the roughness value obtained using the nominal point spacing of 0.25 and 0.5 mm. The value of B, equivalent to 1.25 and 1.34, fit well the roughness obtained with 0.25 and 0.5 mm of nominal point spacing. The wider implication of this analysis is that before using any failure criterion, it is important to consider the context of its formulation. In the case of the modified Grasselli and Egger failure criterion (Eq (1.14)), it is important to recognize that the value of B depends on the circumstance of the computation of the roughness parameter, namely the measurement resolution of roughness. Other contexts can include the range of normal stress considered, the failure modes observed, the types of rocks used, the specific context of the geological origin of the rocks, and the weathering of the rock surfaces.

1.3 **Shear response of concrete-rock interfaces**

From the review of the failure criteria for rock-rock and concrete-rock interfaces, it is clear that there is a necessity for proper failure criteria for concrete-rock interfaces based on the shear responses of concrete-rock interfaces obtained from studies focused only on this type of interface. Such a failure criterion should consider the influence of roughness as a three-dimensional entity and reflect the shear mechanisms active during the shear evolution. Thus, it is important to understand the shear behavior of concrete-rock interfaces better.

Compared to investigating the shear behavior of rock-rock interfaces, the interest in investigating the shear behavior of concrete-rock interfaces is recent but rapidly growing. First, this section presents the testing methods to study the shear behavior of concrete-rock interfaces. Then, the major studies contributing to understanding the shear response of concrete-rock interfaces under low normal loading are discussed.

1.3.1 **Testing methods**

The direct shear test is the most used test to study the shear behavior of concrete-rock interfaces (Saiang, Malmgren and Nordlund, 2005; Z.A. Moradian *et al.*, 2010; Tian *et al.*, 2015; Krounis, Johansson and Larsson, 2016; Mouzannar *et al.*, 2017; Badika *et al.*, 2022). The sample used in this test comprises a rock slab with a shear plane parallel to the horizontal plane on top of which concrete is cast. Depending on the bonding conditions of the problem, the sample can be bonded, partially bonded, or unbonded (Lo KY, Lukajic B, Wang S, Ogawa T, 1990; Z.A. Moradian *et al.*, 2010; Krounis, Johansson and Larsson, 2016). The direct shear test proceeds in two steps. The first step consists of applying the normal loading to the upper box encapsulating one slab; once the initial normal loading is reached, the shear loading is applied as a tangential force in the lower box encapsulating the other slab. During the test, the lower box cannot move in the normal loading direction, while the upper and lower boxes cannot move perpendicular to the shear loading.

During the test, the normal and the shear loading is recorded along with the normal δ_n and the shear δ_s displacement. The normal and the shear stresses are computed by dividing the normal and the shear loading by the initial area of the interface; see Figure 1.14.

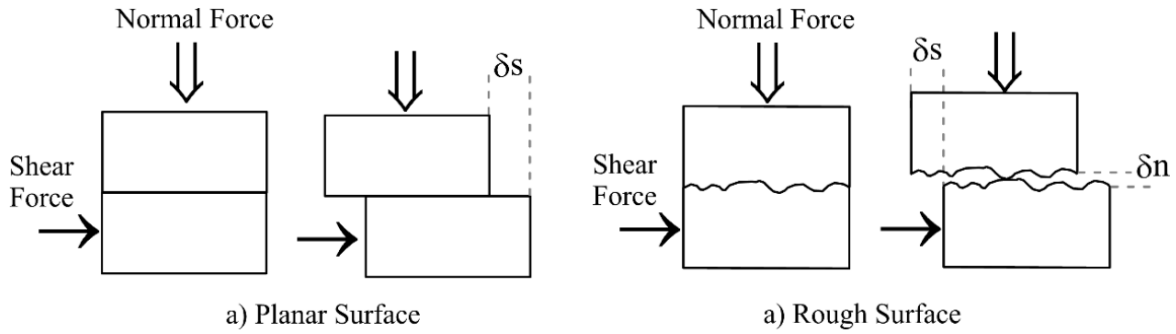

Figure 1.14 Shear evolution during the direct shear test of concrete-rock interfaces for both the (a) flat interfaces and (b) the rough interfaces (Jeffery, 2021)

For concrete-rock interfaces, the direct shear test is usually performed using two boundary conditions: the constant normal stiffness (CNS) and the constant normal loading (CNL). These boundary conditions refer to the state of the normal loading during the second step of the test.

In the CNS conditions, the normal stiffness is maintained constant during the test. The normal stiffness can be controlled by using a system of springs with known stiffness and normal loading (Haque and Indraratna, 2000; Thirukumaran and Indraratna, 2016). The CNS conditions are appropriate to reproduce the shear evolution at the concrete-rock interfaces encountered in rock support systems and rock socketed piles (Johnston, I. W.; Lam, 1984; Lam and Johnston, 1989; Kodikara and Johnston, 1994; Indraratna, Haque and Aziz, 1998; Suits, L & Sheahan, TC & Seidel, Julian & Haberfield, 2002; Gu, Seidel and Haberfield, 2003; Thirukumaran and Indraratna, 2016).

In the CNL conditions, the desired normal loading obtained after the first step of the test is maintained constant during the rest. These boundary conditions can cause significant dilation if the interface tested is rough, and the normal loading is low. The CNL conditions are by far the most used boundary conditions. They are, for example, an appropriate simulation of the shear behavior of concrete-rock interfaces for application in designs and structural stability analysis of concrete-gravity dams (Krounis, Johansson and Larsson, 2016). Experimental studies performed using the CNL boundary conditions are discussed hereafter.

For a better simulation of the shear failure of interfaces encountered, for example, in concrete gravity dams, the direct shear test must be carried out such that there is no rotation of the upper box during the test. Such a rotation can generate stress concentration and yield unrealistic asperities degradation (Grasselli, 2001). To address this problem, Boulon (Boulon, 1995a) presented a direct shear test machine called the BCR3D (Figure 1.15) that reduces the rotation by applying the tangential shear loading on both the upper and the lower shear boxes in opposite directions. This double application of shear loading reduces the rotation risk and maintains the normal and shear stress focused on the active shear zone.

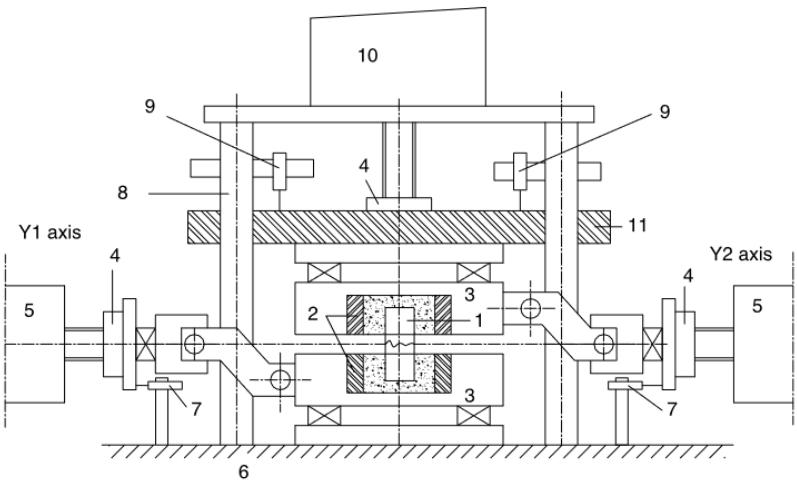

Figure 1.15 BCR3D direct shear test machine: 1 is the sample, 2 is the internal metallic box, and 3 is the external metallic box, 4 loading cells, 5 horizontal actuators, 6 rigid frame, 7 LVDT in the y direction, 8 rigid column, 9 LVDT vertical direction, 10 vertical actuators, and 11 rigid vertical translating system (Buzzi *et al.*, 2008)

As discussed in section 1.1, at least three direct shear tests must be carried out using three normal stresses that generate the same failure mode to complete the failure envelope of the shear strength of concrete-rock interfaces.

Overall, for other parameters of the direct shear test for the investigation of the shear behavior of concrete-rock interfaces, the suggestions proposed by the ISRM (Muralha *et al.*, 2014) for rock-rock interfaces are usually considered. Examples of such parameters include the speed of the shear loading and the sample size in terms of the height of asperities.

Although very rare, the triaxial test can be used to study the shear behavior of concrete-rock interfaces (Lo KY, Lukajic B, Wang S, Ogawa T, 1990). Other researchers have also used the tensile test to study the bonding strength of concrete-rock interfaces (Lo KY, Lukajic B, Wang S, Ogawa T, 1990; EPRI, 1992; Mouzannar *et al.*, 2017).

1.3.2 **Shear evolution of concrete-rock interfaces.**

1.3.2.1 **Experimental studies of the shear behavior of concrete-rock interfaces**

Lo et al. (Lo KY, Lukajic B, Wang S, Ogawa T, 1990) conducted an experimental study composed of triaxial and tensile tests to assess the structural stability of existing concrete gravity dams. The samples used in this study were obtained by drilling foundations of dams. The observation of the extracted cores revealed three bonding states: bonded, partially bonded, and unbonded concrete-rock interfaces. This revelation showed that it is important to consider both the total and the partially bonded interfaces in investigating the shear behavior of concrete-rock interfaces.

Concerning the stability of concrete-gravity dams, EPRI (EPRI, 1992) conducted an experimental study of concrete-rock interfaces with the samples either extracted from existing dams or prepared in the laboratory. The results of this study show that the shear resistance of the concrete-rock interfaces depends on the rock lithologies. Even though some of the dams considered in this study were built at the beginning of the twentieth century, the tensile strength of the bonded interface

was still important, such that it was similar to the tensile strength of concrete. This observation illustrates the importance of the strength of the concrete-rock bond on the shear resistance of concrete-rock interfaces.

The shear behavior of concrete-rock interfaces has also been studied, focusing on other applications. For example, Saiang et al. (Saiang, Malmgren and Nordlund, 2005) conducted an experimental study to investigate the shear behavior of shotcrete-rock interfaces under low normal loading for application in rock support systems. In this study, tensile, compressive, and direct shear tests were performed. The outcomes of the direct shear tests show two typical shear behaviors.

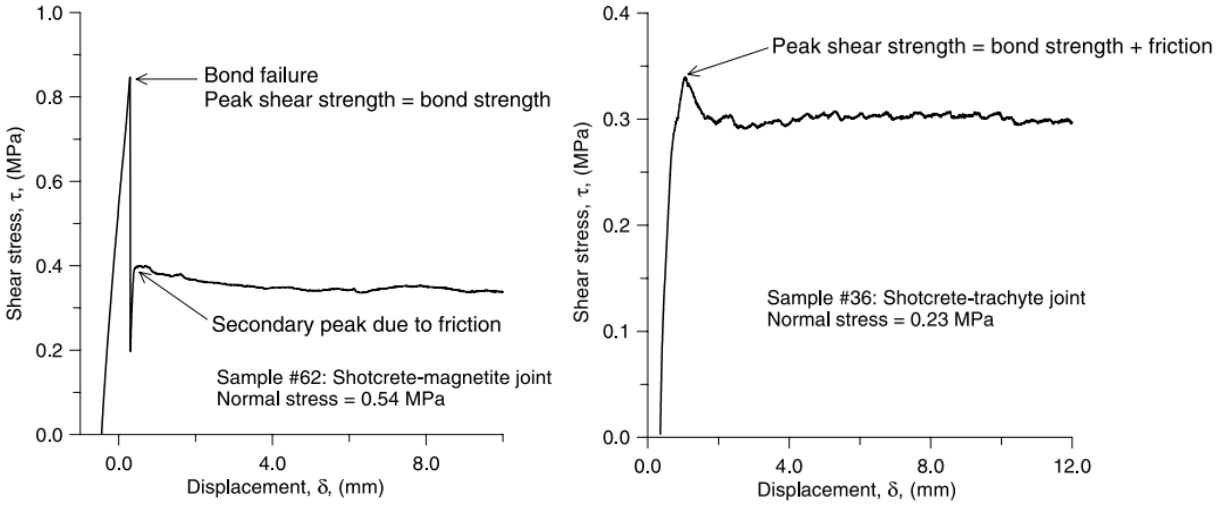

(a) (b)

Figure 1.16 Typical behaviors of concrete-rock interface: (a) with good adhesion and lower normal stress, and (b) with poor adhesion and higher normal stress. Modified from Saiang et al. (Saiang, Malmgren and Nordlund, 2005)

In the first behavior, the shear stress increases with the shear displacement until the peak. Then, it drops suddenly before increasing again to attain a value from which it continues to evolve with little change in magnitude (Figure 1.16 (a)). The strength of the shotcrete-rock bond drives the peak shear strength obtained in this behavior, while the residual shear strength obtained after the peak is driven by the friction of the interface. Furthermore, this behavior is restricted to low normal stress and shotcrete-rock interfaces with good adhesion.

The second behavior is restricted to the results of direct shear tests of samples with poor adhesion, samples with rock surfaces having a JRC between 1-3, and samples tested with high normal stress. The shear evolution increases with the shear displacement up to the peak, then gradually drops to the residual shear strength (Figure 1.16 (b)). This result is interpreted by stating that both the shotcrete-rock bond strength and the interface friction drive the peak and the residual shear strength.

The findings of the investigation carried out by Saiang et al. (Saiang, Malmgren and Nordlund, 2005) highlight the importance of the strength of concrete-rock bond on the shear resistance and give unique insights into the role of normal stress, the roughness, and the rock lithology.

Investigating the shear behavior of concrete-rock interfaces, Liahagen (Liahagen, 2012) and Gutièrrez (Gutiérrez, 2013) carried out direct shear tests of bonded and unbonded smooth and triangular concrete-granite interfaces. The angle of the triangles considered for the bonded interfaces was 40°. The results of this study show that the shear evolution of bonded interfaces is very similar to the results presented by Saiang et al. (Saiang, Malmgren and Nordlund, 2005) concerning the mechanisms influencing the shear evolution. Furthermore, comparing the bonded and unbonded concrete-rock interface results, the authors observed that the roughness has a much-reduced effect on the shear resistance of bonded interfaces than on the shear resistance of unbonded interfaces. This observation supports the relevance of the strength of concrete-rock bond in the shear resistance of interfaces reported in EPRI (EPRI, 1992) and by Saiang et al.(Saiang, Malmgren and Nordlund, 2005).

Moradian et al. (Moradian, Ballivy and Rivard, 2012) recorded acoustic emissions during direct shear tests of bonded and partially bonded concrete-rock interfaces. This study was conducted to understand further the mechanisms active during the shear behavior of concrete-rock interfaces. The results of this study show that, independently of the bonding percentage, the shear evolution monitored by recording the acoustic emissions can be separated into four periods: the pre-peak linear period, the pre-peak nonlinear period, the post-peak period, and the residual period (Figure 1.17).

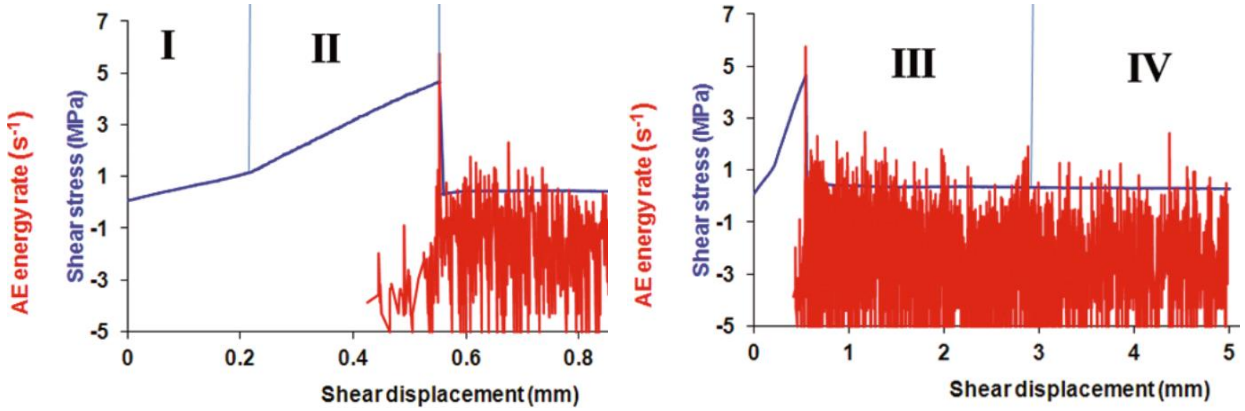

Figure 1.17 Acoustic emissions during the direct shear test on bonded concrete-rock interface under low normal load: evolution of shear stress and logarithmic acoustic emission energy in the shear displacement. Modified from Moradian et al. (Moradian, Ballivy and Rivard, 2012)

The pre-peak linear period (first period) is characterized by increased contact between the two slabs. The progressive failure of second-order asperities characterizes the pre-peak nonlinear period (second period). This period ends when the shear stress reaches the peak, and depending on the normal loading, there is either a failure of the primary asperities or a failure of the bond. The post-peak period (third period) depends on the level of the normal loading, but an increase in acoustic emissions characterizes it. The residual period (fourth period) is characterized by stabilizing the shear stress around the residual shear strength; there might also be asperities degradation but at a smaller scale.

There are no acoustic emissions in the first period for bonded concrete-rock interfaces (Figure 1.17). Depending on the normal loading, some acoustic emissions are recorded in the second period; these are caused by the beginning of the failure of the concrete-rock bond. In the third period, acoustic emissions are boosted because of the drop in the shear stress caused by the failure

of the concrete-rock bond. There are minimum acoustic emissions in the fourth period caused by the motion of sliding along the broken interface.

Figure 1.17 shows that for bonded concrete-rock interface under low normal loading, the concrete-rock bond breaks progressively and not instantaneously, as suggested by Saiang et al.(Saiang, Malmgren and Nordlund, 2005). This observation is evidenced by the recording of acoustic emissions before the peak shear strength. Furthermore, Figure 1.17 confirms that the shear behavior of concrete-rock interfaces under low normal loading depends mainly on the strength of the concrete-rock bond.

Direct shear tests of samples with different bonding percentages were carried out to understand the shear behavior of partially bonded concrete-rock interfaces (Figure 1.18). The results of these tests showed that the lower the bonding percentage, the more gradual the transition from the peak shear strength to the residual shear strength. The lower the bonding percentage, the lower the shear strength. This result was interpreted by stating that for a partially bonded concrete-rock interface, the shear strength depends on the strength of the concrete-rock bond and the friction. This interpretation corroborates and adds more understanding to the second behavior defined by Saiang et al. (Saiang, Malmgren and Nordlund, 2005), which means instead of "poor adhesion," there could be a failure to form concrete-rock adhesion at certain locations of the interface, yielding some approximation of partially bonded interfaces.

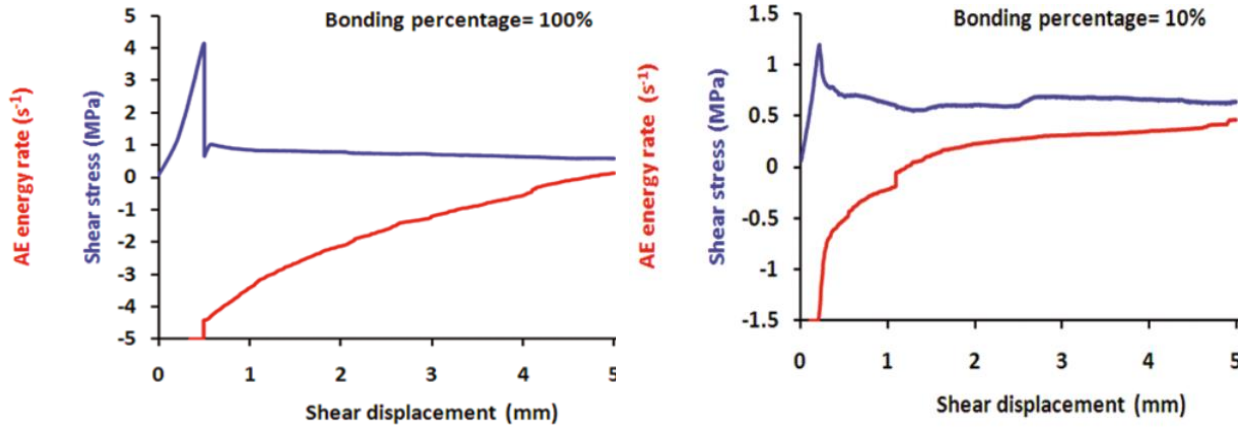

Figure 1.18 Evolution of shear stress and cumulative acoustic emission energy regarding the shear displacement. Modified from Moradian et al. (Moradian, Ballivy and Rivard, 2012)

Assessing the suitability of the peak shear strength obtained in their study to be estimated by the Mohr-Coulomb or the Barton and Choubey failure criterion, Moradian et al. (Moradian, Ballivy and Rivard, 2012) observed that the contribution of the frictional part of these equations was insignificant compared to the contribution of the cohesion. This observation further shows that the strength of the concrete-rock bond is more important in the shear resistance of the interface than the friction, which is in good agreement with the conclusion presented by Liahagen (Liahagen, 2012) and Gutièrrez (Gutiérrez, 2013).

Investigating further the influence of bonding percentage on the shear resistance of concrete-rock interfaces, Krounis et al. (Krounis, Johansson and Larsson, 2016) performed direct shear tests of bonded and partially bonded concrete-rock interfaces, focusing on the strain compatibility of the bonded and the unbonded part of the partially bonded interfaces.

Comparing the results of the fully bonded and unbonded interfaces, these authors noted that both interfaces failed at similar shear displacement. From this observation, they conclude that the friction caused by the roughness of the unbonded part of the interface is mobilized before the failure of the concrete-rock bond at the peak. This conclusion fully supports the explanations proposed by Moradian et al. (Moradian, Ballivy and Rivard, 2012) and Saiang et al. (Saiang, Malmgren and Nordlund, 2005) concerning the shear behavior of partially bonded or bonded interfaces with poor adhesion.

Most of the studies presented do not investigate separately the influence of the strength of smooth concrete-rock bond on the shear behavior of concrete-rock interfaces. To address this specific case, Tian et al. (Tian *et al.*, 2015) performed direct shear tests of sandblasted concrete-dolomite interfaces under the normal stress of 0, 2, 4, and 6 MPa. The results of these tests show the two behaviors reported by Saiang et al. (Saiang, Malmgren and Nordlund, 2005). For smooth concrete-dolomite interfaces, the first behavior is restricted to interfaces with good adhesion and tested with normal stress between 0-2 MPa. Like in the work presented by Saiang et al. (Saiang, Malmgren and Nordlund, 2005), Tian et al. (Tian *et al.*, 2015) recognize two shear behaviors with the same implications in terms of the driving mechanisms of the shear response.

Most of the studies conducted to investigate the shear behavior of concrete-rock interfaces are based on small-scale samples with sub-metric sizes, attempting to understand the influence of the scale of the sample on the shear behavior of concrete-rock interfaces, Mouzannar et al. (Mouzannar *et al.*, 2017) carried out an experimental campaign composed of concrete-rock interfaces using a sample in medium (1mx1m) and small scale (0.148mx0.148m). The results of this study confirm the dependence of the shear resistance of concrete-rock interfaces on the normal stress, roughness, and strength of the concrete-rock bond. The shear resistances of interfaces tested using small-scale samples are higher than those tested using medium-scale samples. Moreover, the cohesion decreases with the increase of the scale of the samples while the friction angle increases with the scale of the sample.

Despite all this progress in understanding the shear behavior of concrete-rock interfaces, some doubts remain regarding, for example, the influence of the coupling roughness and strength of concrete-rock bond on the shear behavior of concrete-rock interfaces.

1.3.2.2 **Influence of roughness on the shear resistance of concrete-granite interfaces**

To investigate the influence of roughness and concrete-rock bond on the shear behavior of concrete-rock interfaces, El Merabi (El Merabi, 2018) performed direct shear tests of smooth, bush-hammered, and rough concrete-granite interfaces using three levels of normal stress (0.5, 1.0, and 1.5 MPa). The results of these tests are analyzed in terms of the type of roughness of the interfaces tested and presented in Badika et al. (Badika *et al.*, 2022).

For the smooth concrete-granite interfaces, it was observed that, independently of the normal stress used, the peak shear strength obtained was not very high compared to the residual shear strength (Figure 1.19). To interpret these results, these authors chose to use the concept of “concrete-rock bonds” instead of the concept of “concrete-rock bond” encountered in the literature (Saiang, Malmgren and Nordlund, 2005; Liahagen, 2012; Moradian, Ballivy and Rivard, 2012; Gutiérrez, 2013; Mouzannar *et al.*, 2017). This change implies that instead of considering the connection of concrete-rock as a single entity with the same strength, the concrete-rock interface can be envisioned as a collection of bonds with different strengths at each location, depending on various parameters. As examples of such parameters, they propose the local shrinkage of concrete during curing (Malmgren, Nordlund and Rolund, 2005; Krounis, Johansson and Larsson, 2016) and the coupling between the chemistry of the minerals composing the granite surface and the roughness

of the granite surface (Shen *et al.*, 2019). A similar interpretation was also adopted by Wilde and Johansson (Westberg Wilde and Johansson, 2013), who reported that there is a variation in the strength of concrete-rock bonds across the interface caused by how clean the surface of the rock before concrete casting, the local properties of the rock and the possibility of a leak in the contact.

Furthermore, this interpretation explains the acoustic emissions recorded by Moradian et al. (Z.A. Moradian *et al.*, 2010) before the peak shear strength. This explanation means that the failure of the concrete-rock bonds is a local and progressive process that depends on the shear strength of bonds. Since there can be a lot of similarities in a rock surface regarding mineral composition and roughness, many bonds have similar strength such that at the peak, there is a sudden failure of many bonds simultaneously. Moreover, the shear behavior that Saiang et al. (Saiang, Malmgren and Nordlund, 2005) interpreted as caused by "poor adhesion" could be related to the difference in the strength of the bonds across the interface. With this consideration, Badika et al. (Badika *et al.*, 2022) state that the closeness between the peak and the residual shear strength obtained in the tests of smooth concrete-granite interfaces is related to the formation of very few strong concrete-granite bonds across the interface.

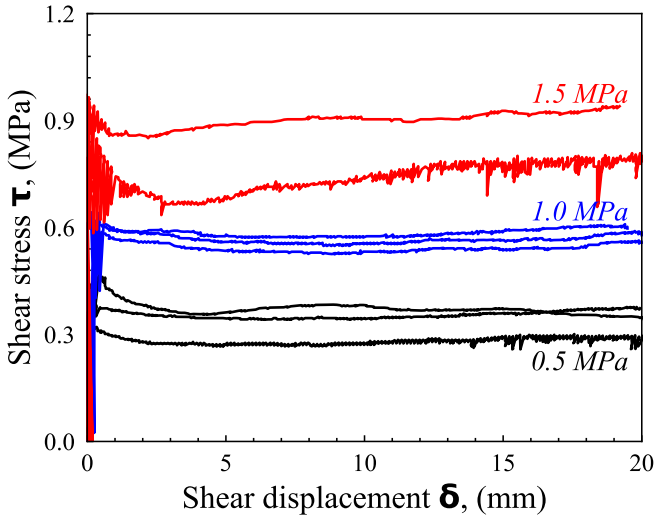

Figure 1.19 Shear stress of smooth concrete-granite interfaces (Badika *et al.*, 2022)

The motivation that led El Merabi (El Merabi, 2018) to perform tests with bush-hammered and rough concrete-granite interfaces came from investigating the influence of two roughness aspects. These aspects are the influence of unevenness and waviness of asperities on forming strong concrete-granite bonds. For this reason, the unevenness was approximated by the micro-roughness generated upon bush-hammering smooth granite surfaces. In contrast, the combination of unevenness and waviness is encountered in the rough concrete-granite interfaces.

Badika et al. (Badika *et al.*, 2022) observed comparing the results of bush-hammered concrete-granite interfaces to the results of smooth concrete-granite interfaces (Figure 1.20), that for all the levels of normal stress considered, the peak shear strength is very high compared to the residual shear strength. This observation means that the formation of a significant proportion of strong concrete-rock bonds is related to micro-roughness in flat concrete-granite interfaces. Dong et al. (Dong *et al.*, 2021) also reported a similar conclusion, stating that adding heuristic groovy-like roughness to the smooth concrete-granite interfaces improved the strength of concrete-rock bonds generated.

Furthermore, the results of the tests with bush-hammered interfaces are very similar to the results reported in other works (Saiang, Malmgren and Nordlund, 2005; Moradian, Ballivy and Rivard, 2012; Tian *et al.*, 2015; Mouzannar *et al.*, 2017). Two types of failure modes are defined according to the normal stress level. The first failure mode is restricted to the normal stress of 0.5 MPa. It is characterized by the sudden transition between the peak and the residual shear strength, and the failure occurs mainly along the interface. The second failure mode is restricted to 1.0 and 1.5 MPa of normal stress; a gradual transition between the peak and the residual shear stress characterizes it. The post-mortem shows that the failure occurs mainly on the interface, but the concrete tips are sheared off and remain attached to granite.

Regarding the mechanisms driving the shear evolution, Badika et al. (Badika *et al.*, 2022) separated the shear evolution of both failure modes into three phases. For the pre-peak phase, the shear evolution depends on the strength of concrete-rock bonds. For the transition between the peak and the residual shear strength, the shear evolution is controlled by the progressive failure of the bonds and the gradual mobilization of friction. For the residual phase, the shear evolution is controlled by friction.

The results of rough concrete-granite interfaces show the two failure modes encountered in bush-hammered interfaces with similar implications regarding the mechanisms driving the shear evolution.

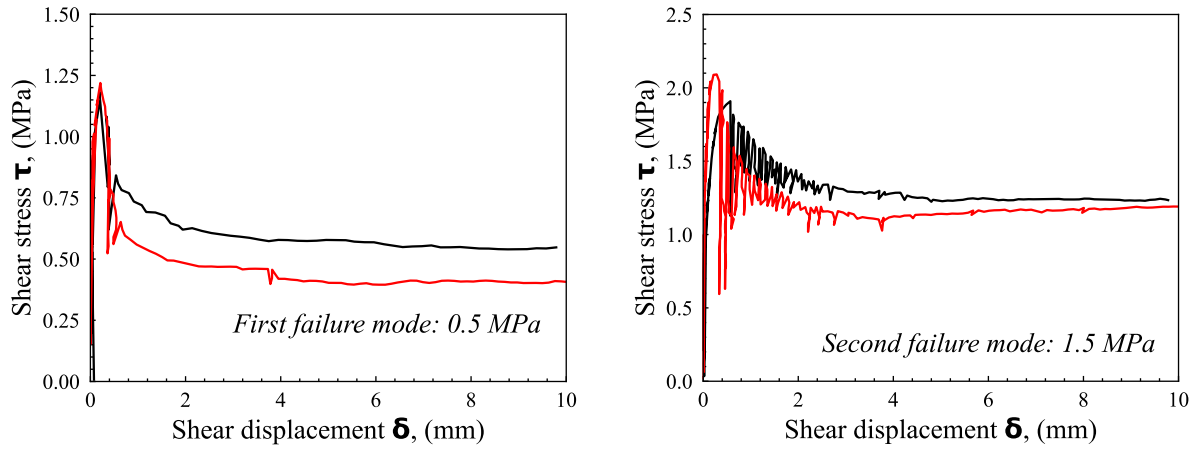

Figure 1.20 Types of shear evolution of bush-hammered concrete-granite interfaces (Badika *et al.*, 2022)

Comparing the results of the bush-hammered and rough concrete-granite interfaces (Figure 1.21), the rough concrete-granite interfaces have a lower cohesion than the bush-hammered concrete-granite interfaces. The authors explained this discrepancy by the difference in roughness in terms of uniformity between the two types of interfaces. Moreover, as expected, the authors reported that the friction angle of the rough concrete-granite interfaces is higher than that of the bush-hammered concrete-granite interfaces. They justified this result by stating that the bush-hammered concrete-granite interfaces are globally flat.

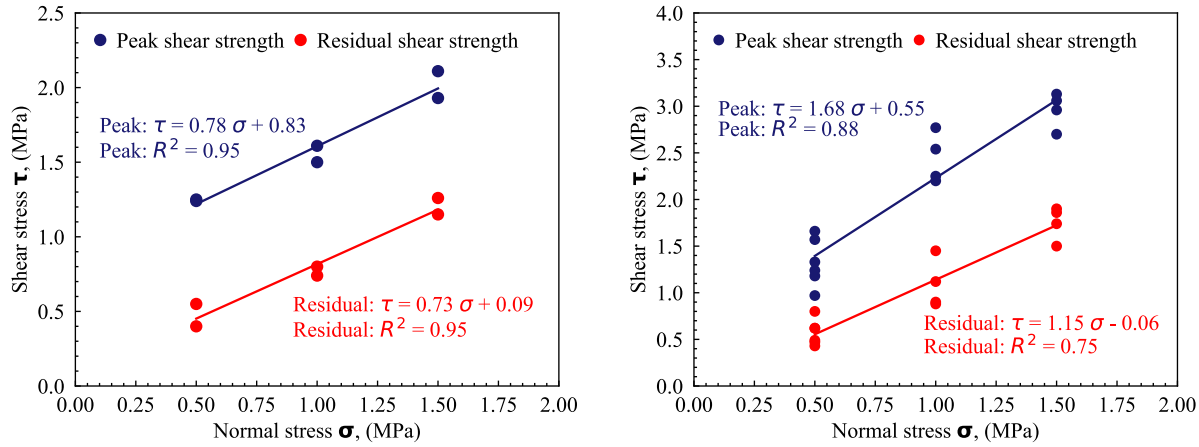

Figure 1.21 Mohr-Coulomb envelop for bush-hammered and rough concrete-granite interfaces (Badika *et al.*, 2022)

1.3.3 **Summary**

The experimental studies of the shear behavior of concrete-rock interfaces have helped improve understanding of the parameters influencing the shear resistance. The main mechanisms active during the shear process have been identified from this understanding.

Despite the progress in the experimental investigation of the shear behavior of concrete-rock interfaces, it is worth noting that all the failure criteria presented and all the experimental studies discussed focused on the static shear behavior of rock-rock and concrete-rock interfaces and did not take into consideration the possibility of the shear failure of concrete-rock interfaces as a result of dynamic shear loading. However, structures such as concrete gravity dams can experience a dynamic shear loading during their lifetime. For this reason, this loading condition should be considered for both scientific interest and design and durability considerations.

1.4 **Consideration for dynamic shear testing of interfaces**

This section discusses considerations relevant to the dynamic testing of concrete-rock interfaces. Probable wave sources of dynamic shear loading that can act on a concrete-rock interface in a geotechnical structure include impacts, explosions, blasting, rockbursts, seismic events, earthquakes, and repetitive or cyclic loading (Zhang and Zhao, 2014). In this thesis, a pioneering experimental study to investigate the dynamic shear behavior of concrete-rock interfaces is carried out. This experimental study focuses on the dynamic shear behavior of interfaces where the shear loading is applied using impact loading with high strain rates.

In the literature, the dynamic behavior of geomaterials under high strain rates is usually investigated using the split Hopkinson pressure bars system (SHPB).

1.4.1 **Principle of the SHPB**

The SHPB comprises the striker bar, the incident or input bar, and the transmitted bar (Xia and Yao, 2015); see Figure 1.22. A gas gun launches the striker bar, impacting the end of the incident bar and resulting in a compressive wave propagating on the incident and the striker bar. The compressive wave propagating in the bar is called an incident pulse and is usually denoted ε_i, the

duration of this pulse depend on the wave velocity on the bar. When the incident pulse ε_i reaches the specimen, it is separated into two parts; the first part is the reflected wave ε_r which propagates back to the incident bar while the second part is the transmitted wave ε_t which loads the specimen. To record the incident, the reflected and the transmitted wave, measurement system such as strain gauges can be used. The computation of the results of tests performed using the SHPB is usually carried out using the one wave analysis method (Mohr, Gary and Lundberg, 2010). However, to ensure that the computation using the one wave analysis yields accurate results, certain testing conditions, such as the mechanical balance of the sample (stress equilibrium), must be verified, the failure sequence must be adequate, and the inertia and friction effect must be minimized (Dai et al., 2010). The SHPB has been used in various testing methods to investigate the dynamic shear behavior of geomaterials. The principal dynamic testing methods for geomaterials, including the SHPB, are discussed hereafter. Furthermore relevant dynamic responses of the concrete-rock interfaces tested using testing methodology that include the SHPB are also presented.

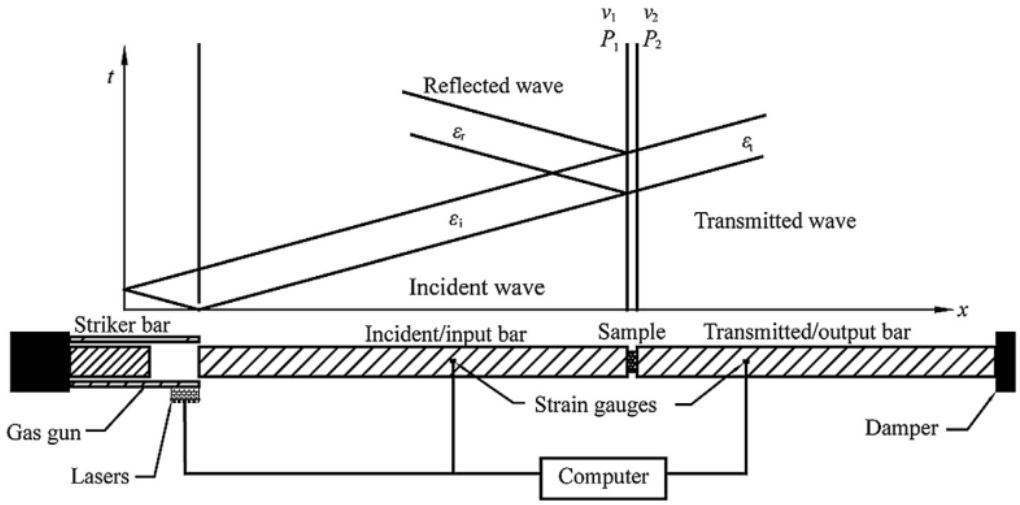

Figure 1.22 Schematic of the split Hopkinson pressure bar and a displacement (x) time (t) of stress propagation in the test (Xia and Yao, 2015).

1.4.2 **Dynamic testing of geomaterials**

1.4.2.1 **Dynamic compression tests**

Figure 1.22 illustrates the dynamic compression test using the SHPB. This test is based on the 1D elastic stress wave propagation in the bars. Longer bars are usually used to ensure the unidimensionality of the stress wave, and lower impact velocities are used to maintain the stress wave elasticity (Xia and Yao, 2015). In this test, it is important to maintain a homogeneous deformation in the sample. The homogeneous deformation of the sample is usually controlled by reducing the inertial effect (Davies and Hunter, 1963; Meng and Li, 2003) and the interface friction effect (Bertholf and Karnes, 1975).

Dai et al. (Dai *et al.*, 2010) and Wang et al. (Wang *et al.*, 2021) investigated the dynamic compressive behavior of rocks and concrete using the SHPB.

1.4.2.2 **Dynamic tensile test**

A schematic for a split Hopkinson tension bar system (SHTB) is presented in Figure 1.23. Unlike the SHPB, the SHTB presented has apparatus in the incident and the transmitted bar to absorb the wave. The sample can be glued to the bars using epoxy. Huang et al. (Huang, Chen and Xia, 2010) used the SHTB presented in Figure 1.23 to investigate the dynamic tensile properties of rocks.

However, the SHPB can also perform dynamic indirect tension tests. Xia (Xia, 2012) used a Brazilian test-based disc and a semi-circular Brazilian test-based disc as a specimen for the SHPB to investigate the tensile resistance of rocks.

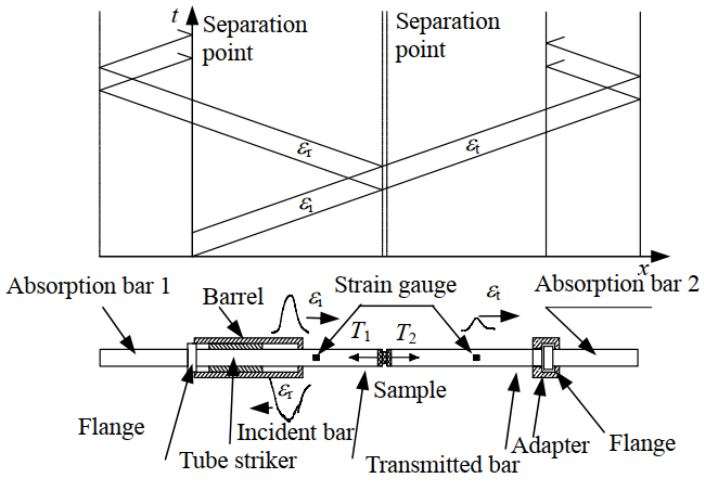

Figure 1.23 Schematic of the split Hopkinson tension bar and a displacement (x) time (t) of stress propagation in the test (Huang, Chen and Xia, 2010)

1.4.2.3 **Dynamic shear test**

Huang et al. (Huang, Feng and Xia, 2011) developed a sample holder to use along with the SHPB to carry out punch-through shear tests to study the dynamic shear resistance of sandstone.

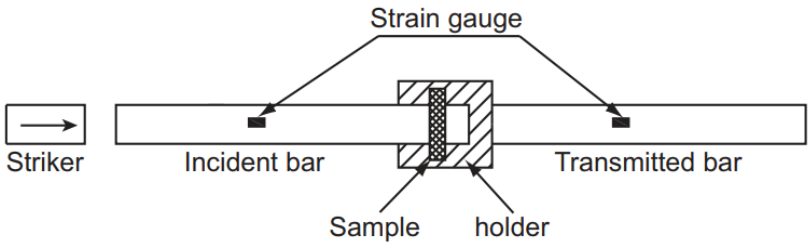

Figure 1.24 SHPB for the punch-through shear test (Huang, Feng and Xia, 2011)

Other uses of the SHPB for the investigation of the shear behavior of geomaterials include the experimental studies carried out by Forquin and Sallier (Forquin and Sallier, 2013), Lukić and Forquin (Lukić and Forquin, 2016), Abdul-Rahman et al.(Abdul-Rahman, Saletti and Forquin,

2021) and Tawfik et al.(Tawfik *et al.*, 2022), who respectively investigated the shear behavior of rocks, concrete, and polymer.

1.4.3 **Dynamic responses of interfaces**

In the literature, only a few studies have investigated the dynamic behavior of rock-rock or concrete-rock interfaces.

Li et al. (Li *et al.*, 2022) introduced a dynamic shear test to investigate the shear behavior of rock-rock interfaces. The test proposed comprises a system to apply confinement stress and uses the SHPB to apply the dynamic shear loading. This test setup is illustrated in Figure 1.25

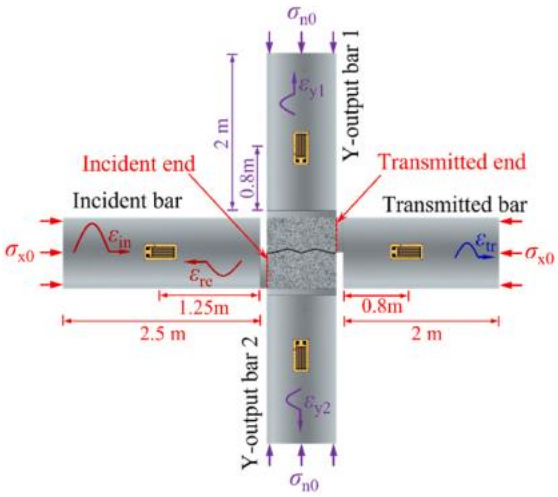

Figure 1.25 Schematic representation of the dynamic shear test proposed by Li et al. (Li *et al.*, 2022)

During this study, Li et al. (Li *et al.*, 2022) demonstrated that achieving mechanical balance or stress equilibrium in the shear tests of interfaces submitted to confinement stress below 12 MPa is very difficult. This difficulty is primarily related to the low impedance of interfaces. Consequently, these authors proposed using the stress pulse collected in the transmitted bar to compute the test results.

With the proposed test setup, Li et al. (Li *et al.*, 2022) conducted an experimental study of the dynamic shear behavior of tooth-shaped granite-granite interfaces submitted to different initial confinement stresses. The analysis of the results of this experimental campaign led the authors to propose a subdivision of the dynamic shear response of rock-rock interfaces into four steps and to identify the mechanisms driving each step. This study is limited to unbonded triangular rock-rock interfaces and does not address the more complex rough interfaces or bonded concrete-rock interfaces.

Qiu et al. (Qiu *et al.*, 2022) presented an experimental and numerical study of the dynamic fracture behavior of concrete-marble interfaces. The sample contains a 60° angular notch and an induced pre-crack to orient the fracture along the interface. The dynamic fracture test performed is carried out using the test setup of the dynamic compression test with the SHPB. The analytical assessment of the results of these tests shows that the roughness of the concrete-marble interface influences the dynamic resistance of the concrete-marble bond. The post-mortem of the tests shows that the

failure mainly occurs at the interface. The crack propagation across the concrete-marble interface has different speeds in the same sample and the samples with similar roughness. This study does not consider the effect of normal stress on the dynamic resistance of the interface.

Zhou et al. (Zhou, Lu and Cai, 2020) executed an experimental study to investigate the influence of the orientation of the concrete-rock interfaces on their static and dynamic tensile strength. The test setup used in this study is the dynamic compression test with the SHPB. The sample is a bi-material disc comprising a concrete-rock interface. The post-mortem of the tests performed shows three failure modes relative to the orientation of the interface. The three failure modes are interface fracture, tensile fracture, and a combination of the first failure modes. Furthermore, this study provides relevant data for the comparative assessment between the static and the dynamic tensile strength of interfaces. This study does not investigate complex interfaces like rough concrete-rock interfaces nor consider the influence of confinement stress.

1.5 **Numerical modeling of the shear behavior of interfaces**

The advances in the numerical modeling presented in this section only address the case of static shear loading, given that investigating the dynamic shear behavior of rock-rock and concrete-rock interfaces is still preliminary.

The development of numerical modeling of concrete-rock interfaces is a direct result of the rapid progress in understanding the shear behavior of these interfaces due to a series of experimental studies carried out in the last few decades.

However, since the investigation of the shear behavior of concrete-rock interfaces is based on the shear behavior of other interfaces, this section is separated into two parts. The first part reviews the recent studies on the numerical modeling of unbonded rock-rock interfaces (rock joints) and unbonded concrete-rock interfaces. The second part reviews the numerical modeling of the bonded cemented bolt and the bonded concrete-rock interfaces.

This presentation focuses on the most used numerical modeling methods, the discrete elements method (DEM) and the finite elements method (FEM).

1.5.1 **Numerical modeling of the shear behavior of unbonded interfaces**

1.5.1.1 **Case of rock-rock interfaces**

The failure modes observed in the post-mortem of shear tests are usually strongly dependent on the asperities breakage during the test. Karami and Stead (Karami and Stead, 2008) investigated the asperity degradation of rock joints using numerical simulations of direct shear tests of rough rock-rock interfaces. The simulated interfaces were selected from the ten standard profiles proposed by Barton and Choubey (Barton and Choubey, 1977). The simulations were performed using a hybrid FEM/DEM code ELFEN. In this code, the failure envelope comprises the Mohr-Coulomb failure surface under compressive conditions and anisotropic crack models in tension. Discrete fractures are generated either inside the fracturing element or along the interface between elements. The results of these simulations show that the degradation of asperities depends mainly on the normal stress. Under low normal stress, the degradation is characterized by wear at the interface, while under high normal stress there is a combination of wear and asperity breakage.

The roughness of interfaces has been proven to be an influencing parameter in the shear behavior of interfaces, and this parameter has been studied using numerical modeling. Park and Song (Park and Song, 2009) investigated the influence of roughness and joint compressive strength (JCS) in the shear resistance of rock-rock interfaces. The investigation was carried out using DEM

simulations of direct shear tests performed using rough interfaces generated by defining the joint contacts at the shear plane. The bond strength between particles was reduced to simulate different weathering conditions characterized by the JCS. The bonded particle model (BPM) is used in these simulations. This model generates a small glue active at the contact between particles and can only transmit forces. The results of this study show that the shear resistance of rock joints and the dilation angle depend predominantly on the friction coefficient.

The BPM was also successfully used in a similar study presented by Yin et al. (Yin *et al.*, 2023) to investigate the influence of the normal stress and the loading rates in the shear strength of rock-rock interfaces.

Given that the mechanical properties of rocks depend on the discontinuities and mineral orientations, Chiu et al. (Chiu *et al.*, 2013) conducted a DEM-based numerical investigation of the anisotropic behavior of jointed rock mass. Two models were used in this numerical study. The first model is the parallel bond model (PBM); this model transmits force and moment between particles. To simulate the jointing effect at the interface, the authors modified the smooth joint contact model (SJCM) by defining friction as a function of the roughness, the normal stress, and the JCS. The SJCM simulates the behavior of the interface between particles without consideration of the orientation of contact. These two models are illustrated in Figure 1.26. The modifications applied to the SJCM rely on the work of Barton and Choubey (Barton and Choubey, 1977). The simulations using the modified SJCM show that the new model performs better than the existing models when mixed failure modes are activated.

The BPM and the SJCM were also successfully used by Shang et al. (Shang, Zhao, et al., 2018), who investigated the shear behavior of rock joints focusing on crack propagation as a function of the presence of rock bridges. These authors also presented in a companion study (Shang, Zhao and Ma, 2018) the results of the investigation of the influence of the CNL and CNS boundary conditions on the shear resistance of interfaces using a similar DEM model.

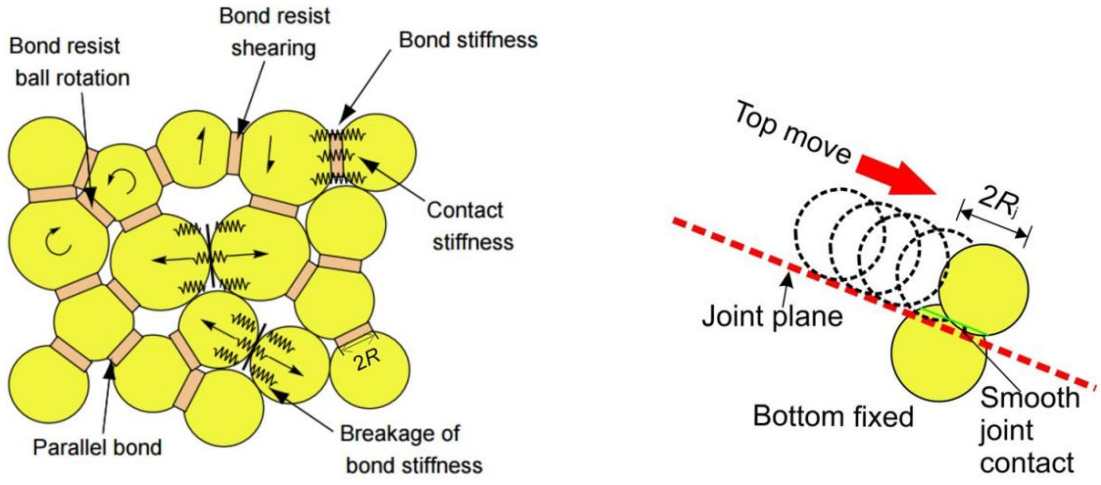

(a) **(b)**

Figure 1.26 Illustration of the **(a)** parallel bonded model and **(b)** smooth joint model Modified from Shang et al.(Shang, Zhao, *et al.*, 2018)

Persistence, a discontinuity characteristic in jointed rock blocks, has also been investigated using numerical modeling. The flat-joint contact model (FJCM) and the SJCM were used by Cao et al.

(Cao *et al.*, 2022) to investigate the influence of persistence on the shear evolution of jointed rock masses. The FJCM simulates the contact between particles in the model using notional surfaces. The results of this study show that the increase in joint persistence causes a decrease in the shear cohesion, friction angle, and shear strength.

1.5.1.2 **Case of concrete-rock interfaces**

Studying the numerical modeling of triangular and fractal unbonded concrete-rock interfaces, Haberfield and Seidel (Haberfield and Seidel, 1999) presented an analytical model that integrates the shear resistance of asperities experiencing contact. The model considers that the asperities slide along each other initially and are later sheared off. The sliding of the triangular asperities is computed using Eq (1.2), proposed by Patton (Patton, 1966). With the increase of the shear slip, the contact area decreases such that stress concentrations in the steepest asperities lead to shearing. The shear stress in this step can be computed using the slope-stability methods. These authors used Sokolovsky's closed-form solution, which also predicts the topography of the failure. Figure 1.27 shows the asperities sliding and shearing process during shear as envisioned in the proposed model. This model performs well in estimating the shear strength of unbonded concrete-rock interfaces but overestimates the shear resistance of rock-rock interfaces.

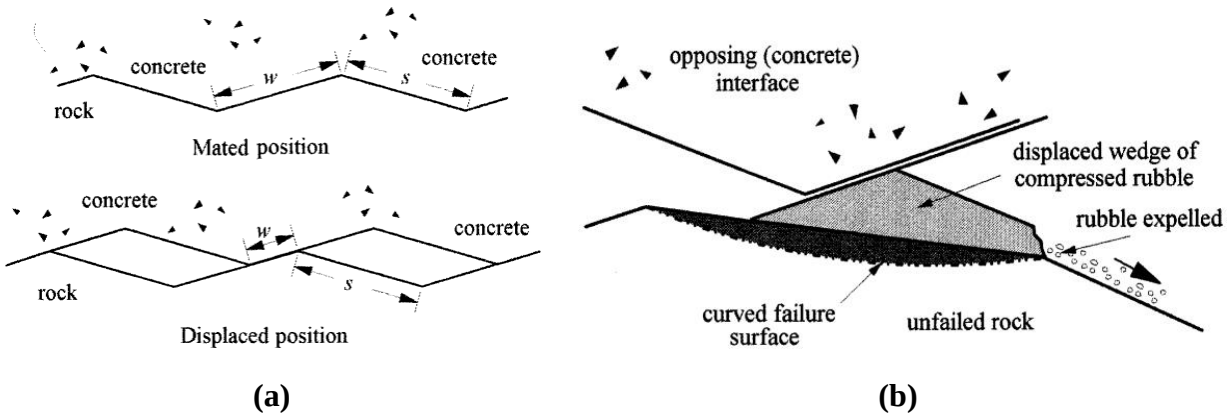

Figure 1.27 a) Asperity sliding and b) Shearing through asperities. Modified from Haberfield and Seidel (Haberfield and Seidel, 1999)

Gutiérrez et al. (Gutiérrez-Ch *et al.*, 2018) used DEM to simulate the shear behavior of unbonded smooth and unbonded triangular concrete-rock interfaces using the FJCM and the SJCM. The SJCM is set to replicate the macroscopic behavior of a set of contacting particles. The parameters of these models were determined by calibration using the results of the UCS tests and the direct shear tests of smooth concrete-rock interfaces. The simulation outcomes show that the model can reproduce the shear behavior, failure modes, and asperity degradation during the shear evolution.

All the models presented focus mainly on the events at the interface. Furthermore, these models also attempt to consider the influence of roughness on the shear resistance in different circumstances of normal stresses. This outcome encourages considering events at the interface and different aspects of roughness in modeling the shear behavior of rough concrete-rock interfaces under the conditions of lower normal loadings.

1.5.2 **Numerical modeling of the shear behavior of bonded interfaces**

Since this thesis is interested in modeling the shear behavior of bonded concrete-rock interfaces, numerical works investigating the shear behavior of bonded interfaces are reviewed. This review first presents the results of the investigation of the shear behavior of cemented bolt systems and then focuses on the concrete-rock interfaces.

1.5.2.1 **Case of cemented bolt interfaces**

Shang et al. (Shang, Yokota, *et al.*, 2018) investigated the shear behavior of mortar-bolt interfaces using DEM simulations. The model is composed of the flat-joint contact model (FJCM), the parallel bonded model (BPM), the SJCM, and the linear model (LM). A schematic representation of the FJCM is shown in Figure 1.28 (a). The BPM simulates the bolt. The SJCM simulates particles overlapping at the mortar-bolt interface and sliding away from each other. The linear model (Figure 1.28 (b)) simulates the contact between particles and the wall. The results of the simulations performed provide two unique insights into the shear response of bonded mortar-bolt interfaces. First, the debonding of the mortar-rock bond is progressive. Second, the failure of concrete is a consequence of the interface interlocking caused by the surficial geometry of the bolt (roughness).

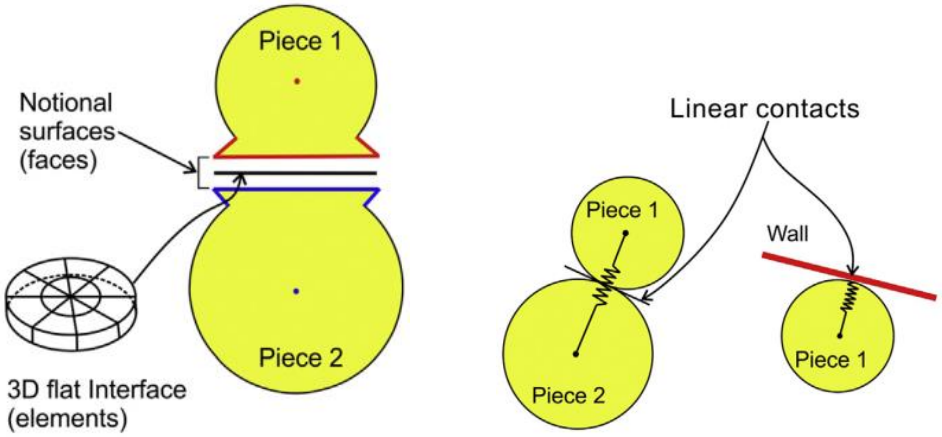

(a) (b)

Figure 1.28 Illustration of the (a) flat joint contact model (FJCM) and the (b) linear model (LM). Modified from Shang et al. (Shang, Yokota, *et al.*, 2018)

Dong et al. (Dong *et al.*, 2020) proposed a FEM numerical model to study the shear behavior of concrete-bolt interfaces. The model uses the concept of cohesive-frictional behavior (Tian *et al.*, 2015), implemented using cohesive elements (cohesive zone) instead of a cohesive surface (Tian *et al.*, 2015). In modeling the shear behavior of interfaces using cohesive zone modeling, the interface is conceived as a plane representing a crack in the domain. The model can reproduce the overall shear responses obtained in experimental tests.

1.5.2.2 **Case of concrete-rock interfaces**

As reported in the experimental studies, the shear behavior of rock-rock interfaces or unbonded concrete-rock interfaces does not represent the shear behavior of concrete-rock interfaces since they do not consider the influence of the concrete-rock bonds in the shear resistance. Furthermore,

compared to the shear behavior of cemented bolt interfaces, the shear behavior of concrete-rock interfaces is different because the characteristics of the bond depend on the minerals present on the rock surface. These observations are also true for numerical modeling.

To simulate the shear behavior of smooth concrete-rock interfaces focusing on the influence of concrete-rock bond, Tian et al. (Tian *et al.*, 2015) proposed a finite element model to reproduce the shear evolution of smooth concrete-rock interfaces. The model assumes a gradual failure of the cohesive bond and is based on an idealization of the shear evolution as a combination of three phases. The three phases are the pre-peak phase, driven by the bond stiffness; the transitional phase, characterized by the progressive failure of the bond and mobilization of friction; and the residual phase, controlled by friction. The model is implemented in Abaqus using cohesive and frictional behaviors. This model has been successfully used in the simulation of foamed smooth concrete-rock interfaces, as presented by Zhao et al. (Zhao, Chen and Zhao, 2018). Furthermore, this model will be presented in more detail in Chapter 2, including the reinterpretation of the shear evolution of concrete-rock interfaces presented in Badika et al. (Badika *et al.*, 2022) to simulate the shear behavior of rough concrete-rock interfaces.

Focusing on the study of the numerical modeling of the shear behavior of concrete-rock interfaces, Dong et al. (Dong *et al.*, 2021) proposed a shear softening constitutive law for concrete-rock interfaces based on an experimental study designed to investigate fracture properties. The constitutive law proposed is a model aimed at characterizing the concrete-rock bond using a traction separation relationship. The proposed law considers the influence of interface geometry. The results of this study show that the proposed model can reproduce the shear response of concrete-rock interfaces expressed as the shear resistance in terms of the CMOD (crack mouth opening displacement).

Moreover, Murali et al. (Murali *et al.*, 2022) investigated the load-bearing mechanisms of rock socketed piles using an experimental and numerical approach. The experiment comprises tests carried out with X-ray CT imaging. The results of the experimental fold of this research show interesting insights into the micro-mechanics of bonded rock socketed piles. Two interface failure mechanisms were observed during the tests: the sliding and the local and progressive shear. DEM-based numerical modeling of the mechanical behavior of rock socketed piles was carried out using the BPM and the cohesive damage plastic model (CDPM). A schematic representation of the CDPM is presented in Figure 1.29. The progressive degradation of the bonds is simulated using damage mechanics included in the CDPM model.

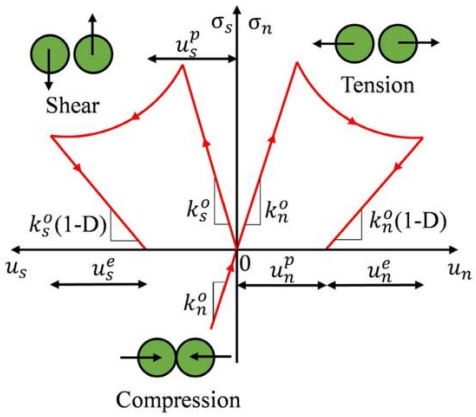

Figure 1.29 Illustration of the Cohesive damage plasticity model – CDPM. Modified from Murali et al. (Murali *et al.*, 2022)

The numerical modeling of bonded interfaces presented emphasizes the necessity of surface interlocking as a consequence of the roughness of the interface. Furthermore, these models find it important to faithfully represent the progressive bond degradation in the contact between particles to reproduce the overall shear response of the interface obtained experimentally.

The numerical models encountered in the literature show that to model the shear behavior of interfaces, it is important to focus on the phenomenon occurring at the interface, consider the different aspects of the influence of roughness, and attempt to reproduce the progressive nature of the shear evolution across the interface.

1.6 **Generation of random fields**

The generation of synthetic rough rock surfaces can play an important role in investigating the influence of roughness on the shear behavior of interfaces. Synthetic rough rock surfaces can be generated using random field theory.

In this section, a brief introduction to the concept of random field theory is presented.

1.6.1 **Concepts of random field theory**

The most important concepts of random field theory, as presented by Wackernagel (Wackernagel, 2003), can be summarized as follows. A field representing a distribution of a desired property or characteristic provides information about regionalized variables $z(x)$. Components of regionalized variable $z(x)$ are called regionalized value, $z(x_\alpha)$. A regionalized variable $z(x)$ results from a random function $Z(x)$. A random function $Z(x)$ is a set of infinite random variables $Z(x_\alpha)$. A random variable $Z(x_\alpha)$ is a random mechanism generating regionalized value $z(x_\alpha)$ at location x_α of the domain. The regionalized value generated depend on the local characteristics of the domain.

A definition of a random function model is important for random field theory and, therefore, for random field simulation. For a property or characteristic to be considered a random function, each sample of this property in a defined domain must satisfy two requirements. First, the values composing the field (sample) must depend on their location in the domain; this means they are regionalized. Second, all the field values must be complex enough that they cannot be modeled by a simple function, which means the probabilistic approach is necessary to characterize the field.

This combination of the concept of regionalization and randomness (probabilistic approach) is at the heart of the definition of the random function model (Wackernagel, 2003). This association is schematically represented in Figure 1.30.

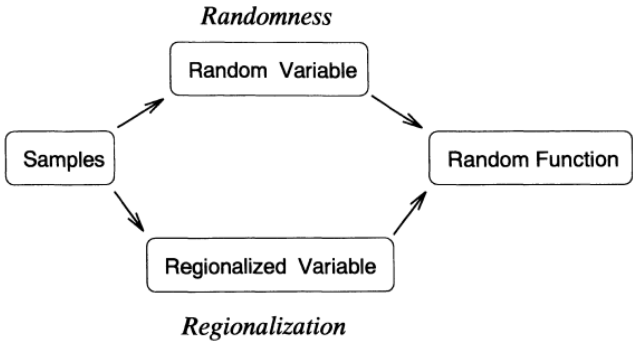

Figure 1.30 Definition of a random function model (Wackernagel, 2003)

To simulate random fields, it is important to consider three further considerations of random field theory: stationarity, data distribution assessment, and field characterization.

1.6.1.1 **Stationarity**

Stationarity is a strategy to remediate the difficulty of deducing every possible distribution function for any field, given only a few realizations of a random function model (Wackernagel, 2003).

Stationarity entails that the characteristics of the random function model remain constant when one moves from one location to another in the domain. This property is also called translation invariance (Wackernagel, 2003). When the stationarity defined above is applied directly to sets of points of a random field, it is called strict stationarity. However, the definition of strict stationarity is too restrictive and cannot be verified in many applications. Therefore, a less strict definition of stationarity is adopted for most problems. There are two possible definitions of loose stationarity. The first one is the second-order stationarity, which requires that only the first two moments (mean and variance) of the field be stationary. The second one is intrinsic stationarity, which implies that only the first two moments of the difference of pairs of points have to be constant in the domain.

These definitions of looser stationarity require that data distributions be Gaussian, which means they can be characterized by the first two moments.

1.6.1.2 **Data transformation**

For most applications in soil and rock mechanics, the data does not usually follow the normal distribution (Fenton and Griffiths, 2008; Casagrande *et al.*, 2018; Jeffery, 2021); this makes it difficult to adopt the loose stationarity as a requirement for the use of random field theory and therefore random field simulations. To address this problem, two approaches can be used.

The first approach is proposed by Fenton and Griffith (Fenton and Griffiths, 2008). It consists of converting a random field with non-stationary mean and variance into a random field with stationary mean and variance using Eq (1.15). The mean of the transformed random field $\mu(t)$ is zero, while the variance of the transformed random field $\sigma(t)$ is equal to one.

$$X'(t) = \frac{X(t) - \mu(t)}{\sigma(t)} \tag{1.15}$$

where $X(t)$ is the random field with non-stationary mean and variance, $X'(t)$ is the transformed random field with a mean equivalent to zero and variance equivalent to one everywhere in the domain, $\mu(t)$ is the mean, and $\sigma(t)$ is the standard deviation.

This approach is adopted in the work presented by Casagrande et al. (Casagrande *et al.*, 2018) and Jeffery et al. (Jeffery *et al.*, 2021).

The second approach to transforming data into a Gaussian distribution is called the quantile-to-quantile normal scores transformation. This approach aims to obtain the standard normal distribution given by Eq (1.16).

$$f_Y(y) = \frac{1}{\sqrt{2 * \pi}} * e^{-\frac{1}{2} * y^2} \tag{1.16}$$

where $f_Y(y)$ is the standard normal probability density function.

The quantile-to-quantile normal scores transformation associates the p-quantile of the data distribution at hand with the p-quantile of a standard normal distribution. This transformation implies that the data variable z with a cumulative distribution $F_Z(z)$ will be transformed into y, which is a normal score value with a standard normal distribution function $F_Y(y)$, see Eq (1.17) (Pyrcz and Deutsch, 2020).

$$y = F_Y^{-1}\big(F_Z(z)\big) \tag{1.17}$$

However, in practice, this transformation is straightforward, as presented in this example provided by Pyrcz and Deutsch (Pyrcz and Deutsch, 2020), refer to Figure 1.31. First, the histogram of the sample is computed and represented at the top left of Figure 1.31. Second, the cumulative distribution of the data is computed; see bottom left of Figure 1.31. At the same time, a standard normal distribution and its cumulative distribution are represented in the top and bottom right of Figure 1.31. To determine the equivalent value of, say, a porosity of 10% in the normal distribution, one projects the cumulative frequency corresponding to the porosity of 10% to the cumulative frequency of the standard normal distribution, which yields a value of -0.45. The value obtained is called a normal score.

Usually, after random field simulations using normalized data, back-transformations are computed to bring the generated realizations back to the initial distribution using the inverse of the processes used for the normalization.

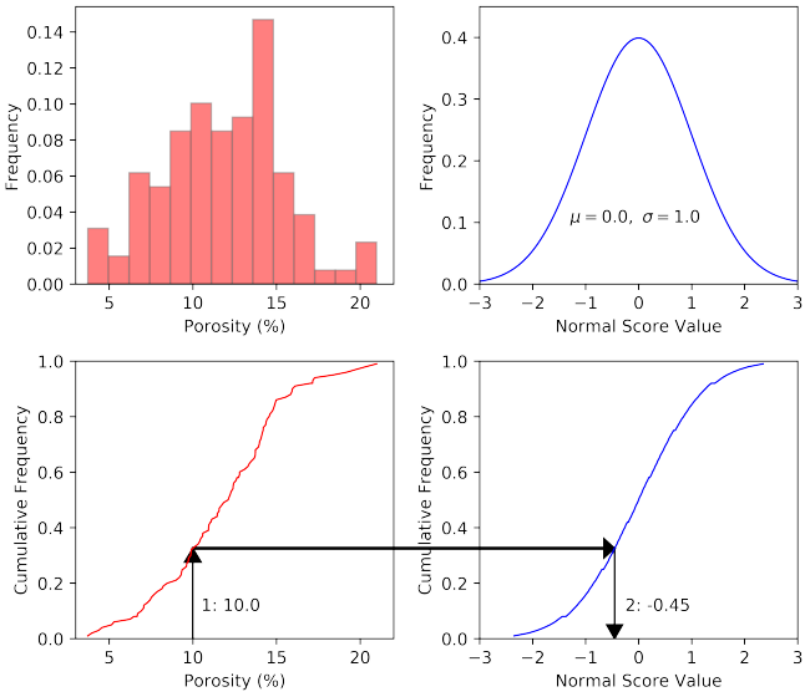

Figure 1.31 Quantile-to-quantile normal scores transformation (Pyrcz and Deutsch, 2020)

1.6.1.3 **Characterization of the field for random field simulations**

After the geostatistic treatments of the data through the considerations of stationarity and data transformation, it is now a question of determining the characteristics of the field to be used in the subsequent analysis of random field simulations. For this purpose, two approaches are commonly used.

The first approach uses autocorrelation functions to determine the correlation length (Jeffery, 2021). In this approach, first, the values of the autocorrelation $\hat{\rho}(d)$ are computed for different lags d using for example Eq (1.18).

$$\hat{\rho}(d) = \frac{\sum(X_t - \bar{X})\,(X_{t+d} - \bar{X})}{\sum(X_t - \bar{X})^2} \tag{1.18}$$

where X_t is a data point, $\bar{X}$ is the mean of the data, X_{t+d} is the data point separated by a lag distance d.

The data obtained using the results of the computation of autocorrelations $\hat{\rho}(d)$ are fitted using a theoretical correlation function to determine the correlation length θ. Fenton and Griffith (Fenton and Griffiths, 2008) proposed two types of theoretical autocorrelation functions, see Eq (1.19).

$$\rho(d) = e^{-\left(\frac{|d|}{\theta}\right)}$$
$$\rho(d) = e^{-\pi\left(\frac{|d|}{\theta}\right)^2} \tag{1.19}$$

where $\rho(d)$ is the autocorrelation function, d is the lag, and θ is the correlation length.

The second approach is the use of variogram analysis. First, variograms are computed for different lag distances. Second, a theoretical covariance function is fitted to the scatter plot of the computed variograms. Last, the parameters of the theoretical covariance function are determined and separated to be used in the subsequent step of the random field simulation. This approach is presented in more detail in Chapter 3.

1.6.2 **Random field generators**

Many algorithms can generate random fields through random field simulations: the fast Fourier transforms, the discrete Fourier transforms, covariance matrix decomposition, the moving average, the local average subdivision, and the turning band method. Each of these algorithms has advantages and disadvantages. However, the choice of one over the others depends on the problem, accuracy of the realizations, computational time, and ease of implementation (Fenton and Griffiths, 2008).

Of all these algorithms, only the local average subdivision (LAS) and the turning bands method (TBM) are addressed because they are the most suitable for generating synthetic rough rock surfaces.

Figure 1.32 shows an example of a one-dimensional random field simulation using the LAS algorithm. The simulation proceeds in a top-down manner. The value at the top Z_1^0 in stage zero is obtained using local averaging theory. To move from stage i to stage $i+1$, each cell of stage i is subdivided into two daughters cells. The regionalized value attributed to each of the two generated cells is obtained by generating two normally distributed values Z_1^i and Z_2^i. Z_1^i and Z_2^i are correlated, the average of Z_1^i and Z_2^i is equivalent to the regionalized value right above them, and the variance of Z_1^i and Z_2^i is in accordance to the local averaging theory.

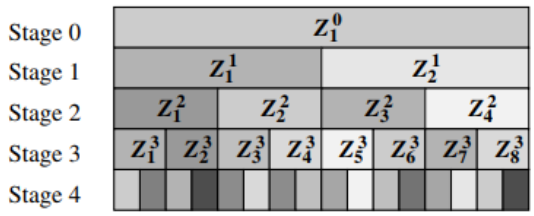

Figure 1.32 One-dimensional application of random field simulation using LAS (Fenton and Vanmarcke, 1990; Fenton and Griffiths, 2008)

The LAS algorithm was used by Casagrande et al. (Casagrande *et al.*, 2018) and Jeffery et al. (Jeffery *et al.*, 2021) to generate synthetic rough rock surfaces.

The turning bands method (TBM) generates random fields by performing unidimensional simulations and computing each regionalized value as the average of the unidimensional realizations (Mantoglou and Wilson, 1982). Further details about this method are presented in Chapter 3.

1.6.3 **Application of random field simulations**

Random field simulation has been recently used to generate synthetic rough rock surfaces. Casagrande et al. (Casagrande *et al.*, 2018) performed random field simulations to generate synthetic rough rock surfaces to estimate the shear strength of rock-rock interfaces using a stochastic approach.

Jeffery et al.(Jeffery *et al.*, 2021) improved the rigor of the methodology proposed by Casagrande et al. (Casagrande *et al.*, 2018). The new methodology consists of transforming a 2D trace of a discontinuity into three daughter profiles (Figure 1.33), performing the random field simulations using as input the parameters of each daughter profile, and superposing the results of the three simulations to obtain one 3D realization. This approach was judged necessary to solve two problems. The first problem was to ascertain that the field of gradients of the synthetic rough rock surfaces generated maintains the same distribution of the input of the random field simulation. The second problem is to satisfy the stationarity requirement in the intermediate and small scale of roughness.

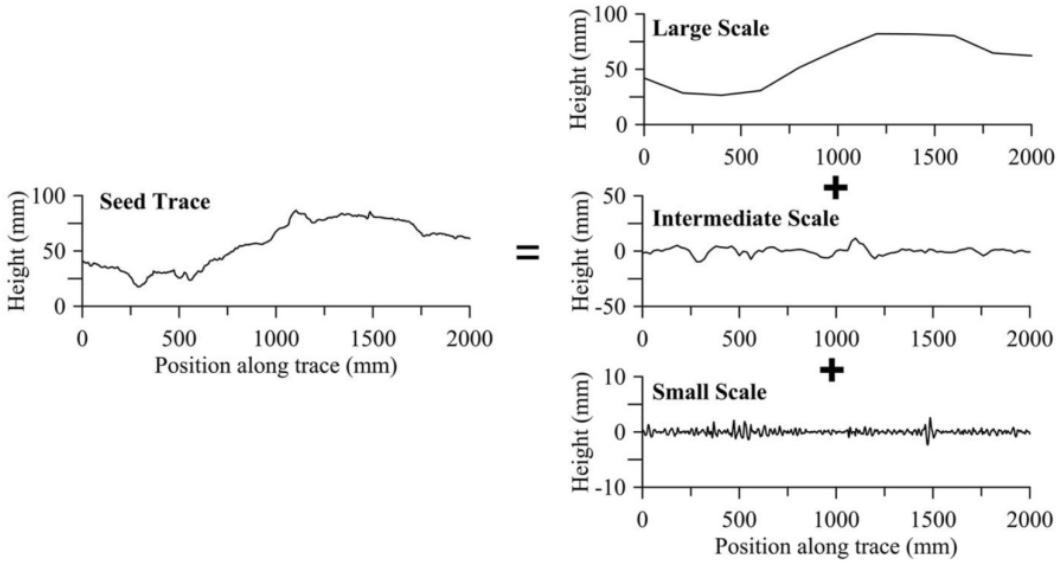

Figure 1.33 Transformation of the 2D trace to obtain three daughter profiles for random field simulation using the LAS algorithm (Jeffery *et al.*, 2021)

Both Casagrande et al.(Casagrande *et al.*, 2018) and Jeffery et al. (Jeffery *et al.*, 2021) use the local average subdivision algorithm (LAS) (Fenton and Vanmarcke, 1990) to perform random field simulations.

1.7 **Concluding remarks**

The investigation of the shear behavior of interfaces in rock mechanics was, until recently, mainly focused on the problem of the shear resistance of rock-rock interfaces. The produced literature has helped identify the most influential parameters contributing to the shear resistance of rock-rock interfaces.

For most applications, the normal stress is usually very low. The main parameters influencing the shear behavior of rock-rock interfaces depend principally on the normal stress, the properties of the rock surface, and the roughness. Of all these parameters, the roughness of a rock surface is the most difficult to characterize. Many failure criteria have been proposed to correlate the parameters influencing the shear resistance of interfaces to the peak shear strength. Most of these failure criteria attempt to characterize properly the influence of roughness on both the mechanisms active during shear and the resistance of the interface.

Since most of the investigations of the shear behavior of interfaces have focused on rock-rock interfaces, until very recently, it was common to consider the concrete-rock interfaces as unbonded. Such a consideration leads to very conservative designs and unrealistic structural stability analysis. For this reason, since the two thousands, a series of investigations of the shear behavior of concrete-rock interfaces have been published. These studies show that, unlike the rock-rock interfaces, the concrete-rock interfaces depend strongly on the concrete-rock bond besides the normal stress and the roughness. This means it is necessary to adapt the existing failure criteria to include the influence of the concrete-rock bond.

Furthermore, other aspects, such as the numerical modeling of concrete-rock interfaces, are also not sufficiently investigated. Moreover, there is a serious need to characterize the shear behavior of interfaces under dynamic shear loading and to propose different investigative approaches to address the computation of the influence of roughness on the shear behavior of interfaces. This is important for all types of interfaces.

2. Numerical simulation of concrete-rock interfaces

The review of the experimental investigation of the shear behavior of concrete-rock interfaces has helped identify the major parameters and mechanisms driving the shear response of these interfaces. It is now possible to move on to numerical modeling.

This chapter presents numerical modeling of the shear behavior of concrete-rock interfaces, focusing on the influence of unevenness and waviness as two roughness scales.

2.1 **Experimental contextualization**

Experimental studies of the shear behavior of concrete-rock interfaces under lower normal loading have highlighted the importance of the normal stress, the roughness, and the concrete-rock bonds on the shear resistance (refer to section 1.3.2).

This numerical work is based on the part of the experimental work conducted by El Merabi (El Merabi, 2018) and discussed in Badika et al. (Badika *et al.*, 2022). The two references are reviewed in section 1.3.2. The normal stresses, the boundary conditions, the size of the samples, and the roughness of the interfaces used in the numerical simulations are as close as possible to the ones used in the aforementioned experimental study. The range of the normal stress considered in this numerical work is below 1.5 MPa. In this range of normal stresses, two failure modes were reported. However, independently of the failure mode, the shear failure occurs along the interface with no significant damage to the concrete or the rock. This simplification means that the shear behavior of concrete-rock interfaces under lower normal loading can be simulated by modeling the concrete-rock interfaces.

The roughness of the rock surface substantially influences the shear resistance of concrete-rock interfaces. For the numerical modeling and the numerical simulations of concrete-rock interfaces, the influence of roughness in the shear resistance is considered by taking into account separately the effect of unevenness or micro-roughness and the effect of waviness or macro-roughness. Moradian et al. (Moradian, Ballivy and Rivard, 2012) also mentioned a similar separation. Micro-roughness forms strong concrete-rock bonds in concrete-hard rock interfaces (El Merabi, 2018). The macro-roughness adds the influence of the surface interlocking in the shear resistance of interfaces.

The behavior law of the numerical modeling simulates the events happening at the concrete-rock interfaces, mainly related to the influence of the concrete-rock bonds.

The conjugated influence of the normal stress, the roughness, and the concrete-rock bonds define the overall shear response of concrete-rock interfaces. This shear response can be separated into three stages (Figure 2.1), first reported by Saiang et al. (Saiang, Malmgren and Nordlund, 2005) with the same implications in terms of the driving mechanisms (discussed in section 1.3.2)

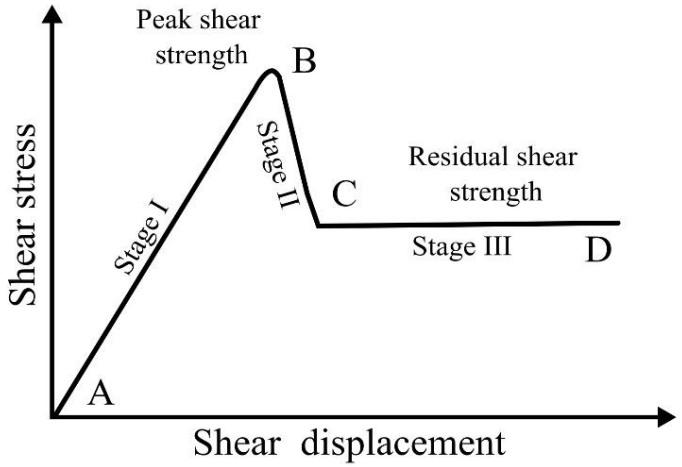

Figure 2.1 Main stages of the shear evolution of concrete-rock interfaces under low normal loading. Modified from Badika et al. (Badika *et al.*, 2022)

2.2 **Numerical Modeling**

The main goal of the numerical modeling presented here is to conduct simulations of direct shear tests of concrete-rock interfaces that reproduce the shear response obtained experimentally as closely as possible. The numerical model discussed is implemented in the finite element software Abaqus standard. This software is selected because it contains compatible behavior laws.

2.2.1 **Behavior law of the concrete-rock interface**

The concrete-rock bonds generated after casting concrete on rock surfaces form interfaces with no significant thicknesses. The implication of this lack of a physical geometry means that the behavior law representing the influence of concrete-rock bonds in the shear response will be modeled as a behavior of the interface. For this reason, the behavior law is computed on each contact constraint generated at the interface between the concrete and the rock slab. The contact constraints are added to enforce the contact behavior (behavior law). The contact model is implemented in Abaqus using surface-to-surface contact since it is less subject to convergence difficulties associated with node-to-surface contact. The number of contact constraints generated is dependent on the number of nodes of the weaker material. The weaker material is usually discretized with a finer mesh. Consequently, the overall resolution of the shear response will be associated with the weaker material (Abaqus Inc, 2014). These contact constraints represent the concrete-rock bonds composing the bonded interface.

The behavior of each concrete-rock bond resisting the loading attempting to fracture the concrete-rock sample along the interface is computed using the traction-separation law, which contains a linear elastic behavior, damage initiation, and damage evolution. However, once the stiffness of a concrete-rock bond starts to degrade, this means there is damage initiation, and the friction

behavior starts to mobilize locally and progressively. The equations associated with each step of this model are presented hereafter and are computed for each contact constraint and locally across the interface.

The stress vector representing the linear elastic behavior is computed as the product of the stiffness matrix with the separation vector according to Eq. (2.1). It is worth noting that this equation is valid until there is damage initiation in the contact constraint (bond).

$$t = \begin{bmatrix} t_n \\ t_s \\ t_t \end{bmatrix} = \begin{bmatrix} K_n & 0 & 0 \\ 0 & K_s & 0 \\ 0 & 0 & K_t \end{bmatrix} \begin{Bmatrix} \delta_n \\ \delta_s \\ \delta_t \end{Bmatrix} \tag{2.1}$$

where t is the stress vector, K_n, K_s, and K_t are the normal and the shear stiffness, δ_n, δ_s, and δ_t are the normal and the shear separation (displacement).

Since concrete-rock bonds rule the shear evolution of concrete-rock interfaces before the peak, the linear elastic behavior, Eq. (2.1), is computed for each concrete-rock bond individually.

The maximum stress criterion, Eq.(2.2), in this numerical modeling marks the damage initiation. If equation Eq.(2.2) is verified in a concrete rock bond, its stiffness degrades according to a damage evolution law. At this point, the linear elastic behavior, Eq. (2.1), is no longer valid.

$$max\left\{\frac{\langle t_n \rangle}{t_n^{\circ}}, \frac{t_s}{t_s^{\circ}}, \frac{t_t}{t_t^{\circ}}\right\} = 1 \tag{2.2}$$

where t_n°, t_s°, and t_t° are the stress resistance of the concrete-rock bond when the separation generated by the stress is purely normal or purely shear-related. The Macaulay bracket indicates that normal compressive stress does not generate separation. These three parameters are specified in the implementation of the model. $\langle t_n \rangle$, t_s, and t_t and are components of the stress experienced by a concrete-rock bond during the shear process.

With the confirmation of the damage initiation in a concrete-rock bond, the stress contribution from the traction-separation law is computed with a penalty introduced using the damage parameter D. This parameter varies from zero before the initiation of the degradation of stiffness to one when a bond fails. Eq (2.3) presents the computation of the stress vector.

$$\begin{aligned} t_n &= \begin{cases} (1-D)\overline{t_n}, & \overline{t_n} \geq 0 \\ \overline{t_n} \end{cases}, \\ t_s &= (1-D)\overline{t_s}, \\ t_t &= (1-D)\overline{t_t}, \end{aligned} \tag{2.3}$$

where $\overline{t_n}$, $\overline{t_s}$, and $\overline{t_t}$ are the stress components computed using Eq. (2.1), $t_{traction}(\overline{t_n}, \overline{t_s}, \overline{t_t})$ is the stress vector representing the contribution of the traction separation law.

Eq (2.4) is used in Abaqus to simulate an exponential stress decay after damage initiation.

$$D = 1 - \left\{\frac{\delta_m^{\circ}}{\delta_m^{max}}\right\}\left\{1 - \frac{1 - exp\left(-\alpha\left(\frac{\delta_m^{max} - \delta_m^{\circ}}{\delta_m^{f} - \delta_m^{\circ}}\right)\right)}{1 - exp(-\alpha)}\right\} \quad (2.4)$$

where δ_m° is the separation obtained when the damage initiation is first detected (Eq.(2.2)). δ_m^{f} is the separation when the bond fails, δ_m^{max} is the maximum separation obtained during the stress history of a bond. α is a non-dimensional parameter that describes the rate of damage evolution. The difference $\delta_m^{f} - \delta_m^{\circ}$ is called plastic displacement and is identified as a parameter of the model.

Once the damage initiation is verified, the total stress depends on the traction-separation law, according to Eq (2.3), and the progressive mobilization of friction. The combination of these two models is called the cohesive frictional model. The frictional behavior is computed using the Coulomb friction law, Eq (2.5).

$$t_{friction} = \begin{bmatrix} t_n \\ D\mu t_n \\ D\mu t_n \end{bmatrix} \quad (2.5)$$

where μ is the friction coefficient.

Combining the behavior law into a single equation yields Eq (2.6).

$$t = t_{traction} + t_{friction} \quad (2.6)$$

where $t_{traction}$ is computed using Eq (2.3) and $t_{friction}$ is assessed using Eq (2.5).

Eq (2.6) summarizes the stress history of a concrete-rock bond from resisting the shear loading captured by a linear elastic behavior, damage behavior, and frictional behavior.

The selection and combination of these behaviors are strongly based on reviewing the experimental studies available in the literature, particularly the tests performed by El Merabi (El Merabi, 2018) and discussed by Badika et al. (Badika *et al.*, 2022). The numerical model presented is used to perform simulations of direct shear tests of bush-hammered and rough concrete-granite interfaces, focusing on separating the contribution of roughness (unevenness and waviness) in the shear response discussed in section 1.3.2.

2.2.2 **Simulation of the direct shear test**

2.2.2.1 **Material properties**

Since the numerical modeling of the shear behavior of concrete-rock interfaces is focused on the shear events at the interface, simple mechanical properties are used for concrete and granite. Table 2.1 presents the material properties used in the simulations. In this table, the properties of the steel are used to simulate the encasing steel box containing the concrete and the rock slab in the BCR3D

(see Figure 1.15), which is the direct shear test machine used in the experimental study conducted by El Merabi (El Merabi, 2018).

Table 2.1 Mechanical properties of concrete, rocks, and steel used in the simulations. Based on the experimental work conducted by Mouzannar (Mouzannar, 2016)

Material	**Density (Kg/m^3)**	**Young's Modulus(GPa)**	**Poisson's ratio**
Concrete	2370	38	0.20
Granite	2608	60	0.25
Steel	8000	193	0.29

2.2.2.2 **Boundary conditions**

Figure 2.2 presents the boundary conditions of the simulations of the direct shear test of concrete-rock interfaces. These boundary conditions are similar to the ones used in the experimental study by El Merabi (El Merabi, 2018) using the BCR3D (Boulon, 1995b). The normal stress is applied as pressure on the top of the upper half steel box encasing the concrete part of the sample. The shear loading is applied in the upper and the lower half steel box in opposite directions. The lower half steel box encasing the rock part of the sample cannot move in the direction of the normal loading. Additionally, the upper and the lower half steel boxes cannot move in the direction perpendicular to the shear loading. The steel box is only important in the simulation to enforce the boundary conditions of the test to be as close as possible to the experimental conditions.

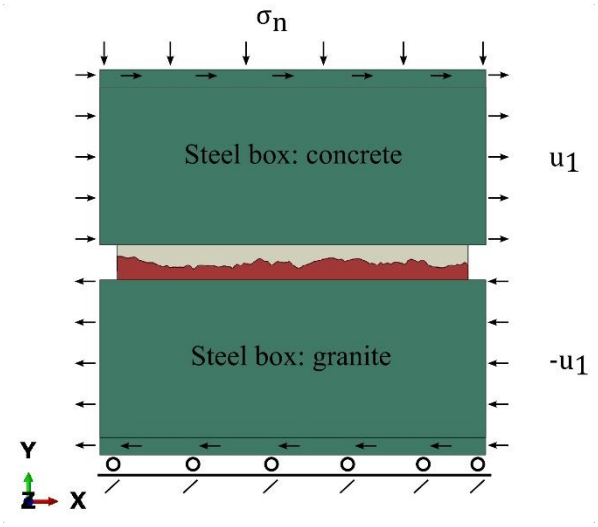

Figure 2.2 Boundaries conditions of the numerical simulations

2.2.2.3 **Mesh generation**

In the simulations, the influence of the micro-roughness is reproduced by the behavior law. The influence of the mesh on the response of the behavior law was carried out. It is worth noting that since the interest of this analysis is to evaluate the mesh sensitivity of the behavior law without including the effect of the surface interlocking, simulations were carried out using flat surfaces. The results of this study show that mesh size has no significant effect on the shear response

obtained. However, it was observed that reducing the mesh size increased the computational cost of the simulation. These results are represented in Figure 2.3.

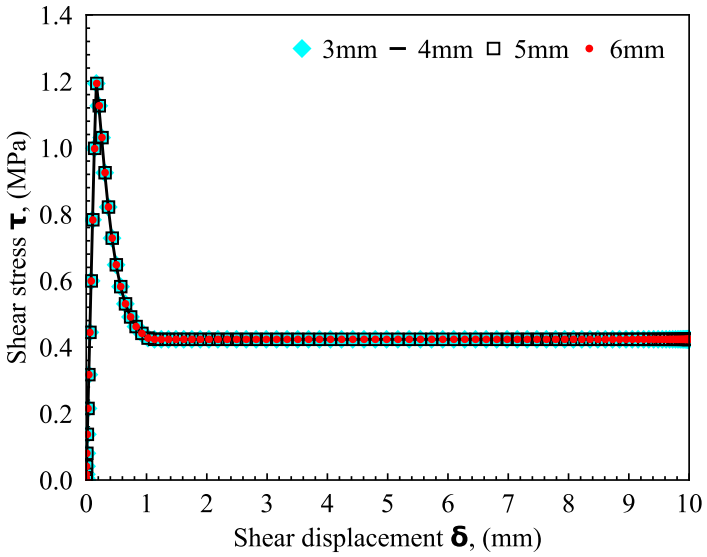

Figure 2.3 Mesh sensitivity of the behavior law using simulation of bush-hammered interfaces

For the simulation of the shear behavior of rough concrete-rock interfaces, it is necessary to simulate the influence of the micro-roughness (unevenness) and the macro-roughness (waviness) on the shear response of the interface. For this reason, it is important to carefully choose the mesh size such that the waviness of the interface is faithfully represented. Considering the mesh sensitivity conducted for the behavior law, an average element size of 4 mm was selected for the simulations. However, it is important to note that the meshing algorithm in Abaqus is free to reduce further the mesh size to fit as close as possible to the surface geometry of concrete and granite, which means depending on the local wavelength of roughness, elements with smaller sizes are generated (Figure 2.4).

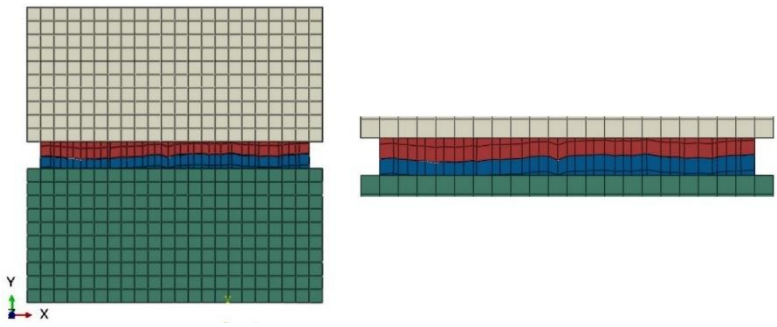

Figure 2.4 Mesh concrete, granite, and steel box, close-up of the interface

All the simulations use the brick element C3D8, which contains 8 nodes, uses linear interpolation, and is fully integrated with 8 integration points. This element is selected because it is less sensitive to hourglassing issues that generate unrealistic deformation.

Meshing rough and complex contacting bodies can yield small penetrations. These penetrations can generate convergence difficulty, so a free strain nodes adjustment routine was applied in the simulation before the first iteration. This node adjustment does not change the waviness of the interface (Figure 2.5).

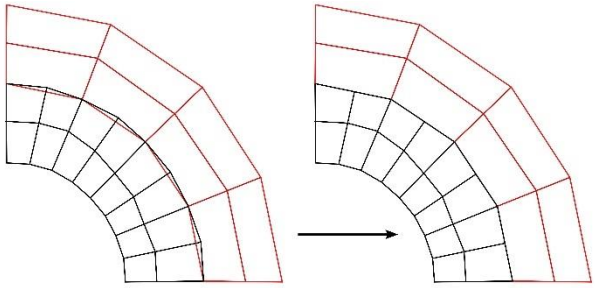

Figure 2.5 Node adjustment to eliminate initial overclosure. Modified from Abaqus. (Abaqus Inc, 2014)

2.2.2.4 **Parameter of the behavior law of the concrete-rock interface**

The only parameters to determine for the simulation of the traction-separation law before failure are the normal and the shear stiffness K_n, K_s, and K_t in Eq. (2.1). These parameters can be determined from the overall shear response of the interface if three conditions can be verified. First, the direct shear test result obtained is free from the influence of the waviness of the interface; second, there is a formation of concrete-rock bonds with very similar strength across the interface; third, there is no localization of the shear resistance across the interface. These three conditions are not easy to reproduce experimentally. Results of tests performed by Saiang et al. (Saiang, Malmgren and Nordlund, 2005) and Tian et al. (Tian *et al.*, 2015) illustrate this difficulty. These authors reported a scattering of stiffness for interfaces tested with similar and low roughness (JRC below three) and submitted to comparable normal loading (Figure 2.6).

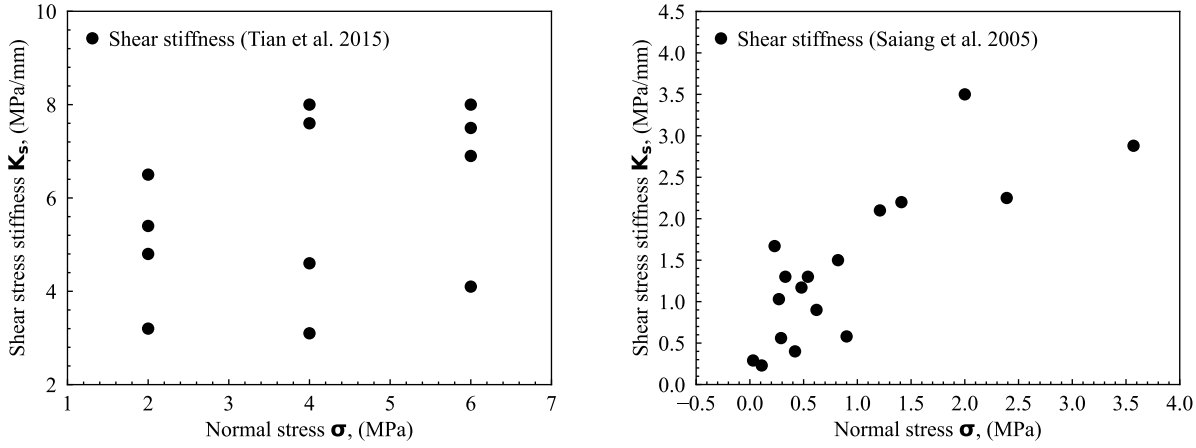

Figure 2.6 Stiffness of concrete-rock bond; a) Concrete-dolomite (Tian *et al.*, 2015) b) Shotcrete-magnetite (Saiang, Malmgren and Nordlund, 2005)

However, the shear responses of bush-hammered concrete-granite interfaces in the tests performed by El Merabi (El Merabi, 2018) are close to satisfying the three conditions stated above. Therefore, they are used as a base to determine the stiffnesses of concrete-granite bonds for all the simulations of concrete-granite interfaces. For this reason, all the model parameters except the friction coefficient (μ) are well-defined based on the shear response of bush-hammered concrete-granite interfaces.

Based on the review of the experimental studies of concrete-rock interfaces, it is clear that the mechanisms acting during the interval between the peak and the residual shear strength of the shear response of concrete-rock interfaces are complex. During this interval, different events contributing to the shear response occur simultaneously. There is a local and progressive degradation of the stiffness of concrete-rock bonds, which eventually leads to local and progressive failure of the bonds. Along with this damage, there is local and progressive friction mobilization. Depending on the normal stress level, there might be a competition of resistance between the concrete-rock bond, the concrete, and the rock material to guide the failure either along the interface or through the asperities. Given this complexity, it is difficult to extract the parameter of the bond by using the overall shear response of the interface. Another alternative would be to design experimental tests to characterize separately the influence of each event, which is not easy to achieve. For this reason, the parameters of the model related to this phase ($t_n^\circ, t_s^\circ, \delta_m^f - \delta_m^\circ, \alpha$) are determined through calibration using the results of direct shear tests of bush-hammered concrete-granite interfaces.

The numerical simulations of direct shear tests with bush-hammered interfaces for calibrating the behavior law were also considered flat. This consideration is reasonable because the bush-hammered interfaces contain mostly unevenness, characteristic of the roughness responsible for forming the concrete-rock bonds that the behavior law is designed to simulate. (Figure 2.7).

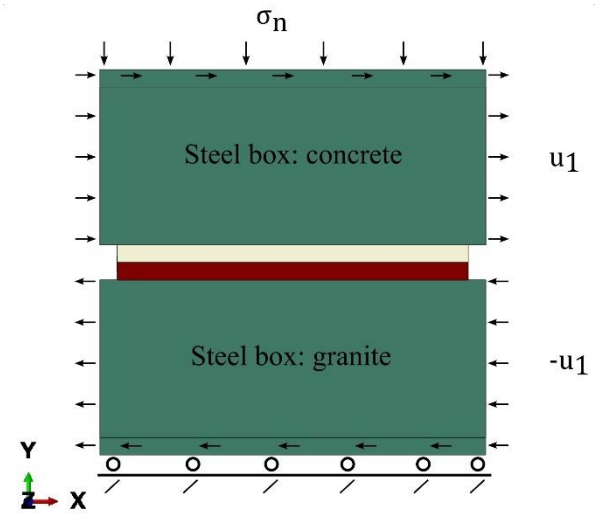

Figure 2.7 Setup of the simulation of bush-hammered interfaces

2.2.2.5 **Calibration and simulation: bush-hammered interfaces**

The calibration proceeds in three steps with the possibility of reiteration between them. In the first step, the normal and the shear resistance of the concrete-granite bond (t_n°, t_s°), are iterated, aiming at reproducing the peak shear strength of the overall shear response of the interface. In the second

step, different values of plastic displacements ($\delta_m^f - \delta_m^\circ$) are tested to produce the appropriate transition between the peak and the residual shear strength. Lastly, different values of the non-dimensional parameter α are tested to produce the correct decay shape from the peak to the residual shear strength.

For each step of the calibration process, a simple objective function, Eq (2.7), is used to guide the selection of appropriate values of the parameters of the model.

$$Objective\ function: \min\left|\Delta(\tau_{num} - \tau_{exp})\right| \tag{2.7}$$

where τ_{num} is the peak shear strength obtained from the results of the simulation of the direct shear test, while τ_{exp} is the peak shear strength obtained experimentally.

The friction coefficient can be extrapolated based on the shear response of the interfaces.

Since two failure modes are possible for concrete-granite interfaces tested using confinement stress below 1.5 MPa, two sets of parameters are obtained to reproduce the different shear responses.

The two sets of parameters are reported in Table 2.2.

Table 2.2 Parameter of the behavior law

Behavior law	**Parameters**	**0.5 MPa 1st failure mode**	**1.0-1.5 MPa 2nd failure mode**	**Unit**
Traction-separation and damage behavior	K_n	15.0	15	GPa/m
	K_s	7.5	7.5	GPa/m
	t_n°	1.0	1.4	MPa
	t_s°	1.2	1.6	MPa
	$\delta_m^f - \delta_m^\circ$	0.9	2.25	mm
	α	4	4	-
Frictional behavior	μ	0.7	0.65	-

Figure 2.8 and Figure 2.9 show the results of the numerical simulations of bush-hammered concrete-granite interfaces. It is worth mentioning that to account for the simplification made for the calibration, which means the assumption that a smooth interface in the simulation could represent the bush-hammered interfaces and to complete the shear response, a friction coefficient of 0.25 was used to simulate bush-hammered interfaces. Furthermore, Figure 2.8 and Figure 2.9 show that the calibrated model can reproduce the shear response of bush-hammered concrete-rock interfaces. Since the bush-hammered concrete-rock interfaces are characterized by micro-roughness, which is responsible for the formation of concrete-rock bonds, the good agreement between the experimental and the numerical shear response obtained demonstrates that the behavior law presented can simulate the influence of the concrete-rock bonds on the shear evolution of interfaces.

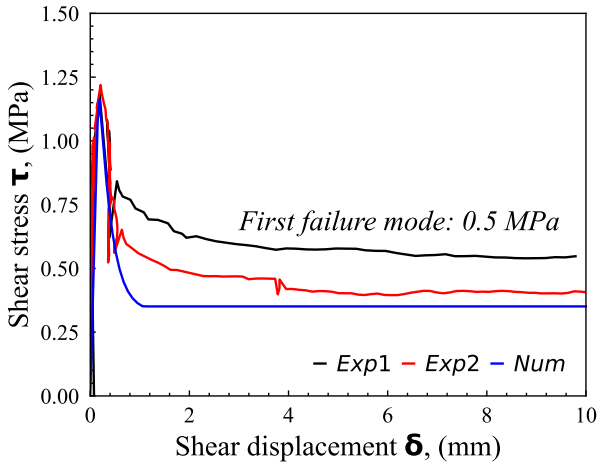

Figure 2.8 Calibration of the interface behavior law first failure mode (0.5 MPa)

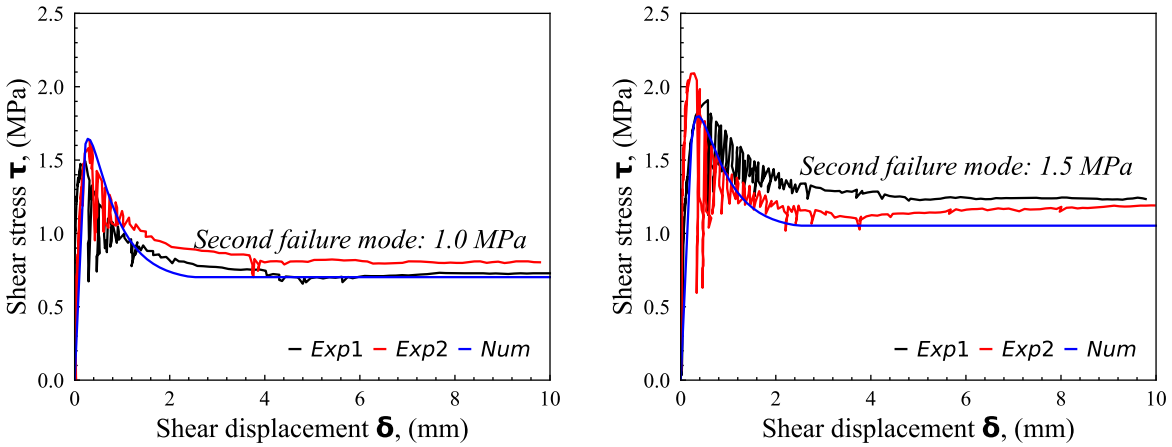

Figure 2.9 Calibration of the interface behavior law second failure mode (1.0-1.5 MPa)

However, the shear evolution of rough concrete-rock interfaces depends on both the micro- and macro-roughness. As established in the precedent analysis, the micro-roughness can be simulated by the calibrated behavior law presented. For the macro-roughness, it is important to include the influence of the surfaces interlocking in the shear response of the interface. Therefore, to simulate the shear behavior of rough concrete-rock interfaces, it is important to use the calibrated behavior law to simulate the micro-roughness. In contrast, the interlocking generated by the macro-roughness can be simulated using the explicit representation of the morphology of the interface.

2.2.3 **Prediction of the shear response of rough concrete-granite interfaces**

2.2.3.1 **Generation of solids**

For the simulation of the rough concrete-rock interfaces, first, the methodology of generating solid parts with an explicit representation of the geometry of the rough concrete-rock interfaces is presented.

Before performing direct shear tests of rough concrete-granite interfaces, El Merabi (El Merabi, 2018) collected the roughness data of the rough granite surfaces using the laser-based scanner developed by Hans and Boulon (Hans and Boulon, 2003). This process is presented in Figure 1.8 (chapter 1). The point cloud or set of x, y, and z coordinates of asperities collected are used to generate solids using COMSOL.

The height of asperities z is assumed to be a function of the location to generate a solid out of a point cloud with no information about the connectivity between the points; this is represented mathematically by Eq (2.8).

$$z = f(x, y) \tag{2.8}$$

where x, y, and z are coordinates of the points composing the point cloud representing the roughness of a rock surface.

Using the assumption represented by Eq (2.8), an interpolation process is used to reconstruct a surface using the point cloud. This process first creates a two-dimensional mesh composed of x and y coordinates. Then, it associates each mesh node to a value of the height of asperity z, either obtained from the point cloud or interpolated for locations not sampled while scanning the rock surface. A parametric surface is created by constructing B-spline surfaces that imitate the possible mathematical surface passing through the points x, y, and z. B-splines are polynomials surfaces created using several piecewise polynomials called knots (Sjodin, 2021). The higher the number of knots, the better the surface quality generated. Figure 2.10 illustrates an example of generating a parametric surface using the point cloud obtained after scanning a rough rock surface.

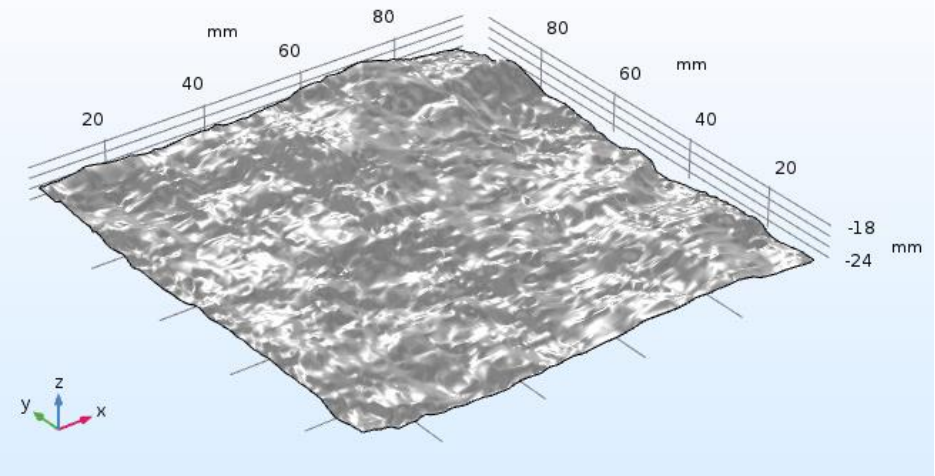

Figure 2.10 An example of a parametric surface generated using the point cloud of a rough rock surface

The parametric surface obtained using the point cloud can then be used in geometric operations with other solid parts to create the final solid representing a rough rock surface (Figure 2.11).

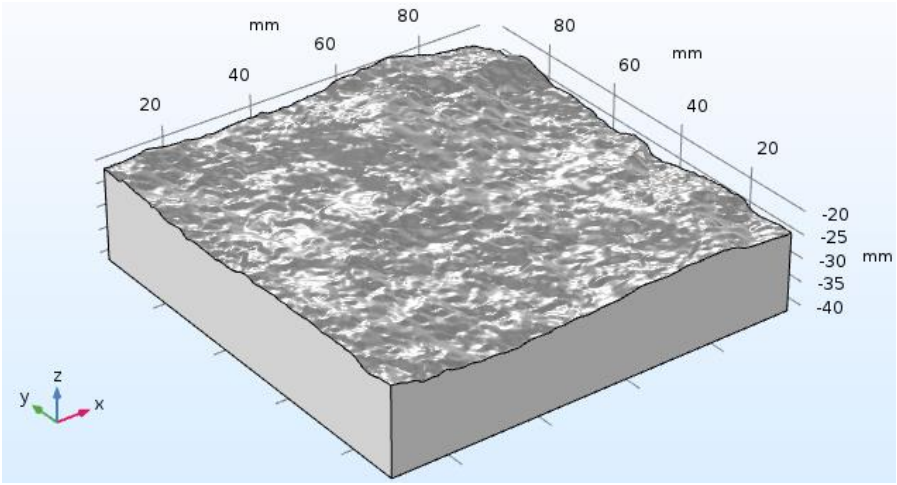

Figure 2.11 Final geometry created out of the point cloud of rough concrete surface.

Once imported into Abaqus, the solid part containing the proper morphology of the rough rock surface is used to create concrete and granite samples using Boolean operations carried out in the assembly module. The concrete and the rock part generated in this process are perfectly matched.

An example of the concrete and granite parts obtained is presented in Figure 2.12

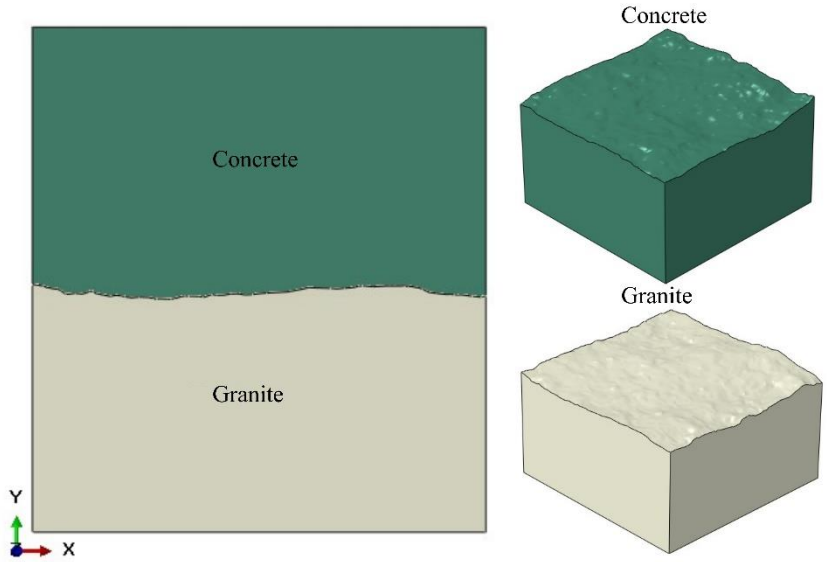

Figure 2.12 Concrete and rock part for the simulation of the shear behavior of rough concrete-rock interfaces

2.2.3.2 **Analysis of the simulation of rough concrete-granite interfaces**

a) Influence of concrete-rock bonds (unevenness): traction separation law

The role of the traction separation law in the numerical modeling of concrete-rock interfaces is to simulate the influence of concrete-rock bonds. This behavior law attempts to reproduce the local and progressive bond degradation across the interface. To evaluate the capability of the behavior law, contour plots of the cohesive surface damage (CSDMG) of the simulation of the shear test of rough concrete-rock interfaces are analyzed in different steps of the shear response. It is worth noting that the CSDMG is the value of the damage parameter *D* (see Eq (2.4)). CSDMG equals 0 when no contact constraint (bond) damage exists. CSDMG is equal to 1 when the contact constraint has failed. The contact constraint undergoes damage evolution for CSDMG between 0 and 1, leading to progressive friction mobilization.

Figure 2.13 shows the evolution of the traction separation behavior of a single contact constraint in terms of the damage parameter CSDMG.

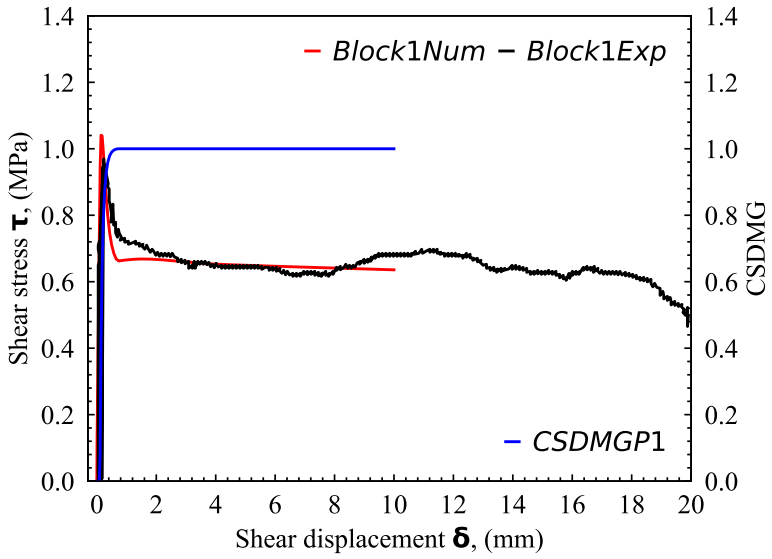

Figure 2.13 Damage evolution at a single contact constraint: CSDMG

In this analysis, four characteristic points are considered: P1 is a point in the pre-peak phase when there is no damage in any contact constraint, P2 is a point in the pre-peak phase when the damage of a contact constraint is first detected, P3 is the point in the shear history equivalent to the peak shear strength, and P4 is the point indicating the instant when all the contact constraints are damaged.

Figure 2.14 shows the distribution of CSDMG in the pre-peak phase of the shear response. The distribution of the CSDMG across the interface is 0, which is an appropriate reproduction of the pre-peak behavior of the shear response of the concrete-rock interface when only the concrete-rock bonds drive the shear response, the linear elastic part of the traction separation behavior characterizes the contact constraint at this point.

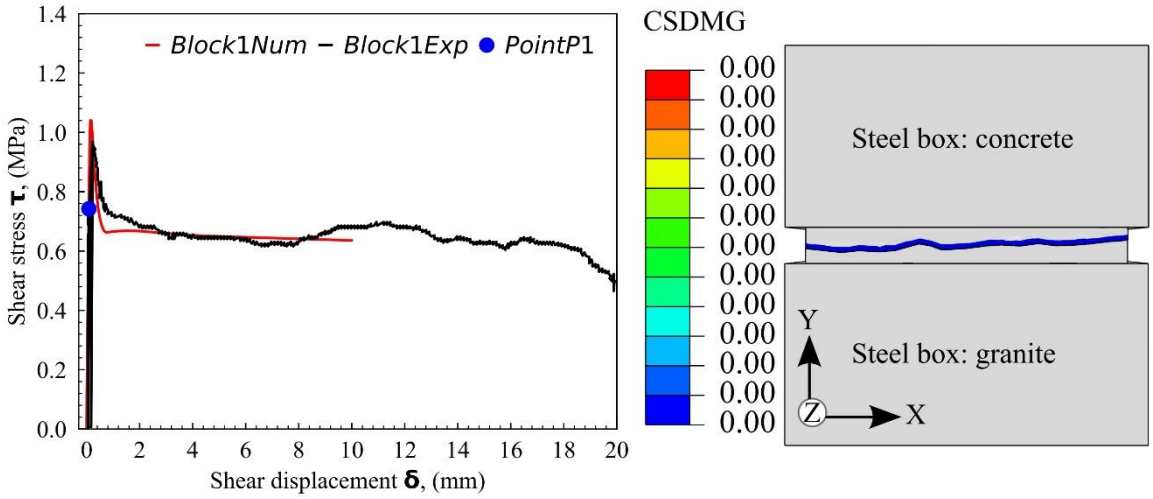

Figure 2.14 Distribution of the cohesive surface damage parameter across the interface during the shear evolution point P1

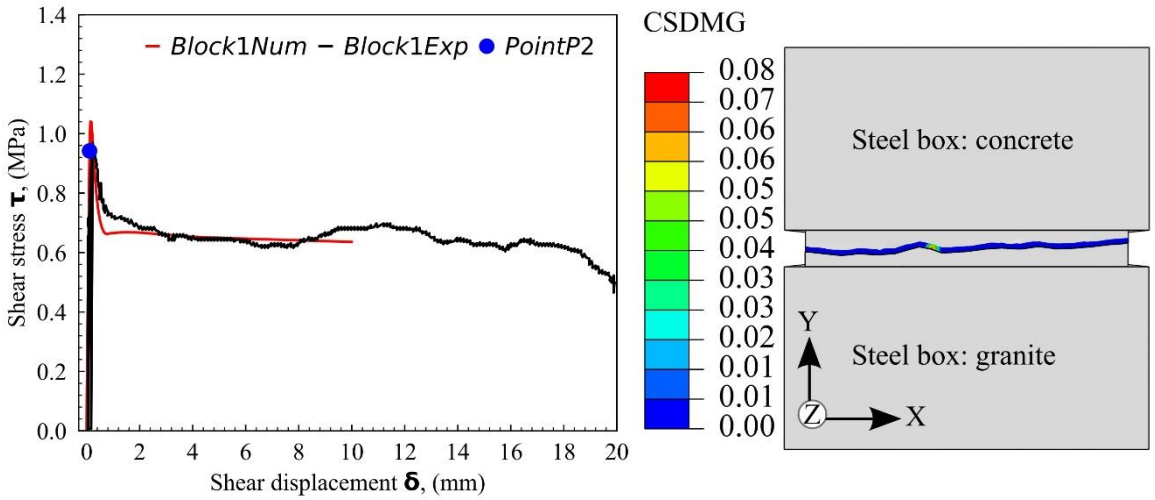

Figure 2.15 Distribution of the cohesive surface damage parameter across the interface during the shear evolution point P2

With the progress of the shear loading, the contact constraints begin to degrade. The damage initiation and the damage evolution characterize this behavior. Figure 2.15 shows the distribution of the CSDMG when the damage initiation is first detected. This figure shows that the traction separation behavior can reproduce the local and progressive degradation of the concrete-rock bonds. It is worth noting that the shear response has not yet reached the peak shear strength. This is interesting because the friction mobilization starts before the peak. Consequently, the peak shear strength receives a contribution of friction of the interface, which also means the contribution of the surface interlocking. This behavior explains acoustic emission recording before the peak shear strength in the experimental tests performed by Moradian et al. (Moradian, Ballivy and Rivard, 2012).

At the peak of the shear response, the degradation of contact constraints has spread across the entire interface. The distribution of CSDMG different from 0 across the interface evidences this behavior (Figure 2.16). This observation agrees with the drastic increase in acoustic emissions at the peak reported by Moradian et al. (Moradian, Ballivy and Rivard, 2012).

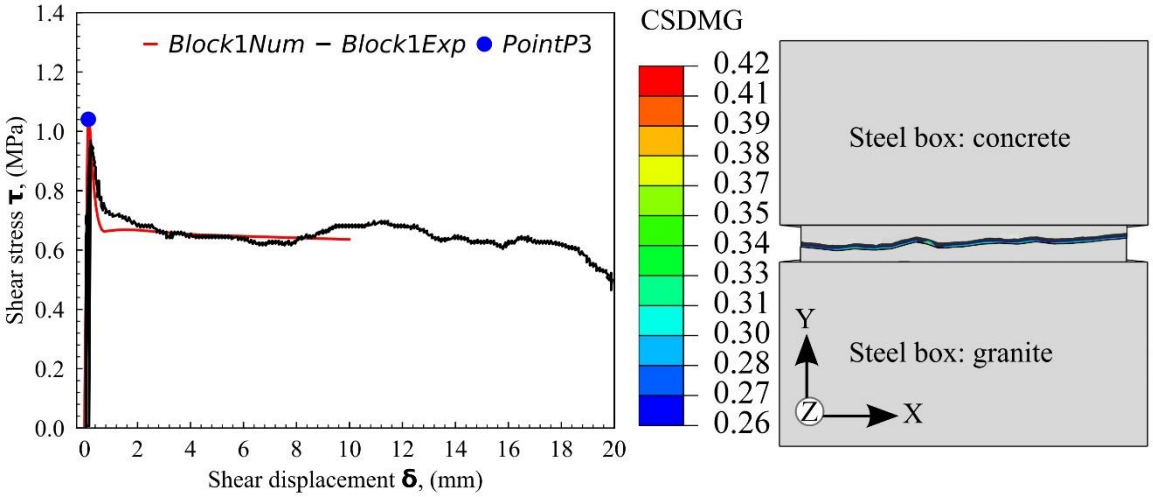

Figure 2.16 Distribution of the cohesive surface damage parameter across the interface during the shear evolution point P3

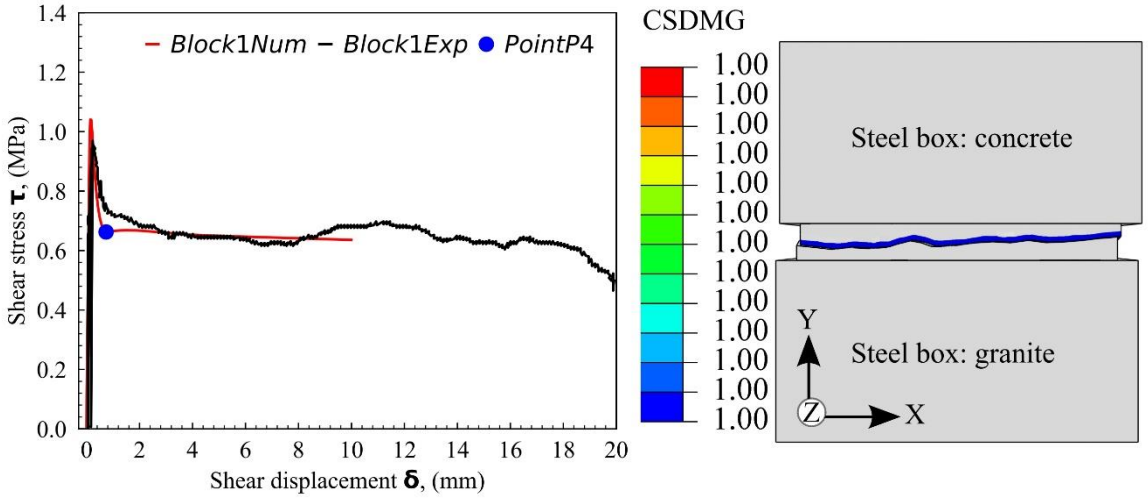

Figure 2.17 Distribution of the cohesive surface damage parameter across the interface during the shear evolution point P4

With the continuing application of the shear loading, the contact constraints degrade until total failure. This behavior is shown in Figure 2.17. The distribution of CSDMG in this figure is equal to 1 across the entire interface. Consequently, the shear response depends on the friction and the surface interlocking.

b) Influence of surface interlocking (waviness): frictional behavior

For the simulation of the shear behavior of rough concrete-rock interfaces, it was decided that the explicit representation of the three-dimensional morphology of the interface through surface interlocking would introduce the influence of the waviness or macro-roughness. In this section, contour plots of the stress are analyzed to verify the influence of waviness in the shear response of the interface. The points P1 to P4 used in the precedent analysis are also used here. In addition, a point PF is added to these markers to indicate the last step of the shear evolution in the simulation.

Figure 2.18 shows the contour plots of the pre-peak phase before detecting damage initiation at any contact constraints. There is minimal (magnitude) stress concentration at locations where the waviness is more significant.

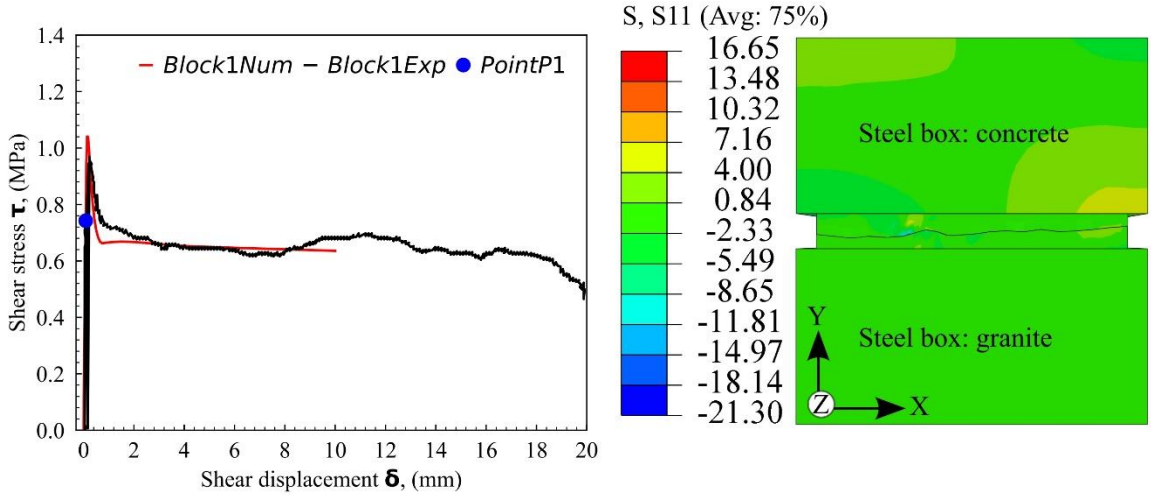

Figure 2.18 Stress concentration: effect of surface interlocking caused by waviness of the interface Point P1

Detecting the first damage initiation at contact constraint does not change the stress concentration locations (Figure 2.19). However, there is an increase in the magnitude of the stress concentration at locations with significant waviness. This increase in stress concentration is due to the continuing application of the shear loading. With the detection of the damage initiation, the overall shear response of the interface begins to receive the influence of the friction of the interface through surface interlocking.

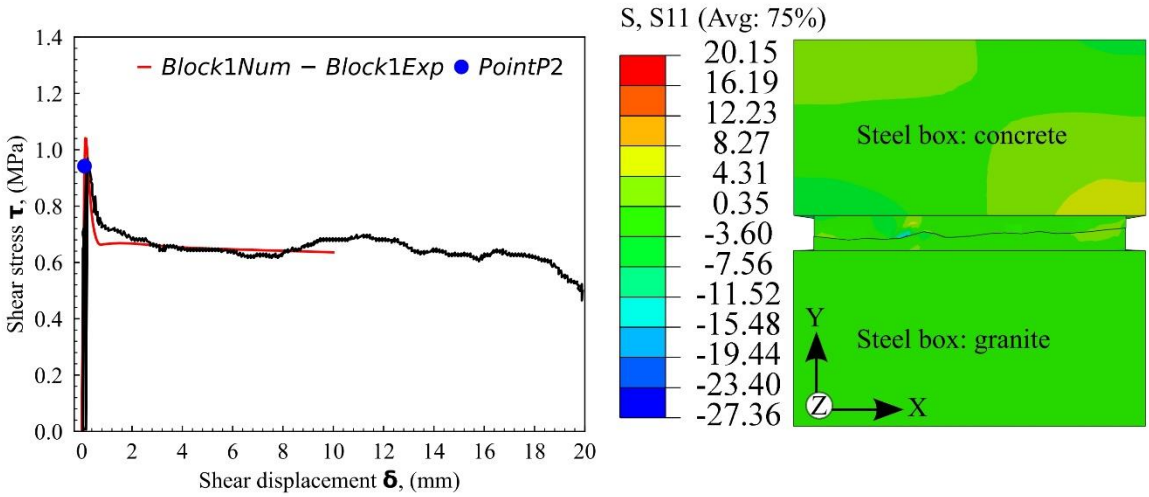

Figure 2.19 Stress concentration: effect of surface interlocking caused by waviness of the interface Point P2

At the peak of the shear response of the interface, there is no significant change in the locations with high-stress concentration nor the magnitude of the stress concentration (Figure 2.20).

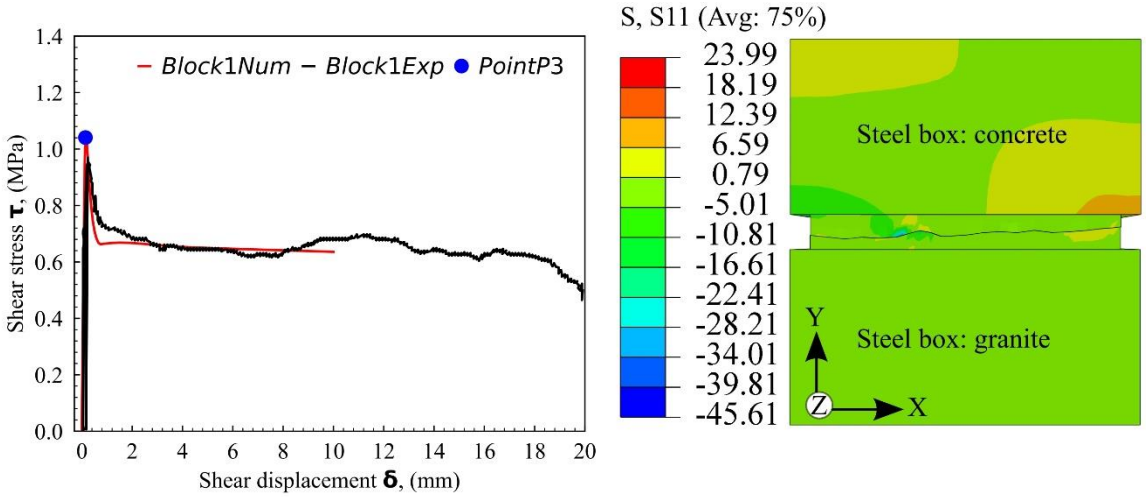

Figure 2.20 Stress concentration: effect of surface interlocking caused by waviness of the interface Point P3

At the transition between the post-peak and residual shear stress stages (Figure 2.21), the area with high-stress concentration is considerably reduced due to the shear displacement and dilation. However, due to the increase of the shear loading and the reduction of the effective area with significant interlocking, there is a significant increase in the magnitude of the stress concentration, indicating more contribution of waviness in the shear response.

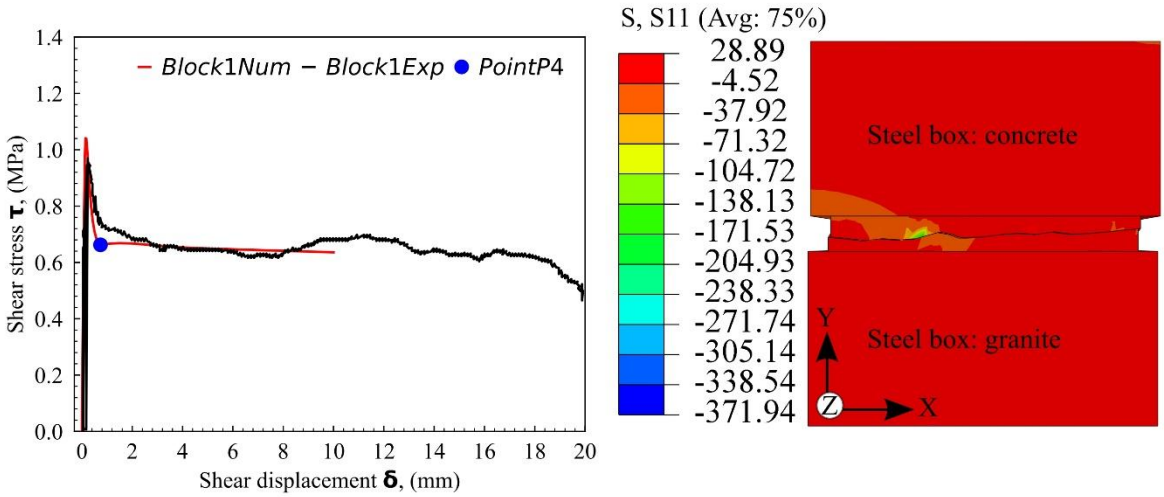

Figure 2.21 Stress concentration: effect of surface interlocking caused by waviness of the interface Point P4

At the end of the simulation (Figure 2.22), the effective contact area reduces dramatically. However, the area with the most significant waviness still controls the influence of surface interlocking in the shear response of the interface. The area with surface interlocking presents a stress concentration with high magnitude.

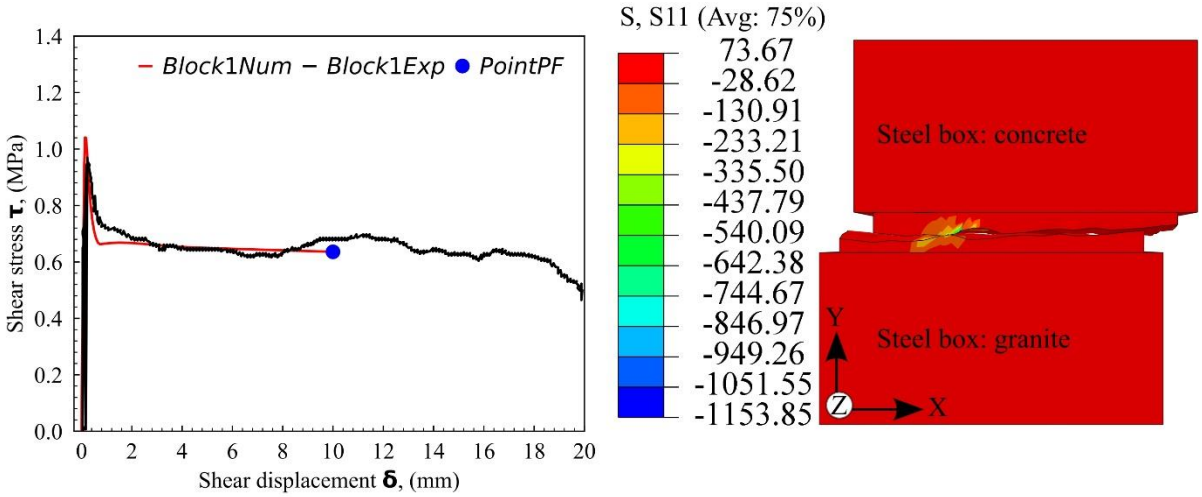

Figure 2.22 Stress concentration: effect of surface interlocking caused by waviness of the interface Point PF

With this analysis, it is clear that the considerations taken for the simulation of the shear behavior of rough concrete-rock interfaces are reasonable. The traction separation behavior can simulate the local and progressive degradation of the concrete-rock bonds. The interface with explicit representation of the three-dimensional morphology also simulates the effect of surface interlocking. With this assessment, the simulations of the direct shear tests of the concrete-rock

interfaces tested by El Merabi (El Merabi, 2018) and discussed by Badika et al. (Badika *et al.*, 2022) were carried out. The results of these simulations are discussed below.

2.2.3.3 **Results and discussion of numerical simulations of rough concrete-granite interfaces**

To simulate the influence of unevenness and waviness of rough concrete-rock interface on the shear response, simulations of direct shear tests of rough concrete-granite interfaces with explicit representation of the morphology of the rock surfaces were carried out using the calibrated model. The results of these simulations are discussed hereafter.

Figure 2.23 to Figure 2.26 compare the experimental and the numerical shear responses obtained in experimental and numerical simulations of direct shear tests carried out under 0.5 MPa, 1.0 MPa, and 1.5 MPa of normal stress. From these figures, it is clear that the numerical simulations using the previously calibrated interface behavior law reproduce the three stages of the shear evolutions proposed in section 2.1 quite well. Furthermore, these figures show that the simulations can capture the influence of surfaces interlocking during shear. This observation is true because, between the shear responses provided for each confinement level, the only parameter changing is the roughness of the interface and, specifically, the waviness or the macro-roughness of the interface. The capability of the simulation to capture the influence of macro-roughness using the explicit representation of the topography of the interface validates the simplification of the influence of roughness on the shear response of concrete-hard rock interfaces as partially dependent on the micro-roughness through the formation of concrete-rock bonds and the macro-roughness through surfaces interlocking during shear.

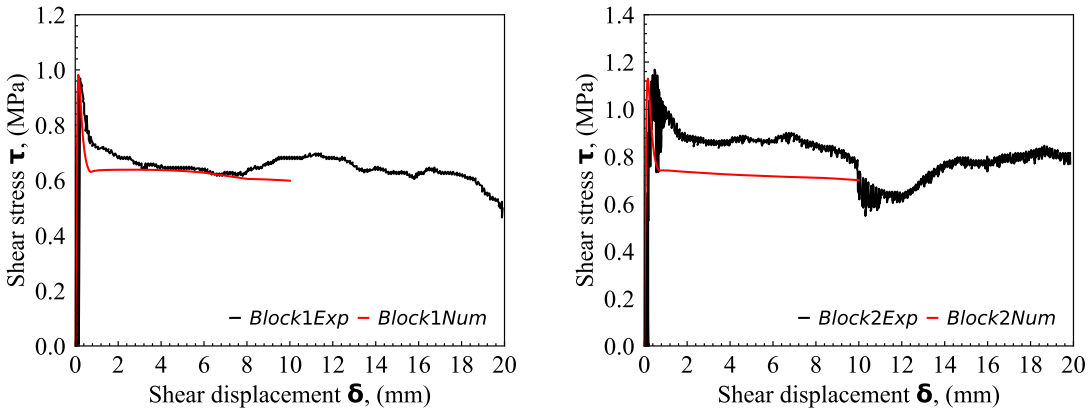

Figure 2.23 Evolution of the shear stress in terms of the shear displacement for tests carried out under 0.5 MPa of confinement: experimental vs. numerical (Block 1 and Block 2)

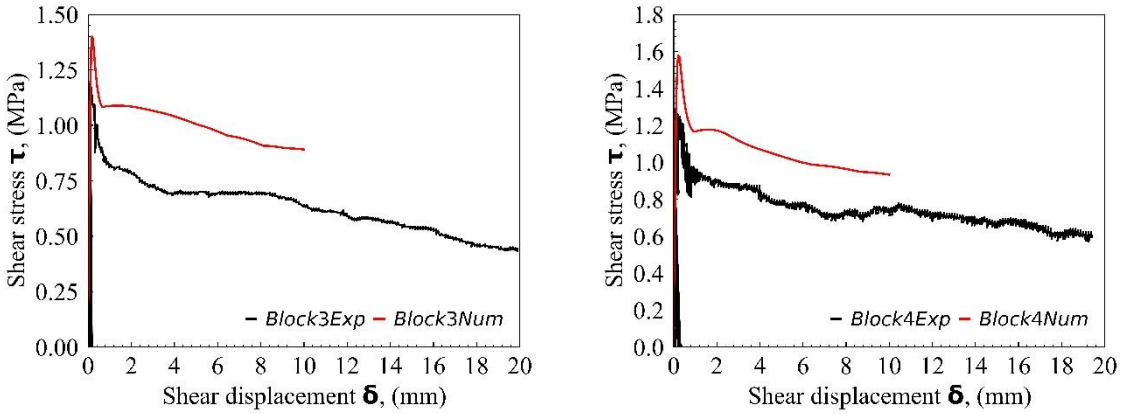

Figure 2.24 Evolution of the shear stress in terms of the shear displacement for tests carried out under 0.5 MPa of confinement: experimental vs. numerical (Block 3 and Block 4)

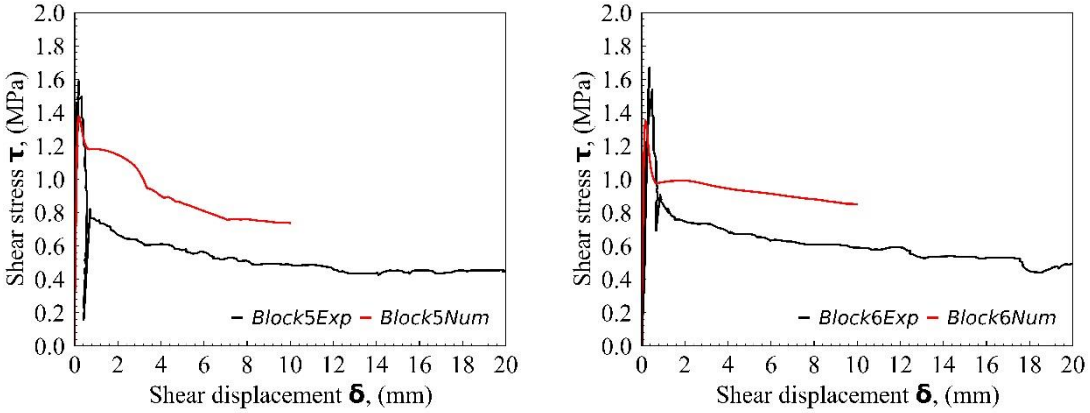

Figure 2.25 Evolution of the shear stress in terms of the shear displacement for tests carried out under 0.5 MPa of confinement: experimental vs. numerical (Block 5 and Block 6)

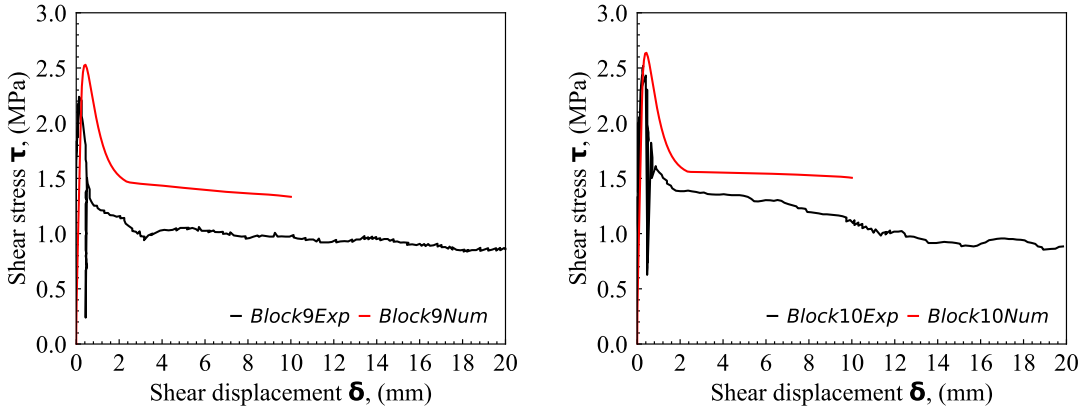

Figure 2.26 Evolution of the shear stress in terms of the shear displacement for tests carried out under 1.0 MPa of confinement: experimental vs. numerical (Block 9 and Block 10)

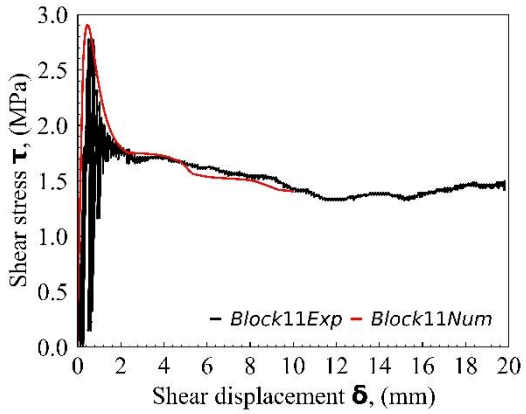

Figure 2.27 Evolution of the shear stress in terms of the shear displacement for tests carried out under 1.0 MPa of confinement: experimental vs. numerical (Block 11)

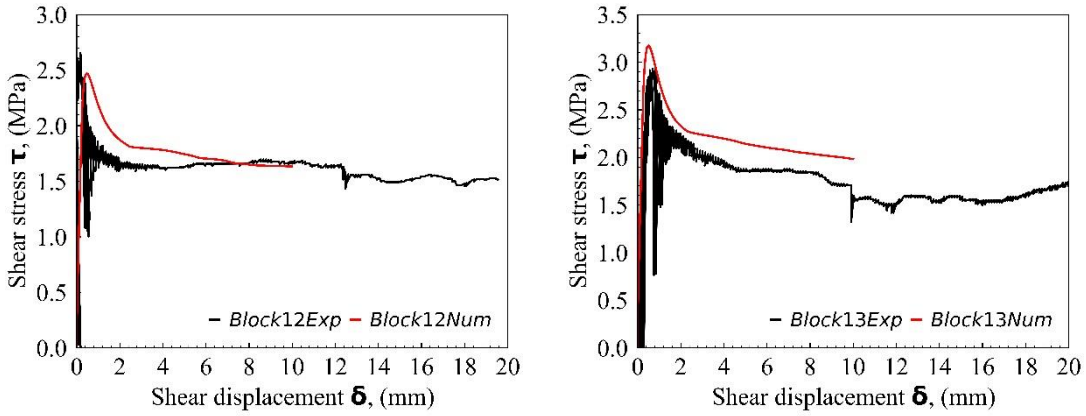

Figure 2.28 Evolution of the shear stress in terms of the shear displacement for tests carried out under 1.5 MPa of confinement: experimental vs. numerical (Block 12 and Block 13)

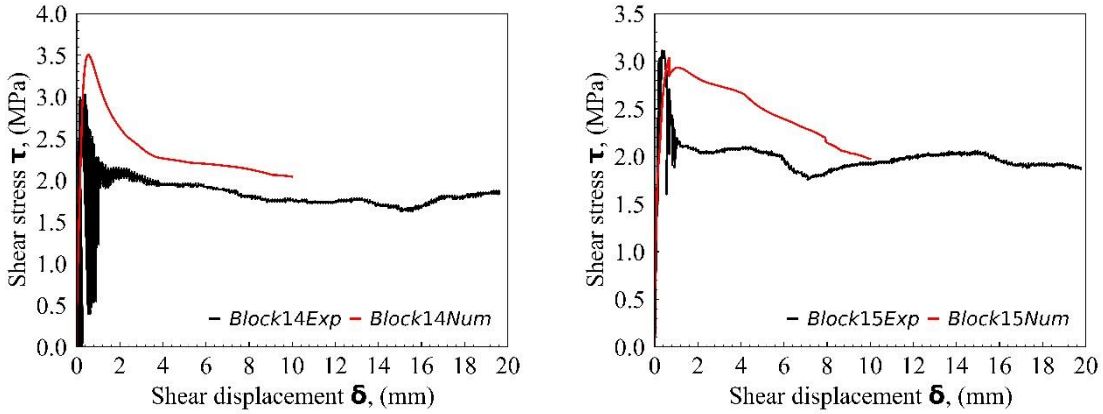

Figure 2.29 Evolution of the shear stress in terms of the shear displacement for tests carried out under 1.5 MPa of confinement: experimental vs. numerical (Block 14 and Block 15)

Table 2.3 Peak and residual shear strength of rough concrete-granite interfaces: experimental vs. numerical

Test	Normal stress (MPa)	Peak shear strength (MPa)	Residual shear strength (MPa)	Error (%)
1	0.5	0.97	0.98	1.25
2	0.5	1.18	1.13	4.25
3	0.5	1.24	1.40	12.88
4	0.5	1.33	1.58	18.75
5	0.5	1.57	1.37	12.46
6	0.5	1.66	1.35	18.52
9	1	2.25	2.53	12.42
10	1	2.54	2.64	3.84
11	1	2.77	2.90	4.86
12	1.5	2.70	2.47	8.53
13	1.5	2.96	3.17	7.23
14	1.5	3.06	3.50	14.47
15	1.5	3.13	3.03	3.06

Table 2.3 shows the experimental and the numerical shear strength of rough concrete-granite interfaces considered in the simulations, along with the percent error between the experimentally and the numerically obtained peak shear strength. From this table, it is clear that the prediction of the numerical simulations regarding the peak shear strength is satisfactory, with the error varying between 1 and 19%. The variation of the percent errors between the experimental and the numerical peak shear strength for different samples could be related to the imperfection of the experimental and the numerical protocol or other parameters, such as the cleanliness of the rock surface or even the simplifications considered in the numerical modeling.

2.3 **Concluding remarks**

The numerical modeling is based on three principal understandings from the growing number of experimental studies on the shear behavior of concrete-rock interfaces. First, shear failure occurs mainly at the interface with no significant damage in the concrete or rock when the normal stress is low. Thus, with the normal stress levels considered in the present study, the shear behavior of concrete-rock interfaces can be modeled, focusing on the events occurring at the interfaces. Second, the contribution of the roughness of the interface on the shear response can be separated in two: the strength of the concrete-rock bonds, which depend on the unevenness of the interface, and the surface interlocking during the test, controlled by the waviness of the interface. Last, the shear response of the concrete-rock interfaces can be separated into three stages, controlled by the concrete-rock bonds, the friction of the interface, or both.

Using these three interpretations, a traction separation law, damage, and frictional behavior are used to model the concrete-rock bonds representing the influence of unevenness. In contrast, the influence of the waviness is considered using the explicit representation of the morphology of the interface. The behavior law of the model is calibrated using the bush-hammered interfaces. The calibrated model reproduces the shear response of direct shear tests of bush-hammered concrete-rock interfaces quite well. Simulations of the direct shear test of the rough concrete-rock interfaces using the calibrated model show that the assumptions related to the influence of the roughness

scale are sound because of the closeness of the shear responses obtained experimentally and numerically.

The successful simulation of the shear behavior of concrete-rock interfaces is important because it defines the possibilities of investigating aspects of the shear behavior of interfaces that cannot easily be studied using laboratory experiments. One such aspect is investigated in the next chapter.

3. Influence of roughness on the shear resistance of interfaces: a new approach

Generally, the experimental and numerical investigation of the shear resistance of rough rock-rock and concrete-rock interfaces is carried out using a handful of rough rock slabs extracted from a single or a few rock blocks detached from a rock mass. Consequently, the distribution and the variety of roughness tested are very limited. This limitation could be one of the reasons for the continuing difficulty characterizing the influence of roughness on the shear resistance of interfaces.

This chapter presents a new methodology to address the control over the distribution and the variety of the rough rock surfaces considered when investigating the influence of roughness on the shear resistance of interfaces. The methodology is based on the numerical work presented in Chapter 2 and is presented as a case study using concrete-rock interfaces under low normal loading (below 1.5 MPa).

3.1 Generation of synthetic rough rock surfaces

This section uses the roughness data collected by El Merabi (El Merabi, 2018) before the experimental tests of rough concrete-granite interfaces (Reviewed in section 1.3.2 and simulated in Chapter 2). These roughness data represent the field of heights of asperities used to generate synthetic rough rock surfaces. This generation of synthetic rough rock surfaces proceeds in three steps. First, the fields of heights of asperities representing each interface tested are normalized. Second, the normalized data obtained are used in the variogram analysis, yielding parameters characterizing each field in terms of spatial correlation and variance. Last, these characteristic parameters are used as inputs of random field simulations to generate synthetic rough rock surfaces. More details about each step are presented below.

3.1.1 The roughness of rough rock surfaces as a random function

Every field of heights of asperities representing a rough rock surface is a dataset that maintains the concept of regionalization since each field value is correctly associated with a specific location in a physical space and maintains a correlation with other heights of asperities located in its surroundings. Moreover, it is very challenging to define a deterministic function to fit all the heights of asperities composing the field. Therefore, a probabilistic approach to characterize the field of heights of asperities is more suitable. Furthermore, the probabilistic approach introduces the concepts of randomness, such as each field value can be envisioned as a result of a random mechanism. Therefore, the association of regionalization and randomness is the base of the definition of random function (Wackernagel, 2003). This association means that the roughness of rough rock surfaces can be considered a random function. Consequently, the random field theory can simulate synthetic rough rock surfaces.

3.1.2 Statistical and geostatistical data processing

The methodology for simulating random fields in this work requires the data to be normally distributed. Unfortunately, the distribution of heights of asperities constituting the rough rock surface, as many other properties of interest in rock and soil mechanics, do not automatically follow a normal distribution (Fenton and Griffiths, 2008; Casagrande *et al.*, 2018). Therefore, the quantile-to-quantile normal score transformation is used to normalize the distribution of heights of asperities (Deutsch and Journel, 1998; Pyrcz and Deutsch, 2020). This transformation generates Nscore values, representing the normalized distribution of the heights of asperities (Figure 3.1).

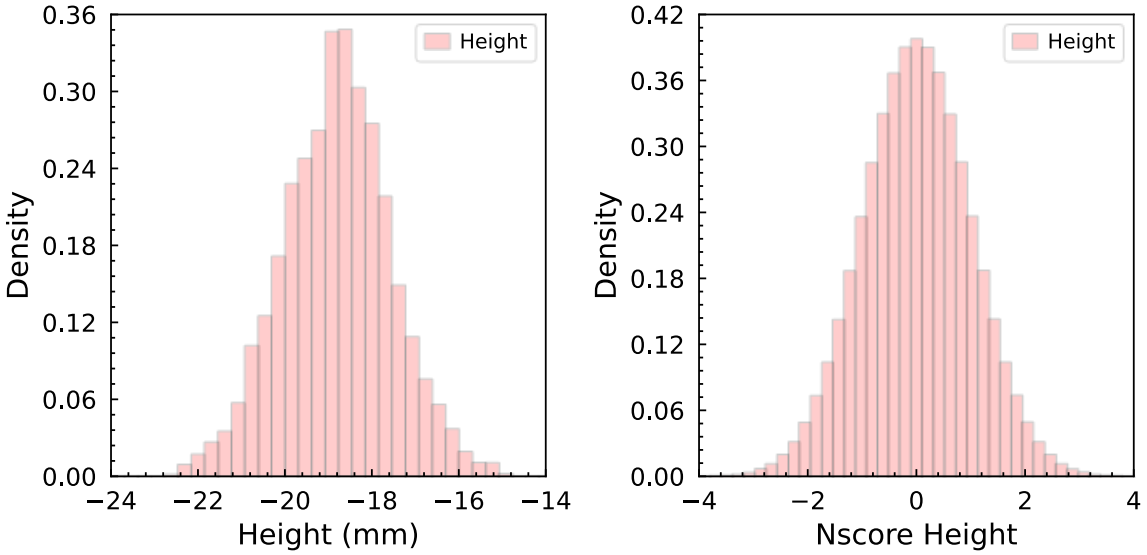

Figure 3.1 Data transformation for the rough granite sample used in test 10 (Refer to Chapter 2). Nscore values are transformations of heights of asperities such that the field is normalized.

A further requirement for the simulation of random functions using the random field theory is that the statistical characteristics of the first and the second moment (mean and variance) must remain constant within the domain. This requirement is the consideration of stationarity. In this research, the intrinsic stationarity hypothesis is used. This hypothesis means that the stationarity has to be satisfied only for the sums of differences between pairs of points, leading to the concept of variogram (Wackernagel, 2003).

A variogram function is an expression of the dissimilarity between pairs of points x and $x + h$ and is computed using Eq (3.1).

$$\gamma(h) = \frac{1}{2}E[(Z(x+h) - Z(x))^2] \qquad (3.1)$$

where E[ ] is the mathematical expectation.

In this research, the interest is in the generation of fields of correlated data; for this reason, the expression of similarity is more desired than the expression of dissimilarity. Consequently, instead of the variogram function, the covariance function is the one that is used in the random field simulation.

The covariance function is defined based on the concept of intrinsic stationarity of the two first moments (mean E[ ] and variance var[ ]) of a random function $Z(x)$, see Eq (3.2) and Eq (3.3).

$$E[Z(x+h) - Z(x)] = m(h) = 0 \qquad (3.2)$$

$$var[Z(x+h) - Z(x)] = 2\gamma(h) \qquad (3.3)$$

For all points x and $x + h$, the covariance function is defined according to Eq (3.4).

$$E[Z(x) * Z(x+h)] - (E[Z(x)])^2 = C(h) \qquad (3.4)$$

The variogram function can be computed using the covariance function;

$$\gamma(h) = C(0) - C(h) \qquad (3.5)$$

The covariance function used in this research is the spherical model, Eq (3.6). This model is selected because it best fits the shape of point cloud values obtained after calculating variograms of rough granite surfaces. The quality of fitting the covariance function to the shape of the variogram points calculated is important because these functions are designed to capture the general characteristics of a field. Using covariance functions instead of simple variogram points also adds a physical meaning to the characterization of a field (Wackernagel, 2003).

$$C_{sph}(h) = \begin{cases} b * \left(1 - \frac{3}{2} * \frac{|h|}{a} + \frac{1}{2} * \frac{h^3}{a^3}\right) & for\ 0 \leq |h| \leq a \\ 0 & for\ |h| > a \end{cases} \qquad (3.6)$$

where a represents the range and b represents the sill.

The spherical covariance function is defined using three parameters: the nugget effect, the range, and the sill. The nugget effect is associated with the unreliable variation of variogram values when smaller distances between pairs of points are considered. According to Eq (3.1), this means smaller values of h. This parameter is not considered in the present study because the rough granite surfaces used in the variogram analysis are small and well-sampled. The range a is the distance between pairs of points at which the values of the variograms begin to stabilize. The variogram value when the range a is reached is called the sill b. The range a is an expression of the correlation distance between the points of a field. The sill b can be interpreted differently depending on the geostatistical context. In this study, the sill is an expression of the variance of the data used in the computation of variograms. Since all the data are normalized, the sill is limited to one. This consideration can be interpreted as if the variogram values are above the sill; the data are inversely correlated. The data are directly correlated if the variograms are below the sill (Samson and Deutsch, 2021). The range a and the sill b are used as the inputs of the random field simulations aiming at reproducing the correlation between the points with controllable variance.

The fields of heights of asperities used in this study were collected by El Merabi (El Merabi, 2018) before conducting direct shear tests of rough concrete-granite interfaces. The results of the experimental study conducted by El Merabi are reviewed in section 1.3.2, and the numerical simulations of these tests are presented in Chapter 2. The fields of heights of asperities are first normalized using the quantile-to-quantile normal score transformation, and then the normalized data obtained is used to compute variograms. The variogram points are fitted to a spherical covariance function defining the range a and the sill b. The range a and the sill b obtained are used in the random field simulation presented hereafter to obtain new synthetic rough rock surfaces with similar correlation distance and controllable variance.

The simulation of random fields, as implemented in this thesis, is restricted to isotropic random fields; this means that the covariance function is assumed to be constant independently of the direction of the vector h.

Figure 3.2 shows the result of a variogram analysis of the natural rough granite surface used in test 10 (Refer to Chapter 2). It is worth noting that the data used in this analysis results from the quantile-to-quantile normal score transformation (Refer to Figure 3.1). The results of this variograms analysis yield two sets of sill-range $(1, 25)$ and $(1, 20)$ used as input parameters of two random field simulations to generate synthetic rough rock surfaces. The results comprise parts of the entire dataset of synthetic rough rock surfaces generated for this study. It is worth noting that this process is repeated for all the rough granite surfaces used in the tests performed by El Merabi (El Merabi, 2018), the results of which are discussed by Badika et al. (Badika *et al.*, 2022), reviewed in section 1.3.2 and used in the numerical work developed in chapter 2.

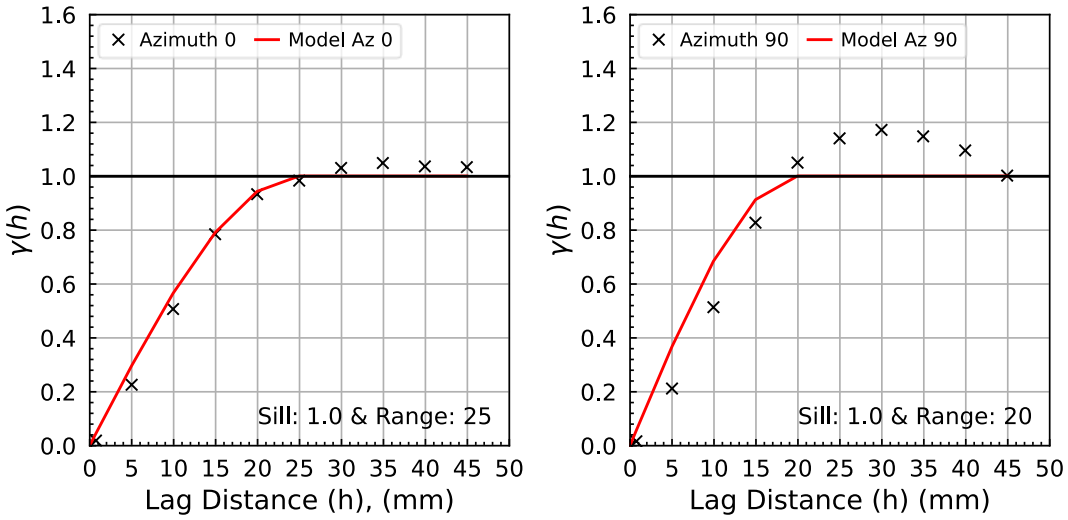

Figure 3.2 Variogram analysis of the rough granite surface used in test 10 (Refer to Chapter 2), two directions (see azimuth)

3.1.3 **Simulation of random fields using the turning band method**

The simulation of random fields is a process that receives statistics and or geostatistics characteristics of a field of correlated data and generates a series of fields of correlated data. Each field of correlated data generated possesses statistics and or geostatistics characteristics within an acceptable range of variation of the simulation inputs. The average of the statistics and or geostatistics of all the fields of correlated data generated after a simulation is equal or as close as possible to the inputs of the simulation.

In this work, random field simulations are carried out using as inputs the range a and the sill b of spherical covariance functions used to fit the variograms computed using the points cloud representing the heights of asperities of rough granite surfaces. The outputs obtained in these simulations are fields of heights of asperities denominated synthetic rough rock surfaces. These synthetic rough rock surfaces have geostatistical characteristics (range a and sill b) within an acceptable range of the ones of the rough granite surfaces used in the computation of the input parameters of the random field simulations. Synthetic rough rock surfaces with defined roughness values are then selected from the database of synthetic rough rock surfaces generated.

This thesis uses the turning bands method to perform random field simulations. This method has a solid geostatistical background and uses variogram analysis. A summary of the method is provided below. A more detailed presentation of the turning bands method can be found in the literature (Matheron, 1973; Journel and Huijbregts, 1976; Mantoglou and Wilson, 1982; Chilès and Delfiner, 2012)

The turning bands method reduces two-dimensional and tridimensional problems into unidimensional ones. Consequently, instead of performing tridimensional simulations straight away, a series of unidimensional simulations are carried out along a set of lines. Then, a single regionalized value is determined by computing the weighted sum of the projected values in the unidimensional realizations according to Eq (3.7).

$$z_s(X) = \frac{1}{\sqrt{N_l}} \sum_{1}^{N_l} z_i(< \overrightarrow{OX_l}, \overrightarrow{u_l} >) \qquad (3.7)$$

where N_l, the number of lines and the subscript s indicates the simulated synthetic value.

A simplified presentation of the turning bands methods is presented (Figure 3.3).

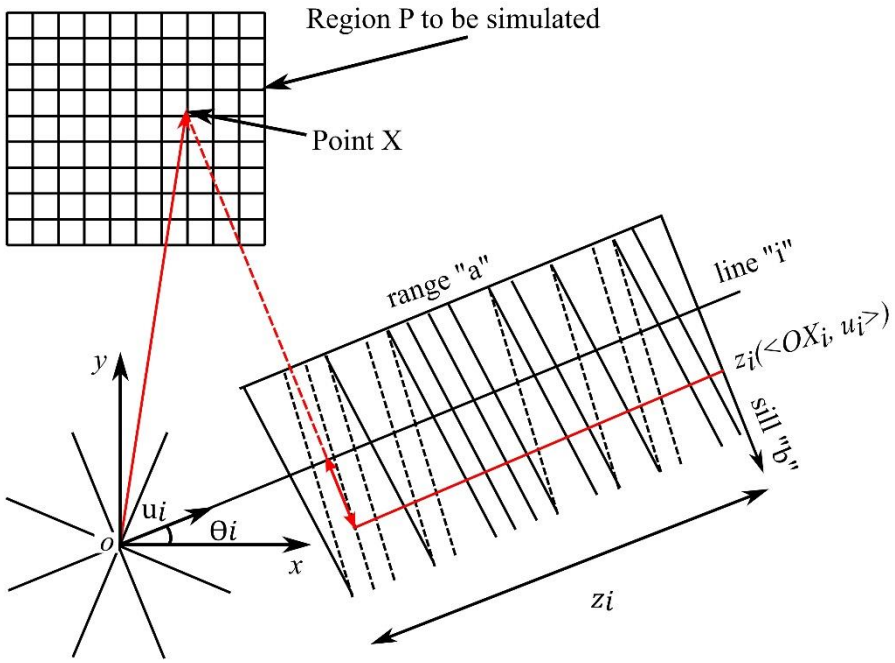

Figure 3.3 Turning bands method. Inspired by Mantoglou and Wilson (Mantoglou and Wilson, 1982), Lantuéjul (Lantuéjoul, 1994), and Emery and Lantuéjul (Emery and Lantuéjoul, 2006)

Suppose P is a synthetic rough rock surface (Figure 3.3). A simulation of one height of asperity z associated with the location (x,y) in the realization P is presented. For this, an arbitrary origin of axes x and y named O is established. From O a set of lines passing through the origin O is generated. These lines are usually uniformly distributed within a circle and separated by an angle θ. Among this set of lines, a line i is selected, i forms an angle θ_i with the x axis. Along the line "i," a realization z_i with zero mean and unidimensional covariance function $C_1(h)$ is generated. If

one considers a vector $\overrightarrow{OX}$ going from the origin of axes O to the point being generated in X and the vector $\overrightarrow{u_i}$ along a line i, orthogonally project $\overrightarrow{OX}$ onto $\overrightarrow{u_i}$, this yields a new vector $\overrightarrow{OX_i}$, define the contribution of z_i in the simulation of the point X as $z_i(X_i)$, which means $z_i(X_i) = z_i(< \overrightarrow{OX_i}, \overrightarrow{u_i} >)$ (<> is the inner product). Figure 3.3 illustrates this process.

The direct relationship between the three-dimensional covariance function and the unidimensional covariance function is given by Eq (3.8); the demonstration of this equation can be found in Mantoglou and Wilson (Mantoglou and Wilson, 1982) and Matheron (Matheron, 1973).

$$C_1(h) = \frac{d}{dx}[h * C_3(h)] \quad (3.8)$$

where $C_1(h)$ is the unidimensional covariance function, and $C_3(h)$ is the three-dimensional covariance function.

$C_3(h)$ is computed using three-dimensional data representing a natural rough rock surface. In this thesis, since the spherical covariance function is used to fit the variogram, that is to say $C_3(h)$ computed according to Eq. (3.6), its unidimensional equivalent $C_1(h)$ can be determined using Eq (3.9).

$$C_1(h) = \begin{cases} b * \left(1 - 3 * \frac{|h|}{a} + 2 * \frac{h^3}{a^3}\right) & for\ 0 \le |h| \le a \\ 0 & for\ |h| > a \end{cases} \quad (3.9)$$

Furthermore, the random field simulation using the turning bands method used in this research is implemented using the Matlab computer program presented in Emery and Lantuéjoul (Emery and Lantuéjoul, 2006).

3.1.4 **Synthetic rough rock surface generator**

The random field simulation to generate synthetic rough rock surfaces proceeds in six steps (Figure 3.4).

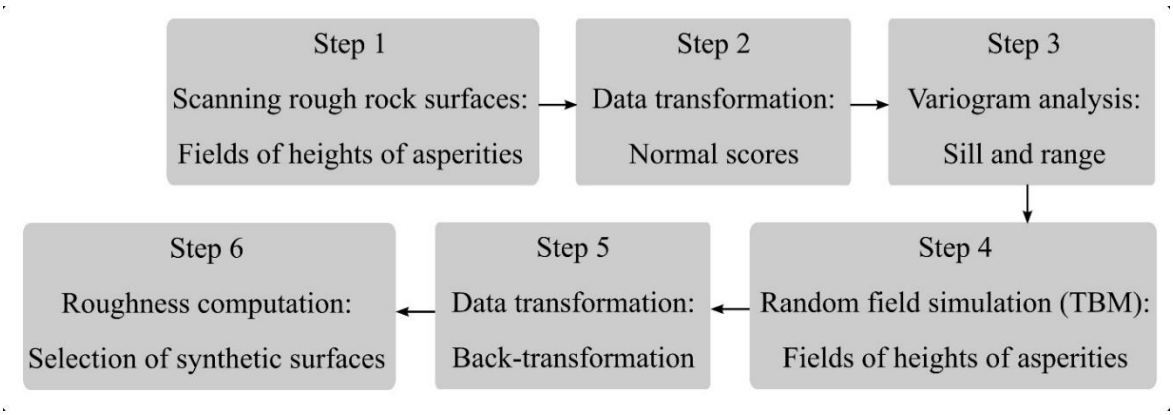

Figure 3.4 Synthetic rough rock surface generator using random field simulation

The first step involves collecting the roughness information of natural rough rock surfaces. Figure 1.8 illustrates this step. Granite blocks with natural rough surfaces were scanned using the laser-based scanner developed by Hans and Boulon (Hans and Boulon, 2003). The characteristics of this scanner are reviewed in section 1.2.2. From the scanning, fields of heights of asperities were obtained as part of the experimental work carried out by El Merabi (El Merabi, 2018).

The second step consists of applying the quantile-to-quantile normal score transformation to obtain normal distributions of the fields of heights of asperities.

The variogram analysis is carried out in step three. This analysis determines the covariance function parameters used as inputs of the random field simulation. Figure 3.2 illustrates the result of a variogram analysis.

In step four, the random field simulation using the turning bands method is carried out. Figure 3.5 illustrates the theoretical variogram from which the simulation inputs were drawn, the variograms of the simulated fields, and the average of the variograms of the simulated fields.

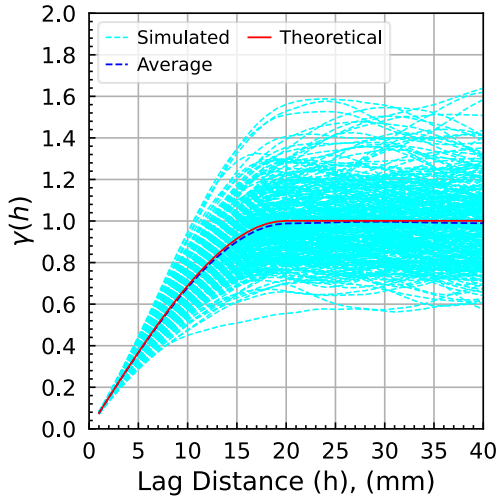

Figure 3.5 Variograms of simulated rough rock surfaces

In step five, the back-transformation is carried out to transform the synthetic surfaces obtained from normal distribution to the original distribution of the field used as input.

The last step is the computation of roughness parameters of the synthetic rough rock surfaces to select synthetic rough rock surfaces with specific roughness values. The roughness characterization is performed using the Grasselli roughness parameter $\theta^*_{max}/(C+1)$ (Bryan S.A. Tatone and Grasselli, 2009). The reasons for selecting this roughness parameter are discussed in section 1.2.3.

Figure 3.6 illustrates two synthetic rough rock surfaces generated.

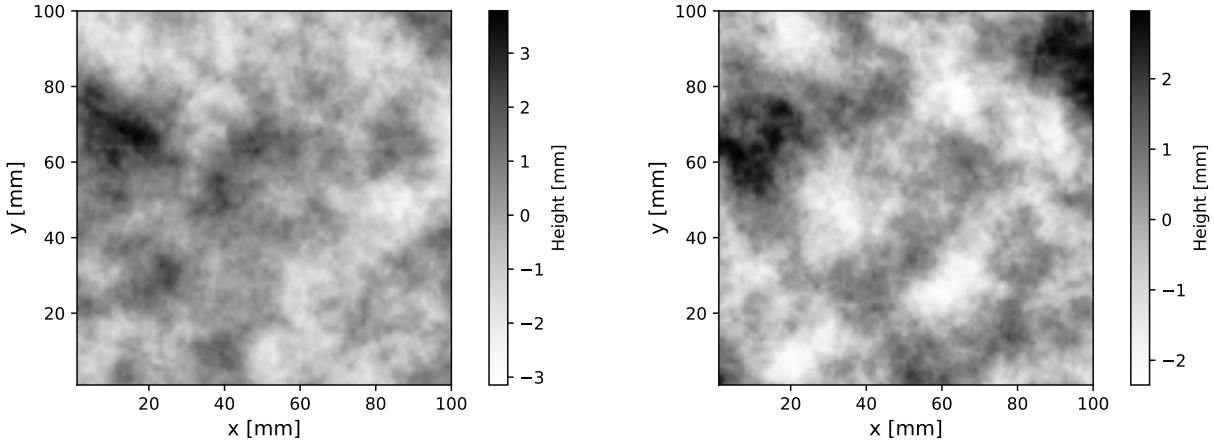

Figure 3.6 Synthetic rough rock surfaces generated; (a) sample 1 and (b) sample 2

Figure 3.7 shows the results of the random field simulation performed in terms of the roughness of the synthetic rough rock surfaces generated. 334 synthetic rough rock surfaces were generated with the roughness $\theta^*_{max}/(C+1)$ varying between 6 and 24. These synthetic rough rock surfaces are hereafter used in the simulation (FEM) of direct shear tests of concrete-rock interfaces to investigate the influence of roughness on the shear resistance of interfaces.

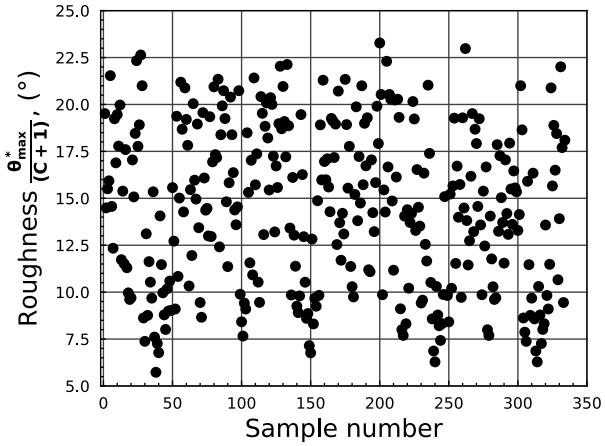

Figure 3.7 Roughness of the synthetic rough rock surfaces generated; $\boldsymbol{\theta^*_{max}/(C+1)}$

3.2 **Results of the finite element simulations**

It is worth noting that all the details of the finite element simulations of the direct shear tests using the synthetic rough rock surfaces can be found in Chapter 2. The results of these simulations are presented in this section.

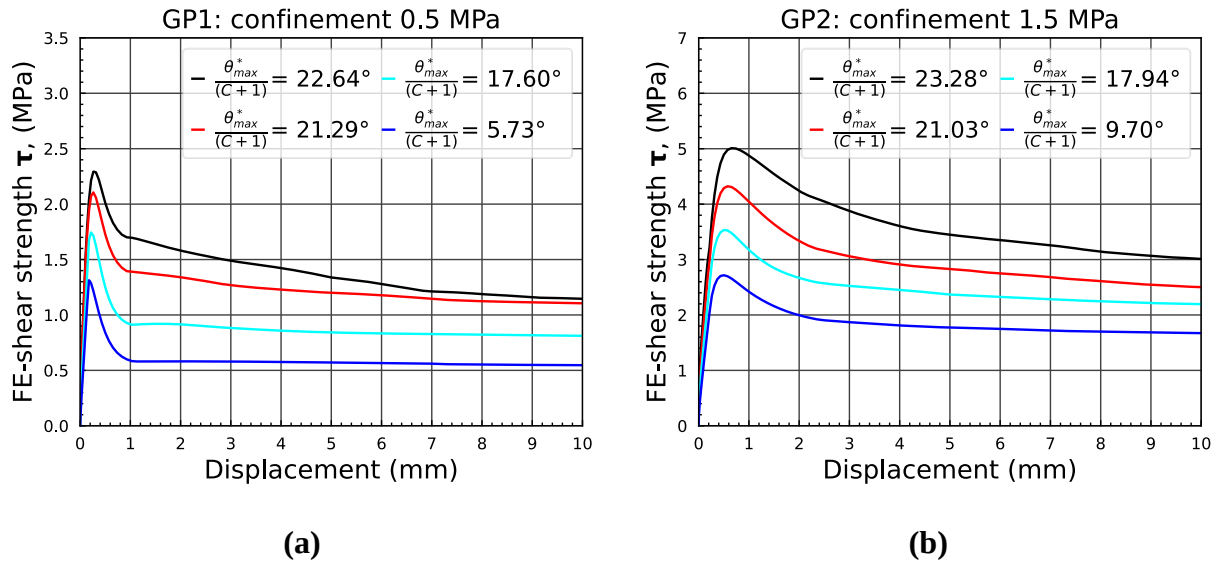

(a) **(b)**

Figure 3.8 Selected results of the finite element simulations: (a) first failure mode (0.5 MPa) and (b) second failure mode (1.5 MPa)

Figure 3.8 presents a selection of the shear responses obtained using the numerical simulations of the direct shear test of synthetic rough rock surfaces. The shear evolution obtained comprises a pre-peak phase followed by a post-peak phase and is completed by a residual phase. The succession of these phases is the reproduction of the main stages of the experimental results (Saiang, Malmgren and Nordlund, 2005; Z. A. Moradian *et al.*, 2010; Moradian, Ballivy and Rivard, 2012; Krounis, Johansson and Larsson, 2016; Mouzannar *et al.*, 2017; Badika *et al.*, 2022). From this figure, it is clear that the roughness of the interfaces influences the peak shear strength. Furthermore, these figures also show that the peak shear strength depends on the confinement stress. It is worth noting that all the 334 interfaces virtually tested have different roughness values.

Figure 3.9 shows the peak shear strength of the interface in terms of roughness for the two levels of confinement. From these figures, the correlation coefficients between the peak shear strength and the $\theta^*_{\max}/(C+1)$ are 0.88 and 0.85 for the simulations performed with 0.5 and 1.5 MPa of confinement stress, respectively. These results show that the peak shear strength maintains a strong correlation with the roughness of the interface when the confinement stress is below 1.5 MPa.

Figure 3.9 also shows that interfaces with the same or very similar roughness values do not always result in the same peak shear strength. This observation indicates that the relationship between the roughness and the peak shear strength is not one-to-one. The reason for the non-unicity roughness-peak shear strength could be related to the global aspect of the roughness parameters. The $\theta^*_{\max}/(C+1)$ evaluates the global roughness of a rock surface and cannot focus on the local influence of roughness. Rullière et al.(Rullière *et al.*, 2020) also reported a similar observation. This observation indicates that the local aspect of roughness explicitly considered in the finite element simulations performed can significantly influence the shear behavior of interfaces.

Overall, the results of the finite element simulations constitute an extensive database of shear evolutions in terms of the roughness of interfaces tested. With this database, two approaches are used to propose a failure criterion for concrete-rock interfaces under low normal loading. The first failure criterion proposed is an analytical relationship, while the second is a function based on neural network modeling.

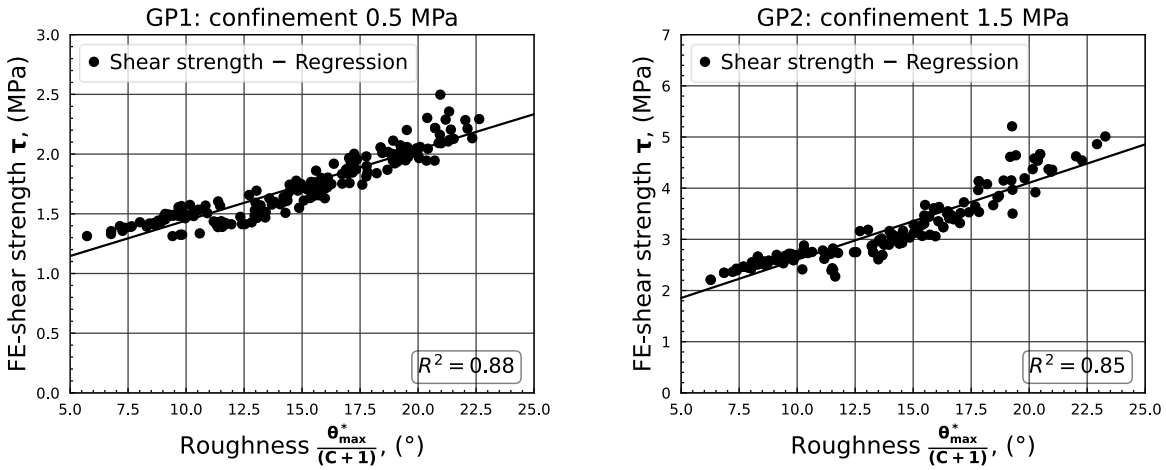

(a) **(b)**

Figure 3.9 Peak shear strength in terms of roughness $\boldsymbol{\theta^*_{max}/(C+1)}$; (a) GP1 confinement 0.5 MPa and (b) GP2 confinement 1.5 MPa

3.3 **New peak shear strength criterion for concrete-rock interface**

3.3.1 **Development of failure criterion for concrete-rock interfaces**

The proposed peak shear strength criterion for concrete-rock interfaces is based on the peak shear strength criterion for rock joints developed by Grasselli and Egger (Grasselli and Egger, 2003); see Eq. (1.7). Further details about this failure criterion are presented in section 1.1.5.

The contribution of roughness in this shear strength criterion can be replaced by the updated expression of roughness presented by Tatone and Grasselli (Bryan S.A. Tatone and Grasselli, 2009); this yield Eq. (3.10).

$$\tau_p = \sigma_n \tan\left[\phi_b + \left(\frac{\theta^*_{max}}{C+1}\right)^{1.8}\right]\left[1 + e^{-\left(\frac{\theta^*_{max}}{C+1}\right)\left(\frac{\sigma_n}{\sigma_t}\right)}\right] \qquad (3.10)$$

where τ_p is the peak shear strength. σ_n is the normal stress. ϕ_b is the basic friction angle. $\theta^*_{max}/(C+1)$ is the roughness parameter. σ_t is the tensile strength of the rock.

For the case of concrete-rock interfaces under low confinement stress, the failure criterion depends on both friction and cohesion. The cohesion c is crucial in the case of low confinement stress because its contribution to the shear resistance of the interface is significant. Therefore, the cohesion c is included in Eq. (3.10), generating Eq. (3.11). Eq. (3.11) is a failure criterion for concrete-rock interfaces.

$$\tau_p = \sigma_n \tan\left[\phi_b + \left(\frac{\theta^*_{max}}{C+1}\right)^{1.8}\right]\left[1 + e^{-\left(\frac{\theta^*_{max}}{C+1}\right)\left(\frac{\sigma_n}{\sigma_t}\right)}\right] + c \quad (3.11)$$

where c is the cohesion.

For the synthetic rough rock surfaces generated, $\theta^*_{max}/(C+1)$ varies between 6º and 24º. The normal stress in the finite element simulations is 0.5 and 1.5 MPa. If one assumes the tensile strength is equivalent to 1 MPa, $e^{-(\theta^*_{max}/(C+1))(\sigma_n/\sigma_t)}$ varies between 0 and 0.08 MPa and can be simplified to 0 in Eq. (3.11). This simplification generates Eq. (3.12).

$$\tau_p = \sigma_n \tan\left[\phi_b + \left(\frac{\theta^*_{max}}{C+1}\right)^{1.8}\right] + c \quad (3.12)$$

Eq. (3.12) represents the proposed peak shear strength criterion for concrete-rock interfaces in the case of low confinement stress.

3.3.2 **Validation of the new failure criterion**

The shear responses obtained in the finite element simulations of direct shear tests using synthetic rough rock surfaces are used here to assess the capability of the proposed failure criterion to estimate the peak shear strength of concrete-rock interfaces.

For each synthetic rough rock surface virtually tested, the normal stress σ_n used in the simulation, the basic friction angle ϕ_b (30°), the roughness parameter $\theta^*_{max}/(C+1)$ computed using the roughness data and the cohesion are used as input of Eq. (3.12) to obtain the peak shear strength τ_p. The identification of the cohesion parameter is detailed below.

The cohesion of concrete-rock interfaces depends on the normal stress, the failure modes, and the strength of the concrete-rock bonds. The cohesion of the concrete-rock interface is usually determined indirectly using the fitting of the Mohr-Coulomb failure envelope computed, for example, using the results of direct shear tests. For the cohesion defined using this approach to be valid, all the shear test results must be within a range of normal stress representing the same failure mode. In the specific case of concrete-granite interfaces under low normal stress, as considered in this research, the cohesion is determined using the results of the direct shear tests of bush-hammered concrete-granite interfaces. The fitting includes the shear strength of interfaces under three normal stress levels: 0.5 MPa, 1.0 MPa, and 1.5 MPa. Within this interval of normal stress, two failure modes were identified (Badika *et al.*, 2022). It is worth noting that the higher the normal stress, the more damaged the interface and the lower the cohesion. The cohesion defined using the data of the two failure modes is expected to be underestimated in the case of shear strength under 0.5 MPa of confinement stress and overestimated in the case of confinement stress between 1 and 1.5 MPa. The computation of the failure envelope yields a cohesion of 0.83 MPa. Updating this value for the two failure modes produces a cohesion value of 0.99 and 0.69 MPa.

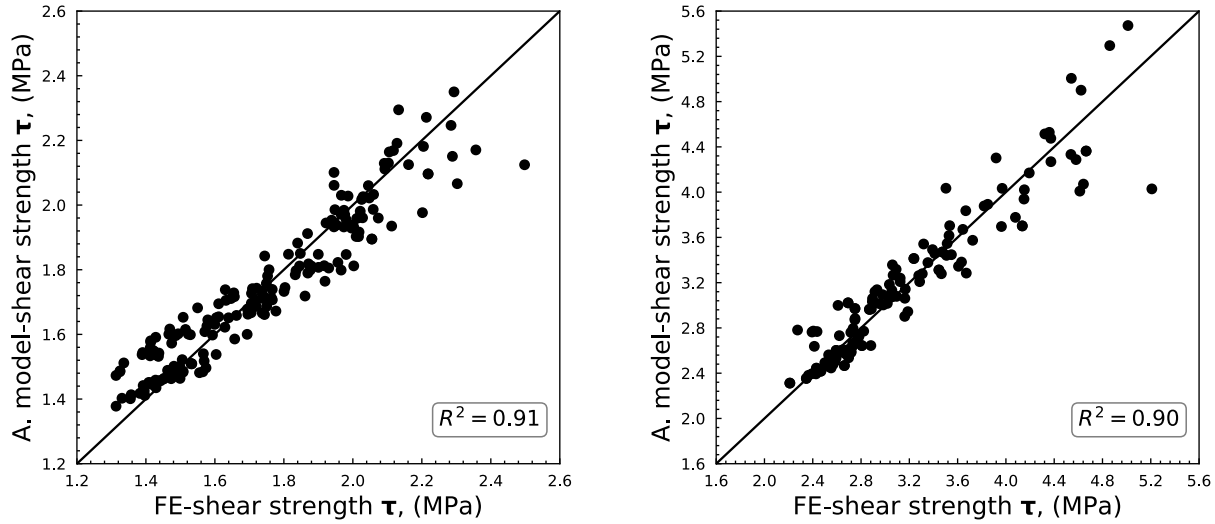

(a) **(b)**

Figure 3.10 Shear strength estimated using the analytical model in terms of numerically obtained peak shear strength: a) first failure mode (0.5 MPa) and b) second failure mode (1.5 MPa)

The peak shear strength of all the synthetic rough rock surfaces simulated using Eq. (3.12) is presented in Figure 3.10 (a) for the first failure mode and in Figure 3.10 (b) for the second failure mode. The correlation coefficient between the estimated and the simulated peak shear strength is 0.91 for the first failure mode and 0.90 for the second failure mode. These coefficients show that the proposed peak shear strength criterion can estimate the peak shear strength of concrete-rock interfaces under low normal stress.

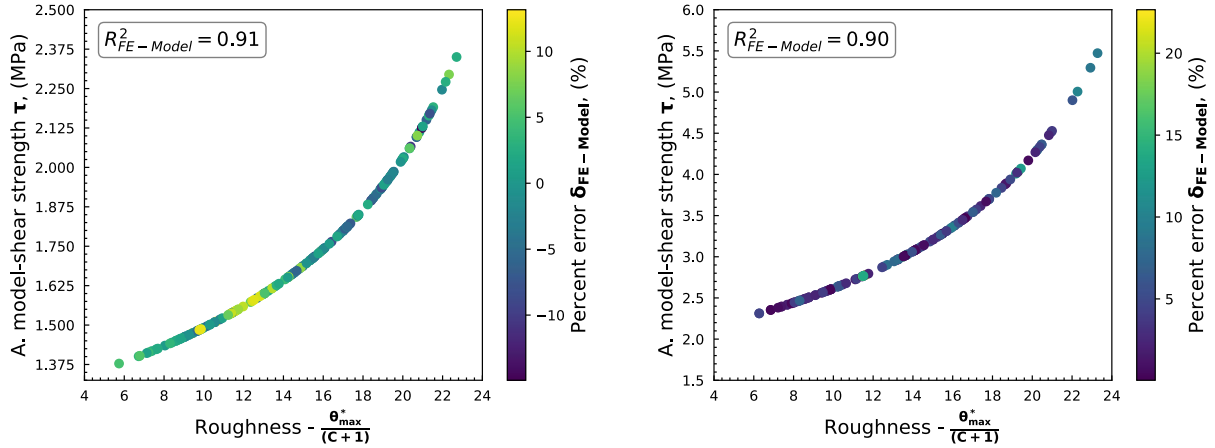

(a) **(b)**

Figure 3.11 Error of the estimated peak shear strength in terms of the simulated peak shear strength: a) first failure mode (0.5 MPa) and b) second failure mode (1.5 MPa). A. model in the y-axis stands for analytical model.

The percent error of the estimated peak shear strength compared with the finite element simulated peak shear strength is presented in Figure 3.11 (a) for the first failure mode and Figure 3.11 (b) for the second failure mode. These two graphs show that the percent error of the model is within fifteen percent for the first failure mode and twenty percent for the second failure mode. Furthermore, the shape of these two figures is associated with including the roughness value inside a tangential operation in the proposed failure criterion, Eq. (3.12). It is also worth pointing out that the two failure modes were defined for concrete-granite interfaces where shear failure mostly occurs along the interfaces for confinement stress below 1.5 MPa.

From Figure 3.11, it is clear that Eq. (3.12) supposes that the relationship between the roughness and the peak shear strength is one-to-one. Indeed, the local roughness seems to influence the shear resistance of the interface significantly, as shown in the analysis of the results of the finite elements simulation of direct shear tests using synthetic rough rock surfaces in section 3.2. To address the limitation of the bijective nature of the relationship roughness-peak shear strength as assumed in Eq. (3.12) and to take advantage of complex statistical aspects of the database of shear evolutions obtained by finite element simulation, neural network modeling is investigated as a complementary alternative to define a failure criterion for concrete-rock interfaces.

3.4 **Estimation of peak shear strength of concrete-rock interfaces using neural network modeling**

To take advantage of the considerable size of the database of simulations of direct shear tests using synthetic rough rock surfaces, neural network modeling is assessed as an alternative to estimating the shear resistance of interfaces. Neural network modeling is very effective in extracting complex statistical correlations in a dataset to perform a specific task. This methodology is gradually being applied more and more to a variety of problems in engineering. Here, a brief illustration of the application of neural network modeling in rock mechanics research is presented. Then, a new neural network-based approach is introduced to estimate the shear resistance of concrete-rock interfaces.

3.4.1 **Applications of neural network modeling in mechanics of geomaterials**

Artificial neural networks (ANN) application in rock mechanics research has grown substantially in the last twenty years. This growth has been fueled by the availability of powerful computers and data usually collected for mining engineering projects (Khandelwal and Singh, 2009; Alzubaidi *et al.*, 2022; Delavar and Ramezanzadeh, 2023) and the advances in machine learning research overall (Krizhevsky, Sutskever and Hinton, 2017). The advances in machine learning have positioned artificial neural network models as a possible alternative to numerical simulations (Furtney *et al.*, 2022), analytical models (Dantas Neto *et al.*, 2017), and or experimental studies (Furtney *et al.*, 2022; Sakaridis, Karathanasopoulos and Mohr, 2022). Furthermore, ANN models have been used extensively to estimate the rock properties, such as the compressive strength of rock (Meulenkamp and Grima, 1999; Yılmaz and Yuksek, 2008; Rabbani *et al.*, 2012; Rajesh Kumar *et al.*, 2013; Yesiloglu-Gultekin, Gokceoglu and Sezer, 2013; Jahed Armaghani *et al.*, 2016; Miah *et al.*, 2020; Le *et al.*, 2022), elastic modulus (Yılmaz and Yuksek, 2008; Rajesh Kumar *et al.*, 2013), and the major principal strengths (Rukhaiyar and Samadhiya, 2017).

3.4.2 **Neural network modeling**

The neural network model is set as a function f_{NN} that predicts the peak shear strength (τ_{NN}) of a concrete-rock interface using the normal stress (σ_n), the basic friction angle (Φ_b) and the roughness parameter $\theta^*_{max}/(C+1)$, see Eq. (3.13). This function is very similar to the peak shear strength

criterion presented in section 3.3.1; they use the same input parameters and intend to estimate the same output parameter.

$$f_{NN} : \left\{\sigma_n, \Phi_b, \frac{\theta^*_{max}}{(C+1)}\right\} \rightarrow \{\tau_{NN}\} \qquad (3.13)$$

The data for the neural network modeling is composed of 334 entries (rows). Each entry is composed of four values (columns). The first value is the normal stress σ_n used in the simulation. The second value is the basic friction angle Φ_b. The third value is the roughness $\theta^*_{max}/(C+1)$, which represents the roughness of a simulated synthetic rough rock surface. The last value is the peak shear strength (τ_{FE}), the highest shear stress recorded in the shear response obtained via finite element simulation of the direct shear test. The normal stress σ_n, the basic friction angle Φ_b, and the roughness $\theta^*_{max}/(C+1)$ are the input data, while the peak shear strength (τ_{FE}) is the expected output data. The entire data contains 1336 data points.

The columns of the data are feature-wise normalized to make the training of the neural network easier. The feature-wise normalization consists of subtracting each value from the mean of the column and dividing by the standard deviation of the column.

The data is randomly separated into two sets: the training and the validation datasets. The training dataset is used to train neural network models. The validation dataset assesses the performance of trained neural network models.

The proportion of the split is 50% of the data is the training dataset, and 50% is the validation dataset. The division attempts to maintain the distribution of the data. Figure 3.12 illustrates this data separation.

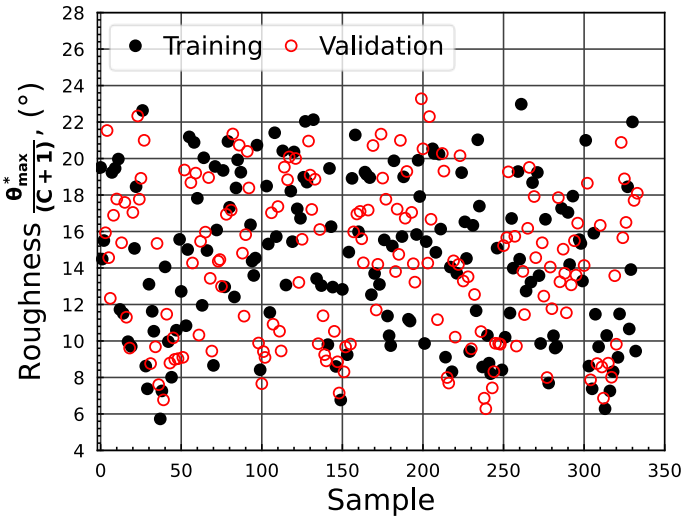

Figure 3.12 Training and validation datasets

After the preparation of the datasets, a brief insight into how the neural network is trained to receive as input the normal stress σ_n, the basic friction angle Φ_b, and the roughness $\theta^*_{max}/(C+1)$ and to produce as output the peak shear strength τ_{NN} is presented.

A typical neural network architecture comprises an input, hidden, and output layer. The input layer is fed with the inputs of the problem, the hidden layers transform the input data into valuable statistical representations, and the output layer provides the prediction or the output data. Figure 3.13 presents an illustration of the architecture of a neural network for the estimation of the peak shear strength of concrete-rock interfaces τ_{NN} using as inputs the normal stress σ_n, the basic friction angle Φ_b, and the roughness $\theta^*_{max}/(C+1)$.

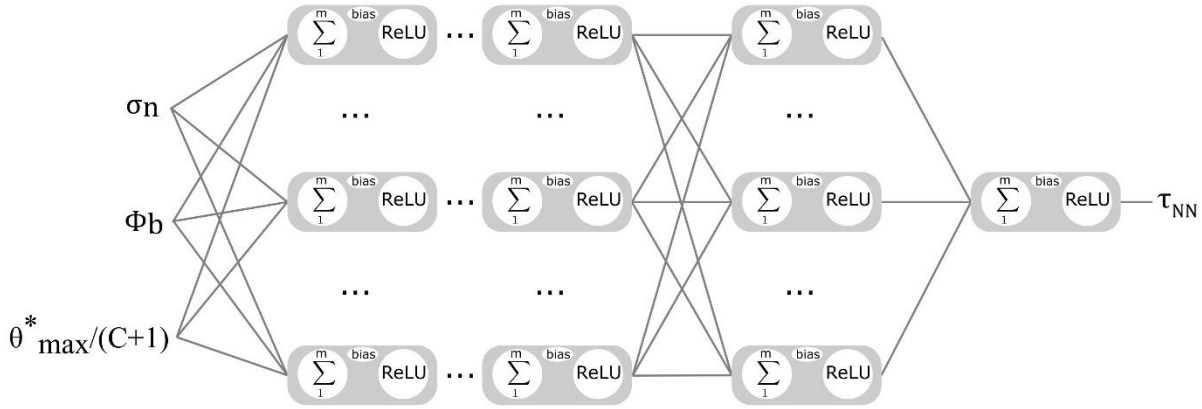

Figure 3.13 Example of a typical neural network architecture (Inspired by Fidle class notes (Gricad-gitlab, 2023)).

Each layer of the neural network comprises one or multiple neurons. The neurons carry out the transformations that layers apply to the input data (σ_n, Φ_b, $\theta^*_{max}/(C+1)$). A neuron computes the weighted average of the incoming inputs, uses an activation function, and returns an output value. The weights constitute the parameters of the neural network model. The activation function modifies the inputs to produce an output. This function is non-linear.

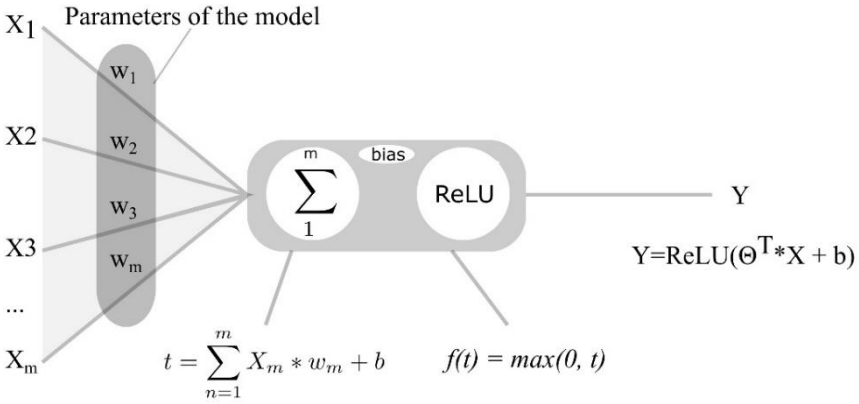

Input	Bias/Weight	Activation function	Output
X_i	θ	ReLU = f(x) = x^+ = max(0, x)	Y

Figure 3.14 Neuron of a neural network (Modified from Fidle class notes (Gricad-gitlab, 2023))

A representation of a neuron is shown in Figure 3.14. In this figure, if the neurons belong to the first layer after the input layer, X_i is equivalent to (σ_n, Φ_b $\theta^*_{max}/(C+1)$). And If the neurons belongs to the output layer, Y is equivalent to the estimated peak shear strength τ_{NN}. Otherwise, X_i are transformations resulting from the preceding layer, and Y is a transformation passed on to the next layer.

Training a neural network implies finding the appropriate values for the weights w_i of the neurons (Figure 3.14) to be able to associate inputs (σ_n, Φ_b $\theta^*_{max}/(C+1)$) to output (τ_{NN}). During one pass of the training of a neural network, the input layer receives one or multiple entries (σ_n, Φ_b $\theta^*_{max}/(C+1)$) from the training dataset. The hidden layers use operations performed by the neurons to transform the input data into more valuable representations. The output layers use the generated representations to predict the output values (τ_{NN}). The predicted values are then compared to the expected values (τ_{FE}) using the loss function; this generates the loss score, which is then used by the optimizer to change the parameters of the neural network (weights, w_i) using a back-propagation algorithm. Notably, the parameters of the neural network model (weights, w_i) are randomly initialized before the first pass.

It is worth noting that the batch size is the number of entries of the training dataset fed to the neural network during a single pass. An epoch is an iteration consisting of one or multiple passes during the training of the neural network model completed when all the training dataset has been used to find the best parameters (weights, w_i) of the neural network model.

During training, after each epoch, the performance of the updated neural network model is assessed using the validation dataset. This means that after each epoch, the model trained so far is used to estimate the peak shear strength τ_{NN} using as input values (σ_n, Φ_b $\theta^*_{max}/(C+1)$) from the validation dataset. The report of the performance of successive neural network models on the training and validation dataset is called the learning curve. From the learning curve, the best neural network model can be selected.

During the training of the ANN model to estimate the peak shear strength of concrete-rock interfaces τ_{NN} different architectures composed of different numbers of layers, neurons per layer, and batch size were assessed. This assessment, called hyperparameters analysis, is important to determine the best architecture. The report of the hyperparameters analysis is presented in section 3.4.3.1.

All the architectures of the neural networks analyzed start with an input layer that receives the input parameters of the model; this means the normal stress σ_n, the basic friction angle Φ_b and the roughness $\theta^*_{max}/(C+1)$. The input layers are followed by hidden layers, each with a defined number of neurons. The output of a neuron is obtained using the activation function ReLU (rectified linear unit). This function screens out all the negative values. The mean squared error (MSE) presented in Eq. (3.14) is the loss function.

$$MSE = \frac{1}{n}\sum_{i=1}^{n}(\tau_{NN} - \tau_{FE})^2 \qquad (3.14)$$

where n is the number of data, τ_{NN} is the peak shear strength predicted by the neural network, and τ_{FE} is the peak shear strength obtained by finite element simulation, τ_{FE} are part of the datasets.

The optimizer used is the Adaptive Momentum Estimation, also called ADAM (Kingma and Ba, 2015). The mean absolute error (MAE) assesses the performance of the neural network model

trained in estimating the peak shear strength of concrete-rock interfaces after each epoch, see Eq. (3.15).

$$\mathrm{MAE} = \frac{1}{n}\sum_{i=1}^{n}|\tau_{NN} - \tau_{FE}| \qquad (3.15)$$

The output layer is the last layer that predicts the peak shear strength τ_{NN}.

Furthermore, all the codes were developed in Keras. Keras is a deep-learning framework for Python where neural network models can be set, trained, and assessed (Chollet, 2021). TensorFlow backend engine handled tensor operations and differentiation (Abadi *et al.*, 2016).

3.4.3 **Results of the neural network modeling**

This section comprises two parts: the hyperparameters and the presentation of the results of the neural network model focusing on estimating the peak shear strength.

3.4.3.1 **Hyperparameters analysis**

The hyperparameter analysis is carried out to define the best neural network architecture for the estimation of the peak shear strength τ_{NN} of concrete-rock interfaces. The hyperparameters considered in this analysis are the number of layers per neural network, the number of neurons in each layer, and the batch size. For each hyperparameter, neural network models with different architectures are assessed regarding the quality of the estimation of the peak shear strength τ_{NN} when tested using the validation dataset (σ_n, Φ_b, $\theta^*_{max}/(C+1)$, τ_{FE}). This assessment uses the MAE (Eq. (3.15)) as a performance indicator.

To consider the oscillations of the performance of models when the training process is repeated, for each neural network model considered, the training was repeated five times, and the average performance was reported.

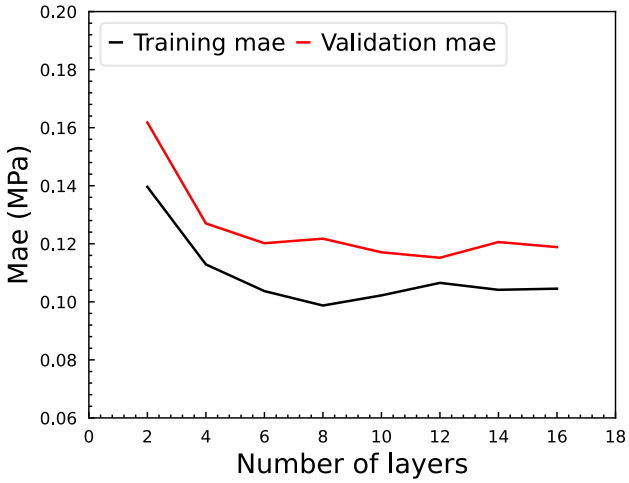

Figure 3.15 Influence of the number of layers on the performance of the model

Figure 3.15 shows the influence of the number of layers on the performance of the neural network models. The performance of the models increases with the increase of the number of layers m. When m is between 2 and 6, it does not vary significatively afterward. Therefore, the number of layers of 6 was adopted for subsequent analysis.

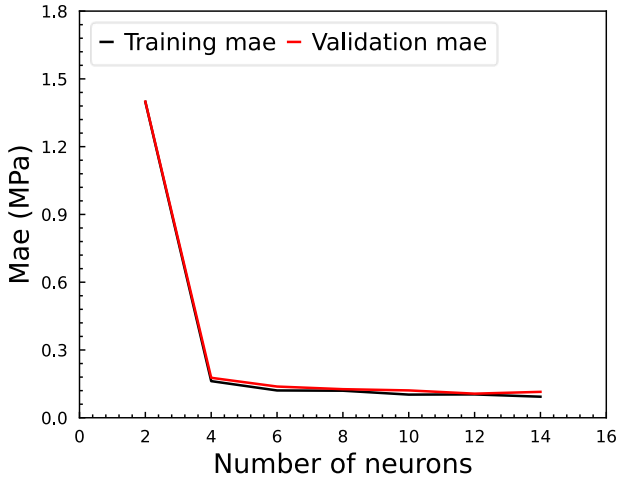

Figure 3.16 Influence of the number of layers on the performance of the model

Figure 3.16 shows the influence of the number of neurons per layer on the performance of the neural network. The performance increases with the number of neurons per layer n when n is below 6. Beyond this limit, the performance of the model becomes less insensitive to the rise of n. For simplicity, the number of neurons of 10 is adopted for subsequent analysis.

The last hyperparameter to consider is the batch size. Batch sizes varying from 2 to 64 were investigated. From Figure 3.17, it is clear that increasing the batch size reduces the performance of the neural network. Therefore, the batch size of 8 was adopted.

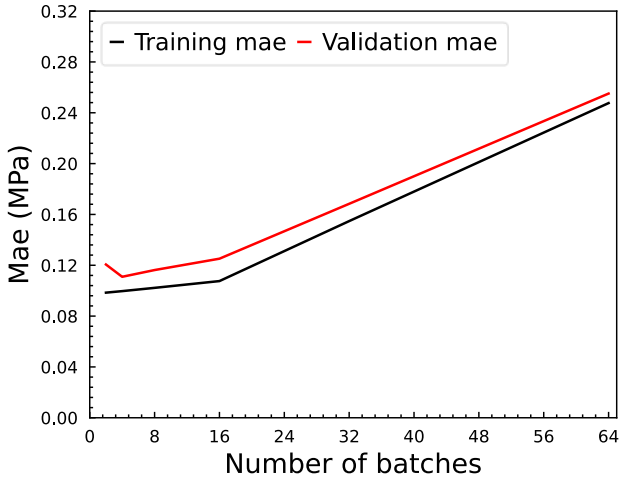

Figure 3.17 Influence of the size of the batch on the performance of the model

From this analysis, the architecture of the most suitable model for estimating the peak shear strength of concrete-rock interfaces contains one input layer, six hidden layers, each hidden layer comprises ten neurons, and one output layer that yields the prediction of the peak shear strength τ_{NN}.

Once the best neural network architecture to estimate the peak shear strength τ_{NN} of concrete-rock interfaces is defined, it is important to assess the variation in the performance of the models trained. For this reason, 100 neural network models with the defined architecture were trained to assess the variation of the performances.

Figure 3.18 shows the results of this assessment. This graph shows that the MAE of the neural network models for the peak shear strength estimation is between 0.10 MPa and 0.15 MPa. This confirms the relevancy of the neural network architecture defined to yield models with similar performances.

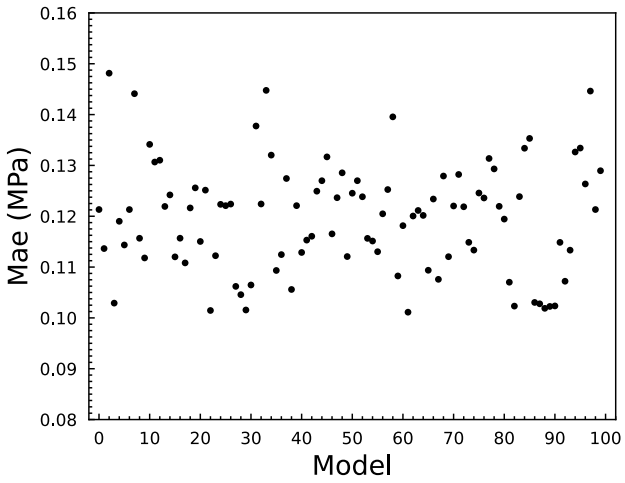

Figure 3.18 Variation of the performance of the model

3.4.3.2 **Performance of the neural network model**

The history of the performance of the neural network models during training is presented in Figure 3.19. The performance of the final model is high, with an MAE of 0.10 MPa in the training data and 0.11 MPa in the validation data. During training, the evolution of the performance of the model on the training dataset and the validation dataset decreases until it reaches a plateau. This steady decrease indicates that the model does not have an issue with overfitting (Chollet, 2021) and that the generalization of the model is sufficient to predict on never-before-seen data.

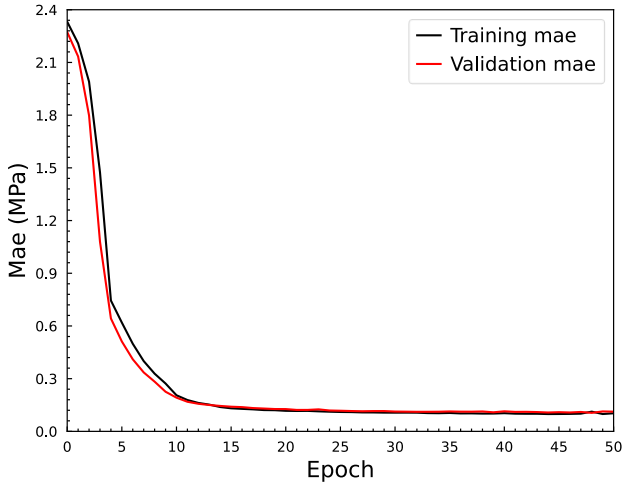

Figure 3.19 Performance of the neural network for the estimation of the peak shear strength

Figure 3.20 (a) presents the estimation of the model when tested with the validation dataset. The correlation between the finite element obtained peak shear strength and the neural network predicted peak shear strength is 0.96 with an MAE of 0.11. Figure 3.20 (b) shows the error of the neural network model prediction on the validation dataset compared to the finite element base values.

Furthermore, the two trends observed in Figure 3.20 (b) are related to the two normal stresses used in the finite element simulation, 0.5 and 1.5 MPa. See section 2.

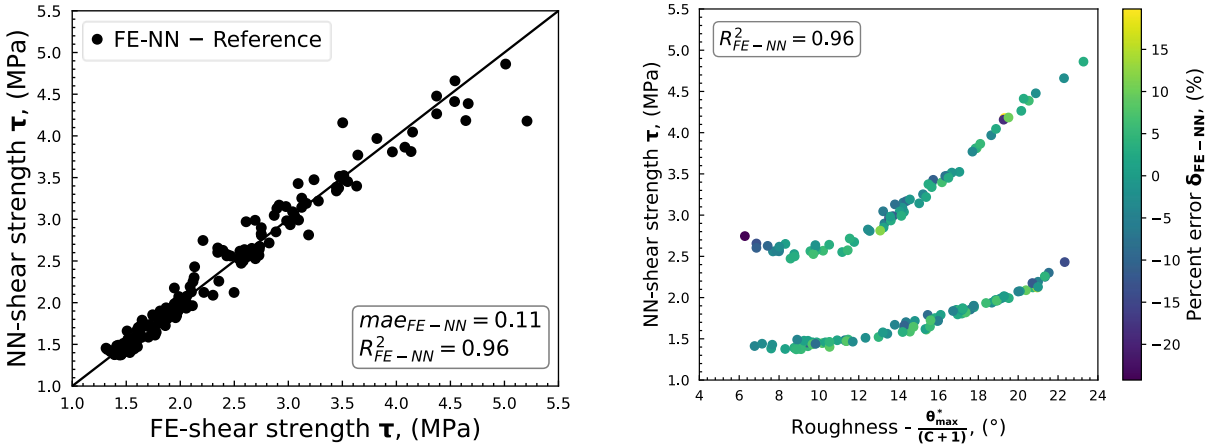

(a) **(b)**

Figure 3.20 FE peak shear strength in terms of NN peak shear strength (validation dataset) and (b) NN predicted peak shear strength in terms of the roughness and percent error (validation dataset)

3.5 **Assessment of the analytical and the neural network model using experimental data**

One last assessment of the performance of the analytical and the neural network model for estimating the peak shear strength of concrete-rock interfaces is carried out using the experimental results of direct shear tests of rough concrete-granite interfaces submitted to 0.5, 1.0, and 1.5 MPa of confinement stress. The results of these tests were briefly reviewed in section 1.3.2 and are fully discussed in Badika et al. (Badika *et al.*, 2022) and in El Merabi (El Merabi, 2018).

However, before applying the two models, the roughness data of the interface tested were interpolated to generate gridded data with a point spacing of 1 mm. This interpolation is important to reach the same point spacing of the synthetic rough rock surfaces, which is relevant because point spacing influences the computation of roughness. The context of the computation of roughness in terms of point spacing can affect the analysis, leading to a definition of a model to estimate the shear resistance of interfaces. The influence of the point spacing on the computation of roughness and the definition of failure criteria is discussed by Tatone et al. (Tatone, Grasselli and Cottrell, 2010).

Figure 3.21 (a) shows the results of the estimated peak shear strength obtained using the analytical model in terms of the experimentally obtained peak shear strength. The correlation of the estimated peak shear strength in terms of the experimentally obtained peak shear strength is 0.20 for the first failure mode (confinement of 0.5 MPa) and 0.84 for the second failure mode (confinement of 1.0 and 1.5 MPa). However, given the low data in each failure mode, it is best to assess the quality of the estimations in terms of the percent error. Figure 3.21 (b) shows the percent error of the estimated peak shear strength in terms of the experimentally obtained peak shear strength. This figure shows that the errors are within 25% of the experimental results for most of the estimated peak shear strength.

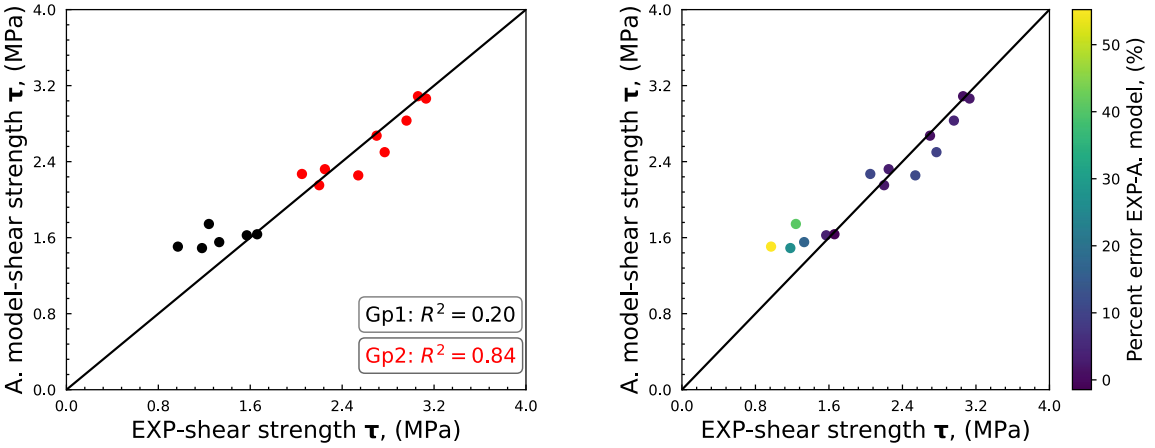

Figure 3.21 Assessment of the analytical model: a) Experimental vs. estimated peak shear strength (0.5, 1.0, and 1.5 MPa) and b) Percent error between the Experimental and the estimated peak shear strength. Gp1 and Gp2 stand for group 1 (here normal stress equals 0.5 MPa) and group 2 (here normal stress equals 1.0 and 1.5 MPa), representing the two failure modes discussed in section 1.3.2 and chapter 2

Figure 3.22 (a) shows the variation of the estimated peak shear strength obtained using the neural network model in terms of the experimentally obtained peak shear strength. It is worth noting that only the experimental rough concrete-granite interfaces tested under 0.5 and 1.5 MPa of confinement stress are considered in this analysis. This selection is due to the limited variation of data used in the neural network modeling regarding normal stress. Only two levels of normal stress are used: 0.5 and 1.5 MPa. The correlation coefficient between the estimated and the experimentally obtained peak shear strength is 0.96 with an MAE (Eq. (3.15)) of 0.21 MPa.

Furthermore, unlike the analytical model, the neural network estimation of the experimental results does not require further information on the failure modes associated with each test. The elevated performance of the neural network model is evident when the estimated data is presented in terms of the percentual error, as shown in Figure 3.22 (b). This figure shows that the estimations provided are quite close to the experimentally obtained peak shear strength for most of the results.

This assessment shows that the two approaches proposed for estimating the peak shear strength of concrete-rock interfaces can be used for the experimental results. The quality of the estimations is interesting and shows the relevance of the new methodology of investigating the influence of roughness on the shear resistance of interfaces.

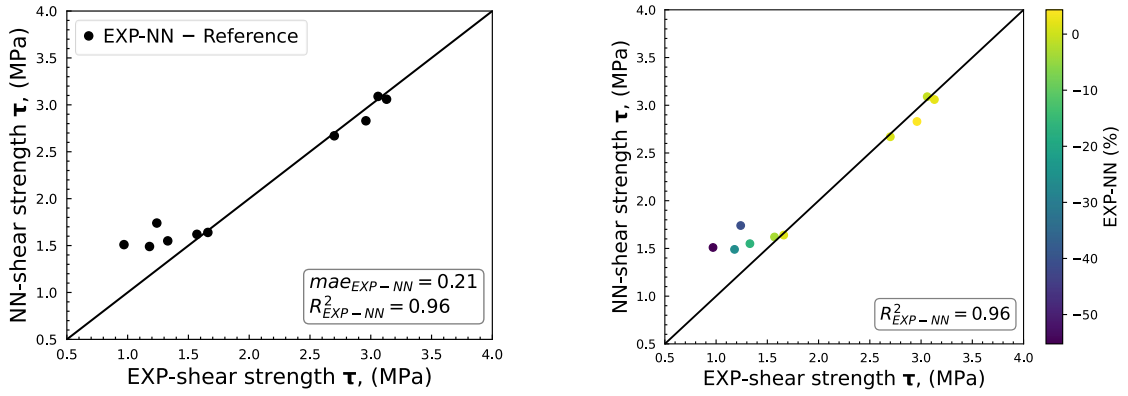

(a) **(b)**

Figure 3.22 Assessment of the neural network model: a) Experimental vs. estimated peak shear strength (0.5 and 1.5 MPa) and b) Percent error between the Experimental and the estimated peak shear strength

3.6 **Discussion: analytical and neural network model**

Figure 3.23 shows the results of estimating the peak shear strength of concrete-rock interfaces using the analytical and neural network models. The correlation coefficient between the estimated peak shear strength and the finite element simulated peak shear strength is 0.91 and 0.90 for the analytical model considering the two failure modes and 0.96 for the neural network model (validation dataset). The performance of both the failure criterion and the neural network model is very high (above 0.85), with the neural network results slightly better than those of the analytical model.

Figure 3.24 shows the error in the estimation of the peak shear strength in terms of the roughness parameter $\theta^*_{\max}/(C+1)$. This error is approximatively between -20% and 20% for both the analytical model and the neural network model.

Moreover, Figure 3.24 also shows that, unlike the analytical model, estimating the shear strength through the neural network model reproduces the non-bijective relationship peak shear strength/roughness observed in the results of finite elements simulation of direct shear tests of synthetic rock surfaces (see section 3.2). Another advantage of neural network modeling is that there is no need to train two models to consider the failure modes. This is possible because the neural network model can distinguish the failure based only on the dataset.

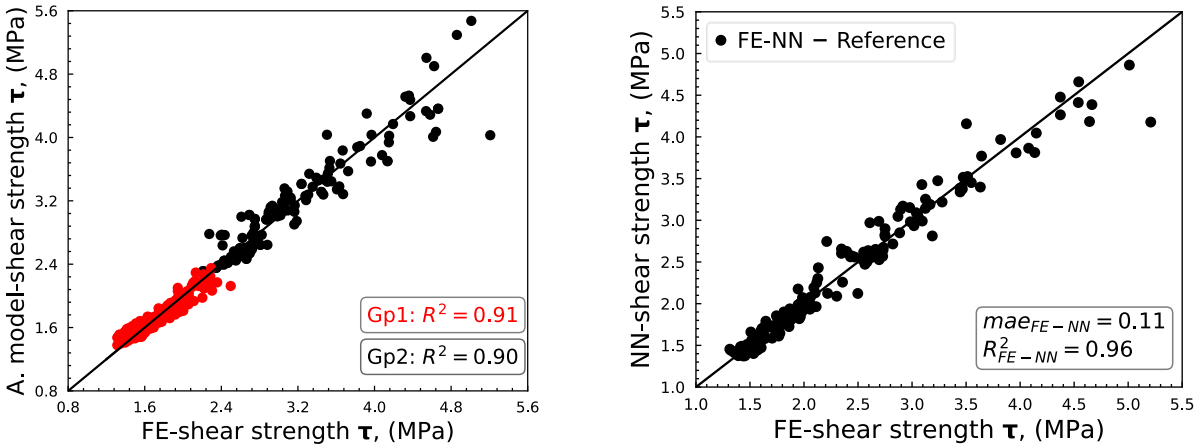

(a) **(b)**

Figure 3.23 Estimation of the peak shear strength (a) Failure criterion (b) Neural network model

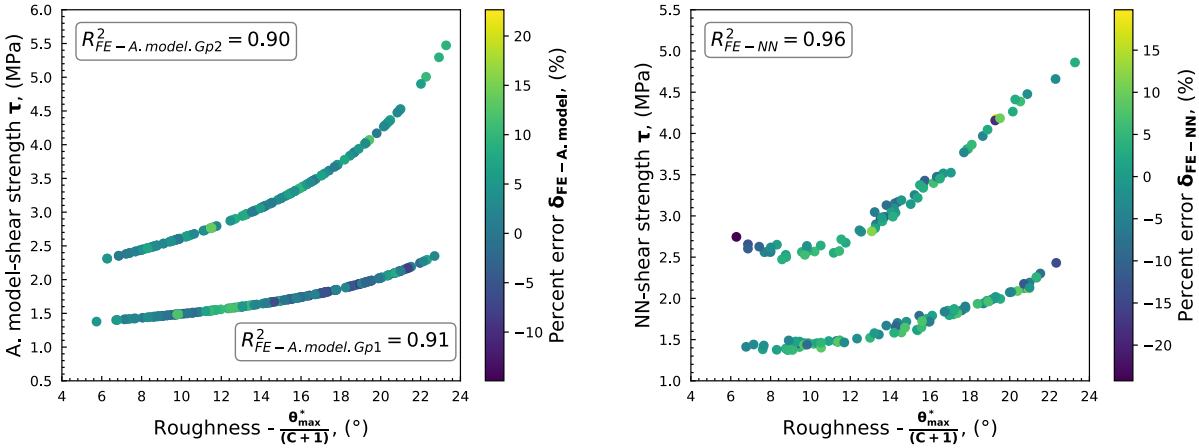

(a) **(b)**

Figure 3.24 Error of the estimation of the peak shear strength (a) analytical model and (b) Neural network model

3.7 **Neural network-based estimation of the shear response of concrete-rock interfaces**

Failure criteria are limited to estimating the peak or the residual shear strength of rock-rock and concrete-rock interfaces. However, estimating the overall shear responses of these interfaces provides more understanding of the shear behavior.

Not many works have focused on estimating the overall shear responses of rock-rock and concrete-rock interfaces. Grasselli and Egger (Grasselli and Egger, 2003) proposed a constitutive law to estimate the evolution of the shear stress of rock-rock interfaces in terms of the shear displacement (Eq. (3.16)). However, the proposed relationships require a knowledge of the peak and residual shear strength, which reduces their relevance since, in most geotechnical problems, it is more interesting to estimate the peak and the residual shear resistance of interfaces before failure.

$$\begin{cases} \dfrac{\tau}{\sigma_n} = 0, & 0 \le u \le u_m \\ \dfrac{\tau}{\sigma_n} = k_s(u - u_m) = \dfrac{1}{\Delta u_p}\dfrac{\tau_p}{\sigma_n}(u - u_m), & u_m \le u \le u_p \\ \dfrac{\tau}{\sigma_n} = \dfrac{\tau_r}{\sigma_n} + \dfrac{\tau_p - \tau_r}{\sigma_n}\dfrac{u_p}{u}, & u \le u_p \end{cases} \quad (3.16)$$

where τ is the shear stress, τ_p is the peak shear strength, τ_r is the residual shear strength, σ_n is the normal stress, u is the shear displacement or horizontal displacement, u_m is the horizontal displacement to mate the two rock slabs during a direct shear test, u_p is the peak shear displacement, Δu_p is the horizontal displacement before the peak and k_s is the shear stiffness.

The problem of developing a methodology to estimate the overall shear responses of interfaces is addressed in this study. Differently from the model proposed by Grasselli and Egger (Grasselli and Egger, 2003), the possibility of proposing an alternative requiring parameters similar to those used in failure criteria is investigated. For this reason, a neural network model is evaluated to estimate the shear responses of concrete-rock interfaces submitted to lower normal loadings (0.5 and 1.5 MPa). The neural network model uses the database of shear responses of simulations of shear tests of concrete-rock interfaces (see section 3.2).

3.7.1 **Neural network modeling for the prediction of the shear response of concrete-rock interfaces**

The neural network model is set as a function f_{NN} which receives as input the normal stress (σ_n), the basic friction angle (Φ_b) and the roughness parameter $\theta^*_{max}/(C+1)$ and predicts the shear stress with the associated shear displacement $\left[[\delta_{s1}, \dots, \delta_{si}], [\tau_{s1}, \dots, \tau_{si}]\right]$, see Eq.(3.17).

$$f_{NN} : \left\{\sigma_n, \Phi_b, \frac{\theta^*_{max}}{(C+1)}\right\} \rightarrow \left\{\left[[\delta_{s1}, \dots, \delta_{si}], [\tau_{s1}, \dots, \tau_{si}]\right]\right\} \quad (3.17)$$

where τ_{si} is the shear stress at the instant "i" and δ_{si} is the associated shear displacement.

The dataset comprises 334 entries, each composed of the data relative to a single simulation of a shear test of the concrete-rock interface. The data of each simulation contains the normal stress

(σ_n), the basic friction angle (Φ_b), the roughness parameter $\theta^*_{max}/(C+1)$ and a vector composed of 236 shear displacement values followed by 236 corresponding shear stress values.

The hyperparameter analysis is carried out to determine the suitable neural network architecture of the model to estimate the shear responses of concrete-rock interfaces. This hyperparameter analysis is similar to the one used to determine the adequate neural network architecture of the model to estimate the shear strength of concrete-rock interfaces (section 3.4).

After hyperparameter analysis, the ideal neural network model for estimating the shear response of concrete-rock interfaces contains one input layer, six hidden layers, each with 25 neurons, and one output layer that yields a 472-long vector representing the shear displacement and the shear stress. The batch size of 8 entries is selected, and the neural network model is trained using 100 epochs. The result of the hyperparameter analysis is presented in Figure 3.25. The discussions of this analysis are similar to the one presented in section 3.4.

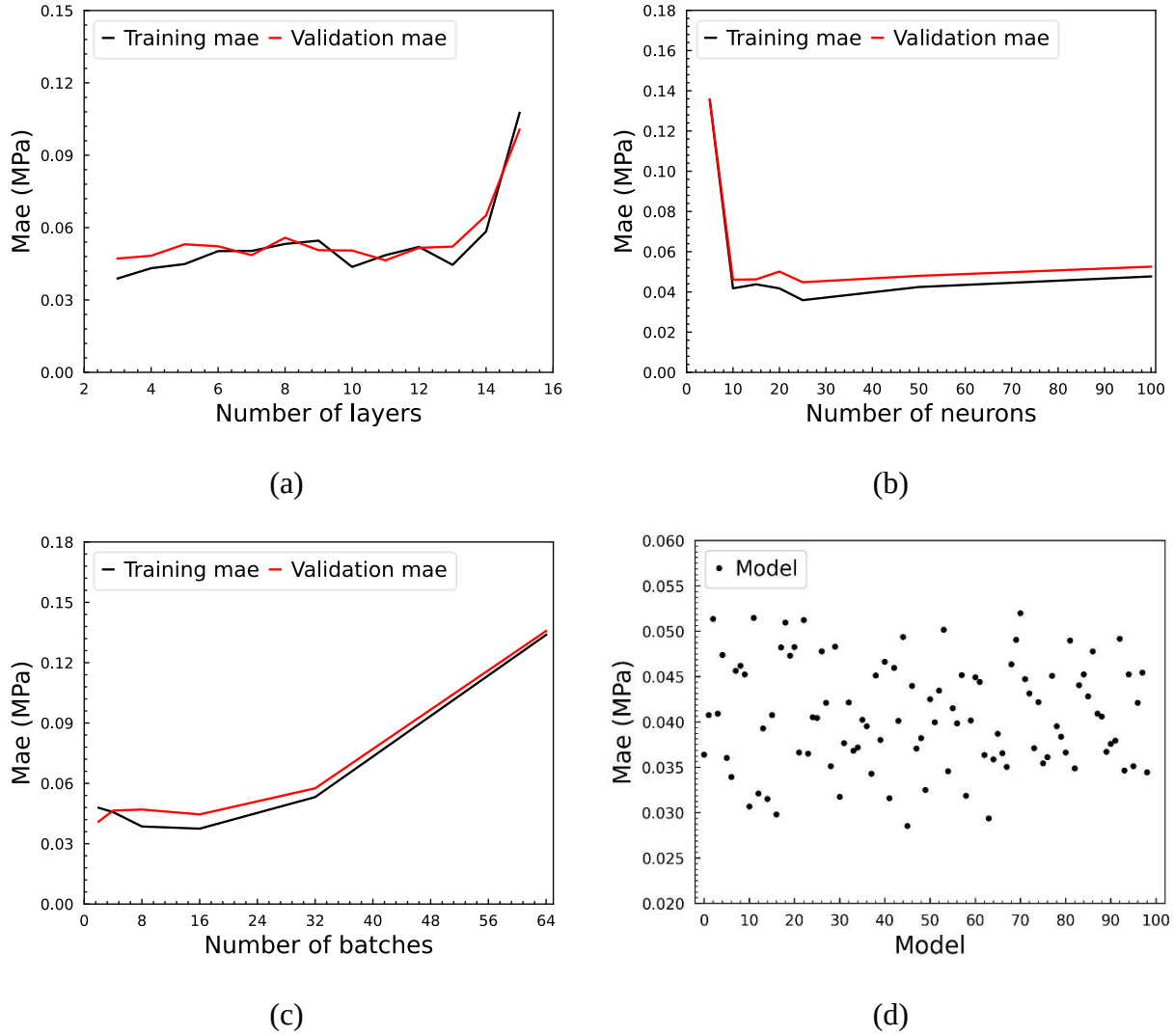

Figure 3.25 Hyperparameter analysis for the neural network model to estimate the shear response of concrete-rock interfaces: (a) Influence of number of layers, (b) influence of the number of neurons per layer, (c) influence of the batch size, and (d) variation of the performance of the model after multiple training

3.7.2 **Results of the neural network modeling to estimate the shear response of concrete-rock interfaces**

3.7.2.1 **Prediction of the peak shear strength using neural network model**

The learning curve of the performance of the neural network model to estimate the shear response of concrete-rock interfaces is presented in Figure 3.26. From this figure, it is clear that the evolution of the performance of the successive neural network models on the training and the validation dataset decreases with the increase in the number of epochs. This observation means that there is no overfitting during the training of the model.

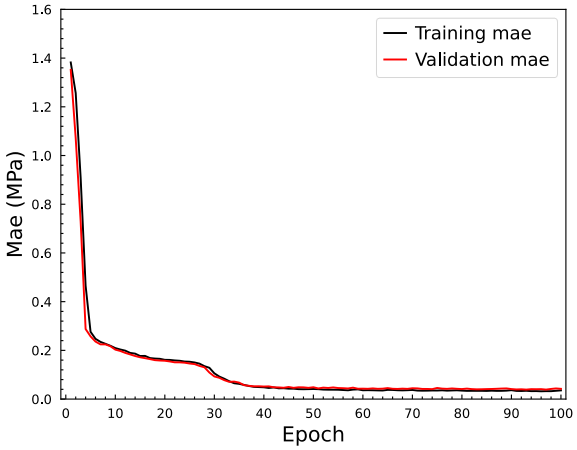

Figure 3.26 Learning curve of the training of the neural network to estimate the shear response of concrete-rock interfaces

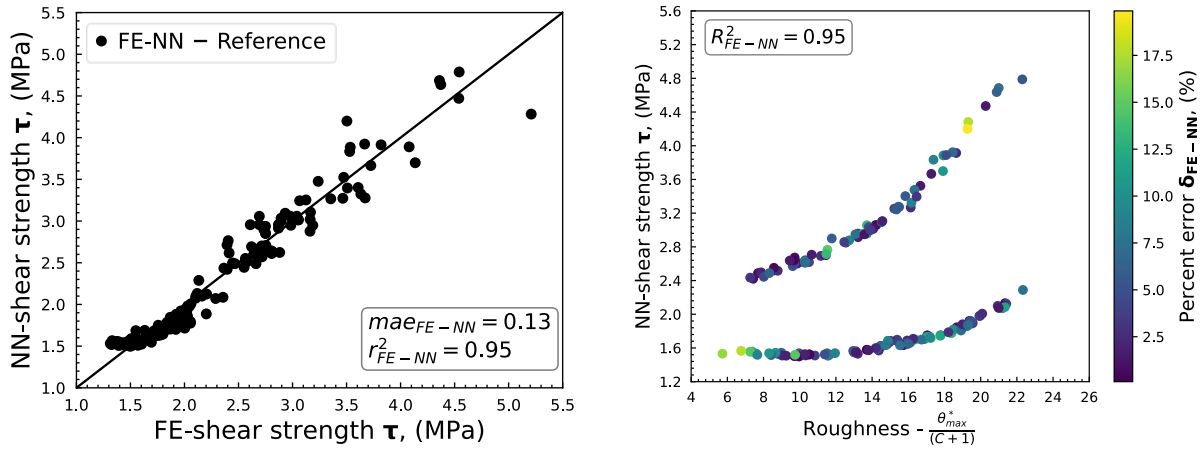

(a) (b)

Figure 3.27 (a) Peak shear strength extracted from the predicted shear response obtained using neural network modeling (validation dataset) in terms of peak shear strength extracted from the shear response obtained using FE simulations and (b) percent error of (a)

Figure 3.27 presents the variation of the peak shear strengths extracted from shear responses predicted by the model in terms of the peak shear strength extracted from the shear response obtained using finite element simulations. A correlation coefficient of 0.95 and an MAE of 0.13 were obtained between the predicted and the simulated peak shear strength, proving that the shear response predicted by the neural network model can reproduce the peak shear strength obtained in the finite element simulation.

3.7.2.2 **Prediction of the peak shear strength obtained experimentally using neural network model**

The experimental results used in this analysis are parts of the work performed by El Merabi (El Merabi, 2018). These results are reviewed in section 1.3.2 and discussed in chapter 2.

Figure 3.28 presents the peak shear strength extracted from the shear response predicted by the neural network in terms of the peak shear strength obtained experimentally. A correlation coefficient of 0.96 was obtained between the predicted and the experimentally obtained peak shear strength. However, this high correlation coefficient should be taken cautiously, given the size of the dataset.

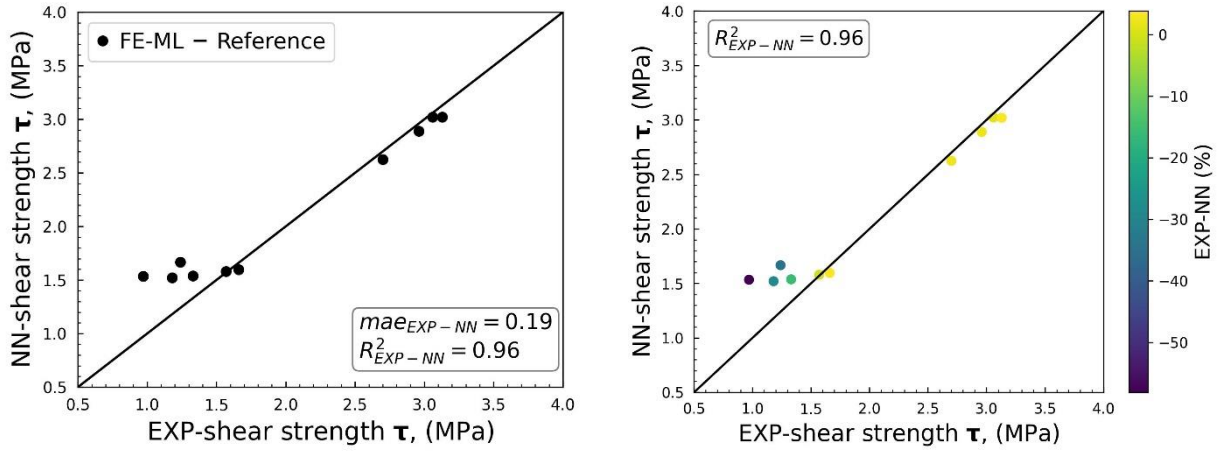

(a) (b)

Figure 3.28 Peak (a) Peak shear strength extracted from the predicted shear response obtained using neural network modeling (Experimental) in terms of peak shear strength obtained experimental tests (b) percent error of (a)

3.7.2.3 **Prediction of the shear response using the validation dataset**

Examples of the neural network prediction of the shear responses of the direct shear test of concrete-rock interfaces using the validation dataset are presented in Figure 3.29 and Figure 3.30, along with the shear responses obtained using finite element simulations. From these figures, it is clear that the predicted shear response reproduces the three main stages of the shear evolution: the shear stress accumulation, the shear slip, and the residual shear stage. Furthermore, the peak and the residual peak shear strength obtained are close to their corresponding values obtained via finite element simulations.

Furthermore, from Figure 3.29 and Figure 3.30, it is clear that the higher the roughness of the interface expressed using the Grasselli roughness parameter $\theta^*_{max}/(C+1)$, the more resistant the interface. This observation highlights the influence of roughness on the shear response of concrete-rock interfaces when the normal stress is low.

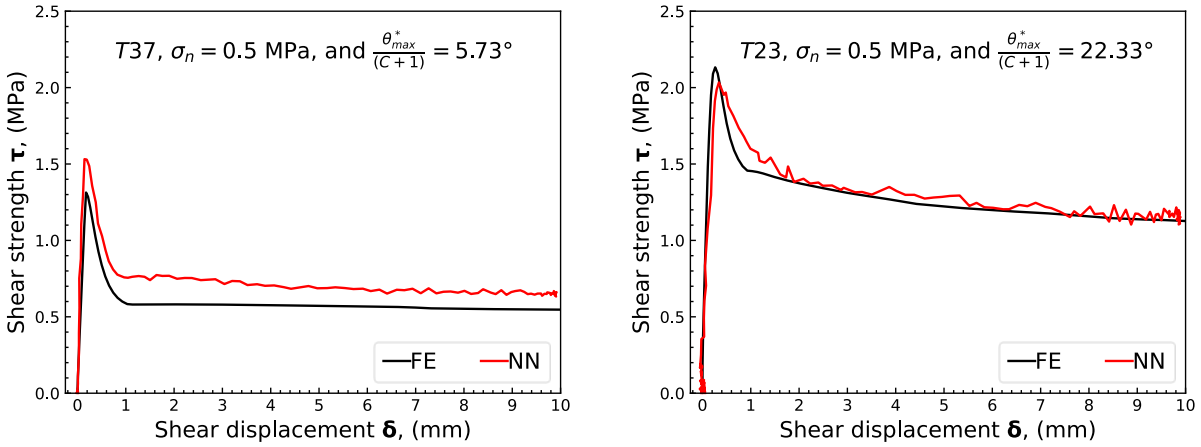

(a) (b)

Figure 3.29 Comparison between the predicted and the numerically obtained shear responses of concrete-rock interfaces using NN and FE simulation: (a) T37 and (b) T26

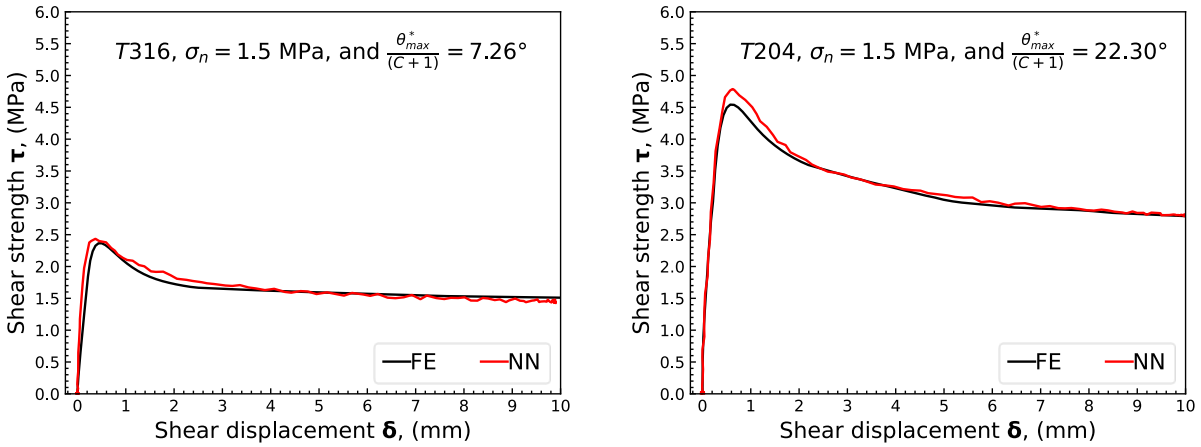

(a) (b)

Figure 3.30 Comparison between the predicted and the numerically obtained shear responses of concrete-rock interfaces using NN and FE simulation: (a) T239 and (b) T261

3.7.2.4 **Prediction of the shear response using the experimental data**

The comparison between the shear responses predicted by the neural network and those obtained in experimental tests are presented in Figure 3.31 to Figure 3.35. It is worth noting here that the results of the experimental studies used in this analysis are part of the experimental campaign

carried out by El Merabi (El Merabi, 2018). This experimental study is reviewed in section 1.3.2 and discussed further in chapter 2. These figures show that the predicted shear response captures the three parts of the shear evolutions and presents encouraging results in reproducing the peak and the residual shear strength of interfaces, which is interesting, given that the peak and the residual shear strength are predicted as single points of a 472-long vector.

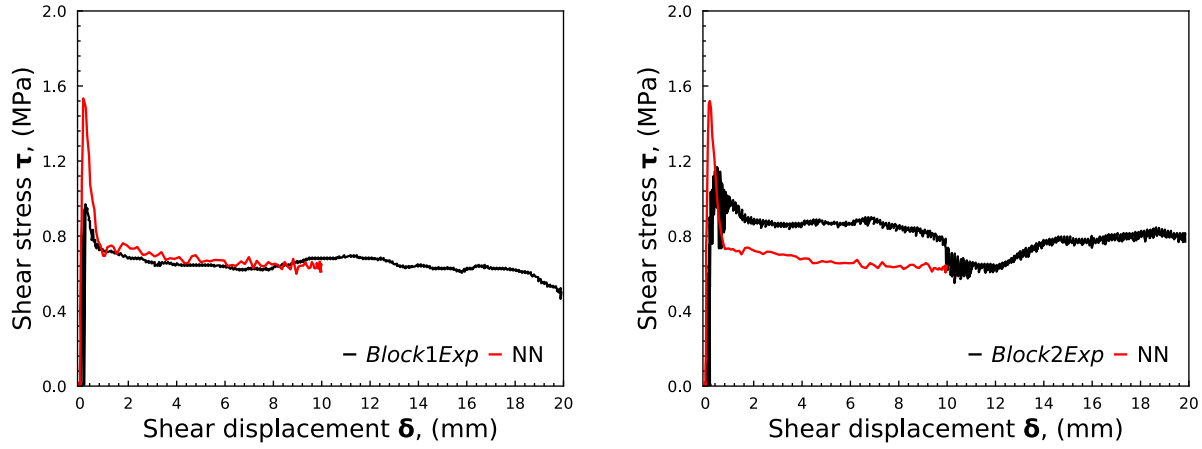

(a) (b)

Figure 3.31 Comparison between the predicted and the experimentally obtained shear responses of concrete-rock interfaces using NN and tests: (a) Block 1 and (b) Block 2

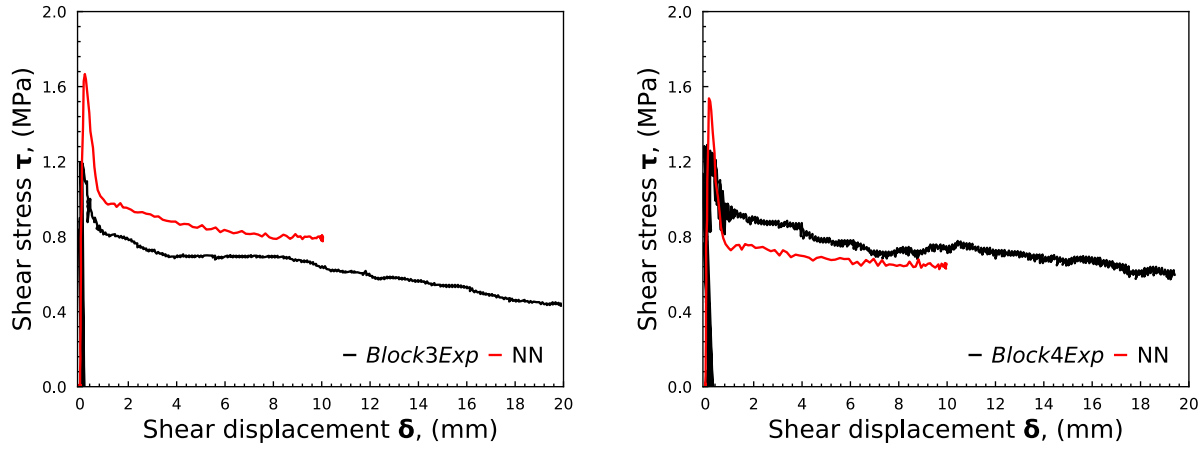

(a) (b)

Figure 3.32 Comparison between the predicted and the experimentally obtained shear responses of concrete-rock interfaces using NN and tests: (a) Block 3 and (b) Block 4

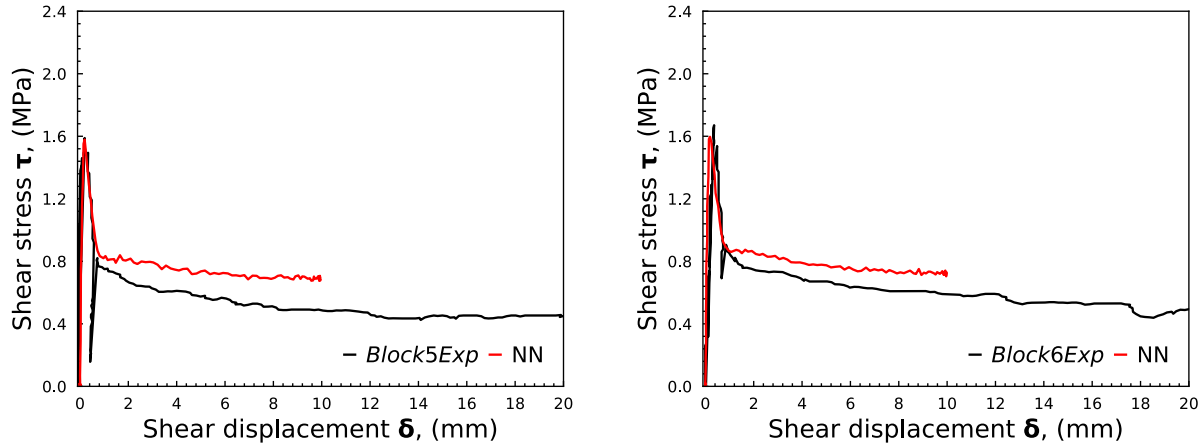

(a) (b)

Figure 3.33 Comparison between the predicted and the experimentally obtained shear responses of concrete-rock interfaces using NN and tests: (a) Block 5 and (b) Block 6

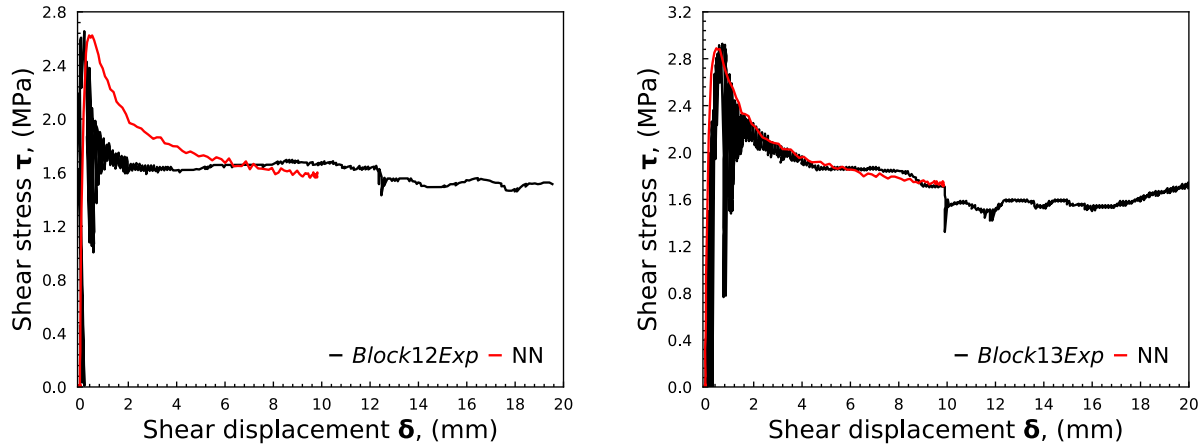

(a) (b)

Figure 3.34 Comparison between the predicted and the experimentally obtained shear responses of concrete-rock interfaces using NN and tests: (a) Block 12 and (b) Block 13

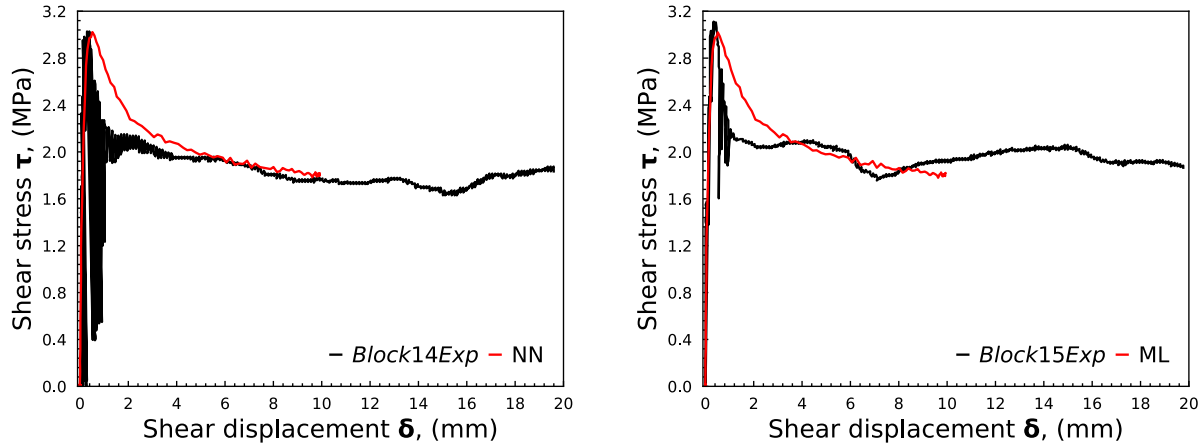

(a) (b)

Figure 3.35 Comparison between the predicted and the experimentally obtained shear responses of concrete-rock interfaces using NN and tests: (a) Block 14 and (b) Block 15

Despite the interesting results obtained in the presented analysis on using neural network modeling to predict the overall shear response of concrete-rock interfaces, some questions remain. One such question is illustrated in Figure 3.36, where the MAE seems to be very low when the entire shear response is used in the assessment (Figure 3.36 legend Model) and is considerably high when only the peak shear strength extracted from the shear response is considered (Figure 3.36 valPeak: validation, ExpPeak: experimental). This discrepancy could be addressed by defining a new evaluation metric that takes the two scales of comparison (overall shear response and only the peak shear strength).

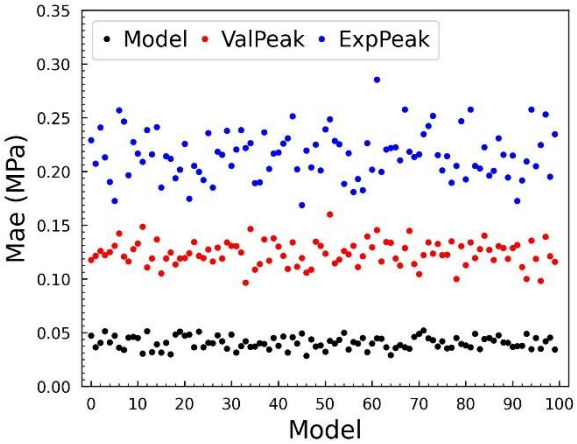

Figure 3.36 Assessment of the MAE: computed using the comparison between the overall shear responses predicted and the FE shear responses obtained (model), calculated using the peak shear strength extracted from the predicted shear response and the peak shear strength obtained via FE simulation (validation) and Experimental tests (ExpPeak**)**

The results obtained in sections 3.4 and 3.7 set the neural network modeling as a suitable methodology for estimating the shear strength and responses of interfaces. However, it is worth noting that improvement in the finite element simulations, the number and the variety of interfaces simulated, and the availability of more experimental results encompassing different types of rocks and different classes of roughness can increase the range of application of the neural network models.

3.7.3 **Comparative analysis of the neural networks models**

Figure 3.37 shows the performance of the neural network models on the validation dataset. It is worth noting that the neural network model used in Figure 3.37 (a) is designed to predict the peak shear strength (for more discussion, refer to sections 3.4, 3.5, and 3.6). Meanwhile, the neural network model used in Figure 3.37 (b) predicts the overall shear evolution of the interface, which means the peak shear strength and the associated shear displacement are but two values in a prediction vector with 472 elements.

The Mae and the correlation coefficient of both models show that the two models have a good performance on the validation dataset (low Mae and high R^2). However, it is clear that the prediction of the model designed to predict only the peak shear strength outperforms the model that predicts the overall shear responses.

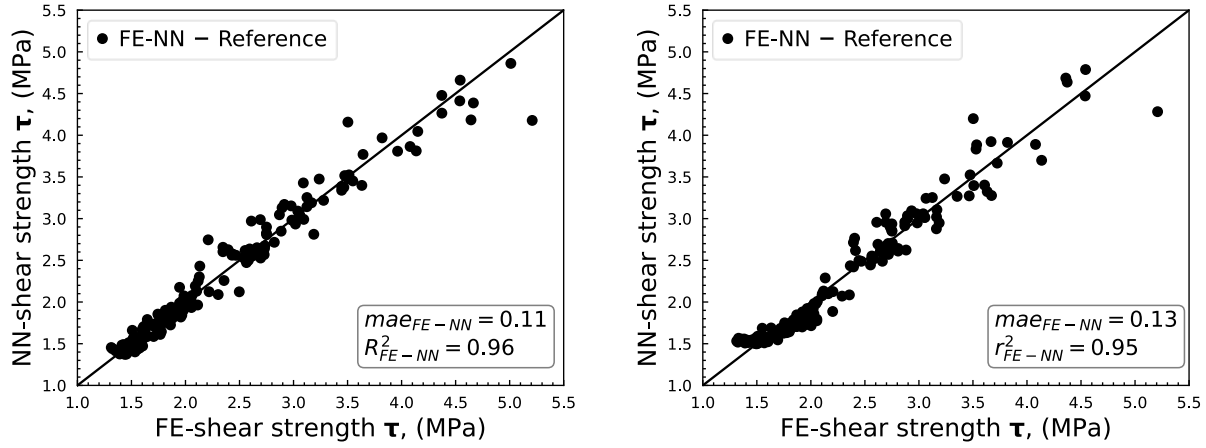

(a) (b)

Figure 3.37 Peak shear strength obtained through neural networks models (validation dataset) in terms of peak shear strength extracted from the shear response obtained using FE simulations: (a) Model that estimates the peak shear strength (section 3.4, 3.5, and 3.6), (b) Model that estimates the overall shear response

Furthermore, it is well known that the training of neural networks does not yield the same model when repeated. The difference between the generated models is due to the random initialization of the backpropagation algorithm and the random shuffling of the dataset before separating into the training and the validation datasets. For this reason, a further analysis of the two neural network models was carried out. The goal of this analysis is to assess the robustness of the models when the training is repeated. To achieve this goal, the training of both models was repeated 100 times, and the performance of the model obtained was assessed using the validation dataset. However, it

is worth noting that the training of the model that predicts the overall shear responses was assessed regarding the overall shear responses and the peak shear strength.

Figure 3.38 shows the results of this analysis. From Figure 3.38, it is clear that the Mae of the model that predicts the overall shear response of the interface is quite low, around 0.05 MPa, when one uses the overall shear responses in the computation of the Mae. However, if one considers only the peak shear strength from the overall shear responses predicted, the Mae obtained is quite high (0.10 to 0.20 MPa) and more dispersed compared to the Mae of the model designed to predict only the peak shear strength (0.10 to 0.14MPa). Despite these differences, the two models have proven an interesting alternative to failure criteria in the problematic of the estimation of the characteristics of the shear evolution of interfaces.

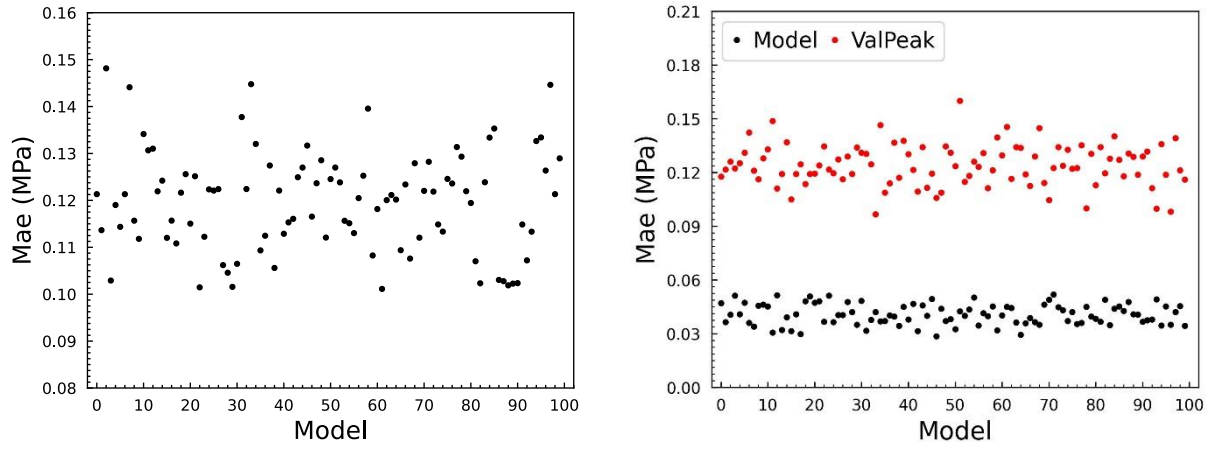

(a) (b)

Figure 3.38 Assessment of the MAE (a) Model that estimates the peak shear strength (sections 3.4, 3.5, and 3.6), (b) Model that estimates the overall shear response

3.8 **Concluding remarks**

This chapter presents a new approach to investigating the influence of roughness on the shear resistance of concrete-rock interfaces. The new approach is tailored to reducing the shortcomings of existing failure criteria caused by the challenge of defining a sufficiently diverse and well-distributed database of rough rock surfaces and performing many shear tests. The approach is presented using the influence of roughness on the shear resistance of rough concrete-granite interfaces under low normal loading as a case study.

The new approach consists of three principal steps. The first step is the generation of many synthetic rough rock surfaces with desired roughness values using random field simulations. The second step is the simulation of direct shear tests using the synthetic rough rock surfaces generated. The last step is analyzing the result of the simulations of direct shear tests of the virtually tested synthetic interfaces and the definition of appropriate models to estimate the shear resistance of interfaces.

The proposed new investigative approach has achieved new insights into the influence of roughness on the shear resistance and shear evolution of concrete-rock interfaces submitted to low normal loading. The shear responses of interfaces with similar roughness values do not result in

similar shear resistances. The reason for the variation of the shear resistances of interfaces with similar roughness values is hypothesized as a consequence of the inability of existing roughness parameters to consider the local aspect of roughness on the overall shear responses. Neural network modeling has been shown as a valid alternative to estimate the shear resistances and the shear response of interfaces. Unlike the classical analytical models, the neural network model can reproduce the non-bijective nature of the relationship between the roughness and the peak shear strength.

4. Static and dynamic shear resistance of concrete-rock interfaces

This chapter aims to investigate the dynamic shear behavior of concrete-rock interfaces. The motivation behind this experimental research is the possibility of geotechnical structures with concrete-rock interfaces to experience dynamic shear loading during their lifetime.

However, investigating the dynamic shear behavior of interfaces between geomaterials is very complex. Different possible wave sources can generate dynamic shear loading. Possible wave sources include seismic, earthquake, impact, explosion, and blasting. Each source generates waves with different properties: P and S waves, interface waves, frequency, and amplitude (Zhang and Zhao, 2014). Furthermore, wave propagation in geotechnical structures will not necessarily focus on the interface between geomaterials. For example, in geotechnical structures comprising concrete and rock, other structures in the rock and the concrete can also be affected. For example, properties such as the porosity of concrete and the discontinuities in the rock mass can affect the overall dynamic response of the structure.

Considering these difficulties, this study focuses on the dynamic shear behavior of concrete-rock interfaces under lower normal loadings. The impact generates dynamic shear loading. The impact loading of interest in this study is the one that is capable of generating a high strain rate. Furthermore, this study is limited to the dynamic shear testing of only concrete-rock interfaces.

Moreover, it is worth noting that this experimental study includes tests of concrete rock interfaces under static loading. The main reason for performing these static shear tests is to generate a fair comparison base between the static and the dynamic shear behavior of concrete-rock interfaces. Such a fair base is necessary to eliminate the effect of the size and geometry of the sample and to have static and dynamic tests performed using the same confinement system.

The methodology used in the dynamic shear tests performed in this study is based on the work conducted by Abdul-Rahman (Abdul Rahman, 2018). This methodology maintains the two steps of the direct shear tests reviewed in section 1.3.1. Unlike the direct shear test, the dynamic shear loading is generated by impact using a split Hopkinson pressure bar (SHPB) system. A confinement ring is used to apply the confinement stress. The use of the confinement ring is justified by the necessity of using a confinement system adequate for the high strain rate nature of the dynamic test and compatible with the SHPB system. The confinement ring applies confinement using its elastic deformation. The measurement of the normal stress is carried out using strain gauges attached to the confinement ring. The use of the confinement ring to apply normal stress leads to a definition of a sample composed of two rock slabs at the extremities between which concrete is cast. Therefore, for each test, two concrete-rock interfaces are tested. The use of this sample geometry also justifies the composition of the SHPB. The SHPB used in this study comprises an input bar in contact with the concrete part of the sample and two output bars in contact with the rock parts of the sample. This configuration allows the processing of the shear response of each interface separately. The methodology for the static shear test is similar to the one used in the dynamic shear test, except the static shear loading is applied using an electromechanical press. The samples used in the static shear tests are equal to those used in the dynamic shear tests, and the confinement stress in both types of tests is applied using the confinement ring.

Even though this study focuses on the dynamic shear behavior of concrete-rock interfaces, its outcomes might prove useful for investigating the dynamic shear behavior of other interfaces, such as rock-rock and concrete-geopolymer interfaces.

This presentation proceeds in three parts. First, the material and testing methods are presented. Second, an experimental campaign is carried out. Last, the results of the tests performed are discussed.

4.1 **Materials and methods**

4.1.1 **Materials**

Three levels of interface roughness are considered in this experimental study to investigate the influence of each on the shear response. These three levels of interface roughness are the smooth, the bush-hammered, and the rough interfaces. Two types of rocks are considered: sandstone and granite. These two rocks are selected because they represent soft rocks and hard rocks. Combining the effect of interface roughness and rock lithology, the interfaces tested are the smooth concrete-sandstone interfaces, the bush-hammered concrete-granite interfaces, and the rough concrete-granite interfaces.

The rock preparation, the concrete formulation, and the protocol of casting concrete on a rock to form samples with concrete-rock interfaces are presented hereafter.

4.1.1.1 **Rock**

The rock slabs used in the sample preparation have a dimension of 30x30x15 mm^3.

Sandstone slabs with smooth surfaces were obtained using a saw-cut machine. Bush-hammered surfaces were generated by bush-hammering smooth granite slabs. The protocol of this process is presented in El Merabi (El Merabi, 2018). The bush-hammering process is necessary to add micro-roughness or unevenness to smooth granite surfaces to ensure the formation of strong concrete-granite bonds (Badika et al., 2022). Three-point bending loading was used to split granite blocks to generate slabs with rough surfaces. After generating smooth, bush-hammered, and rough surfaces, the opposite face of the block was rectified using a sanding machine such that the two opposed surfaces were parallel at the end (Figure 4.1). This rectification is necessary to ensure the shear plane is parallel to the shear direction.

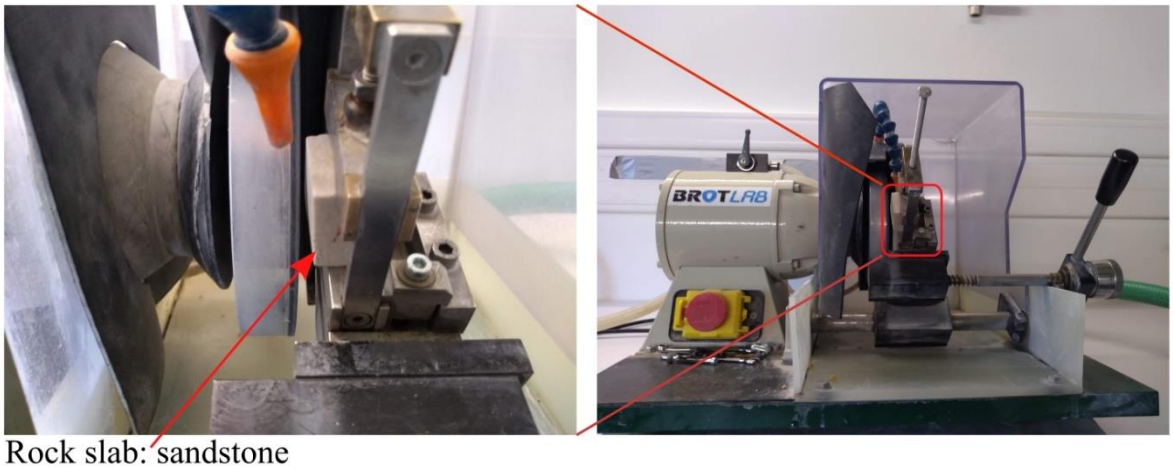

Figure 4.1 Rectification of the rock surfaces using a sanding machine

Before casting concrete, the rock slabs are cleaned and then scanned using the laser-based scanning device developed by Hans and Boulon (Hans and Boulon, 2003) and presented in section 1.2.2. The roughness data were recorded using a point spacing of 0.025 mm.

An illustration of the rocks and the roughness considered is presented in Figure 4.2.

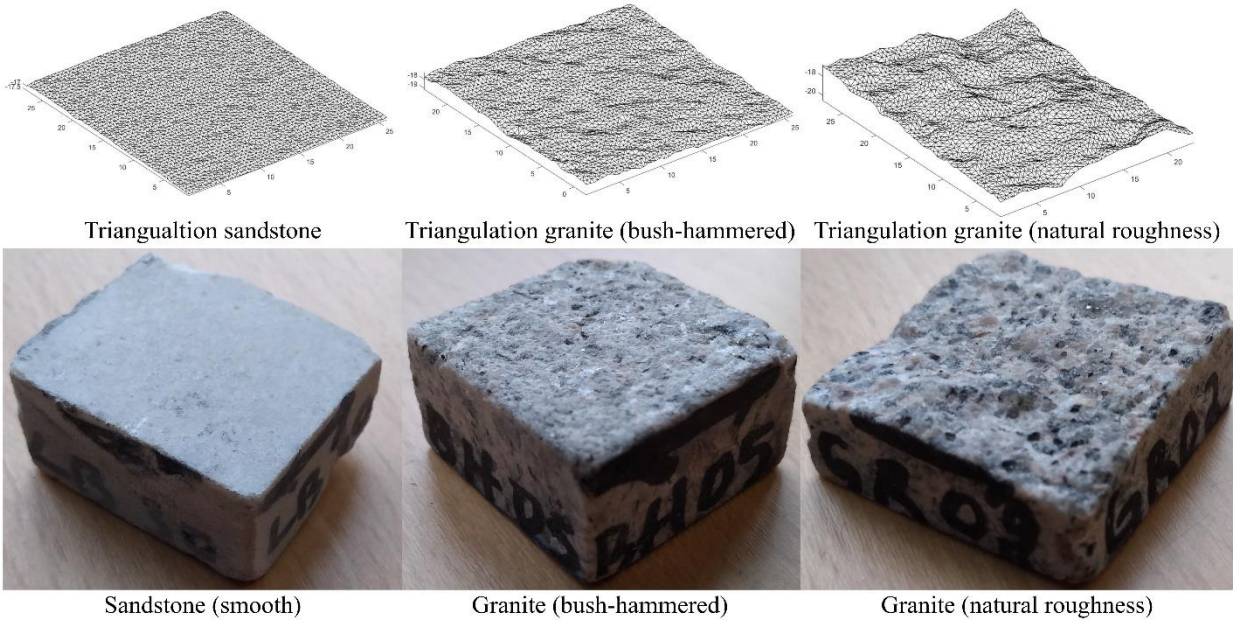

Figure 4.2 Rock slabs and plot of triangulations of the field of heights of asperities to illustrate the difference in roughness level.

The fields of heights of asperities collected from scanning rock surfaces were used for roughness characterization using the Grasselli roughness parameter $\theta^*_{max}/(C+1)$. The maximum, minimum, and average roughness values of smooth sandstones, bush-hammered, and rough granite surfaces are reported in Table 4.1.

Table 4.1 Roughness characterization of rock surfaces

Roughness parameter	$\boldsymbol{\theta^*_{max}}$ $\boldsymbol{/(C+1)}$		
	Max (°)	Min (°)	Average (°)
Smooth concrete-sandstone	4.1826	2.2946	3.0889
Bush-hammered concrete-granite	8.5229	6.7343	7.6631
Rough concrete-granite	16.4642	13.0017	14.2936

4.1.1.2 **Concrete**

The formulation of the concrete used is the R30A7. This concrete composition is ideal for laboratory scale studies where the sizes of samples are usually small. Several experimental works have studied the mechanical properties of this concrete composition. Gabet et al. (Gabet, Malécot and Daudeville, 2008), Piotrowska et al. (Piotrowska, Forquin and Malecot, 2016), and Vu et al. (Vu et al., 2009) carried out experimental studies to investigate the compressive behavior of R30A7 submitted to high confinement stress, Erzar and Forquin (Erzar and Forquin, 2014) investigated

the tensile behavior of R30A7, and Forquin and Sallier (Forquin and Sallier, 2013) studied the shear behavior of R30A7.

The composition of R30A7 is provided in Table 4.2.

Table 4.2 Concrete formula: R30A7

Composition of concrete mixture	
Aggregates D 0.5/8 mm (kg/m3)	1008
Sand Dmax 1.8 mm (kg/m3)	838
Cement CEM I 52.5 N PM ES CP2 (Vicat) kg/m3	263
Water (kg/m3)	169
Density (kg/m3)	2278

The mechanical properties of the rocks and the concrete R30A7 are provided in Table 4.3.

Table 4.3 Mechanical properties of concrete and rocks (Mouzannar, 2016; Abdul Rahman, 2018; Forquin *et al.*, 2022)

Material	Density (kg/m3)	Compressive strength (MPa)	Young's modulus (GPa)	Poisson's ratio
Concrete	2370	30	38	0.20
Granite	2608	133	60	0.25
Sandstone	2372	71	32	0.20

4.1.1.3 **Concrete-rock sample**

Concrete is cast between two rock slabs, generating a concrete-rock sample. This assembly is left to cure for 28 days at ambient temperature. Once the concrete curing is completed, the sample obtained is submerged in water until the test. The concrete-rock sample obtained is a prism of 30x30x70 mm^3 (Figure 4.3) comprising two concrete-rock interfaces.

Figure 4.3 Example of the sample with two concrete-rock interfaces

4.1.1.4 **Testing program**

For both the static and dynamic tests, 20 samples were prepared. The summary of the testing program is presented in Table 4.4.

Table 4.4 Testing program

Interfaces	Smooth concrete-sandstone	Bush-hammered concrete-granite	Rough concrete-granite
Static tests	4	2	2
Dynamic tests	5	4	3

4.1.2 **Methods**

4.1.2.1 **Operation of the confinement ring**

Using the SHPB to apply the shear loading necessitates defining a specific confinement system to apply the normal loading. For this purpose, the confinement ring proposed by Abdul-Rahman (Abdul Rahman, 2018) was selected. This choice was motivated by the simplicity of use.

Applying the normal loading using the confinement ring proceeds in three phases (Figure 4.4). First, the ring is deformed elastically by applying a force F_z using an electro mechanical press. Second, the sample with concrete-rock interfaces is inserted into the dilated ring, and the eventual gap is filled with metal sheets. And last, the force F_z is released, and the ring, unable to recover its original state, applies the normal load to the concrete-rock interfaces with a force F_X. From this procedure, it is clear that the basic idea behind using the confinement ring is to deform the ring and use the elastic energy to apply confinement loading to the sample.

The confinement ring was proposed by Abdul-Rahman (Abdul Rahman, 2018) to investigate the static and dynamic shear behavior of concrete submitted to high confinement stresses. This is different from the objective of this research, which focuses on the static and dynamic shear behavior of concrete-rock interfaces under lower normal loadings. Therefore, a modification of the confinement ring is necessary.

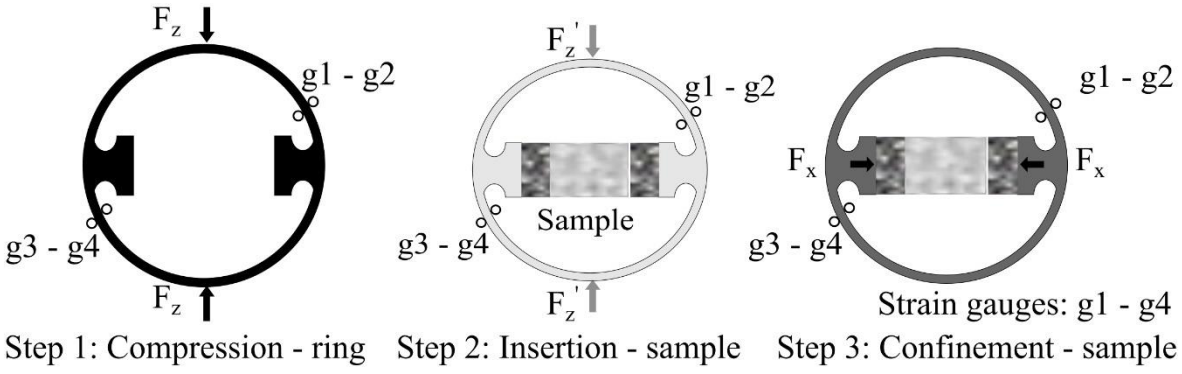

Figure 4.4 Confinement of the sample

4.1.2.2 **Modification of the confinement ring**

Here, a brief presentation of the confinement ring is provided. This presentation focuses on modifying the confinement ring for suitability to generate lower normal loadings. However, a complete discussion of the analytical and numerical method used in the design of the confinement ring is presented by Abdul-Rahman (Abdul Rahman, 2018).

For the modification of the confinement ring, it is necessary to consider three principal aspects. First, it is important to determine the elastic limit of the confinement ring in the direction of the application of the load deforming the ring (z direction in Figure 4.4) and in the direction of the application of confinement stress (x direction in Figure 4.4). Second, it is necessary to define the right geometry of the ring to be able to apply lower confinement stresses. Third, it is necessary to determine the most suitable locations in the ring to measure strain using strain gauges.

To analyze these three aspects, finite element simulations of a quarter of the ring were carried out. The boundary conditions used in these simulations are presented in Figure 4.5.

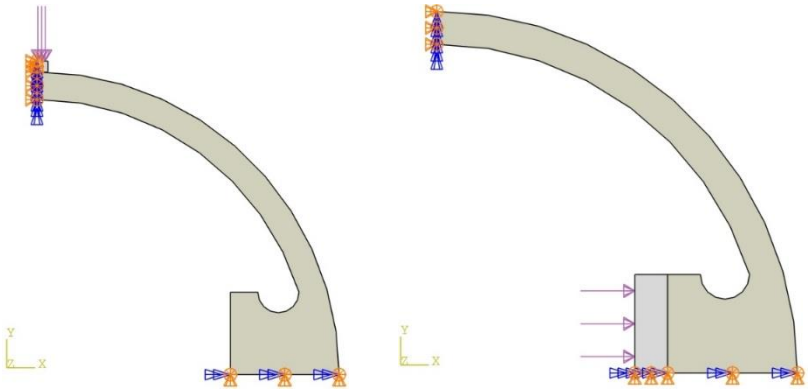

(a) (b)

Figure 4.5 Boundaries conditions used in the simulations to modify the confinement ring: (a) loading the ring, (b) loading the sample

Using these numerical simulations, four rings with varying thicknesses were assessed. The thickness of interest is 5.0 mm, 7.5 mm, 10.0 mm, and 12.5 mm. The rest of the geometry of the ring depends on the pre-existing split Hopkinson pressure bar system at the 3SR laboratory, University Grenoble Alpes, and the considerations of the size of the sample to minimize the inertia effect (Zhang and Zhao, 2014; Xia and Yao, 2015). Other geometrical properties of the confinement ring are presented in Figure 4.6.

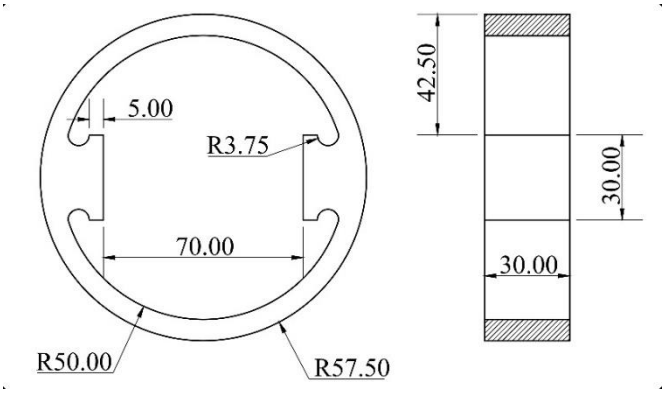

Figure 4.6 Confinement ring

Since the interest in modifying the ring is to obtain high elastic deformation with lower storage of elastic energy, only aluminum was considered in this analysis. The properties of the aluminum used in the simulations are presented in Table 4.5.

Table 4.5 Mechanical properties of Aluminum

Material	**Density (Kg/m^3)**	**Young's Modulus(GPa)**	**Poisson's ratio**
Aluminum	2700	70	0.3

The results of these simulations show that all four confinement rings considered in the analysis can generate lower confinement stress in the sample. Figure 4.7 presents the contour plots of the simulations when all the confinement rings are tested to generate 2 MPa of confinement stress, defined as the upper limit of the range of normal stresses considered in this study.

The hoop strain of the confinement rings when generating 2MPa of confinement stress is plotted in Figure 4.8. This figure shows that the 5.0 and 7.5 mm thickness confinement ring generates high elastic deformation.

Furthermore, from Figure 4.8, it is possible to determine the appropriate location for installing the strain gauges to measure the deformation of the confinement ring. This ideal location is between 15° and 25° along the inside and the outside circumference of the confinement ring. With the consideration of the elastic limit of the rings and the possibility of the increase of the normal stress when testing concrete-rock interfaces with high amplitude roughness, confinement rings with 5.0 and 7.5 mm are selected for this study. The ring with 5 mm thickness is used for tests with initial confinement stress below 1 MPa; for tests with initial confinement stress above or equal to 1 MPa, the confinement ring with 7.5 mm thickness is used.

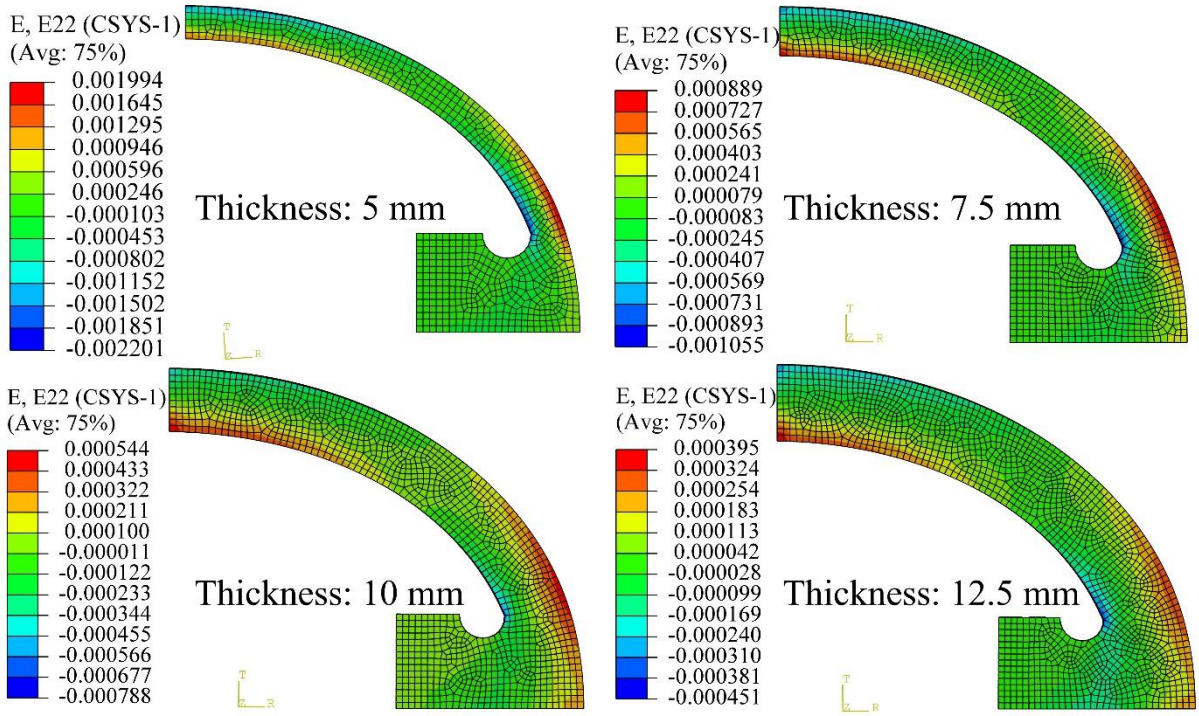

Figure 4.7 Contour plot illustrating the hoop strain in the confinement rings of different thicknesses when generating 2 MPa of confinement stress

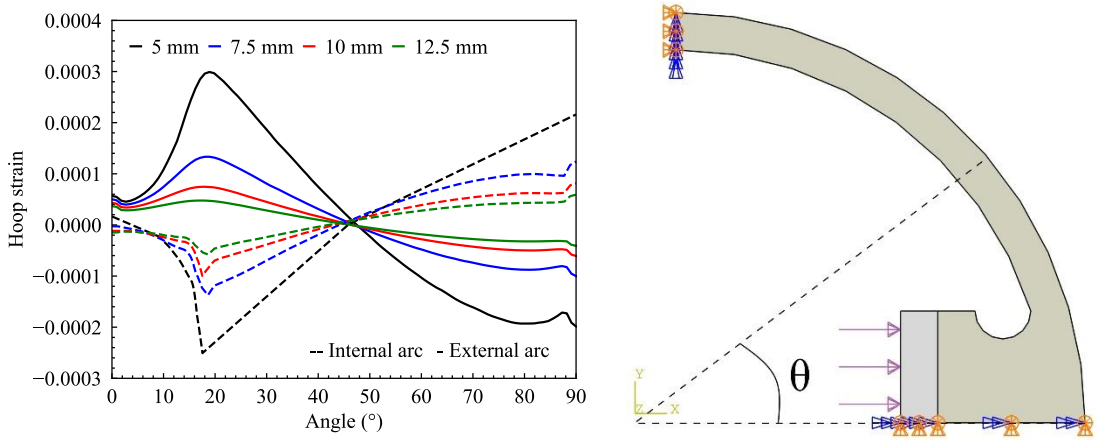

(a) (b)

Figure 4.8 (a) Hoop strain distribution across the outward and the inward circumference of the ring in terms of the angle θ (b) illustration of the angle θ

4.1.2.3 **Calibration of the confinement ring**

Upon reception of the confinement rings from the manufacturer, four strain gauges were attached to each confinement ring at 20° internal and external circumference (Figure 4.9). These strain

gauges were mounted using the quarter bridge configuration. Consequently, the voltage measured by the strain gauges circuit is transformed into strain using Eq (4.1).

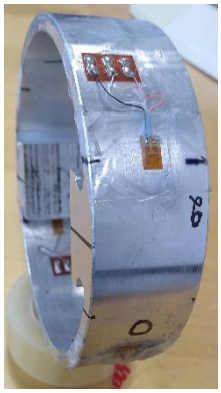

Figure 4.9 Installation of strain gauges

$$\varepsilon = \frac{4}{KGV_{EX}} \Delta V_{measured} \qquad (4.1)$$

where ε is the strain in the confinement ring, K is the gauge factor, V_{EX} is the excitation voltage, and $\Delta V_{measured}$ is the voltage recorded by the strain gauge circuit.

It is worth noting that the strain gauges used in this study are the 2 mm long FCAB-2-23 (K=2.11).

For the calibration (Figure 4.10), the confinement ring is loaded with the force F_Z in the direction of the application of the loading to deform the ring elastically and in the direction of the application of the normal load F_X to the concrete-rock interface (x direction in Figure 4.10.). These two loading conditions yield the correspondence relationships (Eq (4.2) and Eq (4.3)) between the loading applied to the ring F_Z or applied by the ring F_X and the strain due to the deformation of the ring ε_i.

$$\varepsilon_i = \beta_i F_Z \qquad (4.2)$$

$$\varepsilon_i = \alpha_i F_X \qquad (4.3)$$

Combining Eq (4.2) and Eq (4.3) yields the relationship necessary for the computation of the confinement stress applied to the interfaces, Eq (4.4). A more detailed mathematical formulation and operations of the ring can be found in Forquin et al. (Forquin, Abdul-Rahman and Saletti, 2022) and Abdul-Rahman (Abdul Rahman, 2018)

$$\varepsilon_i = \alpha_i F_X + \beta_i F_Z \qquad (4.4)$$

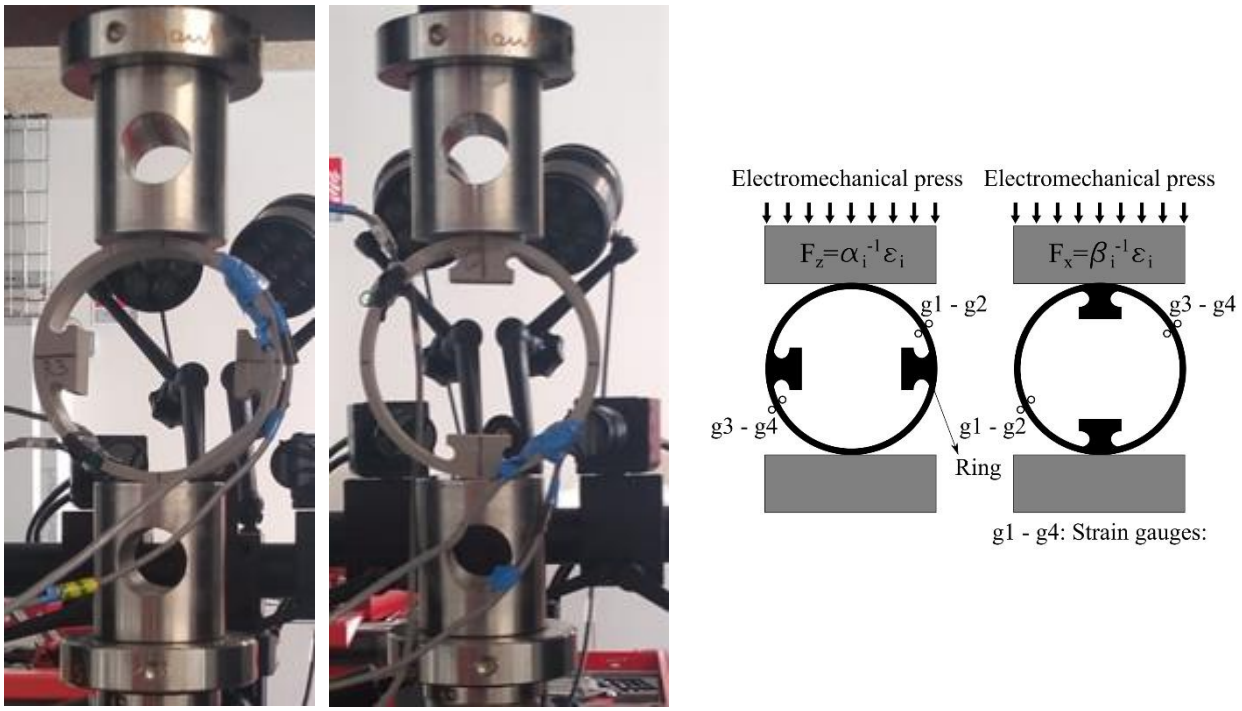

Figure 4.10 Calibration of the ring

The coefficient of correlations α_i and β_i are determined by plotting the calibration curves (Figure 4.11). Using these correlation coefficients and the relationship Eq (4.4), the confinement stress that the ring applies to the concrete-rock interfaces can be monitored before, during, and after the shear test. This measurement is valid for the test conducted using static or dynamic conditions.

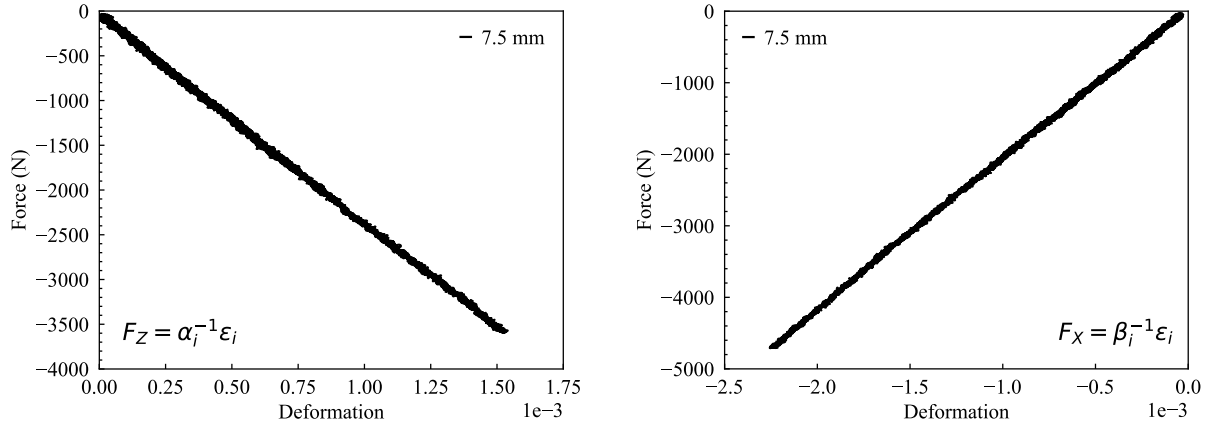

(a) (b)

Figure 4.11 Calibration curves for the confinement ring with 7.5 mm thickness (g1)

The coefficients α and β determined during the calibration of the rings with 5.0 mm and 7.5 mm of thickness are shown in Table 4.6.

Table 4.6 Gauges coefficient after calibration

Stain gauges	Coefficient	Ring 0.5 mm thick	Ring 7.5 mm thick
Gauges g1	$\alpha 1$	- 0.97E-06	-0.43E-06
	$\beta 1$	1.05E-06	0.48E-06
Gauges g2	$\alpha 2$	1.15E-06	0.55E-06
	$\beta 2$	-1.05E-06	-0.50E-06
Gauges g3	$\alpha 3$	-1.00E-06	-0.43E-06
	$\beta 3$	1.10E-06	0.48E-06
Gauges g4	$\alpha 4$	1.11E-06	0.52E-06
	$\beta 4$	-1.01E-06	-0.44E-06

4.1.2.4 **Static shear test**

a) Test setup

The shear test setup in static conditions maintains the basic concepts of the direct shear test presented in section 1.3.1. The confinement stress is applied using the presented confinement ring, and the shear loading is applied using the electromechanical press. During the test, the confinement stress is monitored using the deformation of the ring recorded using the strain gauges (Eq (4.4)).

The shear tests under static conditions are performed using a 0.2 mm/min velocity. This value is adopted from the suggestion of the ISRM (International Society of Rock Mechanics) regarding the shear tests of rock-rock interfaces under static loading (Muralha et al., 2014). The test is concluded when a shear displacement of 3 mm is attained. This displacement is sufficient to ascertain a shear failure at both concrete-rock interfaces and that shear evolution has reached a post-peak phase.

An Instron 100kN is the electromechanical press used.

Figure 4.12 illustrates the shear test setup under static conditions.

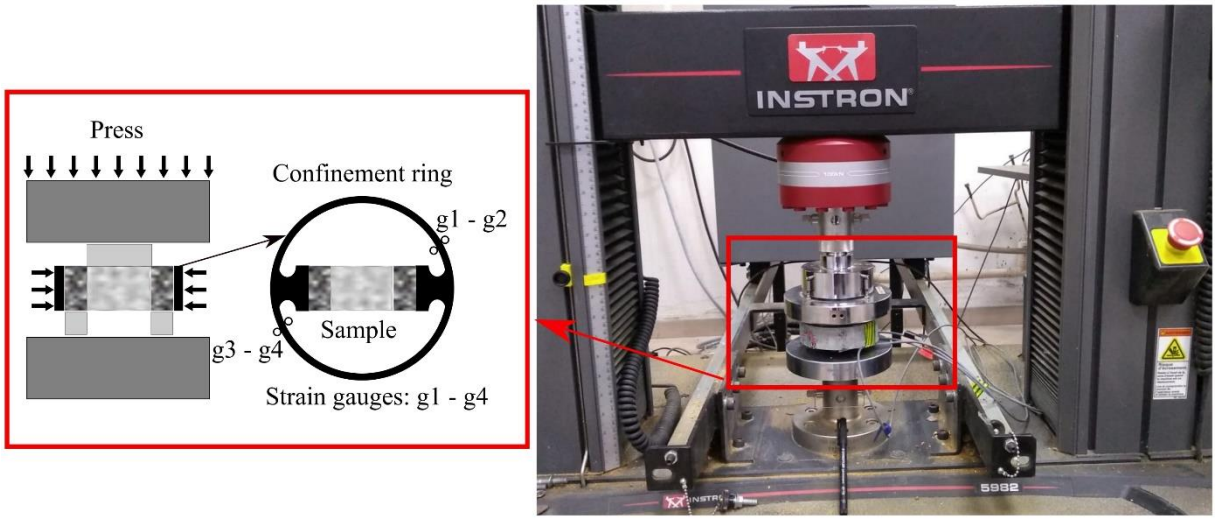

Figure 4.12 Static shear test setup

b) Computation of the static shear response

The average shear response of both interfaces is computed using the applied shear loading and the sum of the two areas of the interfaces. This computation is carried out according to Eq. (4.5).

$$\tau_{shear}(t) = F_{axial}(t)/S_{int} \quad (4.5)$$

where $\tau_{shear}(t)$ is the average shear stress at both interfaces, $F_{axial}(t)$ is the applied shear force, S_{int} is the area of the interfaces.

The confinement stress is computed using the data recorded in the strain gauges using Eq (4.4). and the coefficient of correlation α_i and β_i determined during the calibration of the ring.

4.1.2.5 **Dynamic shear test**

a) Test setup

Figure 4.13 shows the shear test setup under dynamic conditions. Abdul-Rahman et al. (Abdul-Rahman, Saletti and Forquin, 2021) previously used this test setup to investigate the dynamic shear behavior of concrete under high confinement stress. The dynamic shear test of concrete-rock interfaces is similar to the static shear test presented, and the only difference is the technique used to apply the dynamic shear loading. The split Hopkinson pressure bar system is used to apply the shear loading (SHPB). The SHPB used comprises one input bar and two output bars. The material used for the bars is an aluminum alloy. A 1200 mm long bar with a diameter of 45 mm is set as the input bar. The output bars are 1200 mm long and have a 20 mm diameter. The projectile used in this setup is also made of aluminum; it is 370 mm long and has a 45 mm diameter. A gas gun is used to launch this projectile through a steel barrel. The stress wave generated when the projectile impacts the input bar is recorded using two sets of strain gauges mounted in full bridge and attached in two locations at the input bar (g7 and g8 in Figure 4.13). The conversion of the recorded voltage to strain is carried out using Eq (4.6). The transmitted stress wave is recorded in the output bars using a set of strain gauges mounted in a full bridge (g7 and g8 in Figure 4.14).

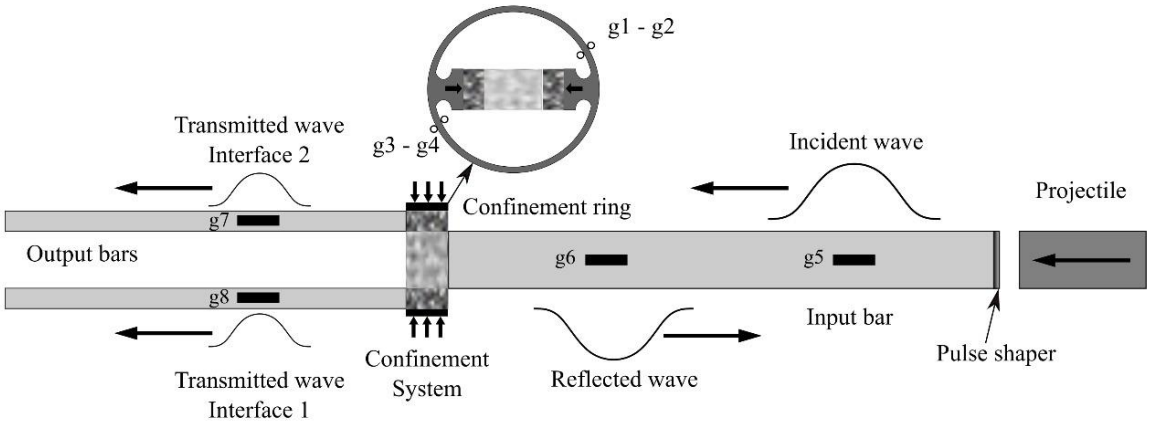

Figure 4.13 Dynamic shear test setup

$$\varepsilon = \frac{2}{KGV_{EX}(1+\mu)} \Delta V_{measured} \qquad (4.6)$$

where ε is the strain in the confinement ring, K is the gauge factor, V_{EX} is the excitation voltage, $\Delta V_{measured}$ is the voltage recorded by the strain gauge circuit, and μ is the Poisson's ratio of the bar.

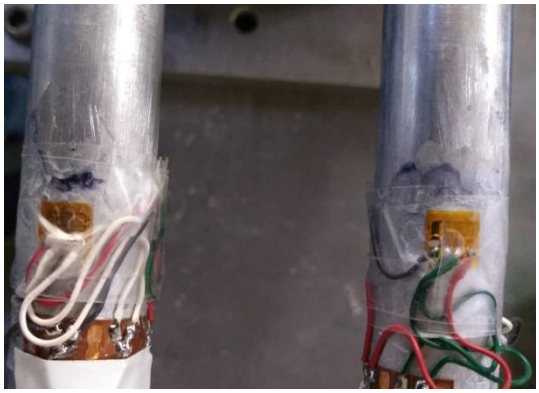

Figure 4.14 Installation of strain gauges in the output bars.

Before the test, the input bar is in contact with the concrete part of the sample, while the output bars are associated with the rock part (Figure 4.15).

Figure 4.15 Dynamic shear test using the SHPB and the confinement ring

Furthermore, a pulse shaper is glued to the impacted surface of the input bar. This pulse shaper is made of lead and has a disc-like geometry of 38 mm and 45 mm of inner and outer diameter and 1 mm of thickness. The pulse shaping technique is motivated by the necessity to promote the formation of an incident wave with a longer rising time (Xia and Yao, 2015). An incident wave

with a longer rising time is important to improve the stress equilibrium. An illustration of a pulse shaper used is presented in Figure 4.16.

Figure 4.16 Pulse shaper

b) Computation of the dynamic shear response

In the testing method that includes an SHPB system composed of input and output bars, it is customary to assess that the mechanical equilibrium between the input and the output is achieved. This equilibrium can be used as proof of the one-dimensionality of the stress wave during the test, which means that the dispersion is negligible. However, achieving stress equilibrium is difficult for low-impedance or brittle materials (Gary and Mohr, 2013).

In this study, the samples are composed of concrete and rock, both brittle and low-impedance materials. Furthermore, these materials are not directly tested, but the interfaces between them. Generally, as considered in this study, concrete-rock interfaces submitted to lower normal loadings have even lower impedance when compared to rock and concrete. Furthermore, the local and progressive aspect of the shear response of rock-rock or concrete-rock interfaces makes achieving the mechanical equilibrium states highly difficult. Li et al. (Li et al., 2022) and Tawfik et al. (Tawfik et al., 2022) also reach similar conclusions regarding the mechanical equilibrium analysis of rock-rock interfaces and geopolymer material submitted to dynamic shear loading.

Considering these observations, only the stress wave signal collected in the output bars is used to compute the dynamic shear response of concrete-rock interfaces according to Eq (4.7).

$$\tau_{\mathrm{int}}(\mathrm{t}) = \mathrm{F_{tr}}(\mathrm{t})/\mathrm{S_{int}} = \ \mathrm{S_{bar}}\,\mathrm{E_{bar}}\varepsilon_{\mathrm{tr}}(\mathrm{t})/\mathrm{S_{int}} \qquad (4.7)$$

where τ_{int} is the shear stress at each interface, $F_{tr}(t)$ is the force calculated from the transmitted bar, S_{int} is the surface of the interface, S_{bar} is the section of the bar, E_{bar} is the Young's modulus of the bar, and $\varepsilon_{tr}(t)$ is the strain history recorded in the gauges glued to the output bars (g7 and g8 in Figure 4.13).

4.2 **Test results**

4.2.1 **Quasi-static tests**

Figure 4.17 illustrates the static shear test during and after the test. The results of quasi-static tests are hereafter presented for each type of interface tested.

Figure 4.17 Illustration of the static shear test using the confinement ring and the electromechanical press Instron 100 kN

4.2.1.1 **Smooth concrete-sandstone interfaces**

Eight smooth concrete-sandstone interfaces are tested using four samples. The shear responses of one interface of sample StatSCS2 and one interface of sample StatSCS4 are excluded from the following analysis because they have peak shear strength attained at normal stress above 2 MPa, set as the limit for this experimental campaign.

The typical shear responses of smooth concrete-sandstone interfaces are presented in Figure 4.18. The behaviors observed are discussed in section 4.3.

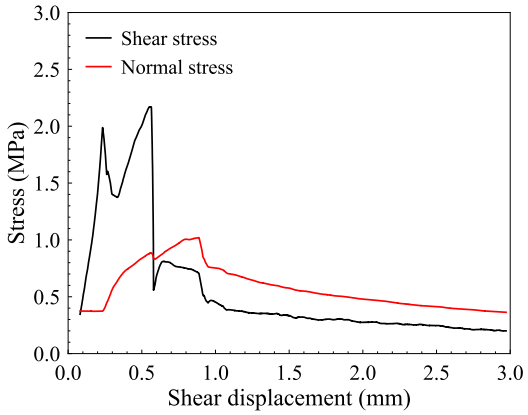

Figure 4.18 Typical static shear response of tests with smooth concrete-sandstone (StatSCS1)

The plot of the peak values obtained in the shear responses in terms of the normal stress is presented in Figure 4.19. The correlation coefficient between the peak shear strength and the normal shear stress is 0.60. The friction angle and cohesion are 44.89 º and 1.57 MPa, respectively. The shear strengths obtained are between 1.99 MPa and 4.07 MPa for the normal stress varying from 0.37 MPa to 1.81 MPa.

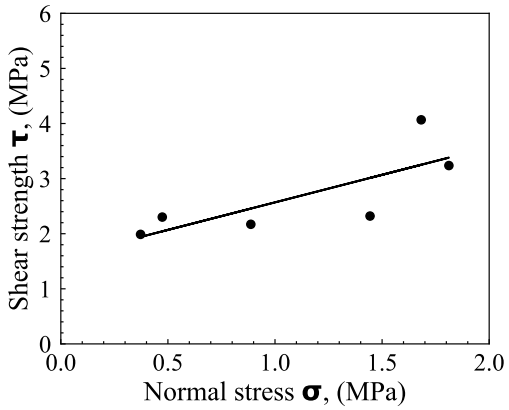

Figure 4.19 Linear regression: static peak shear strength – normal stress. Case of smooth concrete-sandstone interfaces ($\boldsymbol{c = 1.57}$ MPa and $\boldsymbol{\phi_i = 44.89}$ º)

4.2.1.2 **Bush-hammered concrete-granite interfaces**

Three of the four bush-hammered concrete-granite interfaces tested are considered in the subsequent analysis. The result of one of the interfaces of the sample StatBHCG2 is not considered because the peak shear strength was reached at a confinement stress higher than 2 MPa (2.59 MPa).

A typical shear response of bush-hammered concrete-granite interfaces is presented in Figure 4.20. Further discussion is presented in section 4.3.

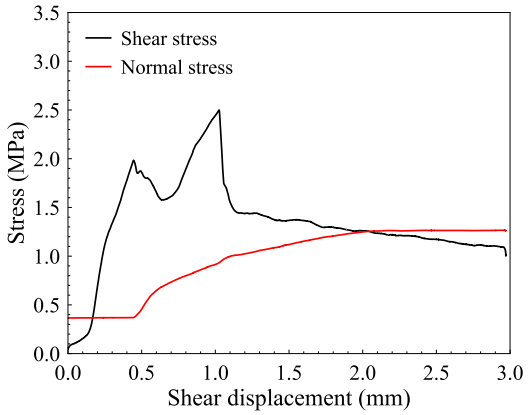

Figure 4.20 Typical static shear response of bush-hammered interfaces (StatBHCG1)

A correlation coefficient of 0.99 is reported between the shear strengths and the normal stress. Figure 4.21 shows the variation of the peak shear strengths in terms of the normal stress. The cohesion and the basic friction angle are 1.56 MPa and 46.9 º, respectively. The variation of the shear strengths is between 1.98 MPa and 3.12 MPa for a variation of normal stress between 0.37 MPa and 1.42 MPa.

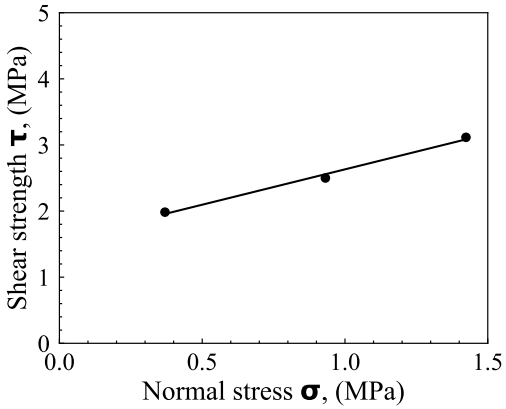

Figure 4.21 Linear regression: static peak shear strength – normal stress. Case of bush-hammered concrete-granite interfaces ($\boldsymbol{c = 1.56}$ MPa and $\boldsymbol{\phi_i = 46.9}$ º)

4.2.1.3 **Rough concrete-granite interface**

The shear responses of the two samples tested are shown in Figure 4.22. Further analysis of these results is presented in section 4.3.

Differently from the static shear tests of smooth concrete-sandstone and bush-hammered concrete-granite interfaces, the static shear tests of rough concrete-granite interfaces are stopped before the 3 mm to ascertain that the increase of the confinement stress does not generate plastic deformation in the ring. It is noteworthy that the elastic limit of the ring with the associated deformation was assessed during the design of the ring through finite element simulations.

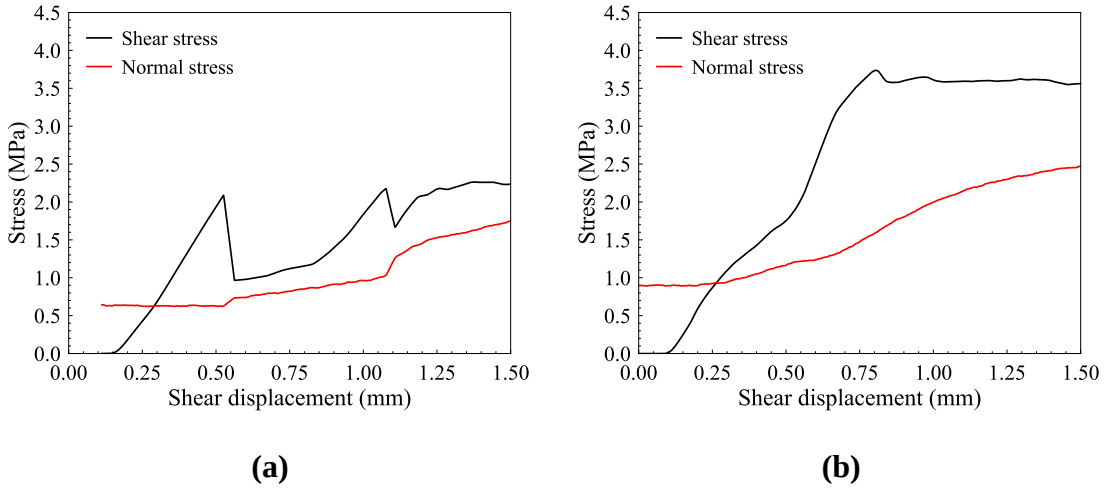

Figure 4.22 Static shear response of rough concrete-granite: (**a**) StatRCG1 and (**b**) StatRCG2

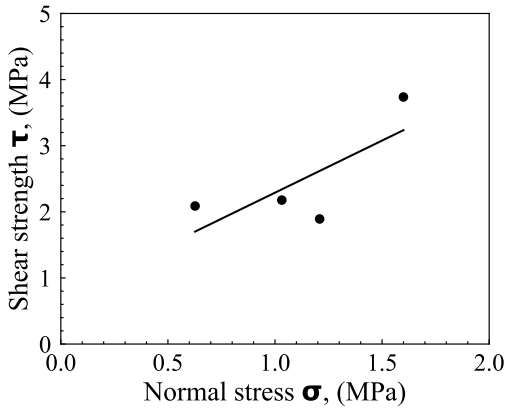

Figure 4.23 Linear regression: static peak shear strength – normal stress. Case of rough concrete-granite interfaces($\boldsymbol{c = 0.71}$ MPa and $\boldsymbol{\phi_i = 57.6}$ º)

Figure 4.23 shows the variation of the peak shear strength with the change of the normal stress. The correlation coefficient between the peak shear strength and the normal stress equals 0.56. The cohesion is equal to 0.71 MPa, and the friction angle is equal to 57.6º. The variation of the peak shear strength is between 1.89 MPa and 3.74 MPa when the normal stress changes between 0.63 MPa and 1.60 MPa.

4.2.2 **Dynamic tests**

Figure 4.24 illustrates a dynamic shear stress test of concrete-rock interfaces (DynSCS1) before and after the test.

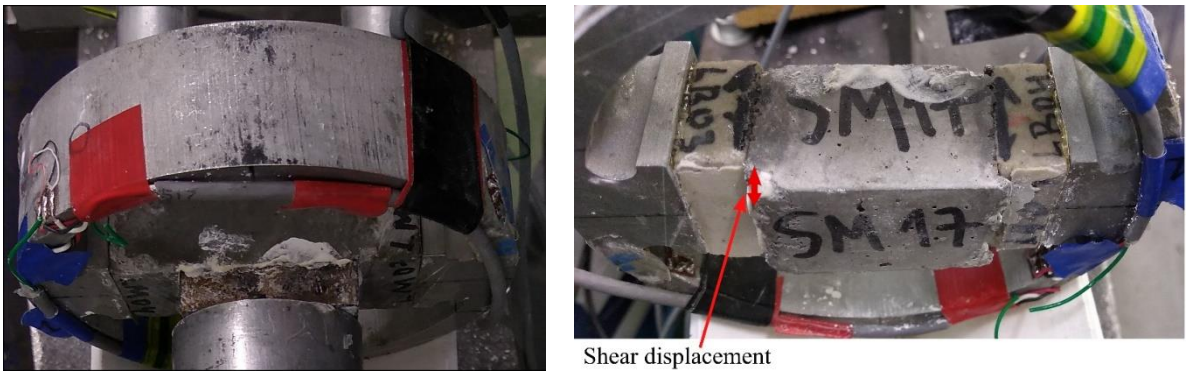

(a) (b)

Figure 4.24 Illustration of the dynamic shear test of concrete-rock interfaces using the SHPB and the confinement ring

Figure 4.25 shows possible dynamic shear responses obtained when testing concrete-rock interfaces using the dynamic shear test presented (Refer to Figure 4.13.).

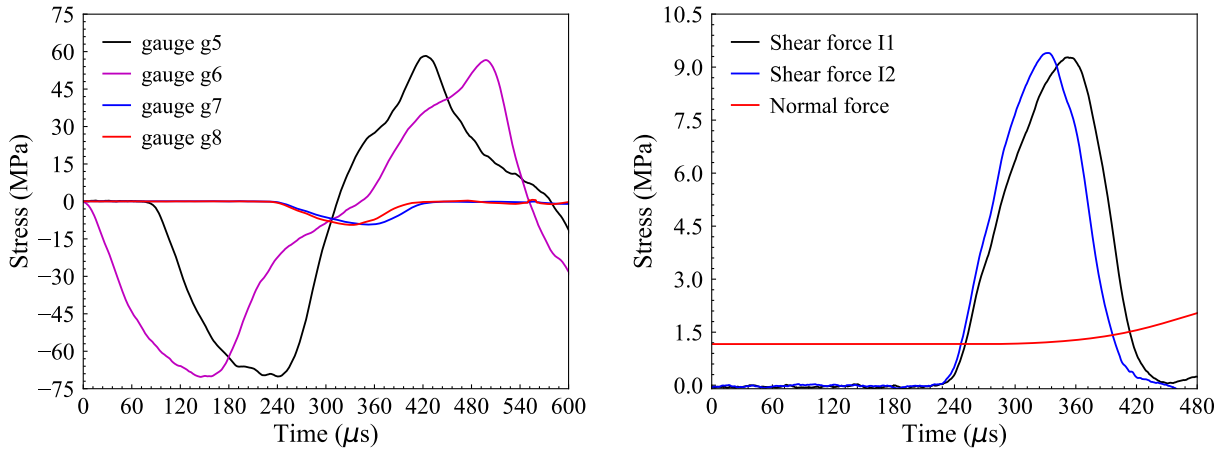

(a) (b)

Figure 4.25 Illustration of the dynamic shear responses of concrete-rock interfaces (DynSCS1). For legend, refer to Figure 4.13.

The shear responses obtained from each type of interface considered are presented hereafter.

4.2.2.1 **Smooth concrete-sandstone interfaces**

Two typical dynamic shear responses of smooth concrete-sandstone interfaces are presented in Figure 4.26. I1 and I2 denote the two interfaces tested per sample in this figure. Section 4.3 discusses these results further.

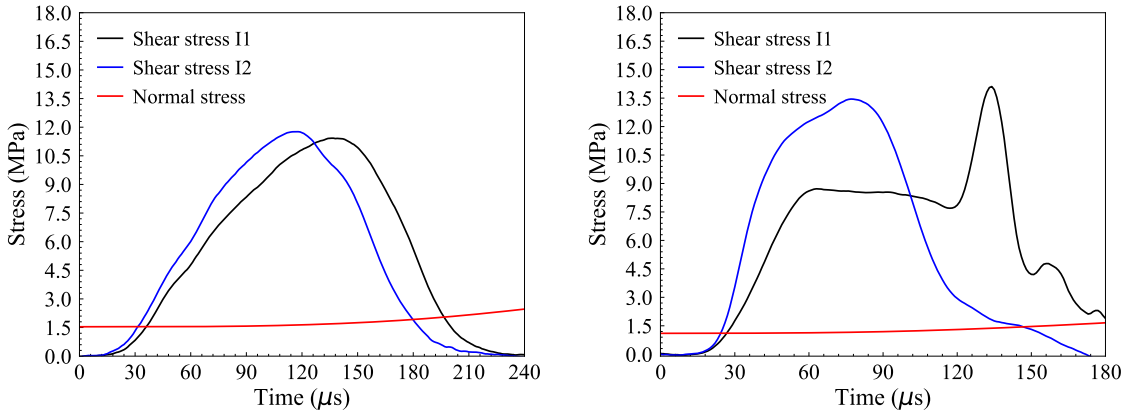

Figure 4.26 Dynamic shear response of smooth concrete-sandstone: (**a**) DynSCS1 and (**b**) DynSCS2

Figure 4.27 shows the variation of the dynamic peak shear strengths in terms of the normal stress. The dynamic peak shear strengths change between 7.67 MPa and 14.11 when the normal stress varies between 0.31 MPa and 1.69 MPa. A correlation coefficient equivalent to 0.14 was obtained between the dynamic shear resistance and the normal stress.

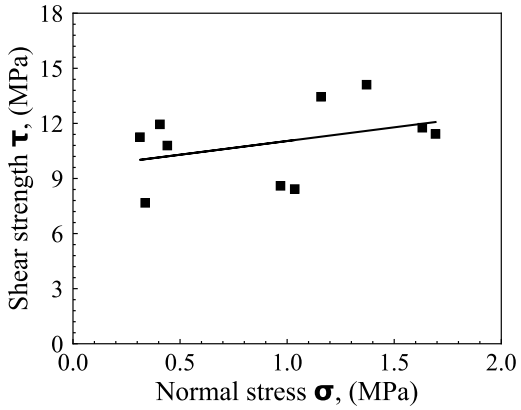

Figure 4.27 Linear regression: dynamic peak shear strength – normal stress. Case of smooth concrete-sandstone interfaces

4.2.2.2 **Bush-hammered concrete-granite interfaces**

Typical dynamic shear responses of bush-hammered concrete-granite interfaces are shown in Figure 4.28.

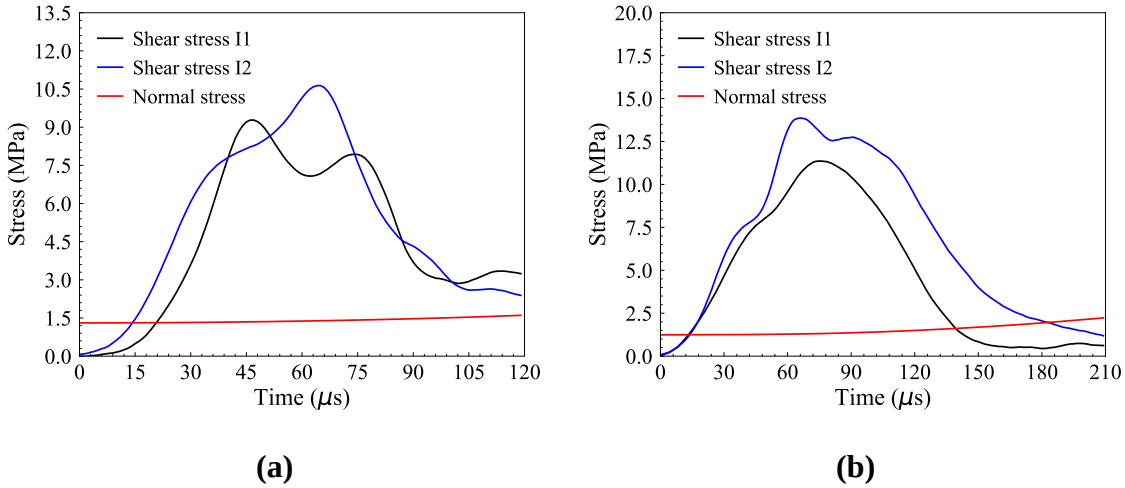

Figure 4.28 Dynamic shear responses of bush-hammered interfaces: (**a**) DynBHCG1 and (**b**) DynBHCG2

The evolutions of the dynamic shear stress in terms of the normal stress are presented in Figure 4.29. A correlation coefficient of 0.07 was obtained between the dynamic peak shear strength and the normal stress. The dynamic peak shear strength variation is between 9.17 MPa and 13.86 MPa when the normal stress changes between 0.48 MPa and 1.39 MPa.

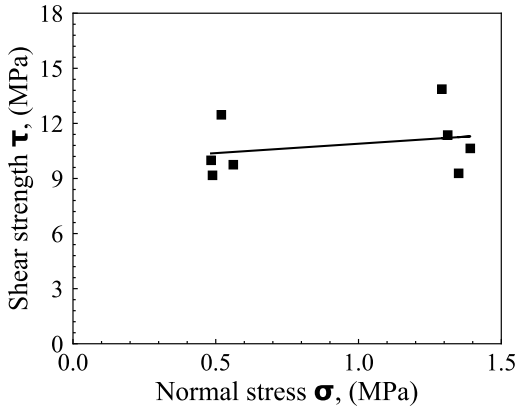

Figure 4.29 Linear regression: dynamic peak shear strength – normal stress. Case of bush-hammered concrete-granite interfaces

4.2.2.3 **Rough concrete-granite interface**

Examples of typical dynamic shear responses of rough concrete-granite interfaces are presented in Figure 4.30.

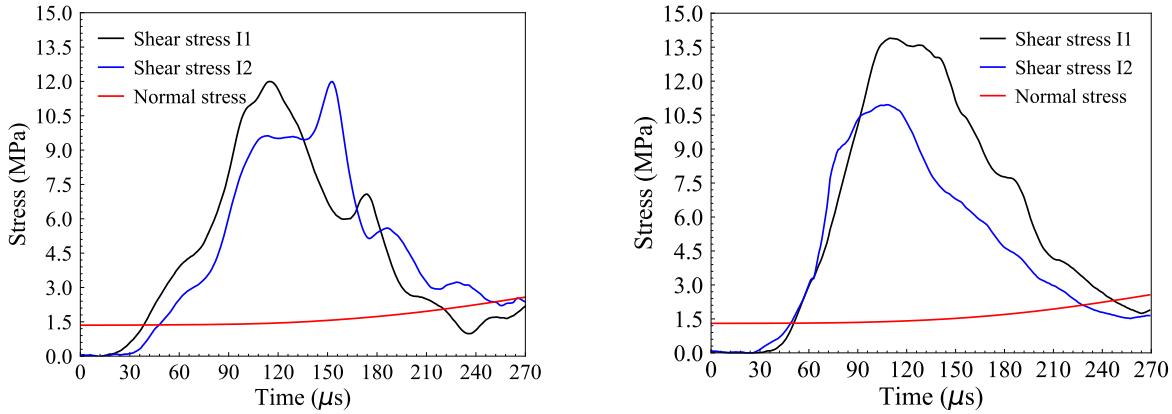

Figure 4.30 Dynamic shear response of rough concrete-granite: (**a**) DynRCG1 and (**b**) DynRCG2

Figure 4.31 presents the evolutions of the dynamic peak shear strength regarding normal stress. A correlation coefficient equivalent to 0.81 was obtained between the dynamic peak shear strength and the normal stress. The cohesion and the friction angle are, respectively, 4.42 MPa and 79.42º. For normal stress varying between 0.52 and 1.57 MPa, the dynamic peak shear strengths obtained are between 6.45 MPa and 13.90 MPa.

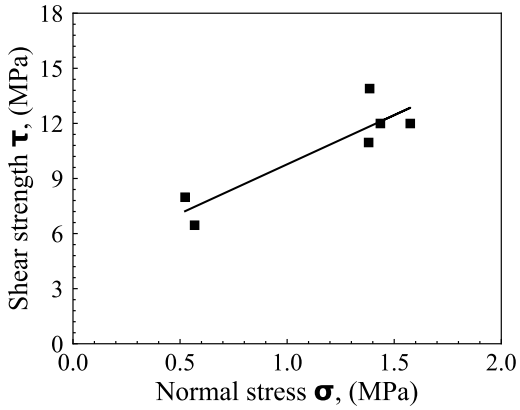

Figure 4.31 Linear regression: dynamic peak shear strength – normal stress. Case of rough concrete-granite interfaces ($\boldsymbol{c = 4.42}$ MPa and $\boldsymbol{\phi_i = 79.42}$ º)

Table 4.7 summarizes the results of the static and dynamic shear tests of concrete-rock interfaces carried out in the experimental campaign. In this table, τ is equivalent to the peak shear strength, while σ is equivalent to the normal stress at a peak of the shear response. It is worth noting again that two concrete-rock interfaces are tested per sample.

Table 4.7 Results of static and dynamic tests

Tests	Interfaces	Sample ID	$\sigma_1\ [MPa]$	$\tau_1\ [MPa]$	$\sigma_2\ [MPa]$	$\tau_2\ [MPa]$
Static	Smooth concrete-sandstone	StatSCS1	0.37	1.99	0.89	2.17
		StatSCS2	1.68	4.07	4.58	5.03
		StatSCS3	0.47	2.30	1.81	3.23
		StatSCS4	1.44	2.32	2.91	6.18
	Bush-hammered concrete-granite	StatBHCG1	0.37	1.98	0.93	2.50
		StatBHCG2	1.42	3.12	2.59	2.97
	Rough concrete-granite	StatRCG1	0.63	2.09	1.03	2.18
		StatRCG2	1.21	1.89	1.60	3.74
Dynamic	Smooth concrete-sandstone	DynSCS1	1.63	11.77	1.69	11.42
		DynSCS2	1.16	13.45	1.37	14.11
		DynSCS3	0.41	11.95	0.44	10.79
		DynSCS4	0.34	7.67	0.31	11.25
		DynSCS5	1.04	8.42	0.97	8.60
	Bush-hammered concrete-granite	DynBHCG1	1.39	9.28	1.35	10.64
		DynBHCG2	1.31	11.36	1.29	13.86
		DynBHCG3	0.51	9.75	0.56	12.47
		DynBHCG4	0.48	9.17	0.49	9.99
	Rough concrete-granite	DynRCG1	1.57	11.99	1.44	11.99
		DynRCG2	1.38	13.90	1.39	10.96
		DynRCG3	0.52	6.45	0.57	7.98

4.3 **Discussion**

4.3.1 **Description of the shear evolution**

It is worth noting that different from the conventional direct shear test (Muralha et al., 2014), in the static and dynamic shear tests used in this experimental campaign, two interfaces are tested using a single source of shear loading.

4.3.1.1 **Static shear response of concrete-rock interfaces**

In section 2.1, the shear evolution of a concrete-rock interface submitted to low normal loading was separated into three stages: the shear stress accumulation, the shear slip, and the residual shear stress stage. The first stage is driven by the concrete-rock bonds; the progressive failure of the bonds and progressive mobilization of friction control the second stage, and the last stage depends on friction.

Even though each shear evolution obtained in the static shear test performed in this experimental campaign represents the shear failure of two interfaces, the mechanisms described above and in section 2.1 can be used to explain it.

The typical shear response of concrete-rock interfaces obtained in the static shear tests performed in this experimental campaign is presented in Figure 4.32. Figure 4.22 shows that the shear evolution of concrete-rock interfaces can be separated into three parts.

In the first part (Figure 4.32, OAB), the shear stress increases until the peak and then drops to local residual shear strength. The first stage of this part (Figure 4.32, OA) is the stress accumulation stage, and the second stage (Figure 4.32, AB) is the shear slip stage. These two stages represent the increase of the shear stress due to the resistance offered by the concrete-rock bonds and the decrease of the shear stress due to the progressive degradation of concrete-rock bonds and

mobilization of friction in one interface of the sample. It is worth noticing that the confinement stress remains constant during the first stage of this part (Figure 4.32, OA).

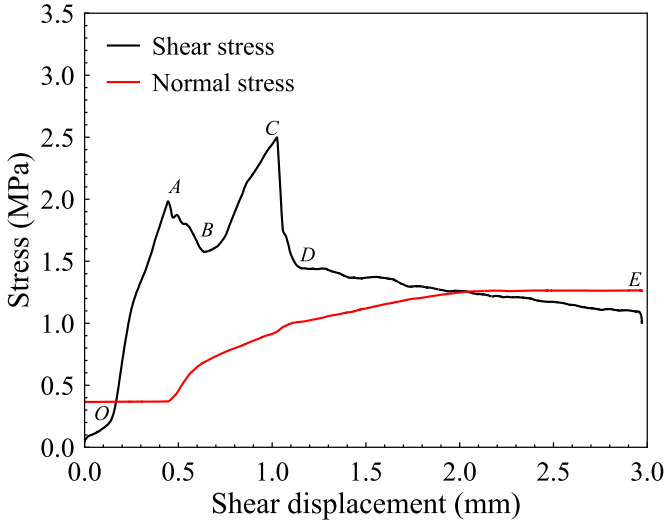

Figure 4.32 Static shear evolution of concrete-rock interface (sample StatBHCG1).

In the second part (Figure 4.32, BCD), the undamaged interface goes through the same process of shear stress accumulation as the interface, which failed in the first part (Figure 4.32, BC) and shear slip (Figure 4.32, CD). Concrete-rock bonds and friction also drive these parts. The concrete-rock bonds are responsible for the increase of the shear stress before the peak (Figure 4.32, C) and the progressive degradation and mobilization of friction controlling the shear stress decrease (Figure 4.32, CD). These two stages (Figure 4.32, BC and CD) represent the failure of the second interface of the sample. Unlike the first stage of the first part (Figure 4.22, OA), the confinement stress increases in the second part (Figure 4.22, BCD). This increase in the confinement stress is expected because, during the test, the concrete part of the sample is the only one subjected to the shear loading. The shear displacement of the concrete part of the sample is only possible if there is a normal displacement of the rock part. This normal displacement results in the dilation of the sample, which consequently leads to an increase in the confinement stress.

In the third part (Figure 4.32, DE), the shear evolutions of both interfaces have reached the residual shear stress stage and depend on friction. The shear response evolves toward the residual shear strength. The confinement stress does not change significantly in this part. It either decreases or reaches a plateau.

For the specific cases of rough concrete-rock interfaces, some peculiarities are observed caused by the complexities introduced by the roughness in the shear response. The two peculiarities are reported in Figure 4.33 (a) and (b).

For concrete-rock interfaces submitted to lower confinement stresses, the shear failure proceeds mainly along the interface such that the shear motion can be characterized as “riding along the asperities,” which means that the post-mortem of the tests shows that there is no significant damage of either the concrete or the rock. This shear motion yields significant normal displacement in the shear test of rough concrete-rock interfaces. This normal displacement leads to the dilation of the sample, which the ring resists. Consequently, the confinement stress applied to the interfaces increases. The confinement stress increase increases the shear resistance of the interfaces, which

justifies the high residual shear stress obtained in the shear responses of rough concrete-granite interfaces compared to the peak shear strength (Figure 4.33 (a)). The increase in the confinement stress and the residual shear stress are the first possible peculiarities when discussing the results of static shear tests of rough concrete-granite interfaces using the confinement ring to apply the normal stress. The second possible peculiarity is no shear slip after the first peak shear strength, which means that the stress accumulation stage in the second interface initiates right when the shear slip stage of the first interface is supposed to start. This behavior could be caused by the complexity of the influence of roughness on the shear response of interfaces and the competition of shear resistances between the two interfaces. This second peculiarity is shown in Figure 4.33 (b).

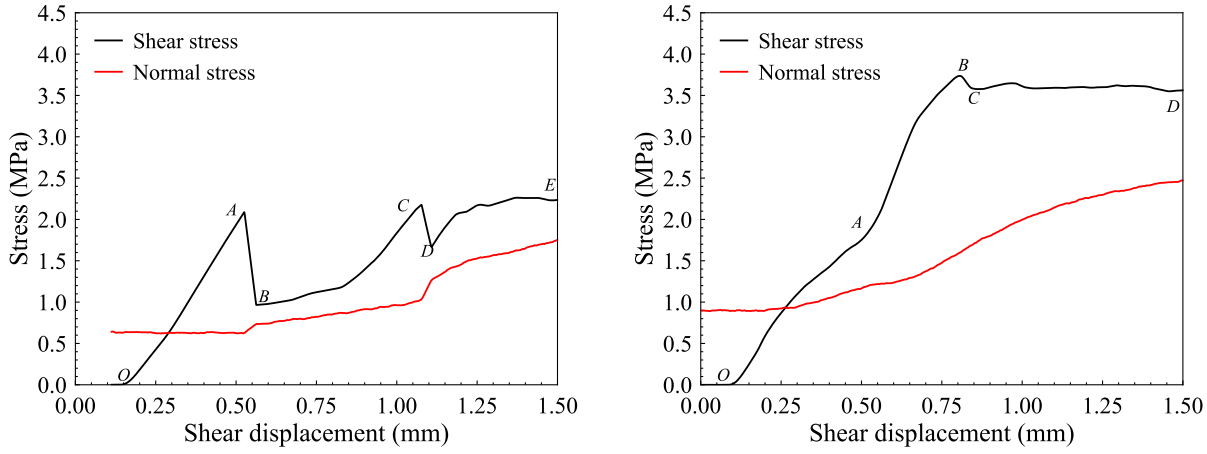

Figure 4.33 Static shear responses of rough concrete-granite: (**a**) StatRCG1 and (**b**) StatRCG2

4.3.1.2 **Dynamic shear response of concrete-rock interfaces**

Like the static shear evolution of concrete-rock interfaces presented, the dynamic shear response of concrete-rock interfaces can also be separated into three stages. However, unlike in the static shear tests, in the dynamic shear tests, the shear responses of each sample interface are recorded and computed separately. Figure 4.34 shows the typical dynamic shear evolutions of concrete-rock interfaces. This figure shows that the dynamic shear responses are plotted in terms of times and not displacement, unlike the exploitation of the static shear tests. The plot shear stress/time does not constitute any concern to the interpretation of the test since the different stages of the shear response can easily be identified by observing the peak and residual shear strength.

The first stage of the dynamic shear evolution (Figure 4.34, OA) corresponds to the shear stress accumulation stage observed in the static shear responses. However, the shape of the curve obtained in this stage is curvilinear, which differs from the more linear appearances observed in the stress accumulation stages of the static shear responses of concrete-rock interfaces (Figure 4.32, OA and BC). This curvilinear shape is hypothesized to indicate a double mobilization of concrete-rock bonds and friction.

The second stage of the dynamic shear response (Figure 4.34, AB) corresponds to the shear slip stage encountered in the static shear evolutions. The reduction of the influence of the concrete-rock bonds in the shear response and the increase of the influence of friction drive this stage.

The last stage of the dynamic shear evolution of concrete-rock interfaces is equivalent to the residual shear stress stage described in the static shear response of concrete-rock interfaces. It is driven by friction (Figure 4.34, BC).

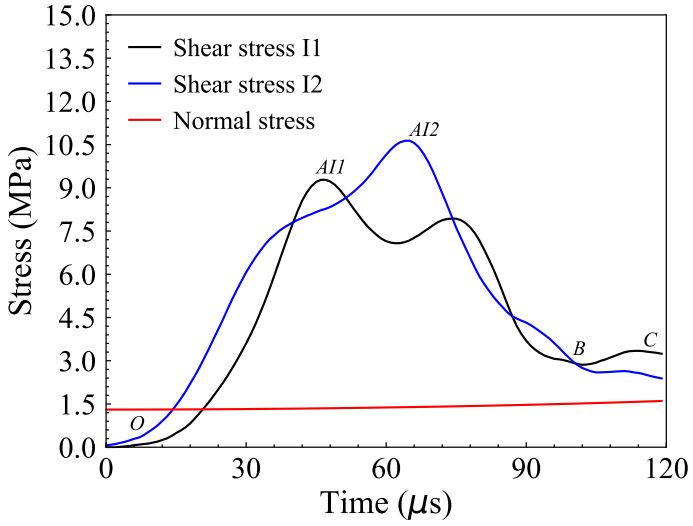

Figure 4.34 Dynamic shear response of concrete-rock interface (DynBHCG1)

Usually, the shear loading is applied in static shear tests of interfaces until a defined shear displacement is attained. This shear displacement is defined such that it guarantees that the shear failure will proceed until the shear response reaches the residual shear stress stage. This association implies that the shear loading is linked to the shear response of the interface. In the dynamic shear test of interfaces presented in this study, the shear loading is applied using the split Hopkinson pressure bars system. The shear loading is applied as a stress wave with defined energy that cannot be changed to, for example, ensure that the three stages of the shear evolution are attained properly (Figure 4.26 (a)).

The peculiarities of the dynamic shear response of concrete-rock interfaces are discussed hereafter.

First, like in the static shear test, in the dynamic shear test, the confinement stress increases during the test because of the dilation of the rock parts of the sample necessary to allow the shear displacement of the concrete part of the sample.

Second, the shear responses of the two concrete-rock interfaces tested per sample do not simultaneously reach the dynamic peak shear strength. The local aspect of the shear resistance can explain this discrepancy. The local shear resistance of concrete-rock interfaces might depend on the influence of the local roughness, the strength of the concrete-rock bonds locally due to the local roughness, and the local mineral composition.

Last, some dynamic shear responses of concrete-rock interfaces can present unusual features caused by the local competition of the shear resistance between the tested interfaces. For example, in Figure 4.35, there is a plateau (Figure 4.35, AB) in the shear response of one interface. The combination of the competition of shear resistances between the interfaces and the local shear resistance of the interfaces causes this plateau by concentrating the action of the shear loading at one interface during the shear history.

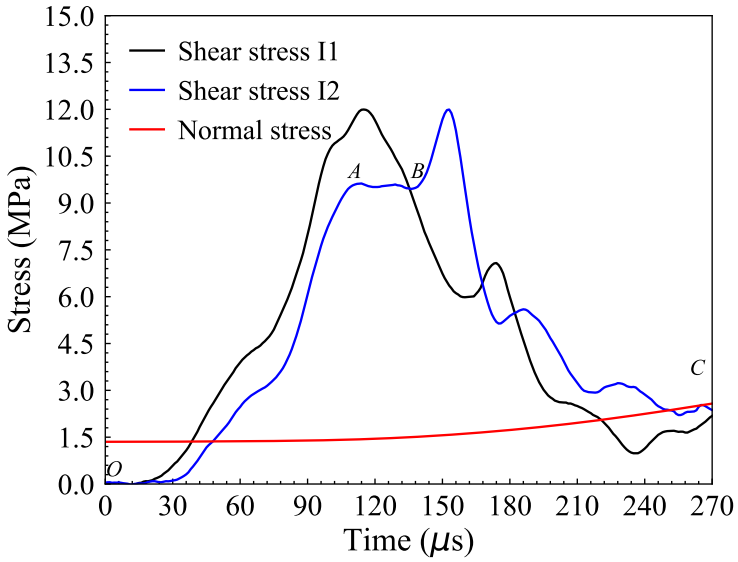

Figure 4.35 Dynamic shear response of concrete-rock (DynRCG1)

4.3.2 **Shear resistance of concrete-rock interfaces**

The change of the static and dynamic peak shear strength with the variation of the normal stress for the smooth concrete-sandstone, bush-hammered concrete-granite, and rough concrete-granite interfaces tested and analyzed are presented in Figure 4.36. In this figure, the normal stresses are equivalent to the normal stresses when the static or dynamic peak shear strength is reached. Furthermore, each square and dot in Figure 4.36 represents a dynamic and a static peak shear strength on one interface.

The correlation coefficients between static peak shear strengths and normal stresses are equal to 0.60, 0.99, and 0.56 for the smooth concrete-sandstone, bush-hammered concrete-granite, and rough concrete-granite interfaces. The correlation coefficient is higher for the bush-hammered concrete-granite than for the smooth concrete-sandstone interfaces. This comparative assessment could indicate that the bush-hammering process generates surfaces with a similar local distribution of micro-roughness or unevenness, consequently leading to a similar local distribution of concrete-rock bonds with similar strength.

The correlation coefficients of dynamic peak shear strength - normal stress are low for the smooth concrete-sandstone and the bush-hammered concrete-granite interfaces, respectively, 0.14 and 0.07. In contrast, a correlation coefficient of 0.81 was obtained for the rough concrete-granite interfaces for dynamic peak shear strength - normal stress. The low correlation coefficient of the smooth concrete-sandstone and bush-hammered concrete-granite interfaces could indicate that for low confinement stress (below 2 MPa), the normal stress does not significantly affect the dynamic peak shear strength of concrete-rock interfaces.

Since the peak shear strength of rough concrete-granite interfaces depends on the concrete-rock bonds and the roughness of the interface, and given that the rough concrete-granite interfaces tested do not have the same roughness, only a qualitative assessment of the evolution of the static and dynamic peak shear strength of rough concrete-granite interfaces in terms of the normal stress is possible. Nevertheless, it is worth noting that the normal stress seems to have a stronger effect on

the dynamic shear resistance of rough concrete-granite than on the smooth concrete-sandstone and the bush-hammered concrete-granite interfaces (see the inclination of fitting lines in Figure 4.36).

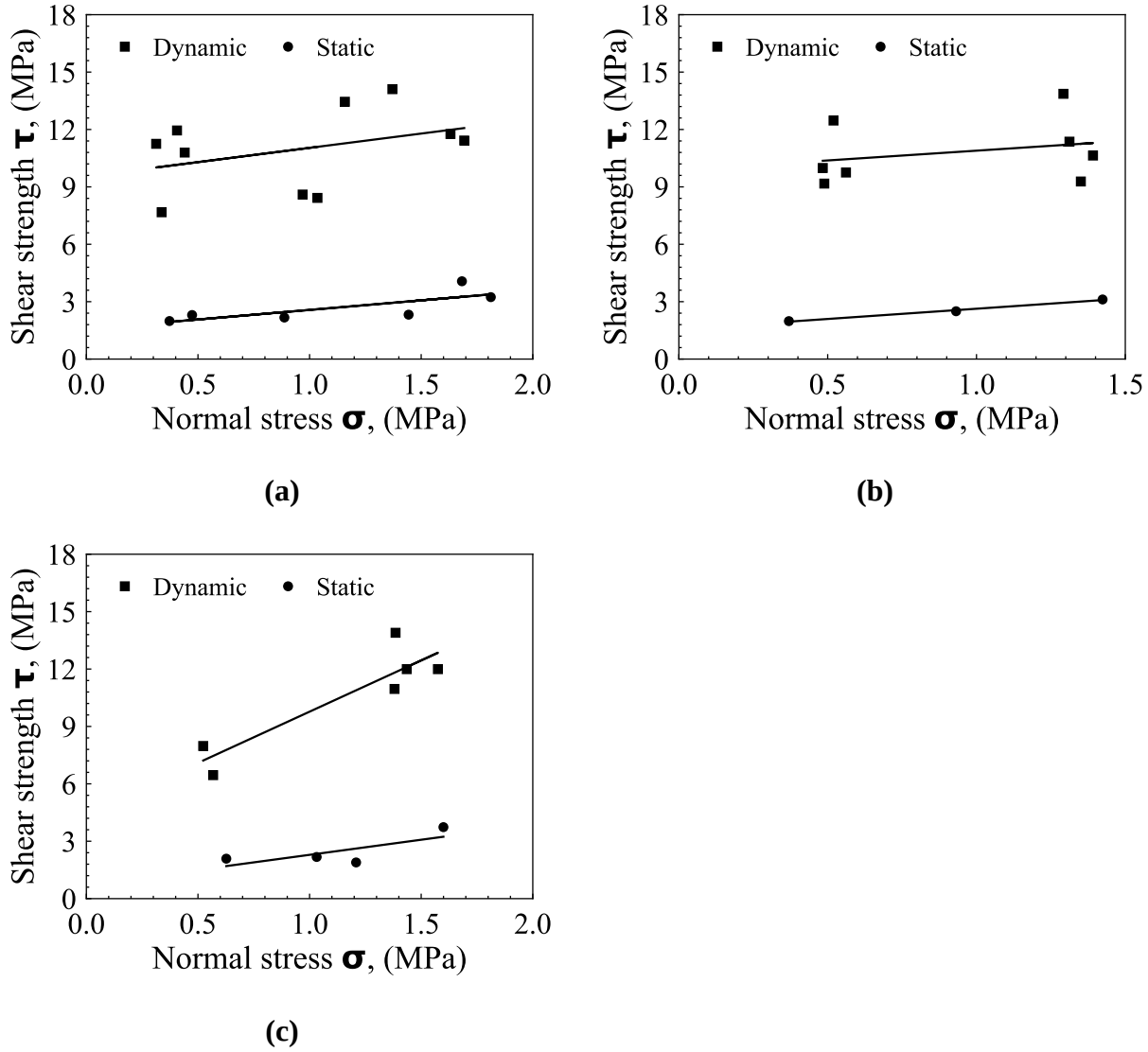

Figure 4.36 Shear resistance in terms of confinement stress: (**a**) smooth concrete-sandstone, (**b**) bush-hammered concrete-granite, and (**c**) rough concrete-granite interfaces

Moreover, in Figure 4.36, the dynamic peak shear strengths of the rough concrete-granite interfaces of sample DynRCG3 (Table 4.7), tested with confinement stress of 0.5 MPa, are lower than the dynamic peak shear strengths obtained with smooth sandstone-concrete and the bush-hammered concrete-granite interfaces tested with similar confinement stress. This result seems to go against the usually encountered trend that associates the rough concrete-rock interfaces with higher shear strength when compared to smooth or bush-hammered concrete-rock interfaces. However, the true cause for this unusual result cannot objectively be identified. Nevertheless, some possible explanations are presented: (1) roughness distribution locally across the interface, (2) the roughness parameter expresses the global roughness without proper consideration of local roughness aspects.

4.3.3 **Comparative evaluation of the static and dynamic peak shear strength of concrete-rock interfaces**

The dynamic peak shear strengths of concrete-rock interfaces are three to four times the ones of their static counterparts (Figure 4.36). This difference shows that the shear behavior of concrete-rock interfaces subjected to lower confinement stresses (below 2 MPa) is strain rate sensitive.

Figure 4.37 shows the evolution of static and dynamic peak shear strength of smooth concrete-sandstone and bush-hammered concrete-granite interfaces tested in this thesis. The static and dynamic tensile strength results of concrete-limestone interfaces published by Zhou et al. (Zhou, Lu and Cai, 2020) are also plotted in Figure 4.37. It is worth noting that the study conducted by Zhou et al. (Zhou, Lu and Cai, 2020) does not consider the influence of confinement stress.

In Figure 4.37, each filled square and filled dot represent the static and dynamic peak shear strength of smooth concrete-sandstone and bush-hammered concrete-granite interfaces regarding the normal stress (lower x-axis). In addition, each unfilled square and unfilled dot represent the static and dynamic tensile strength of concrete-limestone interfaces tested by Zhou et al. (Zhou, Lu and Cai, 2020) in terms of the inclination of the concrete-limestone interfaces in comparison to the shear loading (upper x-axis).

Figure 4.27 shows that the dynamic tensile strength of concrete-limestone is much higher than their static counterparts (five times higher). This assessment is similar to the results of the shear tests of smooth concrete-sandstone, bush-hammered concrete-granite, and rough concrete-granite interfaces presented in this thesis.

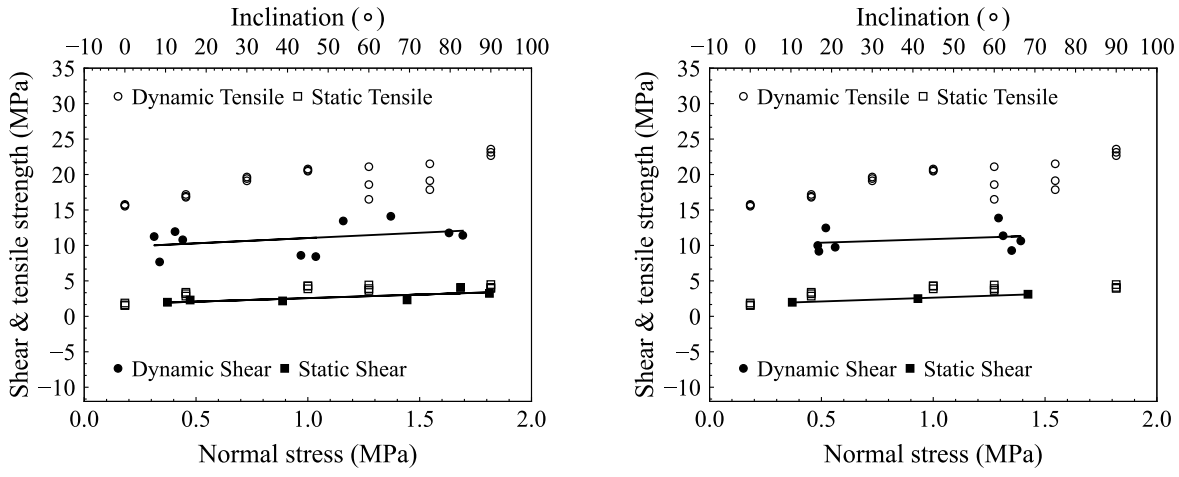

Figure 4.37 Static - dynamic shear / tensile strength of interfaces: (**a**) smooth concrete-sandstone / concrete-limestone and (**b**) bush-hammered concrete-granite / concrete-limestone

4.4 **Concluding remarks**

In this chapter, a pioneering experimental investigation of the dynamic shear behavior of interfaces submitted to low normal loading was carried out using concrete-rock interfaces as a case study. Three types of interface roughness and two types of rocks were used: the smooth concrete-sandstone, the bush-hammered, and the rough concrete-granite interfaces. The dynamic test setup maintains the conventional direct shear test concepts. The normal stress is applied using a confinement ring specially redesigned through finite element simulations to generate low confinement stresses. The shear loading is applied using a split Hopkinson pressure bars system composed of one input and two output bars.

Furthermore, a static test was also used. In the static test, the confinement stress is applied using the modified confinement ring, and the shear loading is applied using an electromechanical press. The interest of the static tests performed was to have a base of comparison with the results of the dynamic shear tests in terms of the sample size and methodology of application of the confinement stress.

The static shear responses obtained can be separated into the three stages usually encountered in the literature. These stages are the shear stress accumulation, the shear slip, and the residual shear stress stage. The concrete-rock bonds drive the first stage. The transition from concrete-rock bond dependency to friction characterizes the second stage. Friction drives the last stage. The similarity of the description of the shear response obtained through the static shear test used sets this test as a possible alternative to the more commonly used direct shear test.

Like the static shear responses of concrete-rock interfaces, the dynamic shear responses of these interfaces can be separated into the stages mentioned above. However, unlike in static, in dynamic, concrete-rock bonds and friction drive the first and the second stages. Furthermore, the normal stress significantly influences the dynamic peak shear strength of rough concrete-granite interfaces. Still, it seems not to influence the strength of smooth and bush-hammered concrete-rock interfaces. Moreover, the preliminary comparative evaluation of the static and dynamic peak shear strength of concrete-rock interfaces shows that the dynamic peak shear strength is three to four times higher than their static counterparts.

5. Conclusions and perspectives

This chapter presents the major findings of the thesis and proposes suggestions for further investigations of the shear behavior of concrete-rock and rock-rock interfaces.

5.1 **Conclusions**

A thorough literature review of the shear behavior of interfaces discusses at length the most relevant experimental works to study the shear behavior of concrete-rock interfaces. Reviewing the shear behavior of concrete-rock interfaces has helped shape the investigative path followed throughout this thesis.

Based on the literature review, the normal stress of interest was defined as below 2 MPa, which covers the most likely normal stresses experienced by concrete-rock interfaces in geotechnical structures such as concrete-gravity dams and grout-based rock support systems. This range of normal stresses is referred to in the thesis as “low normal stress.” Within this range of normal stresses, it was found that the shear failure of concrete-rock proceeds predominantly along the interfaces with negligible damage in neither concrete nor rock. The shear response of concrete-rock interfaces can be separated into three stages: the shear stress accumulation, the shear slip, and the residual shear stress stage. The concrete-rock bonds drive the first stage, the progressive failure of concrete-rock bonds, and the progressive mobilization of friction rules the second stage, while the last stage is controlled by friction. This separation is strongly supported by experimental studies, including an investigation that analyzed the acoustic emissions during shear.

Regarding the influence of roughness, it was possible to identify the unevenness of rock surfaces as the principal requirement for forming concrete-rock bonds in concrete-granite interfaces. Meanwhile, the waviness of the rock surfaces was associated with the contribution to the shear resistance via surface interlocking during shear. Regarding the formation of concrete-rock bonds, it was possible to highlight that the formation of concrete-rock bonds depends on the local property of the interface, principally roughness, and mineral composition. Consequently, the failure of the bonds was also local and progressive. This literature review has helped demonstrate that the shear behavior of concrete-rock interfaces differs from that of rock-rock interfaces. Furthermore, the review also shows that the insights achieved relative to the shear behavior of concrete-rock interfaces submitted to lower normal loadings are sufficient to propose numerical modeling capable of simulating the shear behavior of rough concrete-rock interfaces.

The numerical modeling used to simulate the shear behavior of rough concrete-rock interfaces is based on three major understandings gained from the literature review. First, the shear failure of concrete-rock interfaces under low normal loading occurs mainly along the interfaces, indicating that the numerical modeling must focus on the events at the interface rather than the concrete or the rock. This observation means that the behavior law of the model is applied at the interface. Second, the influence of the roughness on the shear resistance of the interface can be separated in two: unevenness drives the formation of concrete-rock bonds. In contrast, the waviness influences the shear resistance through surface interlocking. This aspect results in characterizing the influence of unevenness using the behavior law. However, including a numerical sample with an explicit 3D representation of the roughness is important to add the contribution of the influence of surface interlocking to the overall shear resistance of the interface. Last, the shear response comprises three stages driven by concrete-rock bonds, progressive degradation of the bonds, and progressive mobilization of friction. These three aspects led to the formulation of the behavior law as a combination of the linear elastic behavior to account for the resistance of the concrete-rock bonds before the initiation of the degradation, the damage behavior to simulate the degradation of the

concrete-rock bonds, and the friction for the last stage of the shear response. This behavior law is calibrated using results of direct shear tests of bush-hammered concrete-rock interfaces because these interfaces contain only unevenness. The bush-hammered and rough concrete-rock interface simulation has shown promising results in reproducing the three stages of the shear evolution and reproducing an acceptable estimate of the peak shear strength. This successful simulation allows the investigation of aspects of the shear behavior that cannot be studied easily using an experimental approach. One of the most important aspects that could be investigated through numerical simulations is the influence of roughness on the shear responses using a large and diverse database of rough rock surfaces.

Using the presented numerical model, a new investigation approach is proposed to study the influence of roughness on the shear behavior of interfaces. The approach is presented using the concrete-rock interfaces as a case study but can also be used for rock-rock interfaces. The goal of the approach is to reduce the limitations of existing failure criteria hypothesized as caused by the characteristics of the database of rough rock surfaces used and the number of tests performed. Usually, the database of rough rock surfaces used in most experimental and numerical studies is restricted to a few rough rock blocks collected in a single discontinuity. Such databases of rough rock surfaces are limited in terms of diversity and distribution of roughness values. Regarding the number of tests, it is inconvenient to experimentally perform many tests because of the cost and the necessary logistics. Since collecting a diverse and well-distributed database of rough rock surfaces is difficult, a different methodology is used in the new approach. The methodology uses the geostatistical characteristics of the roughness of a few rock blocks collected experimentally to generate a diverse and well-distributed database of synthetic rough rock surfaces using random field simulations via the turning bands method. With a diverse and well-distributed database of synthetic rough rock surfaces, numerical simulations of direct shear tests can be performed. The results of these virtual tests constitute a database of shear responses of interfaces from which the effect of roughness on the shear behavior can be properly assessed.

For the case of the concrete-rock interfaces considered, 334 synthetic rough surfaces were generated. The roughness values $\theta^*_{\max}/(C+1)$ of these rock surfaces are well distributed between 5°and 25°. Using the synthetic rough rock surfaces generated, numerical simulations of the direct shear tests of concrete-rock interfaces were performed. The results of these simulations yield a significant database of the shear responses of concrete-rock interfaces. Assessing this database of shear responses of synthetic rough concrete-rock interfaces, it was possible to observe that the direct shear tests of interfaces with similar roughness values do not automatically yield very similar peak shear strength. This observation might explain a lot of strange results encountered in the literature. This non-bijectivity roughness/peak shear strength is hypothesized to be caused by the inability of existing roughness parameters to capture the influence of local roughness in the overall shear response of the interfaces. This explanation is supported by experimental studies showing local and progressive shear failure. Furthermore, addressing the main goal of this new approach, two methodologies are used to propose two failure criteria for concrete-rock interfaces. The first is the conventional analytical relationship based on the failure criterion proposed by Grasselli and Egger (Grasselli and Egger, 2003), and the second is a neural network model. The two failure criteria estimate the shear strength of concrete-rock interfaces using the same input parameters (σ_n, Φ_b, $\theta^*_{\max}/(C+1)$). The two models perform well (above 85%) in estimating the peak shear strength of concrete-rock interfaces tested virtually. These models also show promising results when estimating the peak shear strength of concrete-rock interfaces tested experimentally. However, it is worth to note that the neural network model slightly outperforms the analytical model in estimating the peak shear strength of concrete-rock interfaces obtained experimentally or numerically. Furthermore, unlike the analytical model, the neural network model can reproduce

the non-bijectivity of roughness peak shear strength observed in the results of finite elements simulations.

All the geotechnical structures, whose structural stability depends on the shear behavior of interfaces, can experience a dynamic shear loading during their lifetime. However, in the literature, there is no significant interest in investigating the dynamic shear behavior of interfaces. To address this limitation, in this thesis, an investigation of the dynamic shear behavior of concrete-rock interfaces under low normal loading is carried out. This investigation focuses on the dynamic shear loading generated by impact characterized by high strain rates. Even though this study uses concrete-rock interfaces as a case study, its outcomes can serve as a base for investigating rock-rock interfaces. The testing method used in this investigation is based on the basic concepts of the well-established direct shear test. The first stage of the testing method is characterized by applying the confinement stress using a modified confinement ring designed to produce lower normal stresses. In the second stage, the shear loading is applied using a split Hopkinson pressure bar system (SHPB) composed of one input bar and two output bars. The SHPB has been proven to be a reliable methodology for investigating the dynamic behavior of geomaterials. The confinement ring and the SHPB are instrumented with strain gauges for strain measurement, leading to confinement and shear stress computation. The sample used in this test is a prism containing two rock slabs at the extremities and a concrete cast between them. A static shear test using the confinement ring and electromechanical press to apply the shear loading was also used to compare the static and dynamic shear behavior of interfaces. The static shear tests were performed using the same type of sample. Three types of interfaces and two types of rocks are used in this experimental study. These interfaces are; the smooth concrete-sandstone, the bush-hammered concrete-granite, and the rough concrete-granite.

The tests performed in this experimental campaign showed that the static shear behavior could still be separated into the stress accumulation, the shear slip, and the residual shear stress stage. These stages are also driven by the concrete-rock bonds, progressive failure of the bonds, and progressive mobilization of friction and friction only. This separation is similar to separating the shear behavior of interfaces obtained by performing direct shear tests. Consequently, the simple static shear tests presented in this study can be used as an alternative to the direct shear test. The three stages observed in the static shear responses of concrete-rock interfaces were also encountered in the dynamic shear responses of interfaces. However, unlike static shear behavior, the concrete-rock bonds and friction drive the first and second stages together. The third stage depends on friction only. Furthermore, unlike in the static shear behavior, the normal stress is not strongly correlated to the dynamic peak shear strength except for the case of tests with rough concrete-granite interfaces. Moreover, the preliminary comparative assessment of the static and the dynamic peak shear strength of concrete-rock interfaces shows that the dynamic shear strength is equivalent to three to four times their static counterparts.

5.2 **Perspectives**

The suggestions for further investigation of the shear behavior of interfaces focus on the concrete-rock interfaces submitted to lower normal loadings. This presentation is separated into two folds: experimental and numerical.

Many experimental studies could be carried out on the experimental fold to improve upon the significant knowledge achieved on the shear behavior of concrete-rock interfaces.

The bibliography review and the experimental and numerical work in this thesis show that concrete-rock bonds play a crucial role in the shear behavior of concrete-rock interfaces. However,

some aspects that might affect the formation of these bonds deserve further experimental investigations.

The first aspect concerns the influence of the mineral composition of the rock surface on the formation of concrete-rock bonds. This study could be carried out by testing concrete-mineral (crystal) interfaces, which could yield interesting insights into the influence of the surficial chemistry of the mineral surfaces in the formation of concrete-rock bonds. Another approach to address the same problem could be to perform an extended experimental study to characterize the concrete-rock bonds using a variety of rocks to cover the possible combinations of mineral compositions of rock surfaces. As an example of this second approach, in this thesis, two different types of rocks were used: granite as a representative of hard rock and sandstone as a representative of soft rock. The difference in the formation of concrete-rock bonds for these two types of rocks was noticeable. For granite, the formation of concrete-rock bonds depends on the unevenness at the rock surface. Therefore, there is a need to use bush-hammered interfaces. For the sandstone, due to the chemistry of the surface of this rock, there was no need to add micro-roughness (unevenness) to generate concrete-rock bonds. However, many more types of rocks have to be tested to understand even better the influence of the mineral compositions of the rock surfaces on the formation of concrete-rock bonds.

A second aspect that needs to be investigated is the influence of the local roughness on the shear behavior of interfaces. This is true for rock-rock and concrete-rock interfaces. For this aspect, direct shear tests of interfaces could be carried out with X-ray imaging or other imaging techniques to collect displacement fields across the interfaces during the test. The analysis of these displacement fields could lead to a significant understanding of the influence of the local roughness on the overall shear response of the interface. With such an understanding, the existing roughness parameters and failure criteria could be updated to reproduce the non-bijectivity aspect of the roughness/ peak shear strength.

The third aspect is to carry out more experimental studies to investigate the dynamic shear behavior of interfaces, be it rock-rock or concrete-rock. The testing method presented in this thesis could be used as a base and improved upon for such studies. An example of such an improvement could be including full-field measurement techniques to collect displacement fields using digital image correlation. Furthermore, the investigation of the dynamic shear behavior of interfaces should include more types of rocks and different strain rates.

Moreover, further investigations of the dynamic shear behavior of concrete-rock and rock-rock interfaces should be carried out. These studies should include shear loading generated by wave sources such as explosions, seismic events, earthquakes, and repetitive or cyclic loading.

The fourth aspect could be investigating the effect of concrete shrinking (during curing) on the shear behavior of interfaces. The shrinkage of concrete might generate an uncontrolled and unintended condition of partially bonded concrete-rock interfaces, which could significantly affect the shear behavior of concrete-rock interfaces. Within the scope of this possible research topic, the influence of different types of concrete formulations could also be considered.

The last aspect could be related to the upscaling of the experimental study presented in static and dynamic conditions. This suggestion is important to reduce the size effect that affects the shear resistance determined using laboratory experiments. The size effect is an ongoing issue for designing and assessing the stability of geotechnical structures such as concrete-gravity dams, tunnels, rock slopes, and underground excavations. The outcomes of this study could provide valuable insights and more confidence in the characterization and estimation of the shear resistance

of rock-rock and concrete-rock interfaces, which could lead to less conservative approaches usually adopted in the related industries.

Two improvement propositions can be advanced for further work on the numerical fold.

The first proposition could be related to assessing different methods to implement the model to simulate the direct shear tests of concrete-rock interfaces. Examples of such approaches could include discrete element modeling (DEM) and a hybrid FEM/DEM model. The significance of using DEM totally or partially is to attempt to capture better the micro-mechanics of the shear behavior, principally when there starts to be significant damage around the interface. The interest in using other approaches is also to assess aspects such as the concentration of shear resistance across the interface in conjunction with more improved experimental studies. Furthermore, the presented model should be adapted and then implemented for numerical modeling of the dynamic shear behavior of interfaces with the ultimate goal of simulating the dynamic shear tests performed in this thesis.

The second improvement proposition could be related to upscaling the numerical modeling and failure criteria proposed to simulate or estimate the static and dynamic shear resistance of concrete-rock interfaces compatible with the scale of geotechnical structures.

6. Bibliography

Abadi, M. *et al.* (2016) ‘TensorFlow: Large-Scale Machine Learning on Heterogeneous Distributed Systems’.

Abaqus Inc (2014) *Abaqus. Reference manuals v6.14*. Available at: http://130.149.89.49:2080/v6.14/ (Accessed: 3 May 2023).

Abdul-Rahman, R., Saletti, D. and Forquin, P. (2021) ‘Experimental study of the static and dynamic behavior of pre-stressed concrete subjected to shear loading’, *Engineering Structures*, 234, p. 111865. Available at: https://doi.org/10.1016/j.engstruct.2021.111865.

Abdul Rahman, R. (2018) *Experimental Analysis of the confined behavior of concrete under static and dynamic shear loading, Université Grenoble Alpes*.

Alameda-Hernández, P. *et al.* (2014) ‘Improvement of the JRC Calculation Using Different Parameters Obtained Through a New Survey Method Applied to Rock Discontinuities’, *Rock Mechanics and Rock Engineering*, 47(6), pp. 2047–2060. Available at: https://doi.org/10.1007/s00603-013-0532-2.

Alzubaidi, F. *et al.* (2022) ‘Automated Rock Quality Designation Using Convolutional Neural Networks’, *Rock Mechanics and Rock Engineering*, 55(6), pp. 3719–3734. Available at: https://doi.org/10.1007/s00603-022-02805-y.

Badika, M. *et al.* (2022) ‘Influence of Concrete–Rock Bonds and Roughness on the Shear Behavior of Concrete–Rock Interfaces under Low Normal Loading, Experimental and Numerical Analysis’, *Applied Sciences*, 12(11), p. 5643. Available at: https://doi.org/10.3390/app12115643.

Bandis, S., Lumsden, A.C. and Barton, N.R. (1981) ‘Experimental studies of scale effects on the shear behaviour of rock joints’, *International Journal of Rock Mechanics and Mining Sciences & Geomechanics Abstracts*, 18(1), pp. 1–21. Available at: https://doi.org/10.1016/0148-9062(81)90262-X.

Barton, N. and Choubey, V. (1977) ‘The shear strength of rock joints in theory and practice’, *Rock Mechanics Felsmechanik Mecanique des Roches*, 10(1–2), pp. 1–54. Available at: https://doi.org/10.1007/BF01261801.

Barton, N., Wang, C. and Yong, R. (2023) ‘Advances in joint roughness coefficient (JRC) and its engineering applications’, *Journal of Rock Mechanics and Geotechnical Engineering* [Preprint]. Available at: https://doi.org/10.1016/j.jrmge.2023.02.002.

Beer, A.J., Stead, D. and Coggan, J.S. (2002) ‘Estimation of the Joint Roughness Coefficient (JRC) by visual comparison’, *Rock Mechanics and Rock Engineering*, 35(1), pp. 65–74. Available at: https://doi.org/10.1007/s006030200009.

Bertholf, L.D. and Karnes, C.H. (1975) ‘Two-dimensional analysis of the split hopkinson pressure bar system’, *Journal of the Mechanics and Physics of Solids*, 23(1), pp. 1–19. Available at: https://doi.org/10.1016/0022-5096(75)90008-3.

Boulon, M. (1995a) ‘A 3-d direct shear device for testing the mechanical behaviour and the hydraulic conductivity of rock joints.’, in *Proc. Mechanics of Jointed and Faulted*. Vienna, Austria, pp. 407–413.

Boulon, M. (1995b) ‘A 3-D direct shear device for testing the mechanical behaviour and the

hydraulic conductivity of rock joints', in *Proceedings of the Second International Conference on Mechanics of Jointed and Faulted Rock MJFR-2*. Vienna, Austria, pp. 407–413.

Brown, S.R. and Scholz, C.H. (1985) 'Broad bandwidth study of the topography of natural rock surfaces', *Journal of Geophysical Research*, 90(B14), p. 12575. Available at: https://doi.org/10.1029/JB090iB14p12575.

Buzzi, O. *et al.* (2008) 'Leaching of rock-concrete interfaces', *Rock Mechanics and Rock Engineering*, 41(3), pp. 445–466. Available at: https://doi.org/10.1007/s00603-007-0156-5.

Cao, R. *et al.* (2022) 'Shear behaviour of 3D nonpersistent jointed rock-like specimens: Experiment and numerical simulation', *Computers and Geotechnics*, 148, p. 104858. Available at: https://doi.org/10.1016/j.compgeo.2022.104858.

Casagrande, D. *et al.* (2018) *A New Stochastic Approach to Predict Peak and Residual Shear Strength of Natural Rock Discontinuities*, *Rock Mechanics and Rock Engineering*. Springer Vienna. Available at: https://doi.org/10.1007/s00603-017-1302-3.

Chilès, J. and Delfiner, P. (2012) *Geostatistics*. Wiley (Wiley Series in Probability and Statistics). Available at: https://doi.org/10.1002/9781118136188.

Chiu, C.-C. *et al.* (2013) 'Modeling the anisotropic behavior of jointed rock mass using a modified smooth-joint model', *International Journal of Rock Mechanics and Mining Sciences*, 62, pp. 14–22. Available at: https://doi.org/10.1016/j.ijrmms.2013.03.011.

Chollet, F. (2021) *Deep Learning with Python*. Second Edi. Manning.

Cottrell, B. (2009) *Updates to the GG-Shear Strength Criterion*. University of Toronto.

Dai, F. *et al.* (2010) 'Some Fundamental Issues in Dynamic Compression and Tension Tests of Rocks Using Split Hopkinson Pressure Bar', *Rock Mechanics and Rock Engineering*, 43(6), pp. 657–666. Available at: https://doi.org/10.1007/s00603-010-0091-8.

Dantas Neto, S.A. *et al.* (2017) 'Modelling the Shear Behaviour of Clean Rock Discontinuities Using Artificial Neural Networks', *Rock Mechanics and Rock Engineering*, 50(7), pp. 1817–1831. Available at: https://doi.org/10.1007/s00603-017-1197-z.

Davies, E.D.H. and Hunter, S.C. (1963) 'The dynamic compression testing of solids by the method of the split Hopkinson pressure bar', *Journal of the Mechanics and Physics of Solids*, 11(3), pp. 155–179. Available at: https://doi.org/10.1016/0022-5096(63)90050-4.

Dawson RV, Curtis DD, D.R. (1998) *Sliding resistance of concrete gravity dams.* Montreal.

Delavar, M.R. and Ramezanzadeh, A. (2023) 'Pore Pressure Prediction by Empirical and Machine Learning Methods Using Conventional and Drilling Logs in Carbonate Rocks', *Rock Mechanics and Rock Engineering*, 56(1), pp. 535–564. Available at: https://doi.org/10.1007/s00603-022-03089-y.

Deutsch, C. V. and Journel, A.G. (1998) 'GSLIB: geostatistical software library and user's guide. Second edition', *GSLIB: geostatistical software library and user's guide. Second edition* [Preprint].

Dong, W. *et al.* (2021) 'Study on Shear–Softening Constitutive Law of Rock–Concrete Interface', *Rock Mechanics and Rock Engineering*, 54(9), pp. 4677–4694. Available at:

https://doi.org/10.1007/s00603-021-02536-6.

Dong, X. *et al.* (2020) '3D bolted cohesive element for the modelling of bolt-reinforced rough rock-shotcrete interfaces', *Computers and Geotechnics*, 125(August 2019), p. 103659. Available at: https://doi.org/10.1016/j.compgeo.2020.103659.

El-Soudani, S.M. (1978) 'Profilometric analysis of fractures', *Metallography*, 11(3), pp. 247–336. Available at: https://doi.org/10.1016/0026-0800(78)90045-9.

Emery, X. and Lantuéjoul, C. (2006) 'TBSIM: A computer program for conditional simulation of three-dimensional Gaussian random fields via the turning bands method', *Computers and Geosciences*, 32(10), pp. 1615–1628. Available at: https://doi.org/10.1016/j.cageo.2006.03.001.

EPRI (1992) *Uplift pressures, shear strengths, and tensile strengths for stability analysis of concrete gravity dams.* Denver, USA.

Erzar, B. and Forquin, P. (2014) 'Analysis and modelling of the cohesion strength of concrete at high strain-rates', *International Journal of Solids and Structures*, 51(14), pp. 2559–2574. Available at: https://doi.org/10.1016/j.ijsolstr.2014.01.023.

Fardin, N., Feng, Q. and Stephansson, O. (2004) 'Application of a new in situ 3D laser scanner to study the scale effect on the rock joint surface roughness', *International Journal of Rock Mechanics and Mining Sciences*, 41(2), pp. 329–335. Available at: https://doi.org/10.1016/S1365-1609(03)00111-4.

Fardin, N., Stephansson, O. and Jing, L. (2001) 'The scale dependence of rock joint surface roughness', *International Journal of Rock Mechanics and Mining Sciences*, 38(5), pp. 659–669. Available at: https://doi.org/10.1016/S1365-1609(01)00028-4.

Fenton, G.A. and Griffiths, D. V. (2008) *Risk Assessment in Geotechnical Engineering*, *Risk Assessment in Geotechnical Engineering*. Available at: https://doi.org/10.1002/9780470284704.

Fenton, G.A. and Vanmarcke, E.H. (1990) 'Simulation of Random Fields via Local Average Subdivision', *Journal of Engineering Mechanics*, 116(8), pp. 1733–1749. Available at: https://doi.org/10.1061/(ASCE)0733-9399(1990)116:8(1733).

Fishman, Y.A. (2008) 'Features of shear failure of brittle materials and concrete structures on rock foundations', *International Journal of Rock Mechanics and Mining Sciences*, 45(6), pp. 976–992. Available at: https://doi.org/10.1016/j.ijrmms.2007.09.011.

Fishman, Y.A. (2009) 'Stability of concrete retaining structures and their interface with rock foundations', *International Journal of Rock Mechanics and Mining Sciences*, 46(6), pp. 957–966. Available at: https://doi.org/10.1016/j.ijrmms.2009.05.006.

Forquin, P. *et al.* (2022) 'Investigation of the Mechanical Behaviour of Lingulid Sandstone Emphasising the Influence from Pre-Existing Structural Defects, Part 1: Model Identification Based on Static Experiments', *Applied Sciences (Switzerland)*, 12(21). Available at: https://doi.org/10.3390/app122110806.

Forquin, P., Abdul-Rahman, R. and Saletti, D. (2022) 'A novel experimental method to characterise the shear strength of concrete based on pre-stressed samples', *Strain*, 58(2). Available at: https://doi.org/10.1111/str.12407.

Forquin, P. and Sallier, L. (2013) 'A Testing Technique to Characterise the Shear Behaviour of

Concrete at High Strain-Rates', in, pp. 531–536. Available at: https://doi.org/10.1007/978-1-4614-4238-7_68.

Furtney, J.K. *et al.* (2022) 'Surrogate Models in Rock and Soil Mechanics: Integrating Numerical Modeling and Machine Learning', *Rock Mechanics and Rock Engineering*, 55(5), pp. 2845–2859. Available at: https://doi.org/10.1007/s00603-021-02720-8.

Gabet, T., Malécot, Y. and Daudeville, L. (2008) 'Triaxial behaviour of concrete under high stresses: Influence of the loading path on compaction and limit states', *Cement and Concrete Research*, 38(3), pp. 403–412. Available at: https://doi.org/10.1016/j.cemconres.2007.09.029.

Gary, G. and Mohr, D. (2013) 'Modified Kolsky Formulas for an Increased Measurement Duration of SHPB Systems', *Experimental Mechanics*, 53(4), pp. 713–717. Available at: https://doi.org/10.1007/s11340-012-9664-7.

Grasselli, G. (2001) *Shear strength of rock joints based on quantified surface description*. Ecole polytechnique federale de lausanne. Available at: https://infoscience.epfl.ch/record/32880?ln=en.

Grasselli, G. (2006) 'Manuel Rocha Medal Recipient Shear Strength of Rock Joints Based on Quantified Surface Description', *Rock Mechanics and Rock Engineering*, 39(4), pp. 295–314. Available at: https://doi.org/10.1007/s00603-006-0100-0.

Grasselli, G. and Egger, P. (2003) 'Constitutive law for the shear strength of rock joints based on three-dimensional surface parameters', *International Journal of Rock Mechanics and Mining Sciences*, 40(1), pp. 25–40. Available at: https://doi.org/10.1016/S1365-1609(02)00101-6.

Gricad-gitlab (2023) *Introduction au Deep Learning - Fidle, Gricad-Gitlab*. Available at: https://gricad-gitlab.univ-grenoble-alpes.fr/talks/fidle (Accessed: 4 May 2023).

Gu, X.F., Seidel, J.P. and Haberfield, C.M. (2003) 'Direct Shear Test of Sandstone-Concrete Joints', *International Journal of Geomechanics*, 3(1), pp. 21–33. Available at: https://doi.org/10.1061/(asce)1532-3641(2003)3:1(21).

Gutiérrez-Ch, J.G. *et al.* (2018) 'Distinct element method simulations of rock-concrete interfaces under different boundary conditions', *Engineering Geology*, 240(November 2017), pp. 123–139. Available at: https://doi.org/10.1016/j.enggeo.2018.04.017.

Gutiérrez, M.C. (2013) *Shear resistance for concrete dams Laboratory tests*. NTNU.

Haberfield, C.M. and Seidel, J.P. (1999) 'Some recent advances in the modelling of soft rock joints in direct shear', *Geotechnical and Geological Engineering*, 17(3–4), pp. 177–195. Available at: https://doi.org/10.1023/a:1008900905076.

Hans, J. and Boulon, M. (2003) 'A new device for investigating the hydro-mechanical properties of rock joints', *International Journal for Numerical and Analytical Methods in Geomechanics*, 27(6), pp. 513–548. Available at: https://doi.org/10.1002/nag.285.

Haque, A. and Indraratna, B. (2000) 'Experimental and numerical modeling of shear behaviour of rock joints Experimental and numerical modeling of shear behaviour of rock joints'. Available at: https://ro.uow.edu.au/engpapershttps://ro.uow.edu.au/engpapers/671https://ro.uow.edu.au/engpapers/671.

Huang, S., Chen, R. and Xia, K.W. (2010) 'Quantification of dynamic tensile parameters of rocks

using a modified Kolsky tension bar apparatus', *Journal of Rock Mechanics and Geotechnical Engineering*, 2(2), pp. 162–168. Available at: https://doi.org/10.3724/SP.J.1235.2010.00162.

Huang, S., Feng, X.T. and Xia, K. (2011) 'A dynamic punch method to quantify the dynamic shear strength of brittle solids', *Review of Scientific Instruments*, 82(5), p. 053901. Available at: https://doi.org/10.1063/1.3585983.

Indraratna, B., Haque, A. and Aziz, N. (1998) 'Laboratory modelling of shear behaviour of soft joints under constant normal stiffness conditions', *Geotechnical and Geological Engineering*, 16(1), pp. 17–44. Available at: https://doi.org/10.1023/A:1008880112926.

Indraratna, B., Haque, A. and Aziz, N. (1999) 'Shear behaviour of idealized infilled joints under constant normal stiffness', *Géotechnique*, 49(3), pp. 331–355. Available at: https://doi.org/10.1680/geot.1999.49.3.331.

ISRM (1978) 'International society for rock mechanics commission on standardization of laboratory and field tests', *International Journal of Rock Mechanics and Mining Sciences & Geomechanics Abstracts*, 15(6), pp. 319–368. Available at: https://doi.org/10.1016/0148-9062(78)91472-9.

Jahed Armaghani, D. *et al.* (2016) 'Prediction of the uniaxial compressive strength of sandstone using various modeling techniques', *International Journal of Rock Mechanics and Mining Sciences*, 85, pp. 174–186. Available at: https://doi.org/10.1016/j.ijrmms.2016.03.018.

Jang, H.-S., Kang, S.-S. and Jang, B.-A. (2014) 'Determination of Joint Roughness Coefficients Using Roughness Parameters', *Rock Mechanics and Rock Engineering*, 47(6), pp. 2061–2073. Available at: https://doi.org/10.1007/s00603-013-0535-z.

Jeffery, M. (2021) *A preliminary large scale validation of the Stochastic Approach for Discontinuity Shear Strength By This thesis is dedicated to my wife Jordan*.

Jeffery, M. *et al.* (2021) 'A rigorous multiscale random field approach to generate large scale rough rock surfaces', *International Journal of Rock Mechanics and Mining Sciences*, 142, p. 104716. Available at: https://doi.org/10.1016/j.ijrmms.2021.104716.

Johnston, I. W.; Lam, T.S.K. (1984) 'Frictional characteristics of planar concrete-rock interfaces under constant normal stiffness conditions.pdf'.

Journel, A.G. and Huijbregts, C.J. (1976) *Mining geostatistics, London: Academic*. United Kingdom.

Karami, A. and Stead, D. (2008) 'Asperity Degradation and Damage in the Direct Shear Test: A Hybrid FEM/DEM Approach', *Rock Mechanics and Rock Engineering*, 41(2), pp. 229–266. Available at: https://doi.org/10.1007/s00603-007-0139-6.

Khandelwal, M. and Singh, T.N. (2009) 'Prediction of blast-induced ground vibration using artificial neural network', *International Journal of Rock Mechanics and Mining Sciences*, 46(7), pp. 1214–1222. Available at: https://doi.org/10.1016/j.ijrmms.2009.03.004.

Kingma, D.P. and Ba, J.L. (2015) 'Adam: A method for stochastic optimization', *3rd International Conference on Learning Representations, ICLR 2015 - Conference Track Proceedings*, pp. 1–15.

Kodikara, J.K. and Johnston, I.W. (1994) 'Shear behaviour of irregular triangular rock-concrete

joints', *International Journal of Rock Mechanics and Mining Sciences and*, 31(4), pp. 313–322. Available at: https://doi.org/10.1016/0148-9062(94)90900-8.

Krizhevsky, A., Sutskever, I. and Hinton, G.E. (2017) 'ImageNet Classification with Deep Convolutional Neural Networks', *COMMUNICATIONS OF THE ACM*, 60(6). Available at: https://doi.org/10.1145/3065386.

Krounis, A. (2016) *Sliding stability reassessment of concrete dams with bonded concrete-rock interfaces*. KTH Royal Institute of Technology.

Krounis, A., Johansson, F. and Larsson, S. (2016) 'Shear Strength of Partially Bonded Concrete–Rock Interfaces for Application in Dam Stability Analyses', *Rock Mechanics and Rock Engineering*, 49(7), pp. 2711–2722. Available at: https://doi.org/10.1007/s00603-016-0962-8.

Kulatilake, P.H.S.W., Um, J. and Pan, G. (1998) 'Requirements for accurate quantification of self-affine roughness using the variogram method', *International Journal of Solids and Structures*, 35(31–32), pp. 4167–4189. Available at: https://doi.org/10.1016/S0020-7683(97)00308-9.

Lo KY, Lukajic B, Wang S, Ogawa T, T.K. (1990) 'Evaluation of strength parameters of concrete–rock interface for dam safety assessment.', in *Proceedings Canadian Dam Safety Conference*, pp. 71–93.

Lam, T.S.K. and Johnston, I.W. (1989) 'Shear Behavior of Regular Triangular Concrete/Rock Joints—Evaluation', *Journal of Geotechnical Engineering*, 115(5), pp. 728–740. Available at: https://doi.org/10.1061/(ASCE)0733-9410(1989)115:5(728).

Lanaro, F. (2000) 'A random field model for surface roughness and aperture of rock fractures', *International Journal of Rock Mechanics and Mining Sciences*, 37(8), pp. 1195–1210. Available at: https://doi.org/10.1016/S1365-1609(00)00052-6.

Lantuéjoul, C. (1994) 'Non Conditional Simulation of Stationary Isotropic Multigaussian Random Functions', in, pp. 147–177. Available at: https://doi.org/10.1007/978-94-015-8267-4_13.

Le, T.-T. *et al.* (2022) 'Correlating the Unconfined Compressive Strength of Rock with the Compressional Wave Velocity Effective Porosity and Schmidt Hammer Rebound Number Using Artificial Neural Networks', *Rock Mechanics and Rock Engineering*, 55(11), pp. 6805–6840. Available at: https://doi.org/10.1007/s00603-022-02992-8.

Li, J. *et al.* (2022) 'Study on dynamic shear deformation behaviors and test methodology of sawtooth-shaped rock joints under impact load', *International Journal of Rock Mechanics and Mining Sciences*, 158, p. 105210. Available at: https://doi.org/10.1016/j.ijrmms.2022.105210.

Liahagen, S. (2012) *Stabilitet av betongdammer - Ruhetens påvirkning på skjærkapasiteten mellom betong og berg*. NTNU.

Lukić, B. and Forquin, P. (2016) 'Experimental characterization of the punch through shear strength of an ultra-high performance concrete', *International Journal of Impact Engineering*, 91, pp. 34–45. Available at: https://doi.org/10.1016/j.ijimpeng.2015.12.009.

Maerz, N.H., Franklin, J.A. and Bennett, C.P. (1990) 'Joint roughness measurement using shadow profilometry', *International Journal of Rock Mechanics and Mining Sciences and*, 27(5), pp. 329–343. Available at: https://doi.org/10.1016/0148-9062(90)92708-M.

Magsipoc, E., Zhao, Q. and Grasselli, G. (2020) '2D and 3D Roughness Characterization', *Rock Mechanics and Rock Engineering*, 53(3), pp. 1495–1519. Available at: https://doi.org/10.1007/s00603-019-01977-4.

Malinverno, A. (1990) 'A simple method to estimate the fractal dimension of a self-affine series', *Geophysical Research Letters*, 17(11), pp. 1953–1956. Available at: https://doi.org/10.1029/GL017i011p01953.

Malmgren, L., Nordlund, E. and Rolund, S. (2005) 'Adhesion strength and shrinkage of shotcrete', *Tunnelling and Underground Space Technology*, 20(1), pp. 33–48. Available at: https://doi.org/10.1016/j.tust.2004.05.002.

Mantoglou, A. and Wilson, J.L. (1982) 'The Turning Bands Method for simulation of random fields using line generation by a spectral method', *Water Resources Research*, 18(5), pp. 1379–1394. Available at: https://doi.org/10.1029/WR018i005p01379.

Matheron, G. (1973) 'The Intrinsic Random Functions and', *Applied Probability*, 5(3), pp. 439–468.

Meng, H. and Li, Q.M. (2003) 'Correlation between the accuracy of a SHPB test and the stress uniformity based on numerical experiments', *International Journal of Impact Engineering*, 28(5), pp. 537–555. Available at: https://doi.org/10.1016/S0734-743X(02)00073-8.

El Merabi, B. (2018) 'Mechanical behavior of cohesive concrete-rock joints at the dam-foundation interface : geometrical and mechanical influence of asperities To cite this version : HAL Id : tel-01783168 Bassel El Merabi cohésifs de béton-granite au niveau de l ' interface ba'.

Meulenkamp, F. and Grima, M.A. (1999) 'Application of neural networks for the prediction of the unconfined compressive strength (UCS) from Equotip hardness', *International Journal of Rock Mechanics and Mining Sciences*, 36(1), pp. 29–39. Available at: https://doi.org/10.1016/S0148-9062(98)00173-9.

Miah, M.I. *et al.* (2020) 'Machine Learning Approach to Model Rock Strength: Prediction and Variable Selection with Aid of Log Data', *Rock Mechanics and Rock Engineering*, 53(10), pp. 4691–4715. Available at: https://doi.org/10.1007/s00603-020-02184-2.

Mohr, D., Gary, G. and Lundberg, B. (2010) 'Evaluation of stress-strain curve estimates in dynamic experiments', *International Journal of Impact Engineering*, 37(2), pp. 161–169. Available at: https://doi.org/10.1016/j.ijimpeng.2009.09.007.

Moradian, Z. A. *et al.* (2010) 'Evaluating damage during shear tests of rock joints using acoustic emissions', *International Journal of Rock Mechanics and Mining Sciences*, 47(4), pp. 590–598. Available at: https://doi.org/10.1016/j.ijrmms.2010.01.004.

Moradian, Z.A. *et al.* (2010) 'Evaluating damage during shear tests of rock joints using acoustic emissions', *International Journal of Rock Mechanics and Mining Sciences*, 47(4), pp. 590–598. Available at: https://doi.org/10.1016/j.ijrmms.2010.01.004.

Moradian, Z.A., Ballivy, G. and Rivard, P. (2012) 'Application of acoustic emission for monitoring shear behavior of bonded concrete–rock joints under direct shear test', *Canadian Journal of Civil Engineering*, 39(8), pp. 887–896. Available at: https://doi.org/10.1139/l2012-073.

Mouzannar, H. (2016) *Caractérisation de la résistance au cisaillement et comportement des*

interfaces entre béton et fondation rocheuse des structures hydrauliques. Université de Lyon.

Mouzannar, H. *et al.* (2017) 'Experimental Study of the Shear Strength of Bonded Concrete–Rock Interfaces: Surface Morphology and Scale Effect', *Rock Mechanics and Rock Engineering*, 50(10), pp. 2601–2625. Available at: https://doi.org/10.1007/s00603-017-1259-2.

Muralha, J. *et al.* (2014) 'ISRM suggested method for laboratory determination of the shear strength of rock joints: Revised version', *Rock Mechanics and Rock Engineering*, 47(1), pp. 291–302. Available at: https://doi.org/10.1007/s00603-013-0519-z.

Murali, A.K. *et al.* (2022) 'Experimental and Numerical Investigation of the Load-Bearing Mechanisms of Piles Socketed in Soft Rocks', *Rock Mechanics and Rock Engineering*, 55(9), pp. 5555–5576. Available at: https://doi.org/10.1007/s00603-022-02954-0.

Park, J.-W. and Song, J.-J. (2009) 'Numerical simulation of a direct shear test on a rock joint using a bonded-particle model', *International Journal of Rock Mechanics and Mining Sciences*, 46(8), pp. 1315–1328. Available at: https://doi.org/10.1016/j.ijrmms.2009.03.007.

Patton, F.D. (1966) 'Multiple modes of shear failure in rock', *1st ISRM Congress 1966*, pp. 509–513.

Piotrowska, E., Forquin, P. and Malecot, Y. (2016) 'Experimental study of static and dynamic behavior of concrete under high confinement: Effect of coarse aggregate strength', *Mechanics of Materials*, 92, pp. 164–174. Available at: https://doi.org/10.1016/j.mechmat.2015.09.005.

Pyrcz, M.J. and Deutsch, C. V. (2020) 'Transforming Data to a Gaussian Distribution', *Geostatistics Lessons*, pp. 1–4.

Qiu, H. *et al.* (2022) 'Investigating dynamic fracture in marble-mortar interface under impact loading', *Construction and Building Materials*, 336, p. 127548. Available at: https://doi.org/10.1016/j.conbuildmat.2022.127548.

Rabbani, E. *et al.* (2012) 'Application of neural network technique for prediction of uniaxial compressive strength using reservoir formation properties', *International Journal of Rock Mechanics and Mining Sciences*, 56, pp. 100–111. Available at: https://doi.org/10.1016/j.ijrmms.2012.07.033.

Rajesh Kumar, B. *et al.* (2013) 'Regression analysis and ANN models to predict rock properties from sound levels produced during drilling', *International Journal of Rock Mechanics and Mining Sciences*, 58, pp. 61–72. Available at: https://doi.org/10.1016/j.ijrmms.2012.10.002.

Renaud, S., Bouaanani, N. and Miquel, B. (2020) 'Numerical simulation of experimentally shear-tested contact specimens from existing dam joints', *Computers and Geotechnics*, 125(August 2019), p. 103630. Available at: https://doi.org/10.1016/j.compgeo.2020.103630.

Ruggeri, G. (2004) 'Sliding safety of existing gravity dams - Final report', *International Commission on Large Dams* [Preprint].

Rukhaiyar, S. and Samadhiya, N.K. (2017) 'A polyaxial strength model for intact sandstone based on Artificial Neural Network', *International Journal of Rock Mechanics and Mining Sciences*, 95, pp. 26–47. Available at: https://doi.org/10.1016/j.ijrmms.2017.03.012.

Rullière, A. *et al.* (2020) 'Influence of Roughness on the Apparent Cohesion of Rock Joints at Low Normal Stresses', *Journal of Geotechnical and Geoenvironmental Engineering*, 146(3).

Available at: https://doi.org/10.1061/(ASCE)GT.1943-5606.0002200.

Saiang, D., Malmgren, L. and Nordlund, E. (2005) 'Laboratory Tests on Shotcrete-Rock Joints in Direct Shear, Tension and Compression', *Rock Mechanics and Rock Engineering*, 38(4), pp. 275–297. Available at: https://doi.org/10.1007/s00603-005-0055-6.

Sakaridis, E., Karathanasopoulos, N. and Mohr, D. (2022) 'Machine-learning based prediction of crash response of tubular structures', *International Journal of Impact Engineering*, 166. Available at: https://doi.org/10.1016/j.ijimpeng.2022.104240.

Samson, M. and Deutsch, C. V (2021) 'The Sill of the Variogram', pp. 1–6.

Serasa, A.S. *et al.* (2017) 'Peak Friction Angle Estimation from Joint Roughness Coefficient of Discontinuities of Limestone in Peninsular Malaysia', *Sains Malaysiana*, 46(02), pp. 181–188. Available at: https://doi.org/10.17576/jsm-2017-4602-01.

Shang, J., Zhao, Z., *et al.* (2018) '3D Particle-Based DEM Investigation into the Shear Behaviour of Incipient Rock Joints with Various Geometries of Rock Bridges', *Rock Mechanics and Rock Engineering*, 51(11), pp. 3563–3584. Available at: https://doi.org/10.1007/s00603-018-1531-0.

Shang, J., Yokota, Y., *et al.* (2018) 'DEM simulation of mortar-bolt interface behaviour subjected to shearing', *Construction and Building Materials*, 185, pp. 120–137. Available at: https://doi.org/10.1016/j.conbuildmat.2018.07.044.

Shang, J., Zhao, Z. and Ma, S. (2018) 'On the shear failure of incipient rock discontinuities under CNL and CNS boundary conditions: Insights from DEM modelling', *Engineering Geology*, 234, pp. 153–166. Available at: https://doi.org/10.1016/j.enggeo.2018.01.012.

Shen, Y. *et al.* (2019) 'Influence of surface roughness and hydrophilicity on bonding strength of concrete-rock interface', *Construction and Building Materials*, 213, pp. 156–166. Available at: https://doi.org/10.1016/j.conbuildmat.2019.04.078.

Sjodin, B. (2021) *How to Convert Point Cloud Data to Surfaces and Solids, COMSOL*. Available at: https://www.comsol.com/blogs/how-to-convert-point-cloud-data-to-surfaces-and-solids/ (Accessed: 1 July 2023).

Suits, L & Sheahan, TC & Seidel, Julian & Haberfield, C. (2002) 'Laboratory Testing of Concrete-rock Joints in Constant Normal Stiffness Direct Shear', *Geotechnical Testing Journal*, 25(4), pp. 391–404. Available at: https://doi.org/10.1520/GTJ11292J.

Sujatha, V. and Kishen, J.M.C. (2003) 'Energy Release Rate due to Friction at Bimaterial Interface in Dams', *Journal of Engineering Mechanics*, 129(7), pp. 793–800. Available at: https://doi.org/10.1061/(ASCE)0733-9399(2003)129:7(793).

Tatone, Bryan S.A. and Grasselli, G. (2009) 'A method to evaluate the three-dimensional roughness of fracture surfaces in brittle geomaterials', *Review of Scientific Instruments*, 80(12). Available at: https://doi.org/10.1063/1.3266964.

Tatone, Bryan S. A. and Grasselli, G. (2009) 'A method to evaluate the three-dimensional roughness of fracture surfaces in brittle geomaterials', *Review of Scientific Instruments*, 80(12), p. 125110. Available at: https://doi.org/10.1063/1.3266964.

Tatone, B.S.A., Grasselli, G. and Cottrell, B. (2010) 'Accounting for the influence of measurement resolution on discontinuity roughness estimates', *Rock Mechanics in Civil and*

Environmental Engineering - Proceedings of the European Rock Mechanics Symposium, EUROCK 2010, (March), pp. 203–206. Available at: https://doi.org/10.1201/b10550-45.

Tawfik, A. *et al.* (2022) 'A testing device to investigate the properties of strain-hardening, cement-based composites (SHCC) under impact shear loading', *International Journal of Impact Engineering*, 167, p. 104280. Available at: https://doi.org/10.1016/j.ijimpeng.2022.104280.

Thirukumaran, S. and Indraratna, B. (2016) 'A review of shear strength models for rock joints subjected to constant normal stiffness', *Journal of Rock Mechanics and Geotechnical Engineering*, 8(3), pp. 405–414. Available at: https://doi.org/10.1016/j.jrmge.2015.10.006.

Tian, H.M. *et al.* (2015) 'Experimental and Numerical Analysis of the Shear Behaviour of Cemented Concrete–Rock Joints', *Rock Mechanics and Rock Engineering*, 48(1), pp. 213–222. Available at: https://doi.org/10.1007/s00603-014-0560-6.

Tian, Y. *et al.* (2018) 'Updates to Grasselli's Peak Shear Strength Model', *Rock Mechanics and Rock Engineering*, 51(7), pp. 2115–2133. Available at: https://doi.org/10.1007/s00603-018-1469-2.

Tse, R. and Cruden, D.M. (1979) 'Estimating joint roughness coefficients', *International Journal of Rock Mechanics and Mining Sciences & Geomechanics Abstracts*, 16(5), pp. 303–307. Available at: https://doi.org/10.1016/0148-9062(79)90241-9.

Ulusay, R. (ed.) (2015) *The ISRM Suggested Methods for Rock Characterization, Testing and Monitoring: 2007-2014*. Cham: Springer International Publishing. Available at: https://doi.org/10.1007/978-3-319-07713-0.

Vu, X.H. *et al.* (2009) 'Experimental analysis of concrete behavior under high confinement: Effect of the saturation ratio', *International Journal of Solids and Structures*, 46(5), pp. 1105–1120. Available at: https://doi.org/10.1016/j.ijsolstr.2008.10.015.

Wackernagel, H. (2003) *Multivariate Geostatistics*. Berlin, Heidelberg: Springer Berlin Heidelberg. Available at: https://doi.org/10.1007/978-3-662-05294-5.

Wang, H.-C. *et al.* (2021) 'Dynamic mechanical properties and fracturing behaviour of concrete under biaxial compression', *Construction and Building Materials*, 301, p. 124085. Available at: https://doi.org/10.1016/j.conbuildmat.2021.124085.

Westberg Wilde, M. and Johansson, F. (2013) 'System Reliability of Concrete Dams with Respect to Foundation Stability: Application to a Spillway', *Journal of Geotechnical and Geoenvironmental Engineering*, 139(2), pp. 308–319. Available at: https://doi.org/10.1061/(asce)gt.1943-5606.0000761.

Xia, K. (2012) 'Status of characterization of strength and fracture properties of rocks under dynamic loading', *Rock Fragmentation by Blasting: Fragblast 10*, pp. 41–52. Available at: https://doi.org/10.1201/b13759-10.

Xia, K. and Yao, W. (2015) 'Dynamic rock tests using split Hopkinson (Kolsky) bar system - A review', *Journal of Rock Mechanics and Geotechnical Engineering*, 7(1), pp. 27–59. Available at: https://doi.org/10.1016/j.jrmge.2014.07.008.

Yang, Z.Y., Lo, S.C. and Di, C.C. (2001) 'Reassessing the Joint Roughness Coefficient (JRC) Estimation Using Z 2', *Rock Mechanics and Rock Engineering*, 34(3), pp. 243–251. Available at: https://doi.org/10.1007/s006030170012.

Yesiloglu-Gultekin, N., Gokceoglu, C. and Sezer, E.A. (2013) ‘Prediction of uniaxial compressive strength of granitic rocks by various nonlinear tools and comparison of their performances’, *International Journal of Rock Mechanics and Mining Sciences*, 62, pp. 113–122. Available at: https://doi.org/10.1016/j.ijrmms.2013.05.005.

Yin, X. *et al.* (2023) ‘Rate- and Normal Stress-Dependent Mechanical Behavior of Rock Under Direct Shear Loading Based on a Bonded-Particle Model (BPM)’, *Rock Mechanics and Rock Engineering* [Preprint]. Available at: https://doi.org/10.1007/s00603-023-03486-x.

Yılmaz, I. and Yuksek, A.G. (2008) ‘An Example of Artificial Neural Network (ANN) Application for Indirect Estimation of Rock Parameters’, *Rock Mechanics and Rock Engineering*, 41(5), pp. 781–795. Available at: https://doi.org/10.1007/s00603-007-0138-7.

Yu, X. and Vayssade, B. (1991) ‘Joint profiles and their roughness parameters’, *International Journal of Rock Mechanics and Mining Sciences & Geomechanics Abstracts*, 28(4), pp. 333–336. Available at: https://doi.org/10.1016/0148-9062(91)90598-G.

Zhang, Q.B. and Zhao, J. (2014) ‘A Review of Dynamic Experimental Techniques and Mechanical Behaviour of Rock Materials’, *Rock Mechanics and Rock Engineering*, 47(4), pp. 1411–1478. Available at: https://doi.org/10.1007/s00603-013-0463-y.

Zhao, J. (1997a) ‘Joint surface matching and shear strength part A: joint matching coefficient (JMC)’, *International Journal of Rock Mechanics and Mining Sciences*, 34(2), pp. 173–178. Available at: https://doi.org/10.1016/S0148-9062(96)00062-9.

Zhao, J. (1997b) ‘Joint surface matching and shear strength part B: JRC-JMC shear strength criterion’, *International Journal of Rock Mechanics and Mining Sciences*, 34(2), pp. 179–185. Available at: https://doi.org/10.1016/S0148-9062(96)00063-0.

Zhao, W., Chen, W. and Zhao, K. (2018) ‘Laboratory test on foamed concrete-rock joints in direct shear’, *Construction and Building Materials*, 173, pp. 69–80. Available at: https://doi.org/10.1016/j.conbuildmat.2018.04.006.

Zhou, Z., Lu, J. and Cai, X. (2020) ‘Static and dynamic tensile behavior of rock-concrete bi-material disc with different interface inclinations’, *Construction and Building Materials*, 256, p. 119424. Available at: https://doi.org/10.1016/j.conbuildmat.2020.119424.

List of Figures

Figure 1.1 Mohr-Coulomb failure criterion for interfaces 4
Figure 1.2 Patton failure criterion. Modified from Kounis (Krounis, 2016)..... 5
Figure 1.3 Standards roughness profiles with defined JRC (Barton and Choubey, 1977)..... 7
Figure 1.4 Barton's comb (Barton, Wang and Yong, 2023); a) laboratory and b) field 10
Figure 1.5 Example of an image obtained through the scanner used by Grasselli (Grasselli, 2001) 11
Figure 1.6 Laser-based scanning device developed by Hans and Boulon (El Merabi, 2018)..... 11
Figure 1.7 Definition of a scanning path (El Merabi, 2018) 12
Figure 1.8 Scanning rough rock surfaces using the device developed by Hans and Boulon 12
Figure 1.9 Influence of roughness expressed using the JRC on the estimation of the shear strength (a) JRC=20, (b) JRC=10, and (c) JRC=5, for $\sigma c/\sigma n$ equivalent to 5, 10, 50, and 100 (Barton, Wang and Yong, 2023) 13
Figure 1.10 Contact area at the beginning of the application of the shear loading. (Grasselli, 2001)..... 15
Figure 1.11 Identification of triangles facing the shear direction for roughness analysis. Inspired by Tian et al. (Tian *et al.*, 2018) 16
Figure 1.12 3D roughness computation (Grasselli, 2001)..... 17
Figure 1.13 Influence of the measurement resolution on the computation of $\boldsymbol{\theta max * / C + 1}$ (Tatone, Grasselli and Cottrell, 2010). 180° represents the shear direction considered in the roughness computation. 18
Figure 1.14 Shear evolution during the direct shear test of concrete-rock interfaces for both the (a) flat interfaces and (b) the rough interfaces (Jeffery, 2021) 20
Figure 1.15 BCR3D direct shear test machine: 1 is the sample, 2 is the internal metallic box, and 3 is the external metallic box, 4 loading cells, 5 horizontal actuators, 6 rigid frame, 7 LVDT in the y direction, 8 rigid column, 9 LVDT vertical direction, 10 vertical actuators, and 11 rigid vertical translating system (Buzzi *et al.*, 2008) 21
Figure 1.16 Typical behaviors of concrete-rock interface: (a) with good adhesion and lower normal stress, and (b) with poor adhesion and higher normal stress. Modified from Saiang et al. (Saiang, Malmgren and Nordlund, 2005) 22
Figure 1.17 Acoustic emissions during the direct shear test on bonded concrete-rock interface under low normal load: evolution of shear stress and logarithmic acoustic emission energy in the shear displacement. Modified from Moradian et al. (Moradian, Ballivy and Rivard, 2012) 23
Figure 1.18 Evolution of shear stress and cumulative acoustic emission energy regarding the shear displacement. Modified from Moradian et al. (Moradian, Ballivy and Rivard, 2012) 24
Figure 1.19 Shear stress of smooth concrete-granite interfaces (Badika *et al.*, 2022)..... 26
Figure 1.20 Types of shear evolution of bush-hammered concrete-granite interfaces (Badika *et al.*, 2022)..... 27
Figure 1.21 Mohr-Coulomb envelop for bush-hammered and rough concrete-granite interfaces (Badika *et al.*, 2022) 28
Figure 1.22 Schematic of the split Hopkinson pressure bar and a displacement (x) time (t) of stress propagation in the test (Xia and Yao, 2015). 29
Figure 1.23 Schematic of the split Hopkinson tension bar and a displacement (x) time (t) of stress propagation in the test (Huang, Chen and Xia, 2010) 30
Figure 1.24 SHPB for the punch-through shear test (Huang, Feng and Xia, 2011)..... 30
Figure 1.25 Schematic representation of the dynamic shear test proposed by Li et al. (Li *et al.*, 2022)..... 31
Figure 1.26 Illustration of the (a) parallel bonded model and (b) smooth joint model Modified from Shang et al.(Shang, Zhao, *et al.*, 2018) 33

Figure 1.27 a) Asperity sliding and b) Shearing through asperities. Modified from Haberfield and Seidel (Haberfield and Seidel, 1999) 34
Figure 1.28 Illustration of the (a) flat joint contact model (FJCM) and the (b) linear model (LM). Modified from Shang et al. (Shang, Yokota, *et al.*, 2018) 35
Figure 1.29 Illustration of the Cohesive damage plasticity model – CDPM. Modified from Murali et al. (Murali *et al.*, 2022) 37
Figure 1.30 Definition of a random function model (Wackernagel, 2003) 38
Figure 1.31 Quantile-to-quantile normal scores transformation (Pyrcz and Deutsch, 2020) 40
Figure 1.32 One-dimensional application of random field simulation using LAS (Fenton and Vanmarcke, 1990; Fenton and Griffiths, 2008) 41
Figure 1.33 Transformation of the 2D trace to obtain three daughter profiles for random field simulation using the LAS algorithm (Jeffery *et al.*, 2021) 42
Figure 2.1 Main stages of the shear evolution of concrete-rock interfaces under low normal loading. Modified from Badika et al. (Badika *et al.*, 2022) 46
Figure 2.2 Boundaries conditions of the numerical simulations 49
Figure 2.3 Mesh sensitivity of the behavior law using simulation of bush-hammered interfaces 50
Figure 2.4 Mesh concrete, granite, and steel box, close-up of the interface 50
Figure 2.5 Node adjustment to eliminate initial overclosure. Modified from Abaqus. (Abaqus Inc, 2014) 51
Figure 2.6 Stiffness of concrete-rock bond; a) Concrete-dolomite (Tian *et al.*, 2015) b) Shotcrete-magnetite (Saiang, Malmgren and Nordlund, 2005) 51
Figure 2.7 Setup of the simulation of bush-hammered interfaces 52
Figure 2.8 Calibration of the interface behavior law first failure mode (0.5 MPa) 54
Figure 2.9 Calibration of the interface behavior law second failure mode (1.0-1.5 MPa) 54
Figure 2.10 An example of a parametric surface generated using the point cloud of a rough rock surface 55
Figure 2.11 Final geometry created out of the point cloud of rough concrete surface. 56
Figure 2.12 Concrete and rock part for the simulation of the shear behavior of rough concrete-rock interfaces 56
Figure 2.13 Damage evolution at a single contact constraint: CSDMG 57
Figure 2.14 Distribution of the cohesive surface damage parameter across the interface during the shear evolution point P2 58
Figure 2.15 Distribution of the cohesive surface damage parameter across the interface during the shear evolution point P2 58
Figure 2.16 Distribution of the cohesive surface damage parameter across the interface during the shear evolution point P3 59
Figure 2.17 Distribution of the cohesive surface damage parameter across the interface during the shear evolution point P4 59
Figure 2.18 Stress concentration: effect of surface interlocking caused by waviness of the interface Point P1 60
Figure 2.19 Stress concentration: effect of surface interlocking caused by waviness of the interface Point P2 61
Figure 2.20 Stress concentration: effect of surface interlocking caused by waviness of the interface Point P3 61
Figure 2.21 Stress concentration: effect of surface interlocking caused by waviness of the interface Point P4 62
Figure 2.22 Stress concentration: effect of surface interlocking caused by waviness of the interface Point PF 62
Figure 2.23 Evolution of the shear stress in terms of the shear displacement for tests carried out under 0.5 MPa of confinement: experimental vs. numerical 63

Figure 2.24 Evolution of the shear stress in terms of the shear displacement for tests carried out under 1.0 MPa of confinement: experimental vs. numerical 64
Figure 2.25 Evolution of the shear stress in terms of the shear displacement for tests carried out under 1.5 MPa of confinement: experimental vs. numerical 65
Figure 3.1 Data transformation for the rough granite sample used in test 10 (Refer to Chapter 2). Nscore values are transformations of heights of asperities such that the field is normalized. 70
Figure 3.2 Variogram analysis of the rough granite surface used in test 10 (Refer to Chapter 2), two directions (see azimuth)..... 72
Figure 3.3 Turning bands method. Inspired by Mantoglou and Wilson (Mantoglou and Wilson, 1982), Lantuéjul (Lantuéjoul, 1994), and Emery and Lantuéjul (Emery and Lantuéjoul, 2006) . 73
Figure 3.4 Synthetic rough rock surface generator using random field simulation 74
Figure 3.5 Variograms of simulated rough rock surfaces 75
Figure 3.6 Synthetic rough rock surfaces generated; (a) sample 1 and (b) sample 2..... 76
Figure 3.7 Roughness of the synthetic rough rock surfaces generated; $\boldsymbol{\theta max} * / (\boldsymbol{C} + \mathbf{1})$ 76
Figure 3.8 Selected results of the finite element simulations: (a) first failure mode (0.5 MPa) and (b) second failure mode (1.5 MPa)..... 77
Figure 3.9 Peak shear strength in terms of roughness $\boldsymbol{\theta max} * / (\boldsymbol{C} + \mathbf{1})$; (a) GP1 confinement 0.5 MPa and (b) GP2 confinement 1.5 MPa 78
Figure 3.10 Shear strength estimated using the analytical model in terms of numerically obtained peak shear strength: a) first failure mode (0.5 MPa) and b) second failure mode (1.5 MPa) 80
Figure 3.11 Error of the estimated peak shear strength in terms of the simulated peak shear strength: a) first failure mode (0.5 MPa) and b) second failure mode (1.5 MPa). A. model in the y-axis stands for analytical model. 80
Figure 3.12 Training and validation datasets 82
Figure 3.13 Example of a typical neural network architecture (Inspired by Fidle class notes (Gricad-gitlab, 2023)). 83
Figure 3.14 Neuron of a neural network (Modified from Fidle class notes (Gricad-gitlab, 2023)) 83
Figure 3.15 Influence of the number of layers on the performance of the model..... 85
Figure 3.16 Influence of the number of layers on the performance of the model..... 86
Figure 3.17 Influence of the size of the batch on the performance of the model..... 86
Figure 3.18 k-Folds cross-validation analysis 87
Figure 3.19 Performance of the neural network for the estimation of the peak shear strength 88
Figure 3.20 FE peak shear strength in terms of NN peak shear strength (test dataset) and (b) NN predicted peak shear strength in terms of the roughness and percent error (test dataset) 88
Figure 3.21 Assessment of the analytical model: a) Experimental vs. estimated peak shear strength (0.5, 1.0, and 1.5 MPa) and b) Percent error between the Experimental and the estimated peak shear strength. Gp1 and Gp2 stand for group 1 (here normal stress equals 0.5 MPa) and group 2 (here normal stress equals 1.0 and 1.5 MPa), representing the two failure modes discussed in section 1.3.2 and chapter 2 89
Figure 3.22 Assessment of the neural network model: a) Experimental vs. estimated peak shear strength (0.5 and 1.5 MPa) and b) Percent error between the Experimental and the estimated peak shear strength..... 90
Figure 3.23 Estimation of the peak shear strength (a) Failure criterion (b) Neural network model 91
Figure 3.24 Error of the estimation of the peak shear strength (a) analytical model and (b) Neural network model..... 91
Figure 3.25 Hyperparameter analysis for the neural network model to estimate the shear response of concrete-rock interfaces: (a) Influence of number of layers, (b) influence of the number of

neurons per layer, (c) influence of the batch size, and (d) variation of the performance of the model after multiple training 93
Figure 3.26 Learning curve of the training of the neural network to estimate the shear response of concrete-rock interfaces 94
Figure 3.27 (a) Peak shear strength extracted from the predicted shear response obtained using neural network modeling (validation dataset) in terms of peak shear strength extracted from the shear response obtained using FE simulations and (b) percent error of (a) 94
Figure 3.28 Peak (a) Peak shear strength extracted from the predicted shear response obtained using neural network modeling (Experimental) in terms of peak shear strength obtained experimental tests (b) percent error of (a) 95
Figure 3.29 Comparison between the predicted and the numerically obtained shear responses of concrete-rock interfaces using NN and FE simulation: (a) T37 and (b) T26 96
Figure 3.30 Comparison between the predicted and the numerically obtained shear responses of concrete-rock interfaces using NN and FE simulation: (a) T239 and (b) T261 96
Figure 3.31 Comparison between the predicted and the experimentally obtained shear responses of concrete-rock interfaces using NN and tests: (a) Block 1 and (b) Block 2 97
Figure 3.32 Comparison between the predicted and the experimentally obtained shear responses of concrete-rock interfaces using NN and tests: (a) Block 3 and (b) Block 4 97
Figure 3.33 Comparison between the predicted and the experimentally obtained shear responses of concrete-rock interfaces using NN and tests: (a) Block 5 and (b) Block 6 98
Figure 3.34 Comparison between the predicted and the experimentally obtained shear responses of concrete-rock interfaces using NN and tests: (a) Block 12 and (b) Block 13 98
Figure 3.35 Comparison between the predicted and the experimentally obtained shear responses of concrete-rock interfaces using NN and tests: (a) Block 14 and (b) Block 15 99
Figure 3.36 Assessment of the MAE: computed using the comparison between the overall shear responses predicted and the FE shear responses obtained (model), calculated using the peak shear strength extracted from the predicted shear response and the peak shear strength obtained via FE simulation (validation) and Experimental tests (ExpPeak) 99
Figure 3.37 Peak shear strength obtained through neural networks models (validation dataset) in terms of peak shear strength extracted from the shear response obtained using FE simulations: (a) Model that estimates the peak shear strength (section 3.4, 3.5, and 3.6), (b) Model that estimates the overall shear response 100
Figure 3.38 Assessment of the MAE (a) Model that estimates the peak shear strength (sections 3.4, 3.5, and 3.6), (b) Model that estimates the overall shear response 101
Figure 4.1 Rectification of the rock surfaces using a sanding machine 104
Figure 4.2 Rock slabs and plot of triangulations of the field of heights of asperities to illustrate the difference in roughness level. 105
Figure 4.3 Example of the sample with two concrete-rock interfaces 106
Figure 4.4 Confinement of the sample 107
Figure 4.5 Boundaries conditions used in the simulations to modify the confinement ring: (a) loading the ring, (b) loading the sample 108
Figure 4.6 Confinement ring 109
Figure 4.7 Contour plot illustrating the hoop strain in the confinement rings of different thicknesses when generating 2 MPa of confinement stress 110
Figure 4.8 (a) Hoop strain distribution across the outward and the inward circumference of the ring in terms of the angle θ (b) illustration of the angle θ 110
Figure 4.9 Installation of strain gauges 111
Figure 4.10 Calibration of the ring 112
Figure 4.11 Calibration curves for the confinement ring with 7.5 mm thickness (g1) 112
Figure 4.12 Static shear test setup 113

Figure 4.13 Dynamic shear test setup 114
Figure 4.14 Installation of strain gauges in the output bars. 115
Figure 4.15 Dynamic shear test using the SHPB and the confinement ring 115
Figure 4.16 Pulse shaper 116
Figure 4.17 Illustration of the static shear test using the confinement ring and the electromechanical press Instron 100 kN 117
Figure 4.18 Typical static shear response of tests with smooth concrete-sandstone (StatSCS1) 118
Figure 4.19 Linear regression: static peak shear strength – normal stress. Case of smooth concrete-sandstone interfaces ($\boldsymbol{c = 1.57}$ MPa and $\boldsymbol{\phi i = 44.89}$ º) 118
Figure 4.20 Typical static shear response of bush-hammered interfaces (StatBHCG1) 119
Figure 4.21 Linear regression: static peak shear strength – normal stress. Case of bush-hammered concrete-granite interfaces ($\boldsymbol{c = 1.56}$ MPa and $\boldsymbol{\phi i = 46.9}$ º) 119
Figure 4.22 Static shear response of rough concrete-granite: (a) StatRCG1 and (b) StatRCG2 120
Figure 4.23 Linear regression: static peak shear strength – normal stress. Case of rough concrete-granite interfaces($\boldsymbol{c = 0.71}$ MPa and $\boldsymbol{\phi i = 57.6}$ º) 120
Figure 4.24 Illustration of the dynamic shear test of concrete-rock interfaces using the SHPB and the confinement ring 121
Figure 4.25 Illustration of the dynamic shear responses of concrete-rock interfaces (DynSCS1). For legend, refer to Figure 4.13. 121
Figure 4.26 Dynamic shear response of smooth concrete-sandstone: (a) DynSCS1 and (b) DynSCS2 122
Figure 4.27 Linear regression: dynamic peak shear strength – normal stress. Case of smooth concrete-sandstone interfaces 122
Figure 4.28 Dynamic shear responses of bush-hammered interfaces: (a) DynBHCG1 and (b) DynBHCG2 123
Figure 4.29 Linear regression: dynamic peak shear strength – normal stress. Case of bush-hammered concrete-granite interfaces 123
Figure 4.30 Dynamic shear response of bush-hammered concrete-granite: (a) DynBHCG1 and (b) DynBHCG2 124
Figure 4.31 Linear regression: dynamic peak shear strength – normal stress. Case of rough concrete-granite interfaces ($\boldsymbol{c = 4.42}$ MPa and $\boldsymbol{\phi i = 79.42}$ º) 124
Figure 4.32 Static shear evolution of concrete-rock interface (sample StatBHCG1) 126
Figure 4.33 Static shear responses of rough concrete-granite: (a) StatRCG1 and (b) StatRCG2 127
Figure 4.34 Dynamic shear response of concrete-rock interface (DynBHCG1) 128
Figure 4.35 Dynamic shear response of concrete-rock (DynRCG1) 129
Figure 4.36 Shear resistance in terms of confinement stress: (a) smooth concrete-sandstone, (b) bush-hammered concrete-granite and (c) rough concrete-granite interfaces 130
Figure 4.37 Static - dynamic shear / tensile strength of interfaces: (a) smooth concrete-sandstone / concrete-limestone and (b) bush-hammered concrete-granite / concrete-limestone 131

List of Tables

Table 2.1 Mechanical properties of concrete, rocks, and steel used in the simulations. Based on the experimental work conducted by Mouzannar (Mouzannar, 2016) 49
Table 2.2 Parameter of the behavior law 53
Table 2.3 Peak and residual shear strength of rough concrete-granite interfaces: experimental vs. numerical 66
Table 4.1 Roughness characterization of rock surfaces 105
Table 4.2 Concrete formula: R30A7 106
Table 4.3 Mechanical properties of concrete and rocks (Mouzannar, 2016; Abdul Rahman, 2018; Forquin *et al.*, 2022) 106
Table 4.4 Testing program 107
Table 4.5 Mechanical properties of Aluminum 109
Table 4.6 Gauges coefficient after calibration 113
Table 4.7 Results of static and dynamic tests 125